

POLITECNICO DI TORINO

Collegio di Ingegneria Biomedica

Corso di Laurea Magistrale

in Ingegneria Biomedica

Master Thesis Project

**Finite element analysis of dental restorations
by using Micro-CT based 3D models**



Supervisors

Prof. Lorenzo Peroni

Prof. Alessandro Scattina

Candidate

Matteo Muggeo

Dicembre 2019

Table of contents

1. INTRODUCTION	7
1.1. General Overview	7
1.2. Tooth structure, restoration and materials composition	8
1.3. FEM analysis introduction and dental application	13
2. METHOD	21
2.1. Workflow Definition	21
2.1.1. First procedure	22
2.1.2. Second procedure	32
2.1.3. Third procedure	44
2.2. FEM simulation	60
3. MODELS VALIDATIONS	69
4. RESULTS AND DISCUSSIONS	83
4.1. First model	83
4.2. Second model	92
4.3. Third model	101
5. CONCLUSIONS	111
REFERENCES	113



Quest'opera è stata rilasciata con licenza Creative Commons Attribuzione 3.0 Italia. Per leggere una copia della licenza visita il sito web <http://creativecommons.org/licenses/by/3.0/it/> o spedisci una lettera a Creative Commons, PO Box 1866, Mountain View, CA 94042, USA.

ABSTRACT

Objectives: To create a 3-D FEM model of II-MOD cavity direct restoration tooth from a micro-CT scansion; the aim of this thesis was to define a reliable workflow that allowed FEM tooth model generation. All the required steps were defined to extend their feasibility to different micro-CT scansions, three different methods were compared and their results were assessed to determine the optimum procedure.

After the model generation several simulations were performed by defining all the required parameters; materials, contacts, loads and boundaries conditions were set to simulate a chewing machine load cycle, the simulation was performed through LS-Dyna.

Different loads and boundaries were evaluated:

- First model, with node set load and nodal boundaries conditions
- Second model, with chewing sphere load and nodal boundaries conditions
- Third model, with chewing sphere load and resin disk support to lock the tooth.

The interface shear stress and pressure were assessed through an internal LS-Dyna database, which was previously validated.

Finally, interface tensions were worked out for all the models in order to evaluate the loads and boundary conditions impact on the restorations debonding stress.

Results: Workflow procedure creation was performed by defining all the steps, the final results led to a totally FEM-based procedure where the cavities were directly imported from the Micro-CT slices.

Global stress and displacements were analysed to evaluate the fillers debonding in all the investigated loads and boundaries conditions showing that in the second and third model debonding phenomena were likely to occur on the smaller filler.

The debonding phenomena were assessed through an interface database, which was validated by comparing its results with theoretical distributions, interface shear stress and pressure were proved to be totally reliable.

The interface stress showed peaks on the fillers rear base for all the models, in the second and third model maximum values were located on the upper part of both the interfaces in the region as close as possible to the enamel-chewing sphere contact points.

Finally, first model results were proved to be not coherent with those of the second and third model because of the unrealistic load modelling whereas second and third model showed coherent stress and displacements.

1. INTRODUCTION

1.1. General Overview

When restorations were performed on a tooth with cavities different parameters needed to be evaluated in order to make the better choice; as matter of fact, different restorative materials and techniques were available as well as different adhesive layers.

In modern dentistry, all these choices were taken by the dentist according with his/her experience and no other parameters were taken into account.

The restored teeth underwent a chewing process that consisted in a fatigue load whose effects could lead the restorations to detach from the tooth.

Therefore, the possibility to perform a fatigue FEM analysis could provide an important tool to prevent the fatigue failure by optimizing the restoration parameters.

The aim of this thesis is the evaluation of the tooth restorations debonding phenomena throughout a single load chewing process. As matter of fact, this evaluation will be performed on a tooth FEM model.

The thesis will deal with specific dentistry vocabularies especially related to the restorations that were performed on cavities teeth, all these notions were illustrated in Chapter 1.

Furthermore, Chapter 1 will provide an introduction on the FEM method principles as well as on their application in the dentistry field.

The sample that was taken into account was a molar with II-MOD cavity direct restoration provided by Dental School where a Micro-CT scansion was performed creating digital slices.

Three different attempts were made to define a reliable workflow that allowed converting these slices into a volumetric 3-D FEM model, the 3-D models were created through different software.

The reconstruction attempts results were analysed and compared each other by evaluating several parameters, workflow definitions and three attempts results were illustrated in Chapter 2.

Moreover, the different models parameters in terms of boundaries and loading conditions adopted to perform the simulations were explained in Chapter 2.

Ls-Dyna software was chosen to simulate a single load cycle with different loads and boundaries conditions, three different models were assessed and their results were compared.

In Chapter 4, displacements, global stress and interface stress were evaluated for these models in order to identify the critical debonding regions.

The interface database was validated on a simple model by comparing the results with theoretical values and distributions, the results were showed in Chapter 3.

1.2. Tooth structure, restoration and materials composition

In this section the biological and medical notions to introduce the tooth FEM model creation will be provided.

The tooth is divided into two anatomic parts, which are the root and the crown ^[1].

The crown is the external part of the tooth whereas the root is placed inside the jaw; its function is to immobilize the tooth inside a bony socket, the whole tooth structure is showed in Figure 1.1.

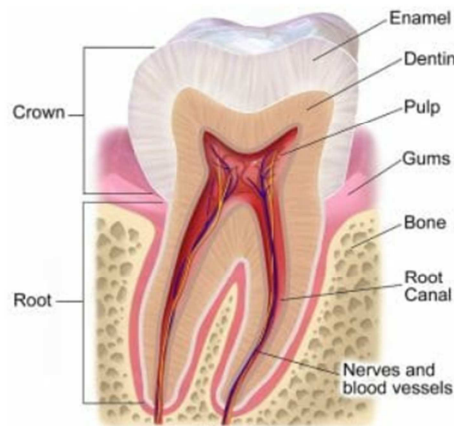


Figure 1.1: Section of tooth with the anatomic parts in evidence ^[2]

The main tooth components are ^[1]:

- Enamel that forms the crown outside part being the hardest component, despite its properties caries could occur if teeth are not properly cleaned.
- Dentine is the internal part protected by enamel because of its less hardness and poorest mechanical properties.
Dentine is made up of hydroxyapatite (45%), organic material (33%) and water (22%) whereas minerals account for 96% of the whole enamel percentage ^[3].
- Pulp that is located in the internal part protected by dentine and enamel and it is composed by nerves and blood, its function is to vascularize the tooth allowing pain and other sensations.
- Cementum, which consists in a thin layer surrounding the root and ensuring contact with jaw.

This complex system is completed by structure around the tooth like periodontal ligament, gingivae and bone.

The complicated tooth structure allows to absorb forces and to relieve stress ^[4], these tasks are performed through the interaction between the components described above.

Tooth can be affected by different pathologies that could compromise its functions, the principal tooth conditions are described in this paragraph.

Cavities are the most common tooth condition, they occur when bolus, acid or bacteria cover tooth with a thin layer by forming a plaque that corrodes enamel ^[5]; consequently, the dentine is exposed leading to potential permanent damages.

1. INTRODUCTION

Gingivitis is an inflammation of the gums that are shown in Figure 1.1, it is generated by a plaque whose formation is caused by a poor dental care, this pathology causes both gums bleeding and swelling leading to periodontitis if not treated properly.

Periodontitis is the gingivitis evolution, the infection could extend to jaw and bones by leading to an important inflammatory response.

Oral cancer is a dangerous condition that includes different tumours:

- Gums Cancer;
- Tongue Cancer;
- Lips Cancer;
- Cheek Cancer;
- Floor of the mouth Cancer;
- Hard and Soft Palate Cancer.

The bigger risk factor for Oral Cancer pathology is the tobacco consumption^[5].

Oro-dental trauma is caused by traumatic events involving the oral system whose world percentage injuries stands at around 20%^[6], these events can be generated by multiple factors such as oral and environmental factors or risk-taking behaviours.

Worldwide, approximately 3.6 billion people (48% of the population) have dental caries in their permanent teeth as of 2016.

World Health Organization estimates that approximately all adults have dental caries at some point time^[6]; these caries need to be restored by paying the appropriate treatments that strongly depends on the specific problems. In USA, a dental care check-up could cost around \$288 whereas a filling procedure price is in an interval between \$50 and \$4500 for different filler materials.

In case a tooth can not be restored a tooth extraction is required, the maximum prices for those surgery with anaesthesia is around \$600^[7]. Therefore, major interests' lies with tooth cavities restoration method study in order to tackle this common and expensive pathology.

When the tooth integrity, function and morphology is compromised resulting from caries or external trauma a dental restoration is performed to restore the dental health^[8].

The restorations are classified into two main types: direct and indirect, both further divided in subcategories by location and size.

- Direct technique involves placing a soft or malleable filling into the prepared tooth building its up, then the filling material shrinks becoming harder and the restoration is performed. Three restorative materials are used in common direct applications^[9] :
 1. Silver Amalgam is a mixed metallic compound, which is characterized by an economic price, long duration and reliability. Drawbacks of this filler are the thermal expansion and the possibility to enclose bolus and bacteria leading to dental caries;
 2. Resin-made Fillings that are widespread for their adaptability to different shapes but they are more expensive and with lower durability than the former fillers;
 3. Glass ionomer Fillings are generated with a mixture of silicate glass powder and polyacrylic acid to form a bactericidal compound.
Teeth that need to bear low forces because of their secondary importance in chewing process are usually made with the latter material.
- Indirect technique is quite different from the previous method; restoration is manufactured outside the mouth with a dental impression of the prepared tooth that is placed inside the mouth in a second time.

1.2. Tooth structure, restoration and materials composition

Since more work has to be done in order to perform an indirect restoration price is higher than direct restoration method, advantages of those restorations are the aesthetic and the stability when the damage is diffused^[9].

Figure 1.2 shows three different forms of indirect restoration methods

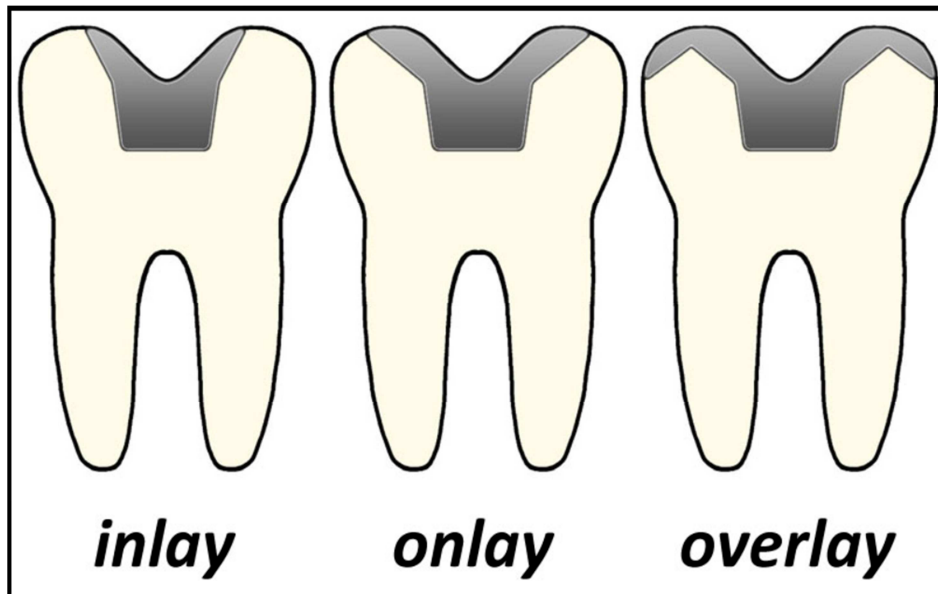


Figure 1.2: Inlays and onlays indirect restorations

Figure 1.3 shows a direct restoration with a gold fillers material, which can be used for restore the anatomic situation but it is expensive.



Figure 1.3: typical example of direct posterior gold restoration^[11]

In both the indirect and direct restorations cement contact with the tooth inner surface is ensured through an adhesive layer, this layer shrinks during the positioning process with an applied temperature gradient^[12].

1. INTRODUCTION

This interface turned out to be a critical part for its function; the stress associated with the shrinkage could lead to gaps creation as well as to generation of cracking either in the tooth or in the filler materials, as shown in Figure 1.4.

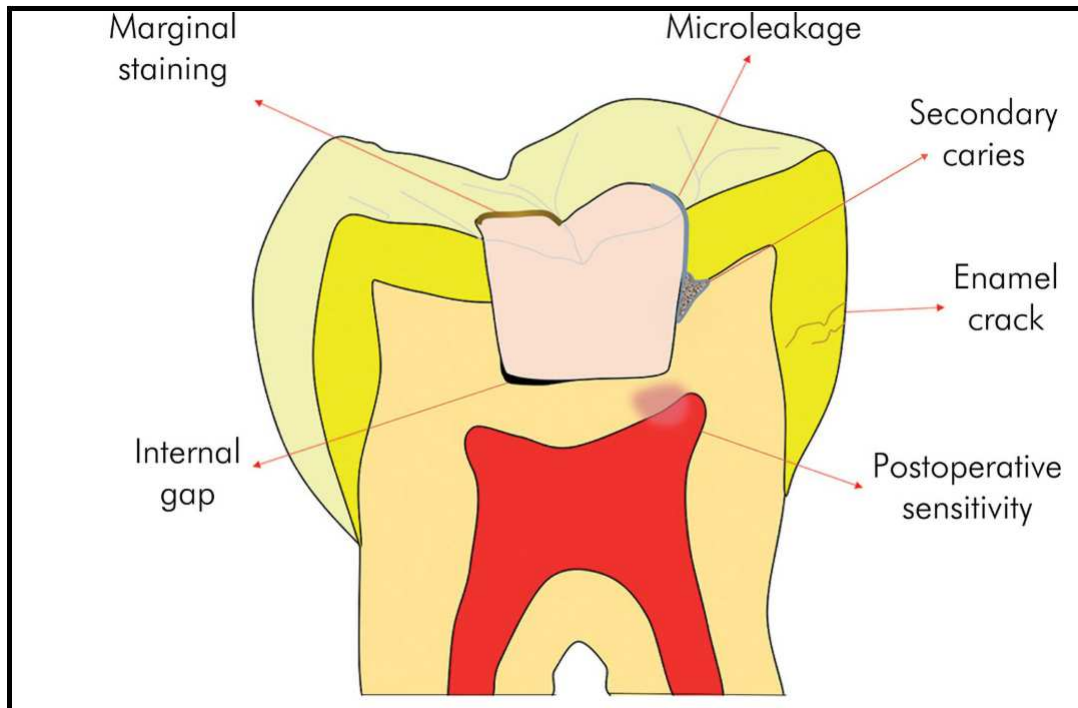


Figure 1.4: crack generation process due to shrinking phenomena ^[13]

Therefore, during chewing process the restorative materials are glued to the tooth by creating a critical interface that could possibly detach during the tooth life. Direct and indirect restoration methods classify the types of surgeries that need to be done in order to restore the normal tooth condition but other classifications are needed to discern the dental cavities.

An American dentist G.V.Black invented a caries classification system to distinguish cavities, which are located in different positions ^[14]:

- Class 1 caries are developmental cavities in the pit and fissures of teeth;
- Class 2 caries cavities form on the proximal (mesial or distal) surfaces on the posterior teeth;
- Class 3 caries cavities form on the interproximal surface (mesial or distal) of anterior teeth;
- Class 4 caries cavities form on the interproximal surface (mesial or distal) of anterior teeth and include the incisal edge;
- Class 5 caries cavities form on the cervical third of the facial or lingual surfaces of the teeth;
- Class 6 caries cavities that involve the incisal or occlusal surface that has been worn away due to abrasion.

A cavity can be further classified in simple, compound and complex. Simple cavity involves only one surface while compound and complex cavities are composed by two and more than two surfaces, respectively.

This thesis will deal with Class 2 mesio-occlusal-distal (MOD) cavities restoration, which is classified into complex cavity; Figure 1.5 shows a typical MOD caries.

1.2. Tooth structure, restoration and materials composition



Figure 1.5: Classic example of MOD cavities ^[15]

These cavities are usually described through a specific system of surfaces that need to be defined in order to understand complex cavity classifications, like the before mentioned MOD-cavities. Therefore, the tooth surfaces are listed below and they are showed in the Figure 1.6 ^[16].

- The distal surface that is away from the midline of the face.
- The facial surface that faces the cheeks or lips. It can be further divided in labial or buccal if surfaces are towards the lips or cheeks, respectively.
- The Incisal verge, which is the biting edge of an anterior tooth.
- Lingual surface that faces the tongue.
- Mesial surface that is closest to the midline of the face.
- Occlusal chewing surface of posterior teeth.
- Proximal tooth surfaces that are next to each other (i.e., distal of lateral incisor and mesial of canine).

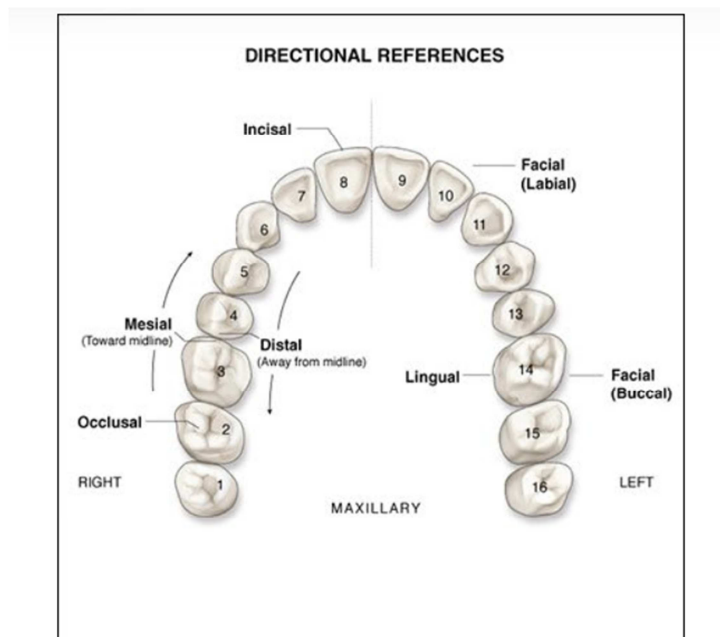


Figure 1.6: Tooth surfaces classification scheme ^[16]

1.3. FEM analysis introduction and dental application

In this chapter FEM method and its application in dentistry will be introduced. Finite element method is one of most useful and popular tools in the engineering world.

A complex volume is divided into smaller regular elements connected each other through nodes and with no interpenetrations. FEM allows simplifying a system of differential equations that can not be solved by approximating those equations with a system of linear equations ^[17].

In this method the displacements are calculated in the nodes through the inversion of the global stiffness matrix by obtaining global system displacements, then elements shape functions are applied to approximate the element internal displacements, after that strain and stress are worked out ^[18].

This method leads to some approximations that should be taken into account when the results are analysed; first, each element is made up of nodes whose number influence the elements degrees of freedom, more nodes per element means more degrees of freedom. The nodes introduction set a limit on the degrees of freedom of the structure increasing its stiffness.

As consequence of that, the number of nodes should be increased for a better modelling but more are the nodes more simulation time will be requested. Therefore, the nodes number should be calculated considering that the elements global displacements are worked out through shape functions that are strongly influenced by them ^[18]. As matter of fact, a certain number of nodes set the degree of the shape functions and the overall element displacements will be evaluated by taking into account the functions complexities. As consequence of that, shape functions introduce a strong approximation by assuming the displacement function and by forcing the displacement on its direction ^[17].

The model generation is a delicate step that determines whether a result can be acceptable or not; all the calculations are performed on a model and not on the real structure, therefore the reality is simplified by creating a model which is supposed to be as close to the physical simulation as possible. This model introduces an irreversible approximation, which should be considered when its results are compared with those of the physical simulations ^[18].

Finally, other parameters could also influence the simulation results, these parameters are mainly the boundaries conditions, the loads and other specific parameters that depend on the simulation; for example, in crash simulation contact modelling plays an important role. Generally, when two or more objects bumping into each other are simulated contacts become a parameter that need to be carefully tuned.

In particular, boundaries conditions as well as contacts are non-linearity sources ^[19].

As mentioned before, complex geometries are divided into simpler elements, the reason lies with the possibility to calculate the real stiffness matrix for those elements through specific equations whereas this is not possible for complicated structures ^[17].

All the stiffness matrix are calculated in local axes systems and then they are converted in a global axes systems, these operations are performed in order to assemble single elements stiffness matrices into the global matrix of the structure.

The figure 1.7 shows how in the assembling procedures some components interact by summing their value because they share information on the same nodes.

1.3. FEM analysis introduction and dental application

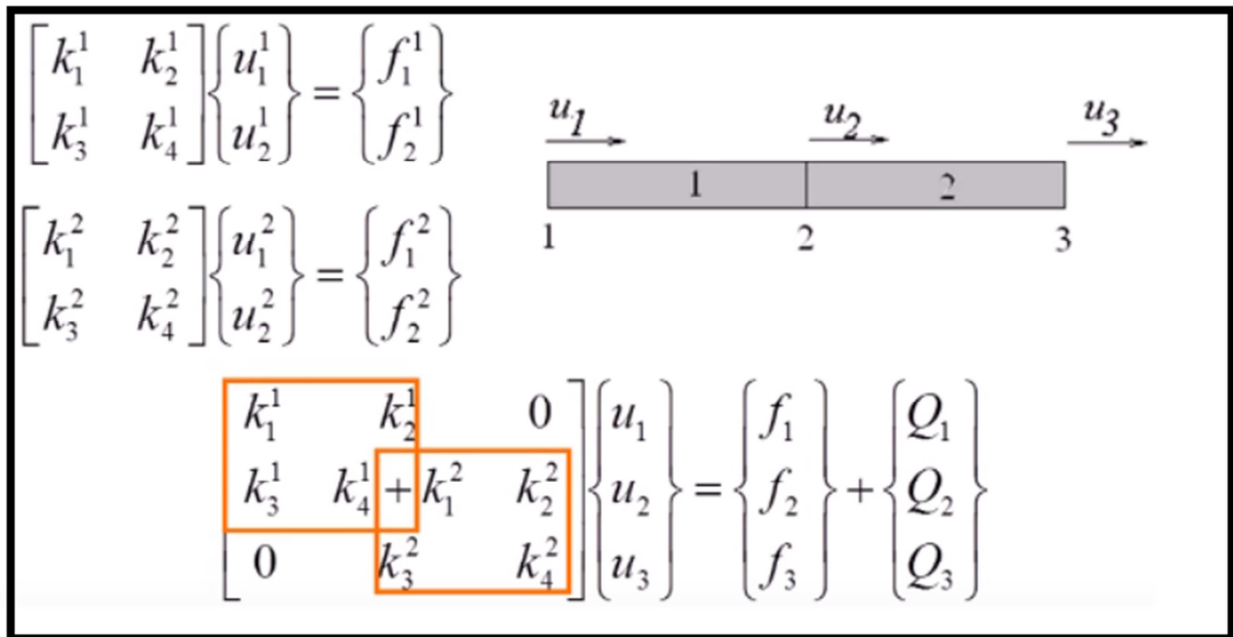


Figure 1.7: Stiffness matrix assembling process ^[20]

The matrix presents some null values, which means that not all the displacements are influenced by all the forces and not all the forces are influenced by all the displacements.

When loads and boundaries conditions are set some of the displacements and force values of the external elements are known, therefore, it is possible the evaluation of all the nodal forces and displacements through the inversion of the stiffness matrix ^[21].

The inversion of global stiffness matrix allow obtaining structural force and displacements. All the nodal global displacements are converted into their local elements systems, then these nodal displacements are fit through shape functions to approximate the internal element displacements fields, an example of shape function is showed in Figure 1.8.

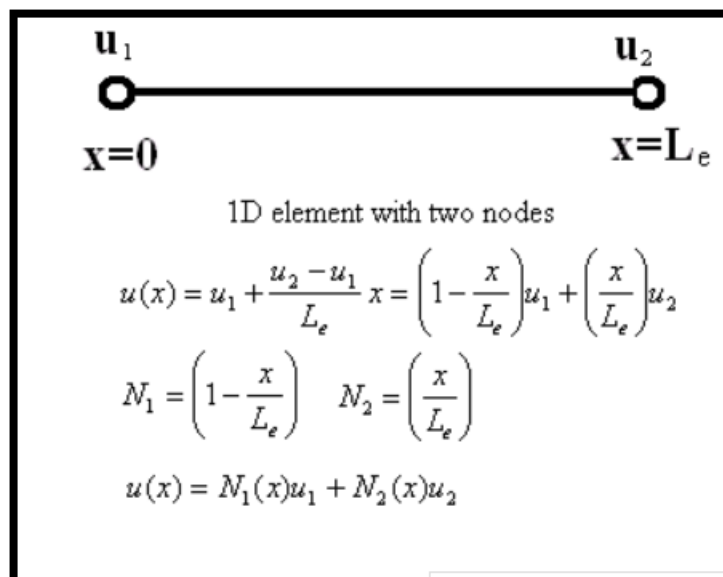


Figure 1.8: Shape function for a two nodes beam element ^[22]

It is therefore possible to work out the displacements in all the elements points.

1. INTRODUCTION

Internal strain distributions can be obtained through the derivation of the shape function as shown in Figure 1.9.

$$\underline{\varepsilon} = [B] \underline{u}^{\text{element}} = \begin{bmatrix} \varepsilon_{11} \\ \varepsilon_{22} \\ 2\varepsilon_{12} \end{bmatrix} = \begin{bmatrix} \frac{\partial N_a}{\partial x_1} & 0 & \frac{\partial N_b}{\partial x_1} & 0 & \frac{\partial N_c}{\partial x_1} & 0 \\ 0 & \frac{\partial N_a}{\partial x_2} & 0 & \frac{\partial N_b}{\partial x_2} & 0 & \frac{\partial N_c}{\partial x_2} \\ \frac{\partial N_a}{\partial x_2} & \frac{\partial N_a}{\partial x_1} & \frac{\partial N_b}{\partial x_2} & \frac{\partial N_b}{\partial x_1} & \frac{\partial N_c}{\partial x_2} & \frac{\partial N_c}{\partial x_1} \end{bmatrix} \begin{bmatrix} u_1^{(a)} \\ u_2^{(a)} \\ u_1^{(b)} \\ u_2^{(b)} \\ u_1^{(c)} \\ u_2^{(c)} \end{bmatrix}$$

Figure 1.9: Strain calculation obtained by the derivation of the shape functions^[23]

Finally, FEM analysis require also material properties, which can be used for calculate the stress distributions after the strain evaluation. Therefore, in order to obtain realistic stress values the material properties should be chosen carefully^[17].

Another important point is to understand how the equations, which make up the matrix are solved in order to obtain the nodal forces and displacements.

The solution is calculated in different times that are established by the simulation time-step, the simulation can be carried out with implicit or explicit methods^[24].

In the implicit methods, the solution is worked out by calculating and inverting the stiffness matrix for all the time-steps.

These operations are computationally intensive, which means that they take a lot of time, leading also to a stable solution for bigger time-steps.

By contrast, in the explicit method the mass matrix is inverted only one time and then the solution is calculated with no need to invert the stiffness matrix^[18]. The drawback of the explicit method is that it is stable within a certain time-step interval with an upper limit that can be analytically worked out, therefore, explicit methods required higher number of time-steps than the implicit method. Implicit and explicit methods both exist because they are useful in different applications, figure 1.10 shows which method is convenient in terms of CPU cost in different situations.

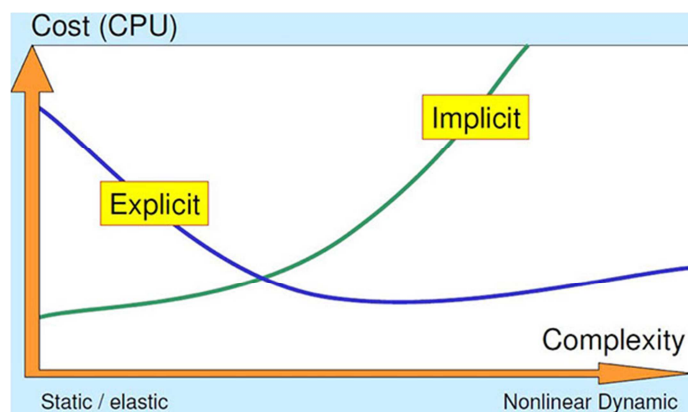


Figure 1.10: Comparison between CPU running time for both implicit and explicit solvers^[24]

Explicit method finds its main application in nonlinear problems with short simulation times such as crash tests otherwise implicit is preferred, the latter method is more suited for elastic and linear

1.3. FEM analysis introduction and dental application

problems. The maximum time step used for the explicit analysis can be defined as half of the minimum time that the sound waves take to pass through the element ^[17].

The tooth FEM analysis that has been carried out in this thesis are nonlinear, which means that the relation between the forces are not directly proportional to the displacements as shown in Figure 1.11. In non-linear explicit analysis the running time raise is caused by the decrease of the stable time-step interval upper limit, therefore, more steps are needed to solve non-linear simulations than those required when the model is linear.

Instead, in non-linear implicit analysis the stiffness matrix need to be assembled and the inversion need to be performed more times than in the linear analysis leading to a simulation time rise ^[25].

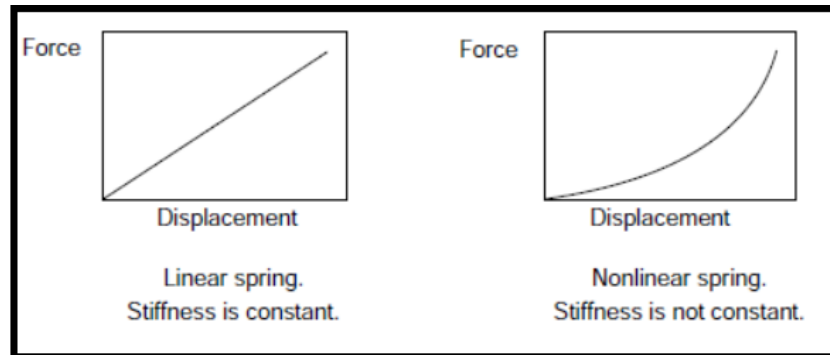


Figure 1.11: difference between linear and nonlinear FEM simulations ^[25]

An important source of non-linearity are materials which could have a non-linear relation between the stress and the strain ^[18], however it depends on the material types since simple materials such as elastic materials have a linear behaviour. As a matter of fact, some materials can be considered linear within a certain interval as shown in Figure 1.12.

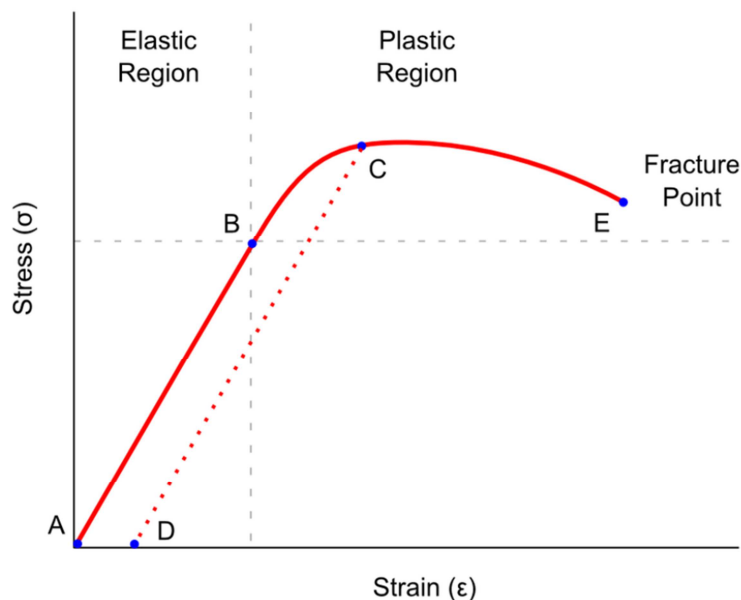


Figure 1.12: Ductile material with an elastic behaviour within a certain strain range ^[26]

Boundaries conditions could certainly be a non-linearity source in FEM analysis since they could change throughout the running times. Certain nodes could change their position coming in contact with boundaries conditions ^[19].

1. INTRODUCTION

The Figure 1.13 clarifies the boundary non-linearity, when the force is applied to the cantilever beam it collides with the stop device by changing its boundaries conditions.

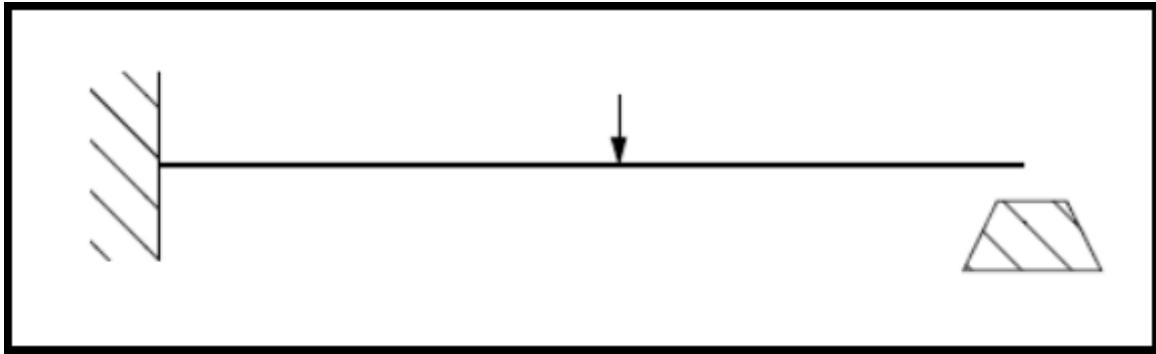


Figure 1.13: An example of nonlinear boundary condition ^[27]

All the contact problems fall into this category of nonlinearity source ^[18].

This thesis will focus on contact modelling in tooth FEM analysis in order to assess the interface debonding conditions between tooth and fillers, as shown in Figure 1.4.

Therefore, a careful contact modelling is needed in order to address this challenging issue.

Contact provides a way to treat interactions between parts allowing the stress propagation.

The contacts are divided in two different main types: penalty-based contacts and constraint-based contacts ^[28].

In the penalty-based contact, a spring is used for connect both the side of the surfaces, when a penetration occurs a distance is defined and springs apply a force against those penetrations, which are proportional to the penetration distance. Penalty formulation is showed in Figure 1.14.

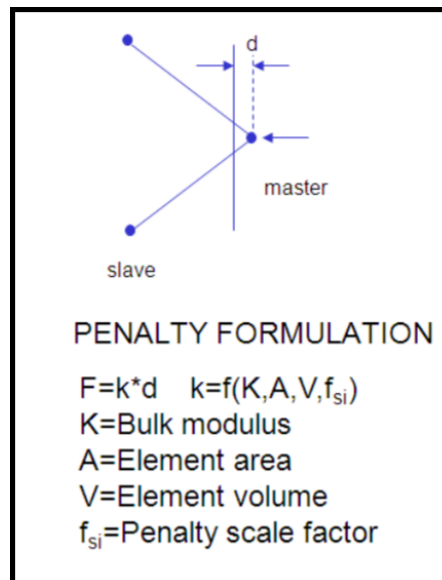


Figure 1.14: LS-Dyna method to work out penalty forces ^[29]

The spring constant depends on the element volumes, element stiffness and contact segment area. In general higher is the penalty forces smaller are the penetrations but the contact stability drops.

1.3. FEM analysis introduction and dental application

The reliability of this contact formulation depends on the similarities between the surfaces stiffness properties. In case they are not similar, contact may not work properly and another formulation is required^[28].

Constraint based method uses also springs whose stiffness can be evaluated by considering the nodal masses that come into contact and the global time step. The resulting contact stiffness turned out to be independent of the material features and fit for very different material contacts. The stiffness can be calculated with the following equation 1.1^[30].

$$k = SOFSCL \times \frac{m}{\Delta t^2} \quad (1.1)$$

Where m is the nodal mass, Δt is the global time step and $SOFSCL$ is a scale factor that is automatically applied to ensure the stability and it is usually set around 0.1.

As mentioned in the overview, FEM simulations will be performed through LS-Dyna that allows choosing among a large numbers of contact models.

These models are widely described in the online documentations provided by Livermore Software Technology Corporation^[30], therefore, only the adopted contact model is introduced in this section.

A penalty-based tied contact is adopted in order to simulate the action of the adhesive layer; tied contact simulates the gluing between surfaces by defining two different surfaces, which are called master and slave, respectively. In tied contact slave nodes are forced to stick the master surface, when the simulation starts slave nodes are checked to establish whether they are enough close to the master segment or not, a criteria is used for this evaluation; the node which are considered close to the master segment are moved to the master surface^[30]. As consequence of that, the geometry could slightly change because of this adjustments. Finally, the tied contact output can be extracted through an interface force database allowing interface stress evaluation.

In this chapter a brief introduction is provided on the FEM method dental application, as matter of fact, it is difficult to find an analytical solution for a large number of biomechanical structures such as dental and maxillofacial implants or tools; in these cases FEM analysis are proven effective providing solutions for all these sectors^[31].

Different techniques have been developed to test the material behaviours in modern dentistry application.

Strain can be measured with a strain gauge, which is composed by an electrical resistance whose length variation detect strains, as shown in Figure 1.15 (a).

Metallic gauge is made up by a metallic sheet forming grid pattern, which allow maximizing the quantity of material parallel to the strain interested direction. The grid is glued to a thin layer called carrier that is in contact with the sample. As consequence of that, the resistance changes with the specimen deformation.

Strain gauges enable to measure small strains with a good sensitivity by using the Wheatstone bridge that allows to detect small variations of resistance, as shown in Figure 1.15 (b).

The strain gauge measurements are accurate but provides only punctual measures making impossible to work out a general distribution of the strains^[31].

Another method to evaluate the overall stress distributions is provided by the photoelasticity^[31].

In nature, some noncrystalline materials are optically isotropic but they become optical anisotropic under a stress condition^[32].

The optical axes are generated in the stress direction, this property can be used to study the stress distribution in complex systems such as biomechanical devices.

The specimen shows a colourful pattern that describes the stress-strain distribution when it is exposed to a white light source, as shown in Figure 1.16 and 1.17.

1. INTRODUCTION

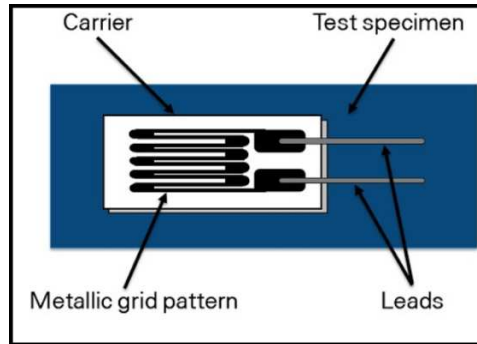


Figure 1.15 (a): Strain Gage general Structure ^[33]

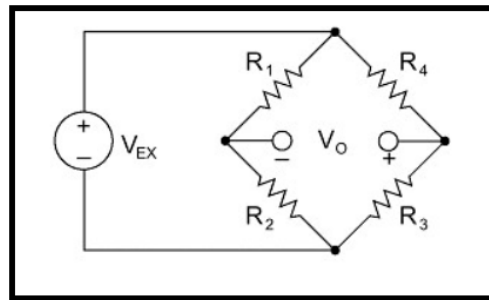


Figure 1.15 (b): Wheatstone Bridge ^[33]

This method is efficient to assess the global stress-strain distribution but only on the surface of the component investigated. An important drawback is the prohibitive cost associated with the analysis on large samples ^[31]. Numerical FEM methods allow evaluating the overall stress distribution with the possibility to obtain different information such as internal forces and energetic distributions.

Numerical technique can be used for perform parametric analysis to understand to what extent a certain parameter could influence the stress-strain distributions without experimental tests ^[34]

Therefore, this method has been widely used to analyse the mechanical behaviour of the biological tissue becoming much more performant then it used to be.

In dental applications, FEM method has mainly been used in three different ways ^[31]:

- Stress and strain interface evaluation around the implants-tooth surfaces;
- Stress test to assess the mechanical resistance of dental instrument;
- Optimization problems, such as the comparison of different resins to find the optimum material in a certain application.

The first above-mentioned application is presented in this work.

In particular, several methods have been studied to assess the interfacial gaps produced by interface tensions, some tracers like fucsin or radioactive markers can be used to quantify their distribution under magnification. This method works properly but it is destructive and the results can be affected by bias.

Another method uses the micro-CT analysis. This method leaves the sample undamaged but images are evaluated through linear measurements leading to a bias. Optical coherence tomography has been developed but it only provides 2-D images with the light penetration limit.

Finally, FEM can be a non-destructive method that allows three-dimensional quantitative evaluations of the debonding phenomena.

The FEM approach that is proposed in this paper allows to model cavities directly from micro-CT data by enabling an evaluation of the stress-strain distributions derived from the contact output.

1.3. FEM analysis introduction and dental application

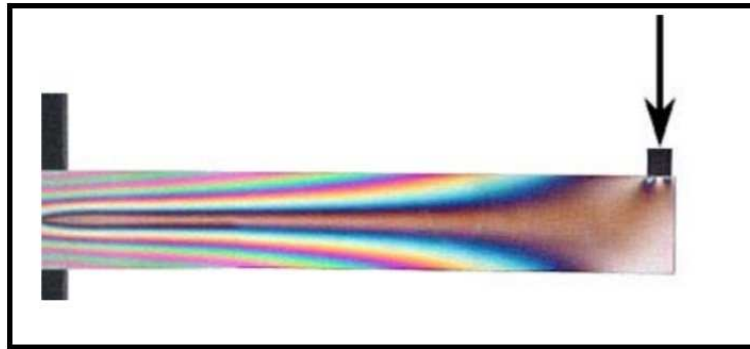


Figure 1.16: Stress pattern obtained through a photoelasticity analysis under a vertical load ^[32].

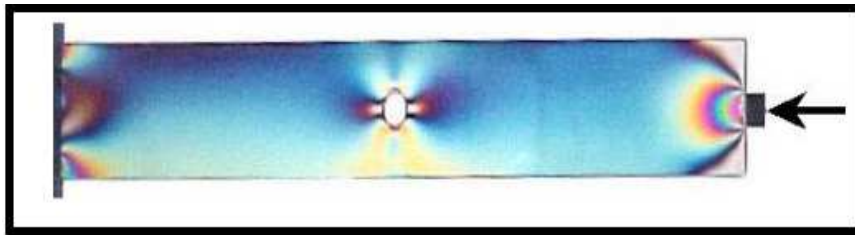


Figure 1.17: Stress pattern obtained through a photoelasticity analysis under an horizontal load ^[32]

2. METHOD

2.1. Workflow Definition

The purpose of this section is to show the workflow that allowed generating the FEM model from micro-CT slices as well as to explain all the attempts performed in order to define the final workflow procedure by comparing their results.

The micro-CT analysis and post-processing was carried out by Dr. Andrea Baldi; the considered sample was a molar with a direct MOD type II restoration whose fillers were composed by a typical direct restoration material, which is Filtek_xte.

Parameter optimization was performed in order to scan a sample without artifacts; this was the most important step for the results accuracy, which was strongly influenced by the imported slices.

A noisy scansion could introduce defects, which could not be fixed throughout the model construction. As consequence of that, a micro-CT parameter optimized protocol was defined in order to minimize noise and artifacts.

Skyscan1172 micro-CT scanner with a Hamamatsu 100/250 source type scanned a molar with the setting showed in Table 2.1.

Table 2.1: Skyscan1172 micro-CT scanner settings

Parameters	Values
Source Voltage (kV)	100
Source Current (μ A)	100
Number of Rows	666
Number of Columns	1000
Image Rotation ($^{\circ}$)	0.37
Image Pixel Size (μ m)	20.27
Filter	Al+Cu
Exposure (ms)	1400
Rotation Step ($^{\circ}$)	0.6
Type of motion	Step and Shoot
Scan Duration	00:47:38

The images pre-processing and corrections were carried out with NRecon software whose outputs allowed importing the images in a segmentation software, Mimics Medical 20.0 was chosen for this purpose.

Table 2.2 shows the optimized NRecon settings to create slices that can be imported in Mimics.

Segmentation process consists in dividing an image into multiple segments that are made up of sets of pixels^[35]; in this application the sets were composed of different tooth parts, which were enamel, dentine and restorative materials.

Therefore, Mimics allowed the creation of different materials, which was a fundamental step in the model generation. Different biologic tissues absorb radiation at different levels, which causes different effects on tomography data related to the radio-density of the tissue.

These radio density differences among anatomic structures were processed by tomography software by using 'Hounsfield Scale', which was a quantitative scale for describing radio density.

2.1. Workflow Definition

Consequently, a filter based on ‘Hounsfield Scale’ allowed an initial part creation.

Table 2.2: NRecon parameters settings

Parameters	Values
First Section	29
Last Section	639
Reconstruction Angular Range (°)	199.80
Smoothing	4
Smoothing Kernel	2 (Gaussian)
Filter cutoff relative to Nyquist frequency (Hz)	100
Filter type description	Hamming (Alpha=0.54)
Threshold for defect pixel mask (%)	50
Beam Hardening Correction (%)	15

2.1.1. First procedure

The first attempt to create a geometry through micro-CT data is described in this section.

A variable sampling was performed in order to import only the slices necessary for the surface reconstruction by avoiding the creation of heavy project files; this sampling was intended to create a realistic but not unmanageable model. Therefore, only the slices following significant tooth shape changes were chosen, as results only 71 out of 610 slices were considered.

A small number of automatic operations were performed in order to create different masks, which were dentine, enamel and restorative material.

Figure 2.1 shows how the slices imported in Mimics Medical appear.

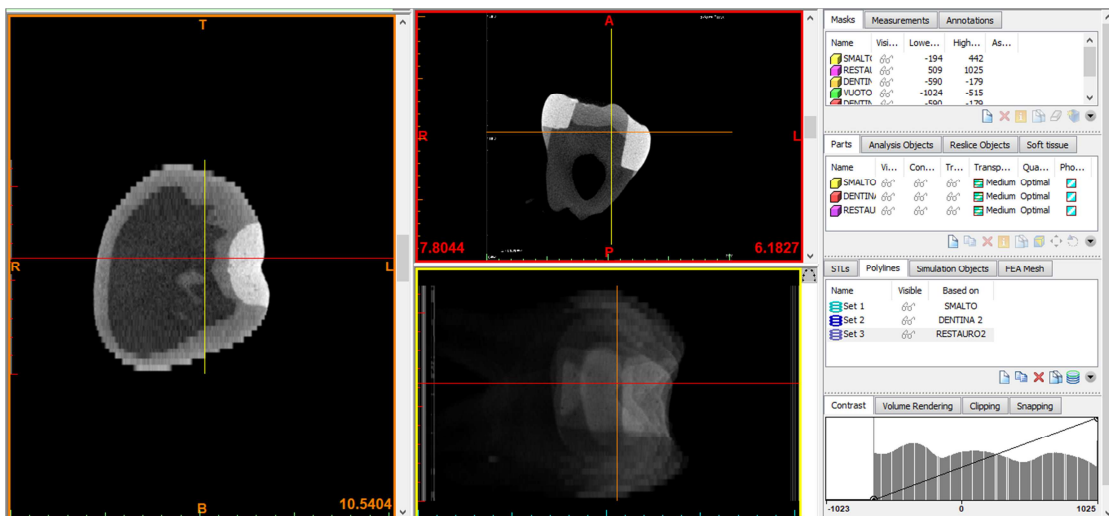


Figure 2.1: Planar and vertical section of the imported tooth

2. METHOD

The masks were created through a Thresholding operation by selecting Hounsfield intervals, which are shown in Table 2.3.

These values should be chosen carefully by taking into account that they need to be determined for all the scansions, in fact, they depend on the biological and restoration material features, on the scansion method and on the samples.

Table 2.3: Hounsfield ranges for different tooth parts

Part	Hounsfield minimum (HU)	Hounsfield maximum (HU)
Dentine	-590	-179
Enamel	-194	442
Fillers	509	1025

Table 2.3 shows the Hounsfield values overlapping among tooth parts, the reason lied with the wide radio density range of the different structures. Therefore, the generated masks overlapped each other and additional operations were needed in order to create separate and adjacent layers that distinguished different tooth materials. Figure 2.2, Figure 2.3 and Figure 2.4 show the masks generated through Thresholding operations.

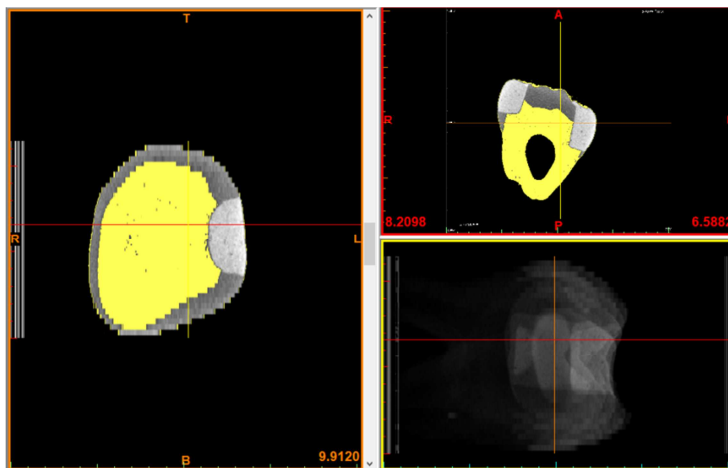


Figure 2.2: Dentine mask generation

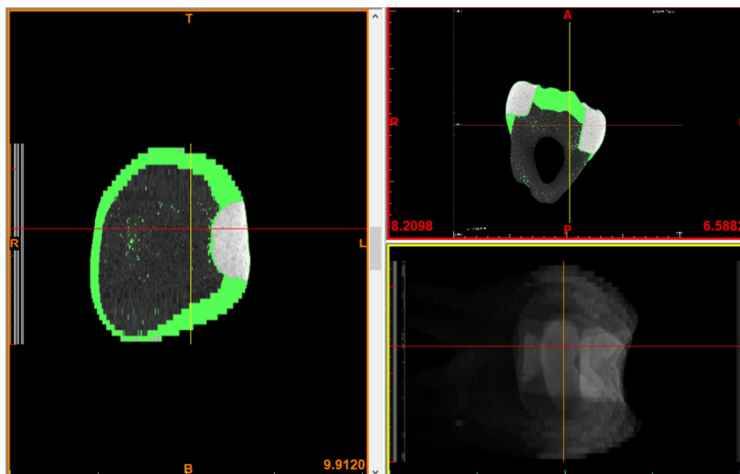


Figure 2.3: Enamel mask generation

2.1. Workflow Definition

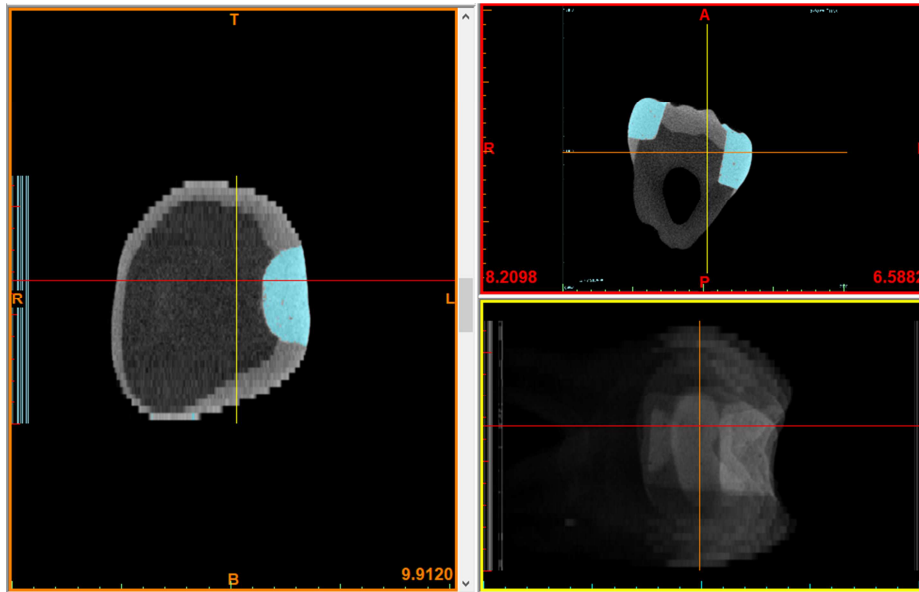


Figure 2.4: Fillers masks generation

Figure 2.2 and Figure 2.3 showed masks overlapping, which was eliminated through manual operations, whereas Figure 2.4 illustrates the fillers mask.

Moreover, as mentioned in the introduction the fillers gluing was ensured with an adhesive layer, the presence of this layer was neglected during the model creation; therefore, an adhesive mask was not generated in Mimics, the specific reasons will be discussed in the method chapter.

As shown in Figure 2.4, the filler masks did not show any overlap with the other layers being in a different Hounsfield range while enamel and dentine Hounsfield overlapped each other, as illustrated in Figure 2.2 and Figure 2.3.

Masks were manually improved with editing tools by redefining all the vertical slices. Therefore, all the flaws were eliminated by ensuring the adjacency between layers.

Mimics provided the possibility to work in different sections but all the operations were performed on the vertical sections, which were directly produced by the micro-CT scansion and not successively reconstructed by Mimics. Consequently, only the vertical images will be shown on the next figures. Figure 2.5 (a), Figure 2.5 (b), Figure 2.5 (c) and Figure 2.5 (d) show upper, medium and lower tooth section after the above-described operations were carried out.

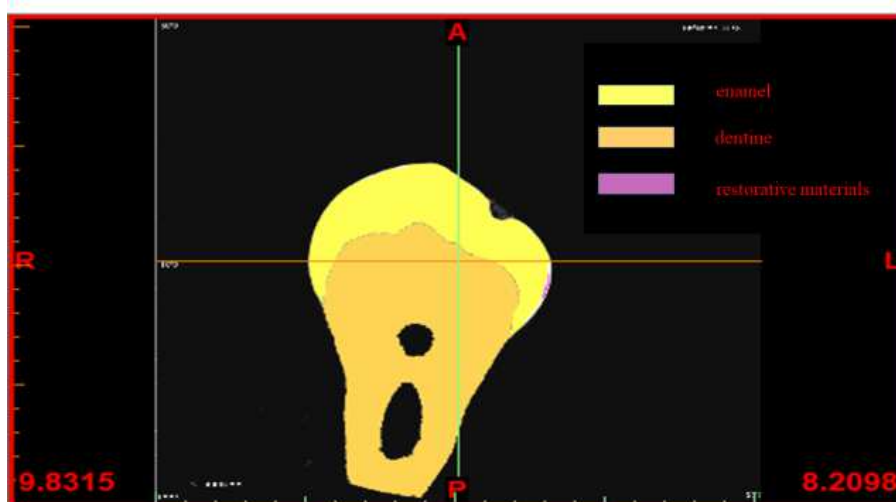


Figure 2.5 (a): Vertical upper tooth slice..

2. METHOD

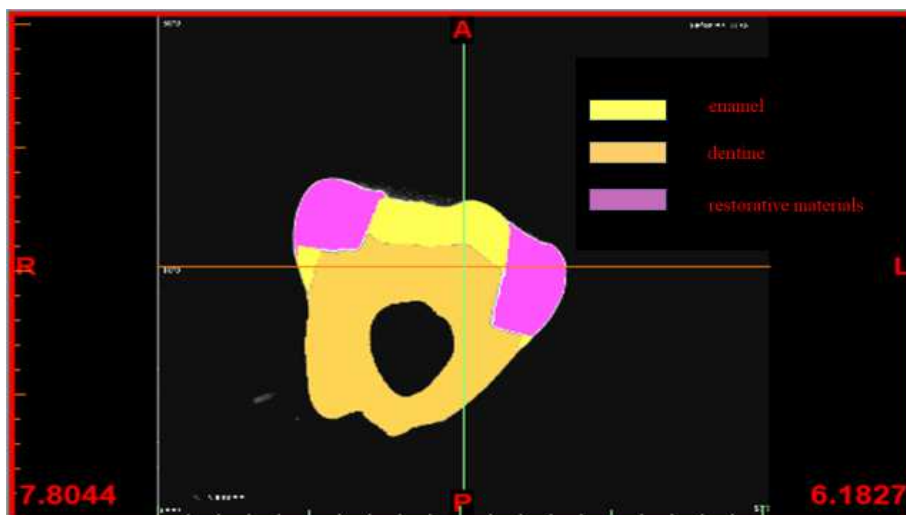


Figure 2.5 (b): Vertical upper-medium tooth slice..

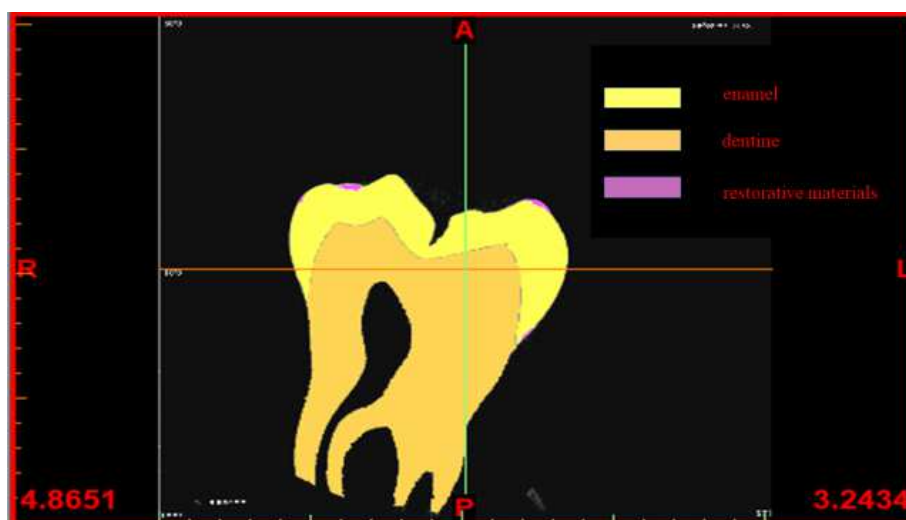


Figure 2.5 (c): Vertical lower-medium tooth slice

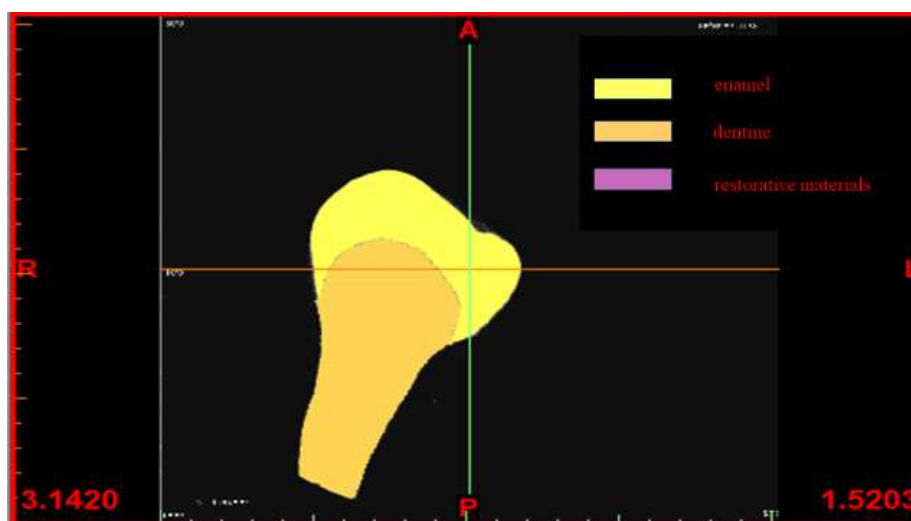


Figure 2.5 (d): Vertical lower tooth slice.

2.1. Workflow Definition

Despite the effort to create perfect masks, the above-described procedure was limited by the human accuracy.

Mimics provides different functions, which allow creating parts or polylines from masks.

The first attempt was to generate polylines from the masks and to import them in a modelling software in order to create final tri-dimensional surfaces; these surfaces could be successively exported in Ls-Dyna where the mesh creation could be carried out through appropriate meshing tools. Figure 2.6 (a), Figure 2.6 (b) and Figure 2.6 (c) show dentine, enamel and fillers polylines.

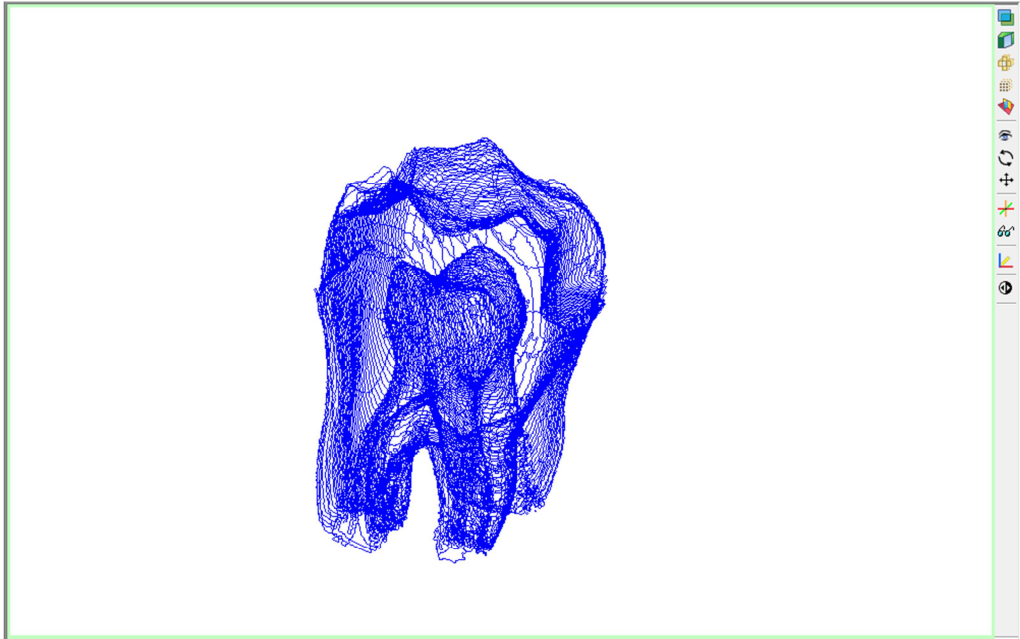


Figure 2.6 (a): Dentine polylines

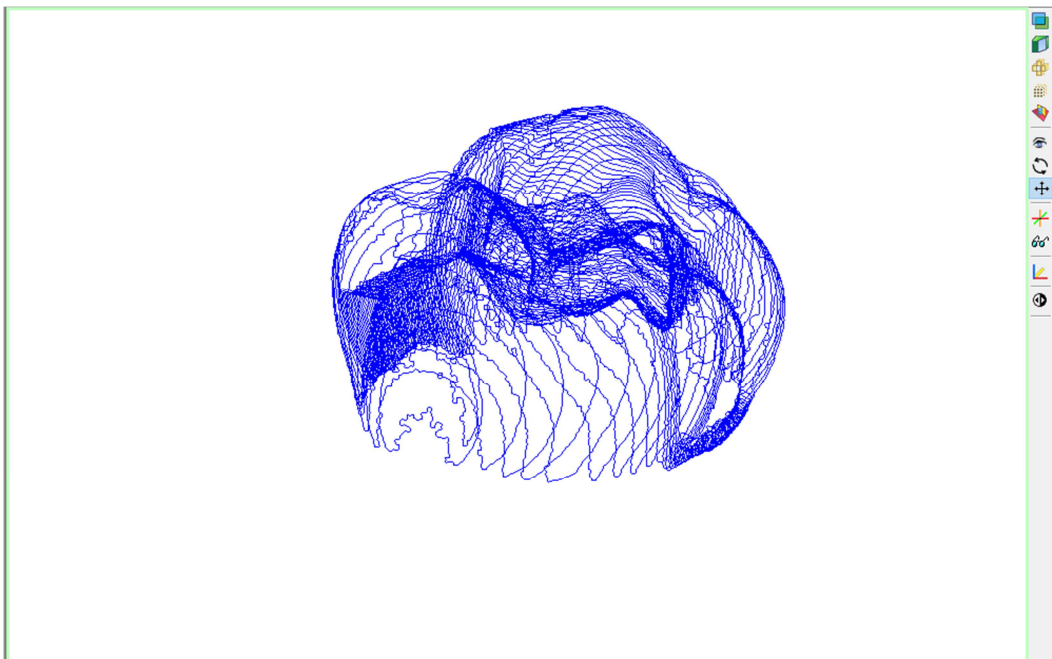


Figure 2.6 (b): Enamel polylines

2. METHOD

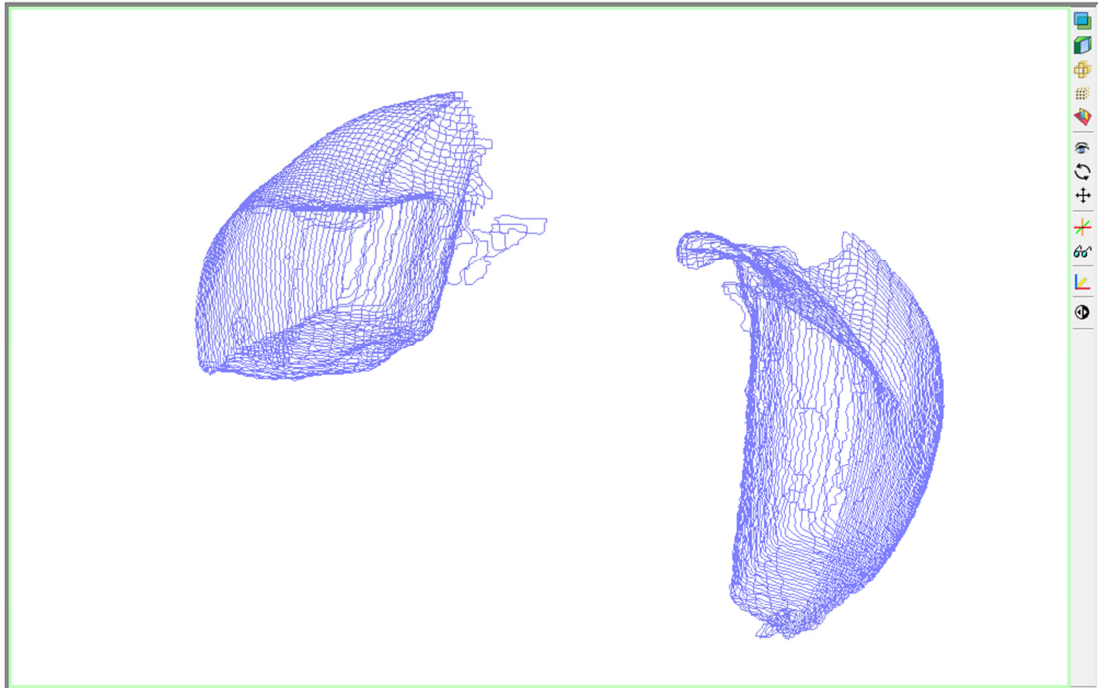


Figure 2.6 (c): Fillers polylines

Rhinoceros was chosen to perform a surface construction through the above-described tooth polylines. The first step was to reconstruct and smooth polylines and to clean them from segmentation errors, in fact, if not properly cleaned they were converted into small polylines as shown in Figure 2.7.

The procedure were carried out on the whole tooth but few slices will be displayed to make the figures more comprehensible.

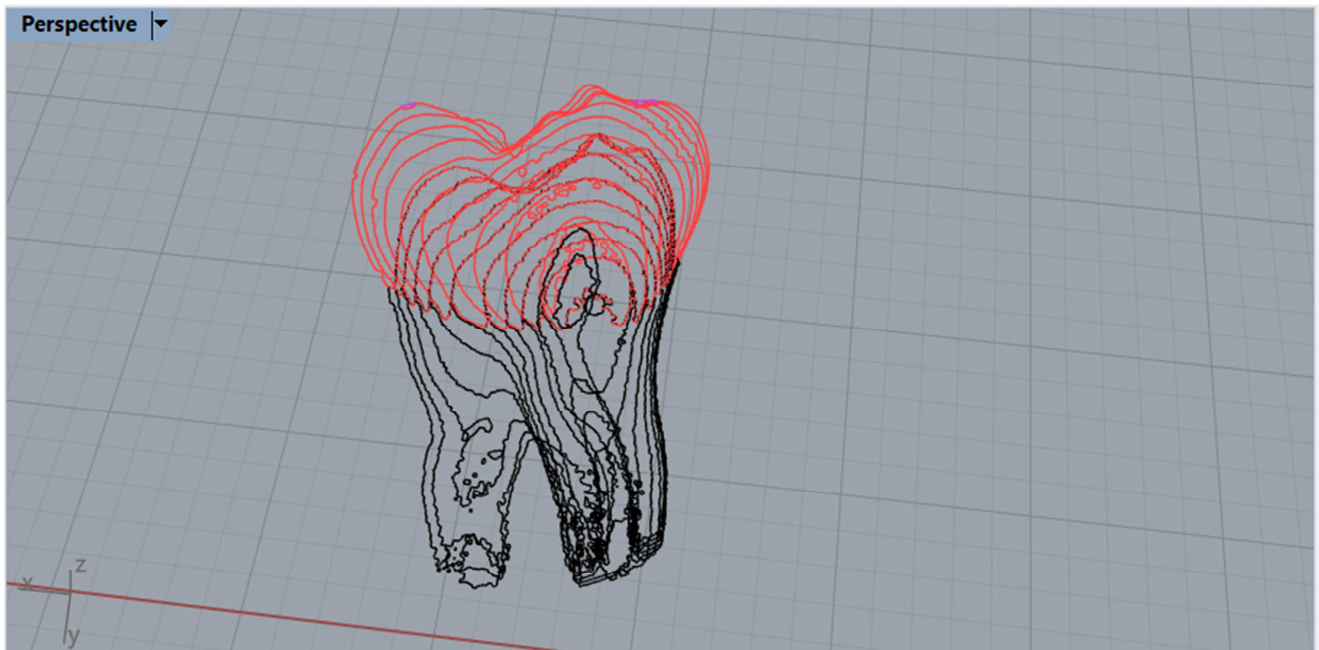


Figure 2.7: Dentine and enamel imported slices portions

2.1. Workflow Definition

These small curves were selected and eliminated and the other polylines were smoothed through specific functions, Figure 2.8 illustrates the step above-described.

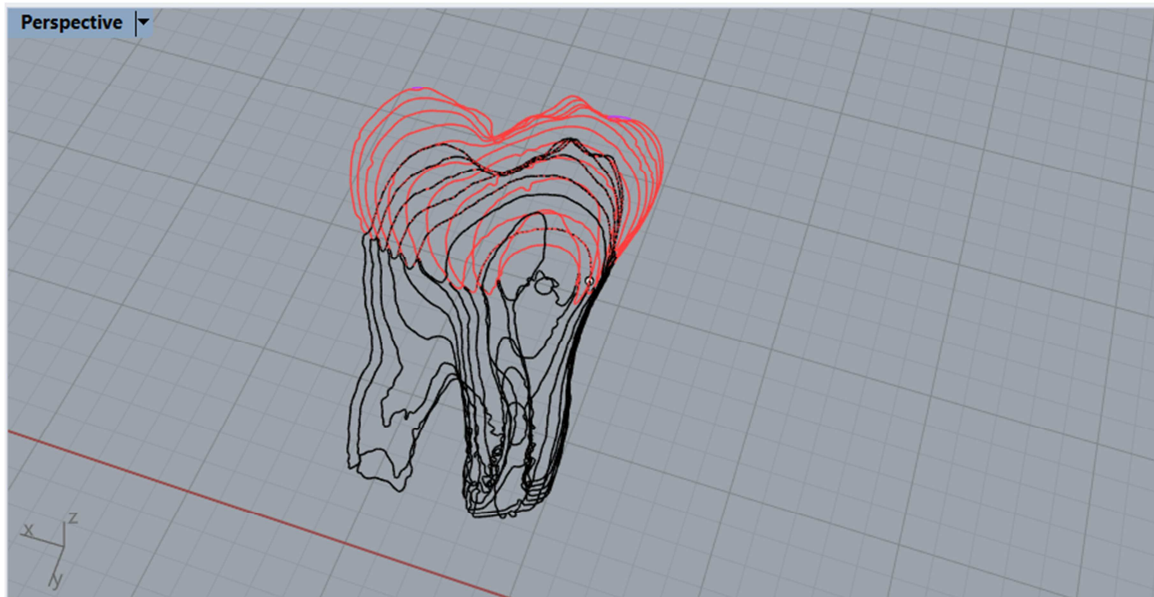


Figure 2.8: Dentine and enamel smoothed polylines after the cleaning procedure.

Then a further reconstruction was manually applied in order to build as much regular polylines as possible preserving the tooth characteristic shapes, this step purpose was to improve the future outcomes of the surface building process. The reconstructed slices are shown in Figure 2.9

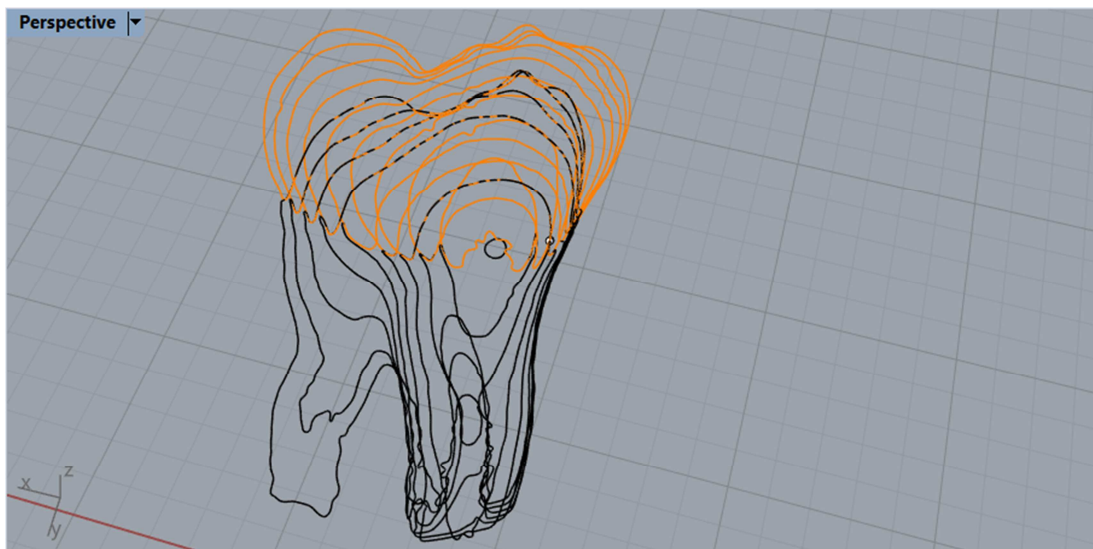


Figure 2.9: Dentine and enamel reconstructed polylines

The next step consisted of lofting the curves to create four different surfaces, which are dentine, enamel and fillers, respectively. The creation stages were :

- Planar Surface creation, which is illustrated in Figure 2.10 (a)
- 3-D Surface creation carried out through Planar surfaces loft, which includes a normal reorientation showed in Figure 2.10 (b), the final results are illustrated in Figure 2.10 (c).

2. METHOD

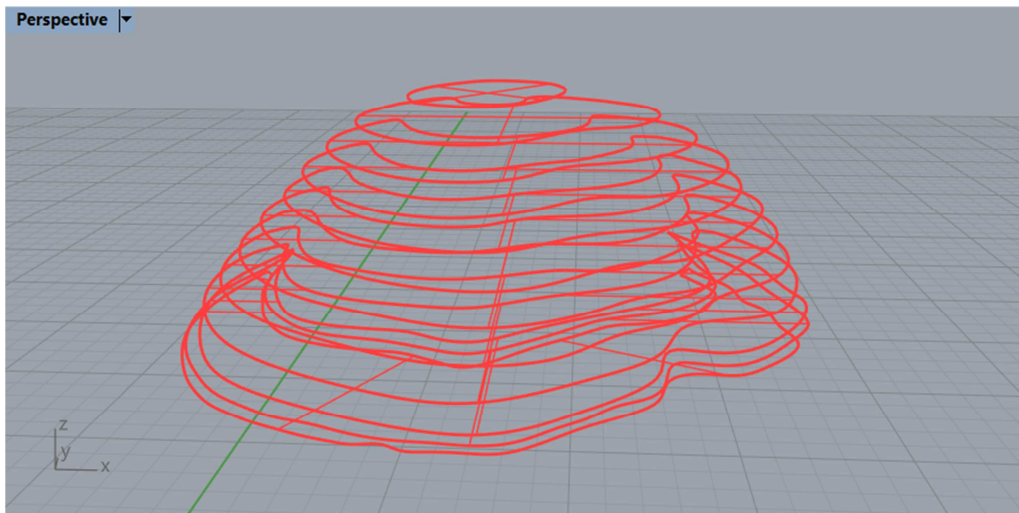


Figure 2.10 (a): Planar surface creation on a enamel portion

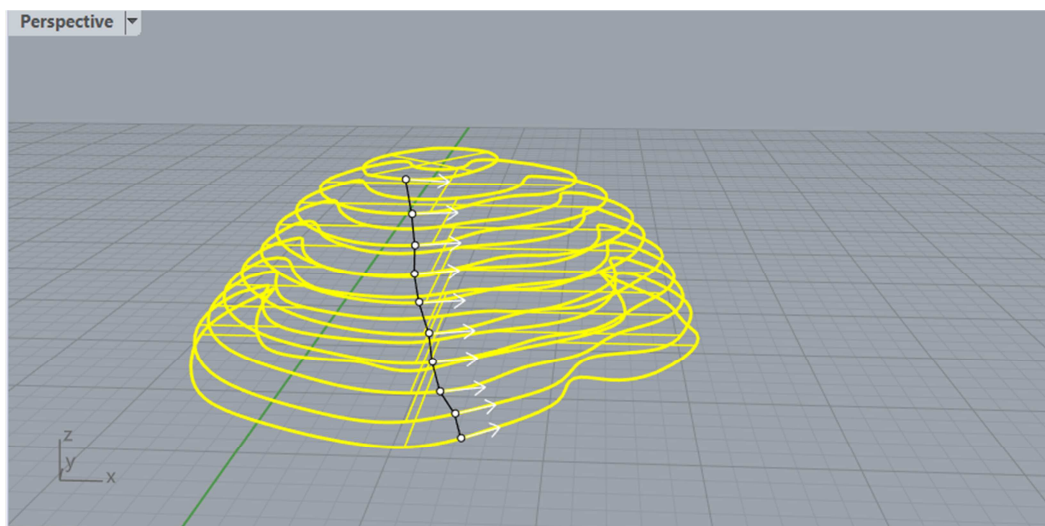


Figure 2.10 (b): Normal surface reorientation on a enamel portion

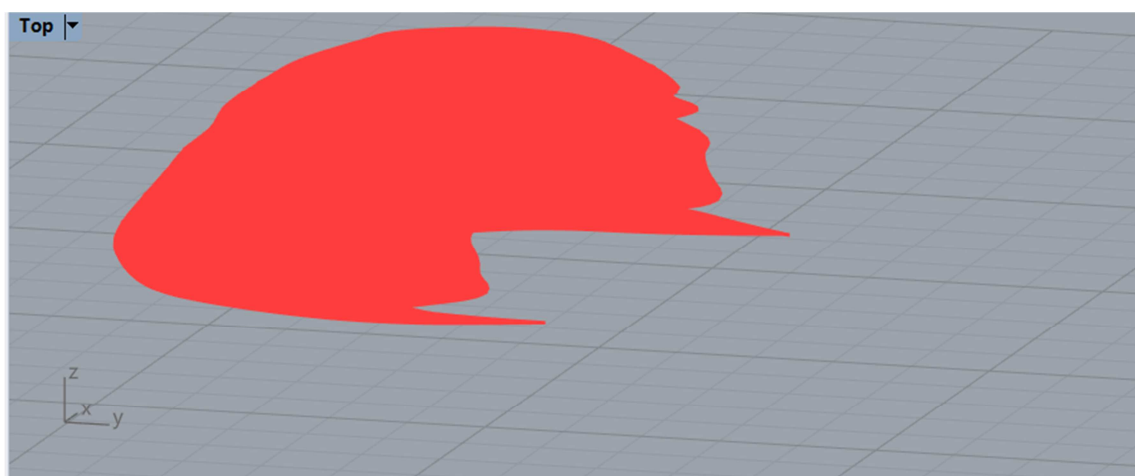


Figure 2.10 (c) : Enamel portion surface creation.

2.1. Workflow Definition

This approach was extended to all the slices by creating the final surfaces, the problems encountered in the surface creation are now discussed.

First, the surface construction process was not accurate between two surfaces especially if the lofted planar surfaces were really different in shape as illustrated on the bottom of Figure 2.10 (c).

Furthermore, planar surfaces were merged with their upper and a lower planar surfaces but in some regions two upper or lower surfaces were on the same level, in this case the surfaces reconstruction was carried out by creating different polysurfaces for the same part to circumvent the problem.

Figure 2.11 (a) and Figure 2.11 (b) illustrates the final reconstructed surfaces of enamel and fillers, respectively.

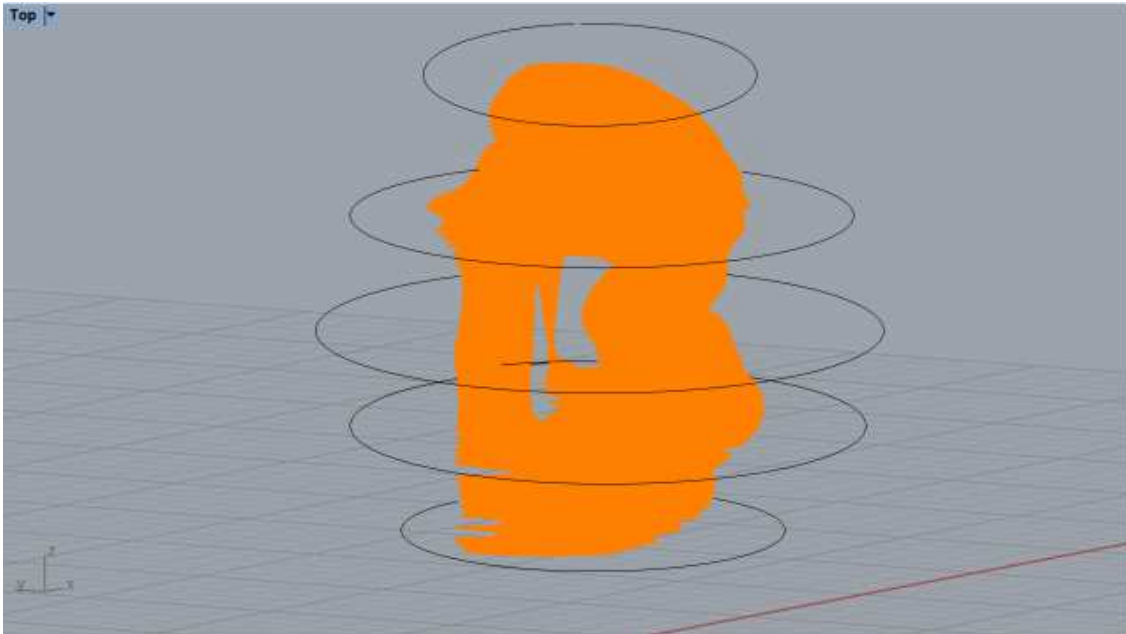


Figure 2.11 (a): Enamel surface reconstruction from polylines

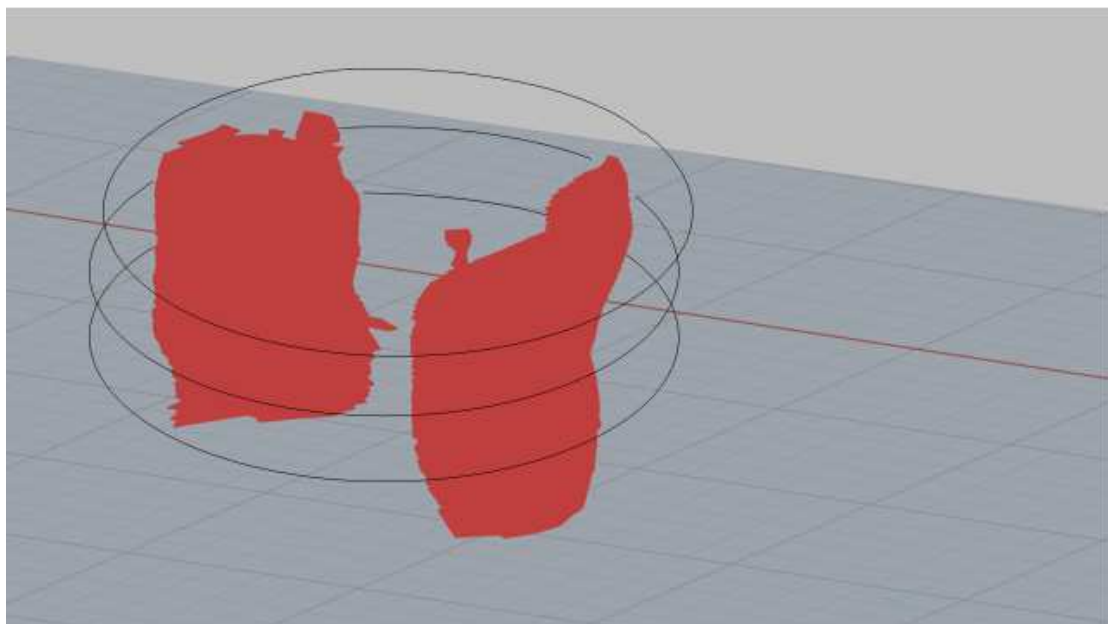


Figure 2.11 (b): Fillers surface reconstruction from polylines

2. METHOD

The surface buiding process of both fillers and enamel showed many problems as discussed before; therefore, before to proceed with the dentine surface generation an attempt to mesh these surfaces were performed.

The idea was to create a two-dimensional mesh from the geoemtry on Ls-Dyna PrePost processor and then to generate a volumetric mesh from the shells with Ls-Dyna volumetric mesh builder. The fillers and enamel polysurfaces were imported on Ls-Dyna PrePost; the results obtained with this procedure showed evident problems because the final surfaces were affected by defects that makes these surfaces impossible to mesh, as shown in Figure 2.12.

As matter of fact, the creation of surfaces through the command loft worked for a limited number of regular polylines; therefore, the high numbers of irregular polylines separated by short distance led to the creation of unconnected and disjointed surfaces.

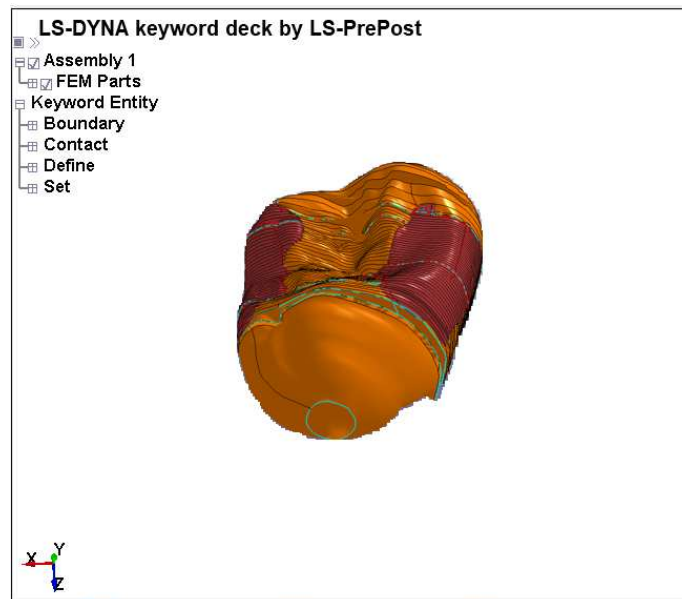


Figure 2.12: Enamel and dentine polysurfaces imported in Ls-Dyna.

The polylines generation from layers was proved ineffective in a reliable workflow definition.

As matter of fact, the desired workflow should be independent by manual operations, which introduced a bias on the reconstruction.

The principal aim of this reconstruction attempt was to create an efficient and reproducible process that allowed the generation of unbiased models in a reasonable time and with the best possible outcomes, a second attempt was made on this direction.

2.1.2. Second procedure

In this second procedure an automatic workflow were defined in order to overcome the problems analysed in the previous section; the slices were selected with the undersampling procedure before-described, furthermore, the layers creation were performed with the same thresholding intervals of the first procedure.

The introduction of morphological operations allowed drastically improving the masks quality after the thresholding filter was applied, in particular these functions enabled to close internal holes and to eliminate gaps between layers, which could create problems in the FEM contacts definitions.

Moreover, a region growing algorithm was applied to eliminate pieces disconnected from the principal layers followed by Boolean operations whose purpose was to create complementary layers through masks sums and subtractions.

In summary, Boolean operations allowed to merge all the layers into an unique mask then two masks were subtracted by the merged layer obtaining a new mask.

These operations were repeated for all the masks by creating three new layers with a perfect contact between them, further explanations will be given in this section.

Masks generated with this procedure are shown in Figure 2.13 (a), Figure 2.13 (b), Figure 2.13 (c) and Figure 2.13 (d).

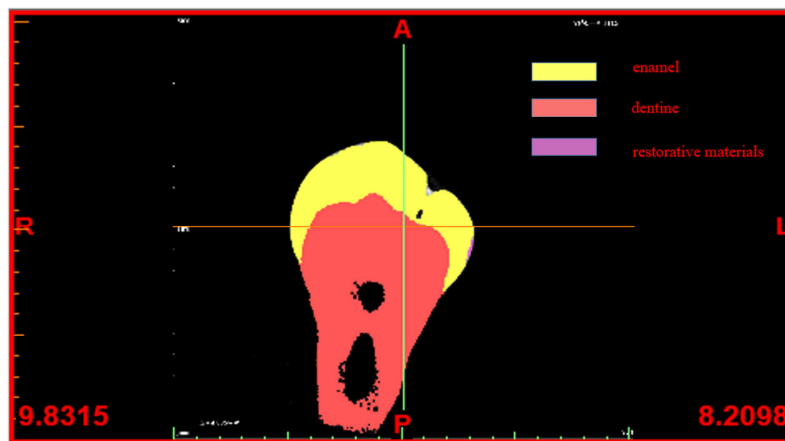


Figure 2.13 (a): Vertical upper tooth slice improved with Morphological and Boolean operations

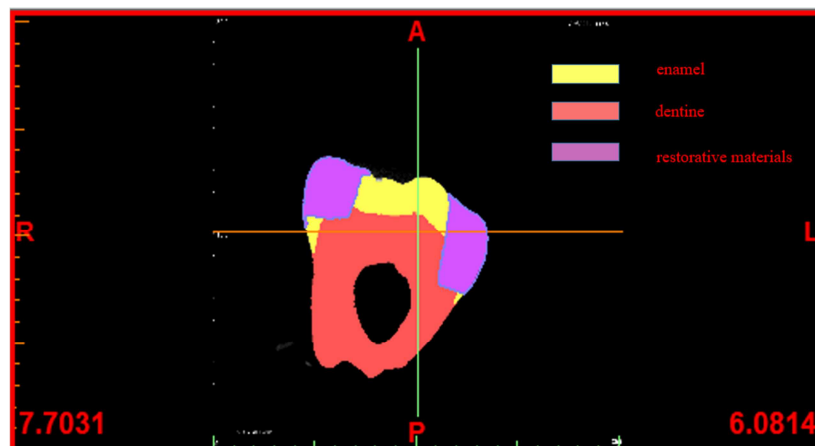


Figure 2.13 (b): Vertical upper-medium tooth slice improved with Morphological and Boolean operations

2. METHOD



Figure 2.13 (c): Vertical lower-medium tooth slice improved with Morphological and Boolean operations

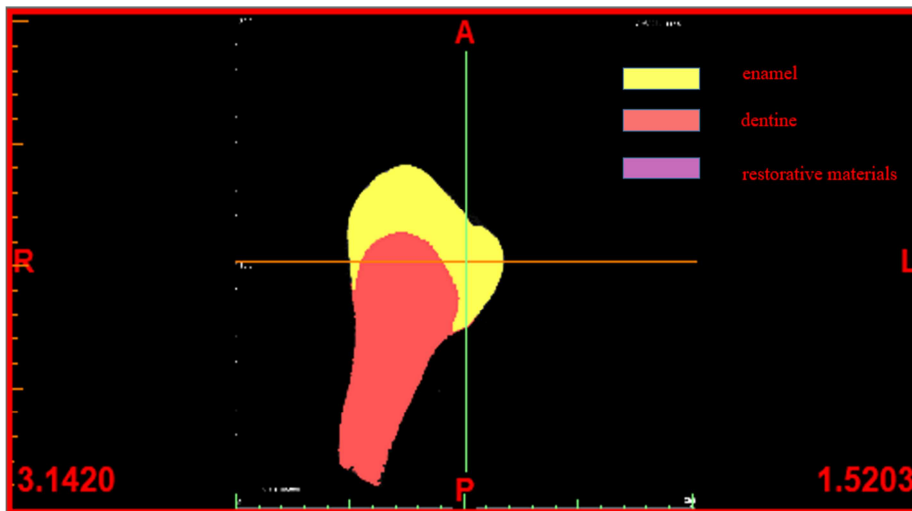


Figure 2.13 (d): Vertical low tooth slice improved with Morphological and Boolean operations

The next step was the high-resolution parts creation from all the masks in order to avoid a manual surface generation, which presented the issue discussed before.

The introduction of this stage was crucial ensuring the automatic generation of surfaces through a masks fitting algorithm provided by Mimics.

Moreover, the creation of these parts were performed almost in real-time whereas the rhinoceros surface generation took almost ten days to be completed; another innovation was the possibility to automatically convert these parts into stereolithography (STL) files.

Stereolithography files are made up raw and unstructured triangle surfaces in a three-dimensional Cartesian coordinate system^[36] creating a two-dimensional mesh.

In the previous procedure the surface that were generated needed to be meshed by creating a shell mesh, which needed to be successively converted into solid elements. Mesh creation could be really challenging especially for deeply irregular surfaces whereas mesh refinements could be performed on a simpler way also for irregular STL files by reconstructing surfaces with appropriate filters, this aspect will be discussed in this chapter.

2.1. Workflow Definition

Figure 2.14 (a), Figure 2.14 (b) and Figure 2.14 (c) show dentine, enamel and fillers parts, respectively.

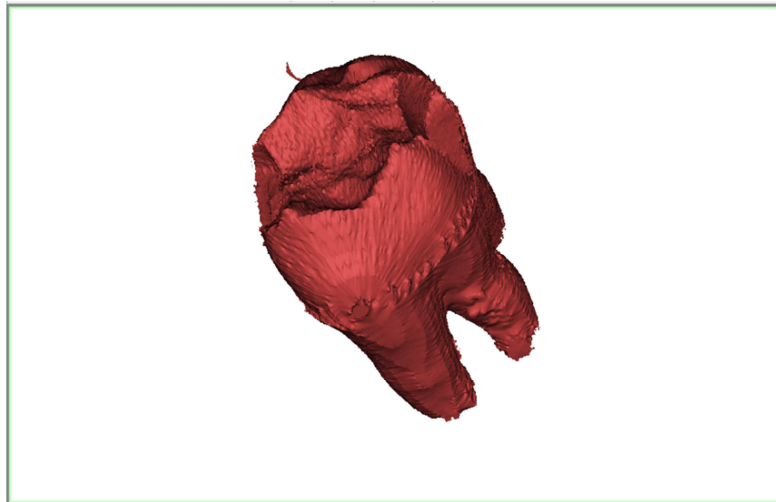


Figure 2.14 (a): Dentine part

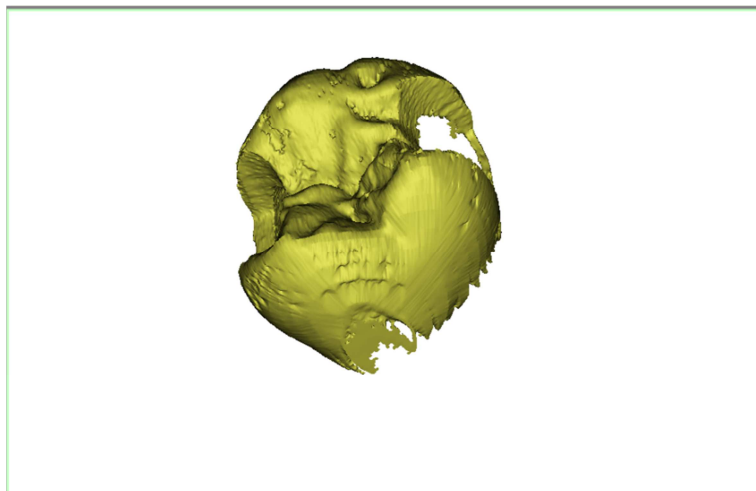


Figure 2.14 (b): Enamel part

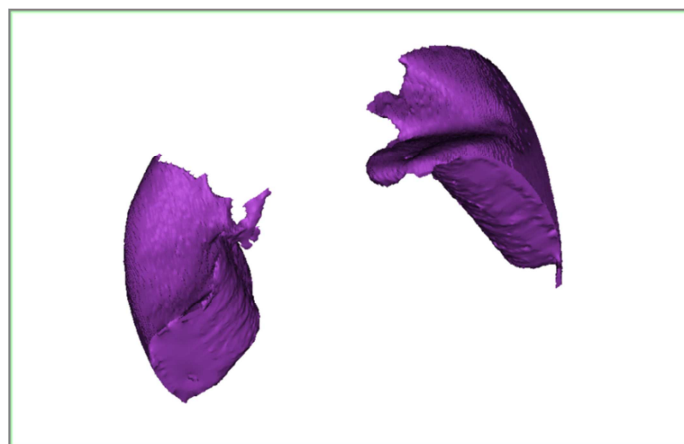


Figure 2.14 (c): Fillers part

2. METHOD

The generated parts presented shape defects and roughnesses whose presence was mainly caused by the poor number of considered slices. In particular, enamel shapes were deeply irregular especially on the dentine border showing peaks, which are illustrated in Figure 2.14 (b).

Surfaces quality could be successively improved by applying smoothing filters, the parameters should be carefully tuned in order to minimize geometry distortions.

Figure 2.15 (a), Figure 2.15 (b) and Figure 2.15 (c) show the improvements on the surface quality after the smoothing process.

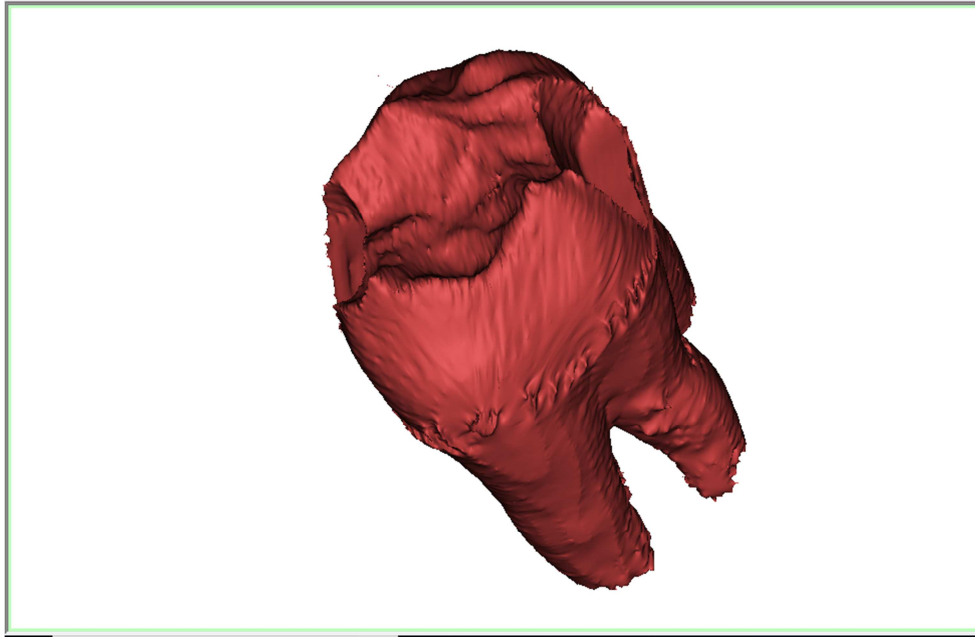


Figure 2.15 (a): Smoothed dentine part

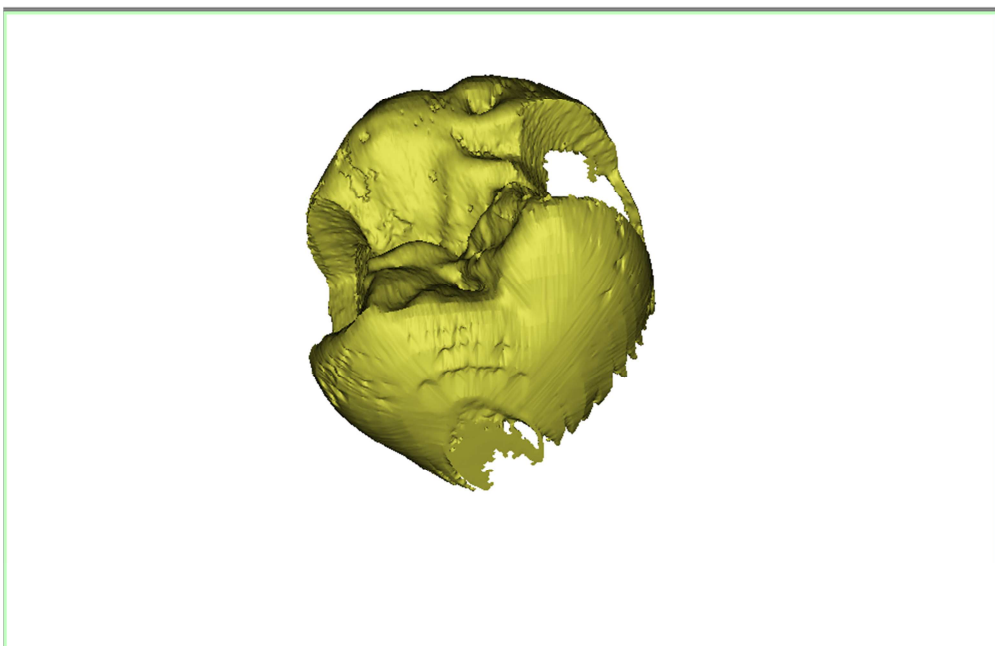


Figure 2.15 (b): Smoothed enamel part

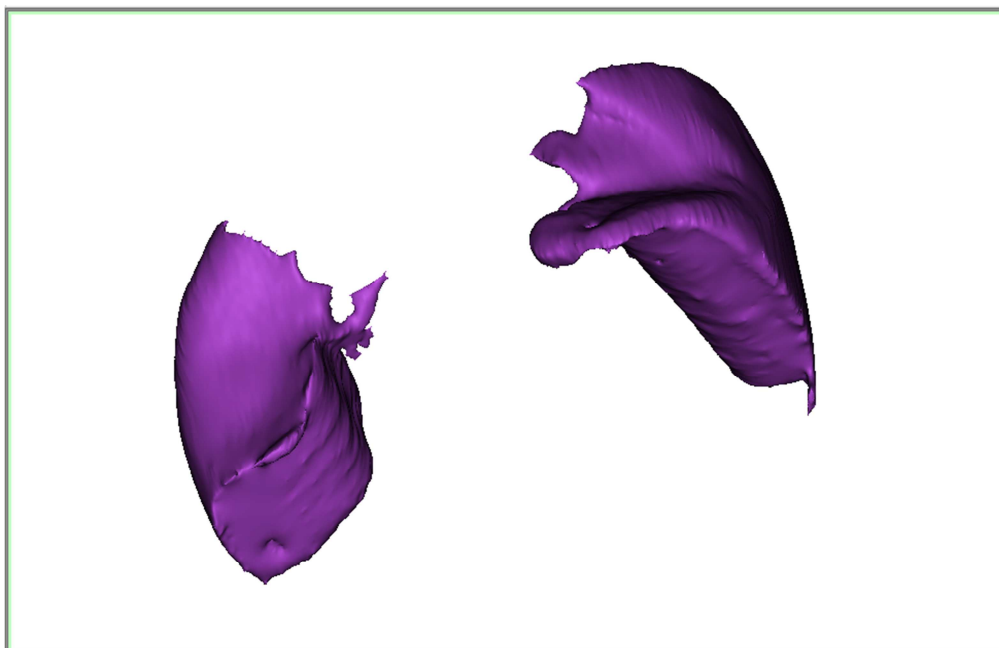


Figure 2.15 (c): Smoothed fillers part

The parts qualities were drastically improved by applying smoothing filters but the surfaces morphologies were slightly modified by compromising the part contacts created with the Boolean operations.

Therefore, Boolean operations were applied a second time on the smoothed parts with the same principles they were applied on the masks; the procedure was performed three times in order to create complementary parts.

Smoothed dentine and enamel were merged into a part, which is shown in Figure 2.16.

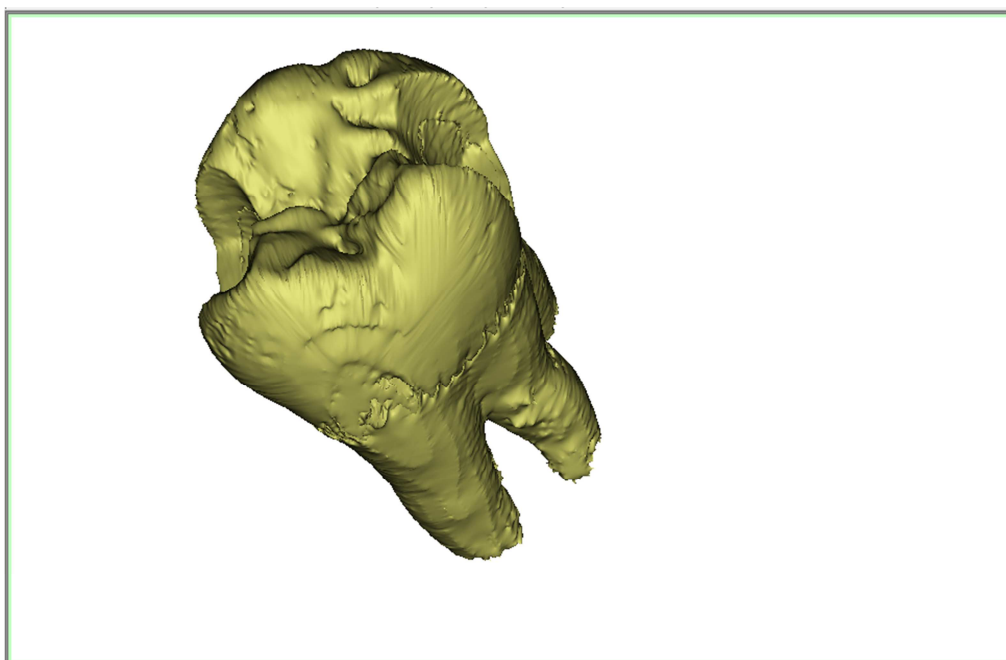


Figure 2.16: Part created by merging dentine and enamel.

2. METHOD

Then the part was merged with the fillers into a final 3-D surface that is illustrated in Figure 2.17

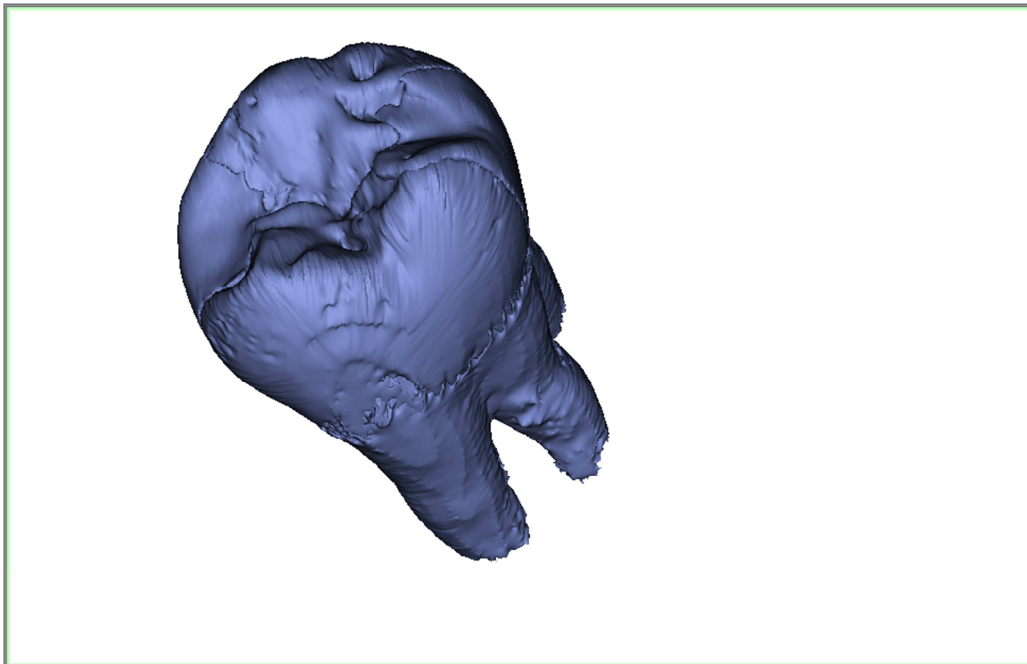


Figure 2.17: Part created by merging dentine, enamel and fillers part.

Finally, fillers were generated by subtracting the part in Figure 2.17 with the part in Figure 2.16, this procedure is shown in Figure 2.18.

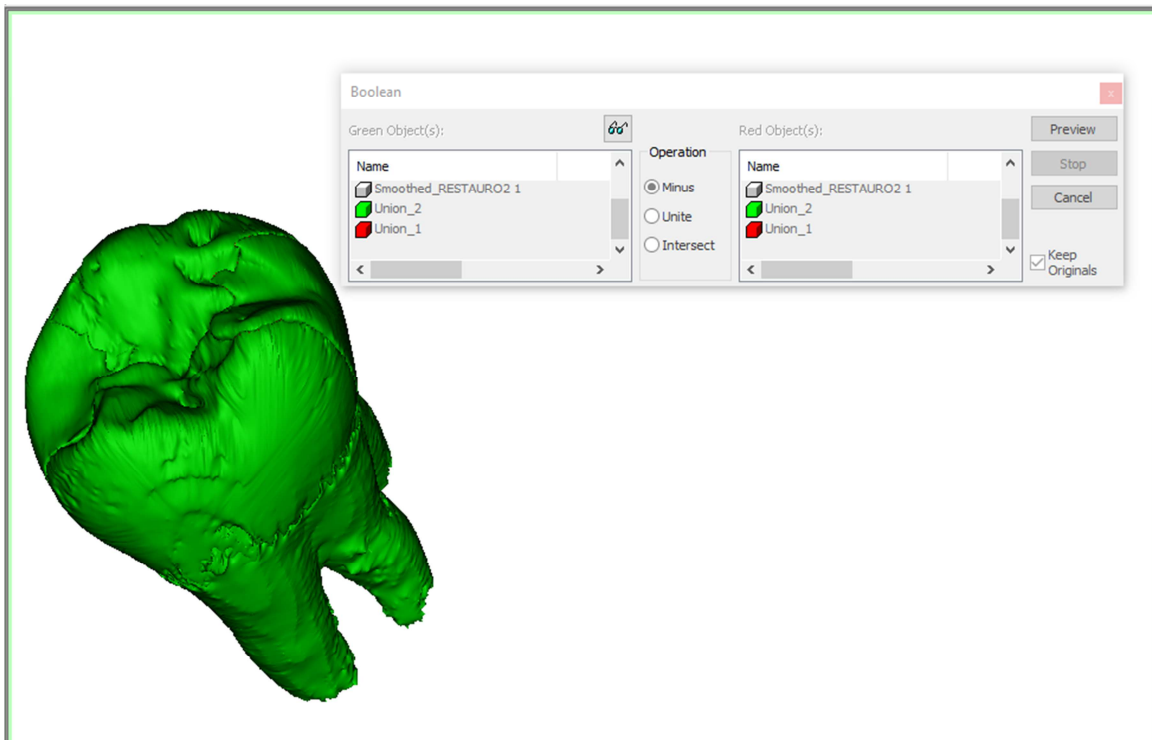


Figure 2.18: Fillers creation process performed through a parts subtraction

2.1. Workflow Definition

The final results was a 3-D surface complementary with both the dentine and the enamel, Figure 2.19 shows the Boolean fillers.

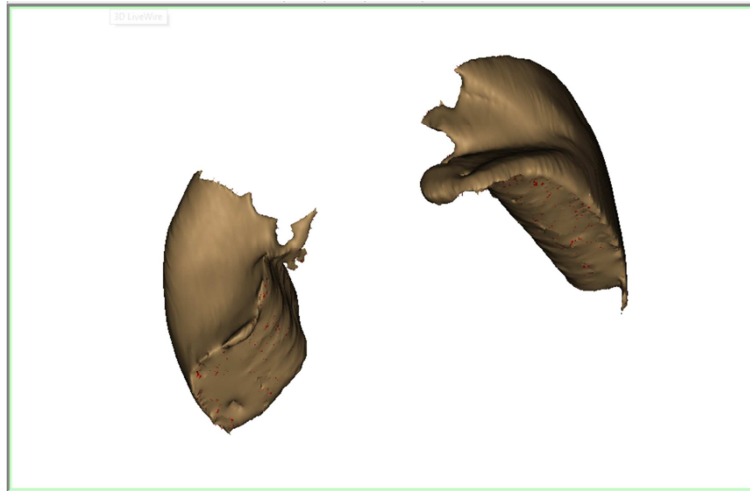


Figure 2.19: Fillers part generated through Boolean operation.

These operations were identically repeated for enamel and dentine by generating three complementary parts, which were successively converted into STL.

As previously mentioned, STL files were made of two-dimensional mesh that could be turned into a volumetric mesh with the Ls-Dyna PrePost solid mesh builder. Nevertheless, these STL were composed by deeply irregular triangular elements, which needed to be adjusted in order to create a tri-dimensional mesh from them. In particular, Ls-Dyna PrePost has a solid mesh builder that allows to create volumetric mesh from shell mesh if the latter mesh meets some requirements like regularity in shape and a limited aspect ratio.

Therefore, a mesh refiner was required to build a regular shell mesh; Meshlab was chosen because it provided a wide range of tools to adjust and to rebuild mesh with better features.

Figure 2.20 (a), Figure 2.20 (b) and Figure 2.20 (c) illustrate the initial STL mesh of dentine, enamel and fillers, respectively.

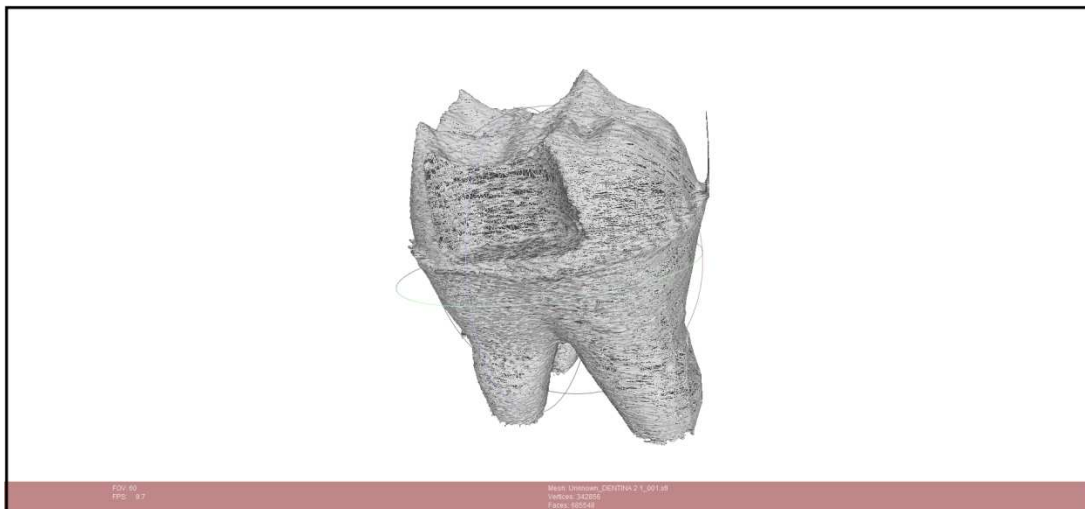


Figure 2.20 (a): Dentine STL

2. METHOD

The Figure 2.20 (a) shows the imported dentine surface mesh, which was made up of 685548 faces. This mesh presented different problems such as the high elements number and low elements quality that required a total mesh rebuilding, the adopted procedure is described step by step in this section. The first step was the element reduction that allowed the generation of a manageable mesh whose elements can be heavily distorted presenting also self-intersecting faces and holes. Therefore, mesh-repairing tools were applied to improve the mesh quality by performing different operations such as closing holes and deleting critical elements. In this attempt, reconstruction methods were adopted for enamel and dentine in order to drastically improve their STL qualities; these methods modified the STL shapes compromising the contacts ensured with Boolean operations, the results are further analysed in this section.

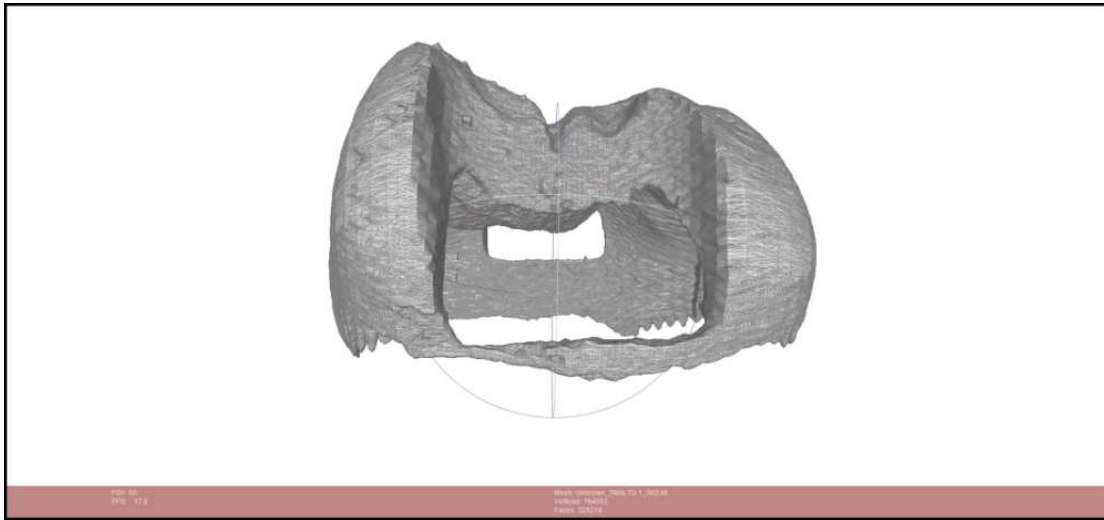


Figure 2.20 (b): Enamel STL

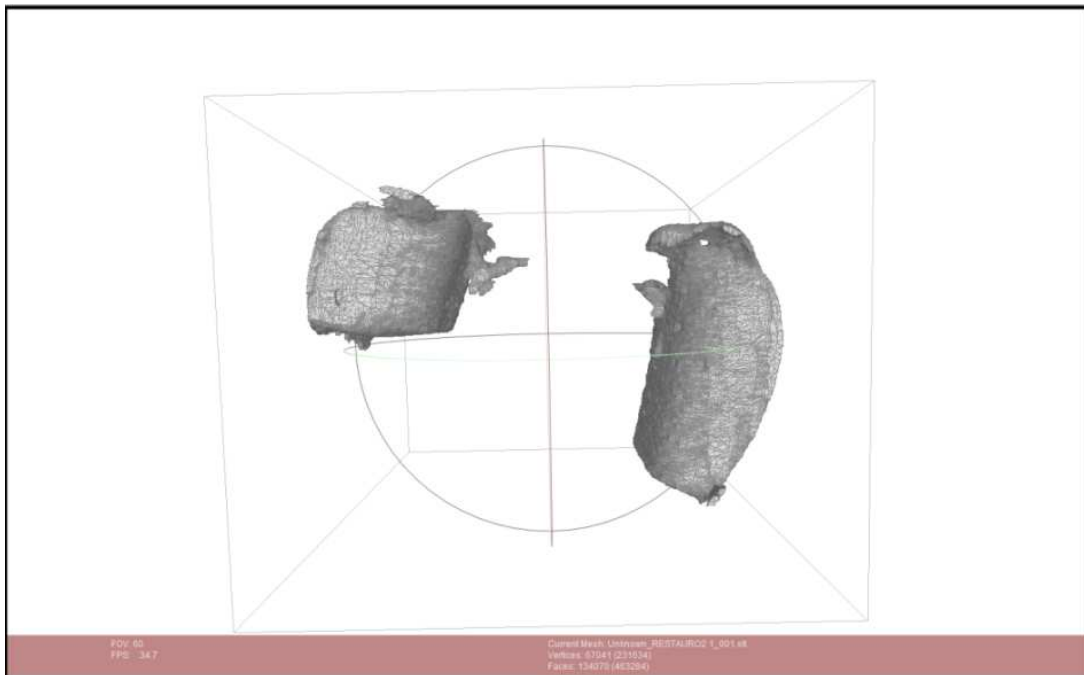


Figure 2.20 (c): Fillers STL

2.1. Workflow Definition

Fillers mesh adjustments were more easily performed than those of enamel and dentine because of its simpler shape, therefore, no reconstruction method was required.

Mesh refinements are showed step by step for dentine STL whose model creation stages applicability is general. First, a reduction of elements was performed obtaining a mesh made up of 21728 elements, the result is showed in Figure 2.21.

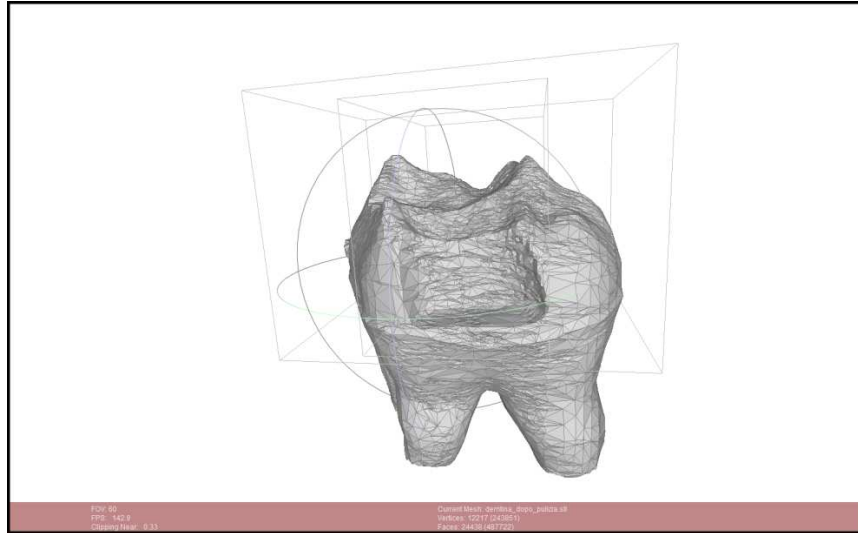


Figure 2.21: Dentine STL element reduction

Then a VCG surface reconstruction algorithm was applied in order to improve the surfaces quality, VCG is a volumetric filter whose output is another surface with more regular elements and shapes^[37]. The quality of the output surfaces could be improved by increasing the resolution in the VCG filter; despite the possibility to achieve high resolution in the reconstruction the output surface morphology was inevitably slightly different from the original dentine surface. The new surface is shown in Figure 2.22.

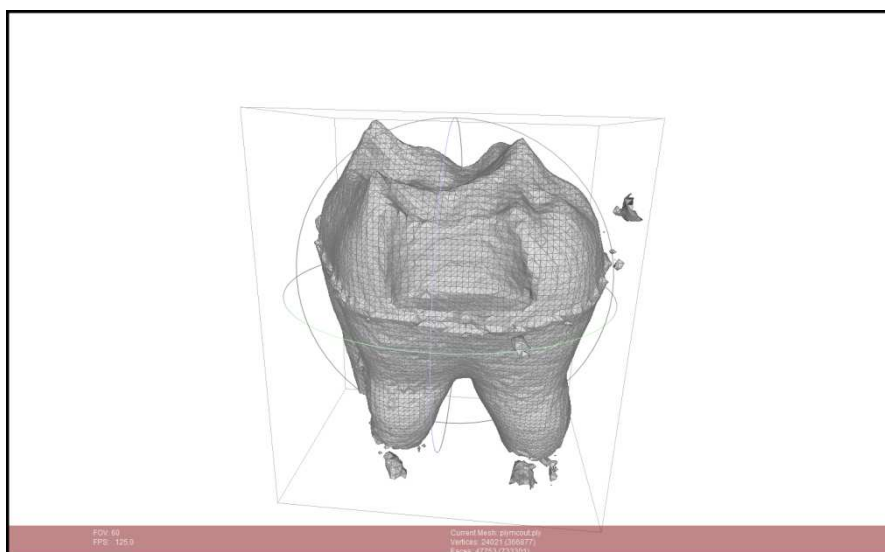


Figure 2.22: Dentine STL surface reconstruction through VCG filter

2. METHOD

Isolate pieces were removed and an element number reduction was performed with a decimation algorithm by activating normal and boundary mesh preservation, the result is showed in Figure 2.23.

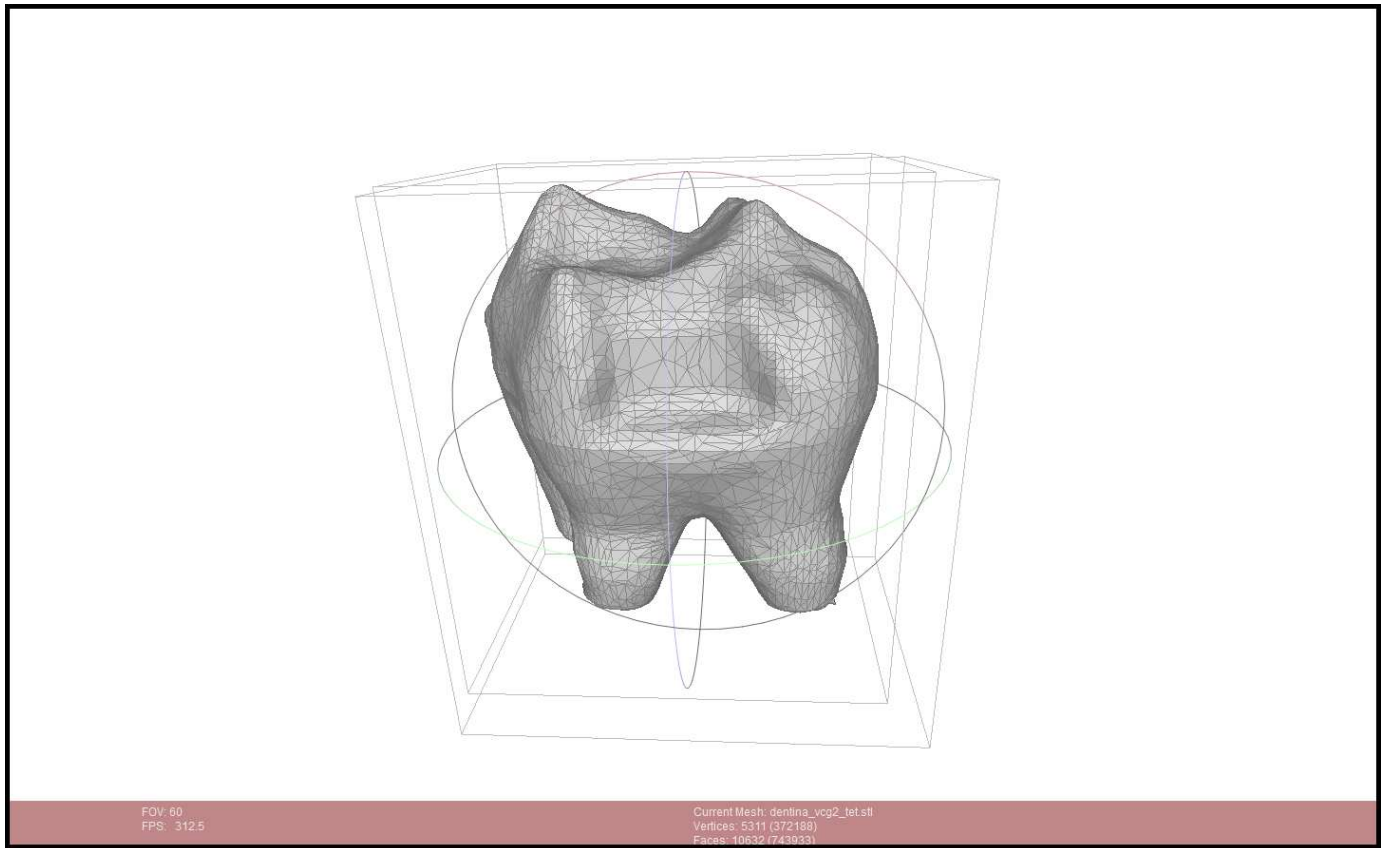


Figure 2.23: Dentine STL surface reconstruction after element reduction and cleaning was performed.

Other small corrections were applied in order to make the mesh fit for volume generation; the elimination of self-intersecting faces was performed and the holes were filled with the automatic function by turning off the default option implemented with self-intersecting algorithms. Finally, superficial normals reorientation was performed on the surface obtained through the described workflow.

This procedure was substantially repeated for all the surfaces but the fillers, which didn't require surface reconstruction.

Reconstruction algorithm introduced deep modifications in the shape by improving the element qualities but with some important drawbacks.

Contact between parts and the model biological accuracy were compromised by these modification; trustworthy results could be only obtained by modifying initial surface as less as possible, which was not possible because of the low quality of the initial data.

The reason lied with the undersampling procedure, which was introduced in order to simplify the model leading to irreversible approximations decreasing the model accuracy.

The Figure 2.24 (a) and Figure 2.24 (b) show the reduced mesh before the adjustments whereas Figure 2.25 (a) and Figure 2.25 (b) illustrate the reconstructed mesh, which was successively converted into a tetrahedron mesh.

2.1. Workflow Definition

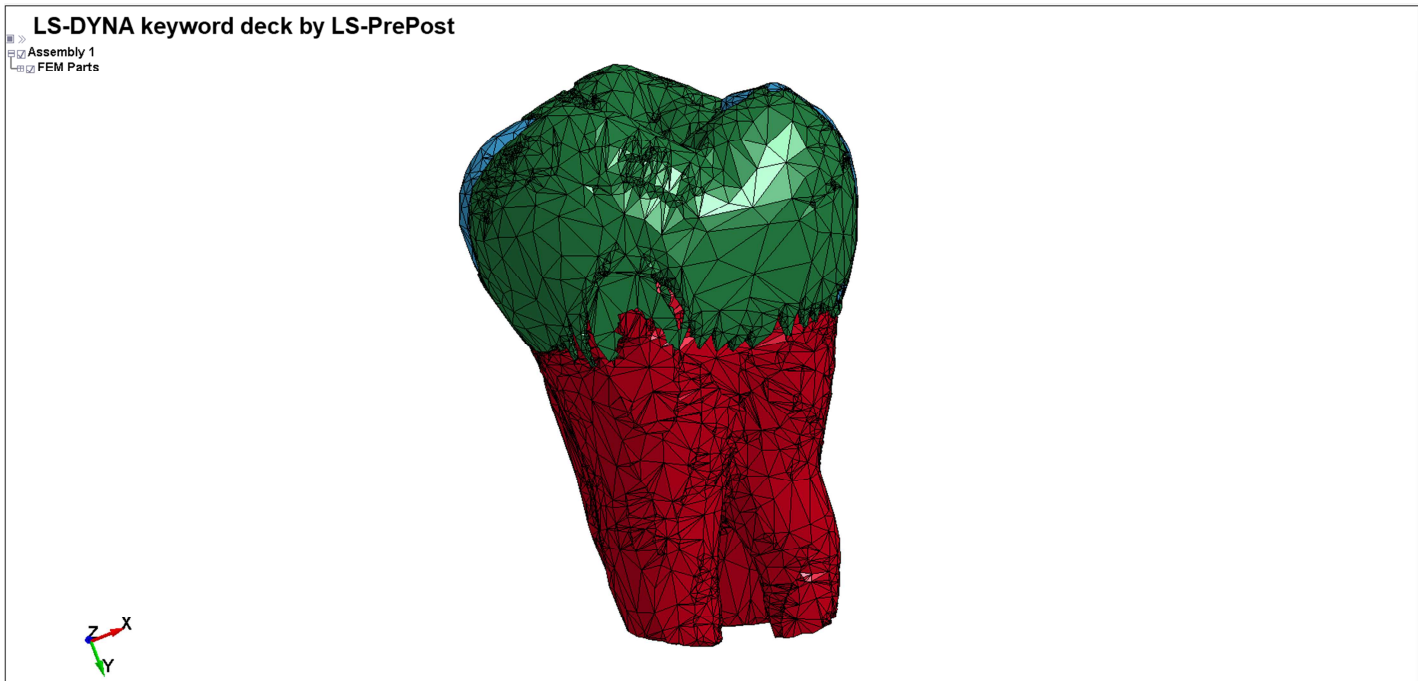


Figure 2.24 (a): lateral view of the tooth mesh before the adjustments

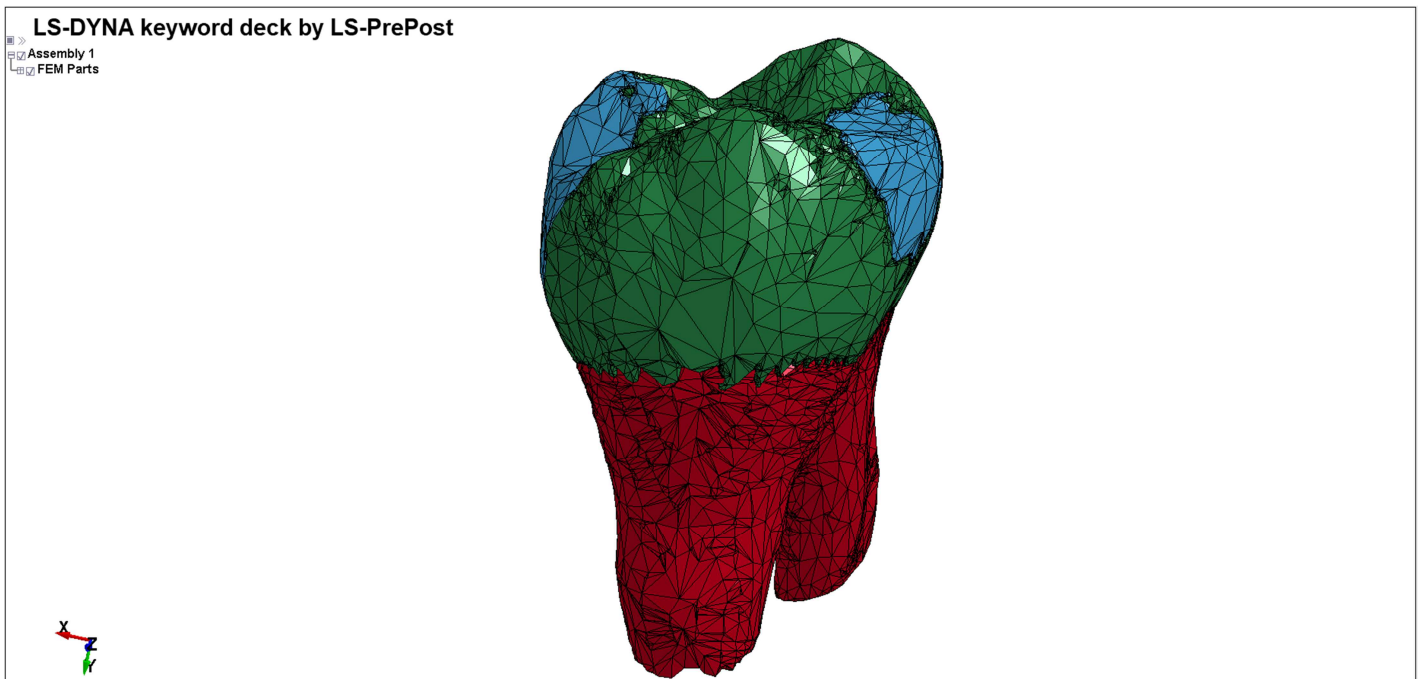


Figure 2.24 (b): frontal view of the tooth mesh before the adjustments

Mesh before the adjustments appeared deeply irregular, the conversion between this model and a 3D solid element was no possible at all, the enamel lateral view clearly shows the enamel defects on the enamel-dentine interface with the presence of unrealistic enamel pointed shapes.

2. METHOD

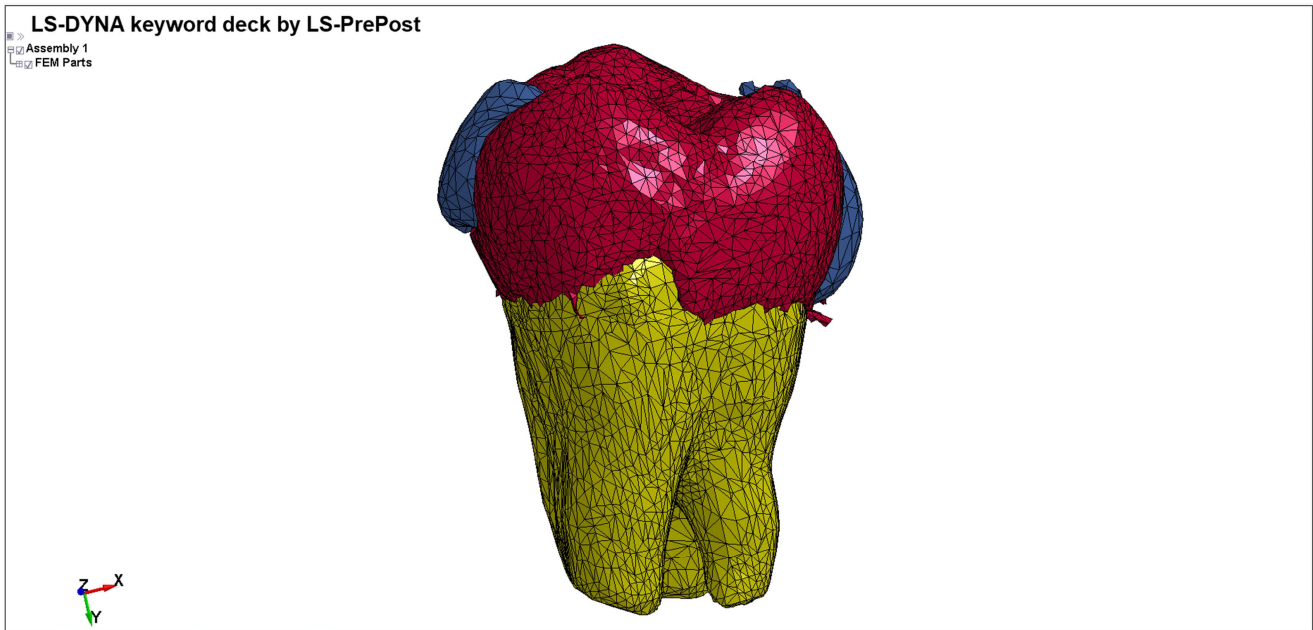


Figure 2.25 (a): lateral view of the tooth mesh after the adjustments were performed

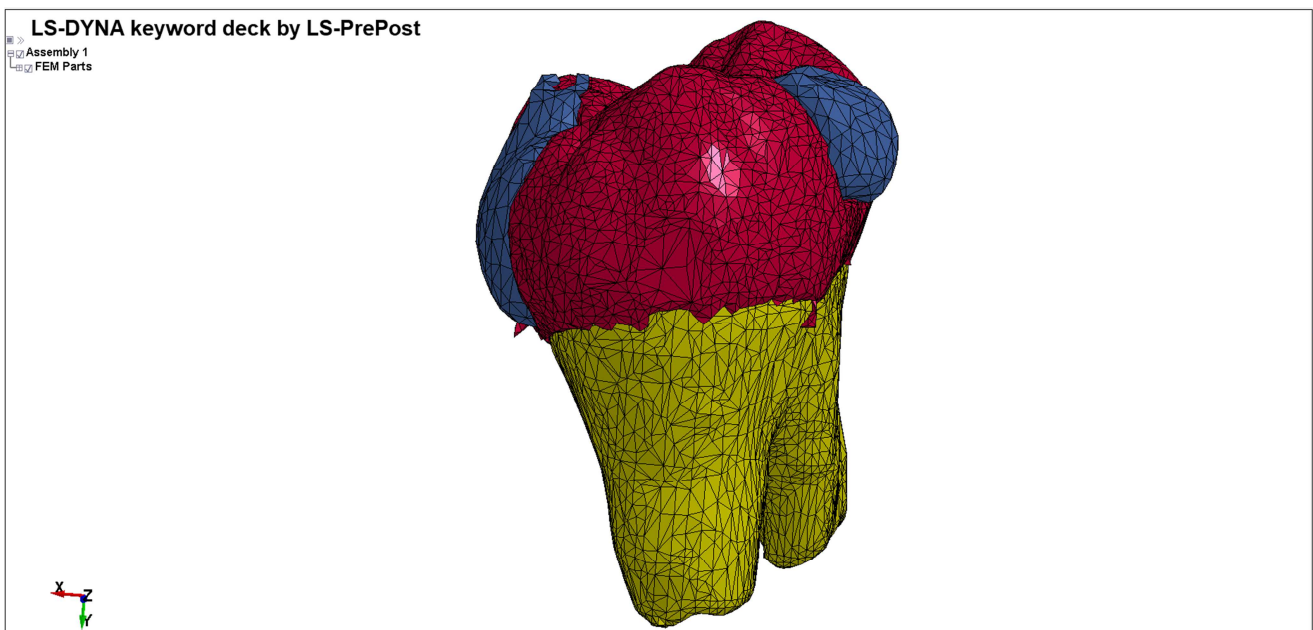


Figure 2.25 (b): frontal view of the tooth mesh after the adjustments were performed

The models showed in Figure 2.25 (a) and Figure 2.25 (b) were finally converted into a tetrahedron solid mesh by allowing FEM simulation.

Despite the new achievements illustrated in Figure 2.25 (a) and Figure 2.25 (b), the biological interface between enamel and dentine presented a non-physiological shape with sharp peaks and protruding elements. Furthermore, also restorative materials jugged out from enamel by creating a non-physiological FEM model.

Finally, a third procedure was similarly performed by considering all the slices to improve the imported STL shapes.

2.1.3. Third procedure

As before mentioned, this third procedure aimed to overcome the shortcomings of the previous model using the automatic operations previously defined. All the scanned slices were imported in Mimics to avoid an initial loss of resolution, as results 610 slices were processed.

Masks definition were performed with the Thresholding values showed in Table 2.3 followed by pre-smoothing operations to improve the shapes regularities.

The same morphological operations and region growing algorithm of the second procedure were applied on the masks as well as the previously-defined Boolean operations whose purpose was to ensure contact between layers.

An important upgrade was introduced to eliminate residual gaps between part, all the masks were dilated of a small number of pixels to ensure the overlap between them, these parts were successively merged into an unique mask. Then in order to obtain one of the layers, the dentine for example, the merged masks were subtracted with both enamel and fillers and the new mask was expanded of the same number of pixels used before.

This procedure was applied for all the masks, in this way internal gaps were definitively eliminated. Figure 2.26 (a), Figure 2.26 (b), Figure 2.26 (c) and Figure 2.26 (d) show the final masks.

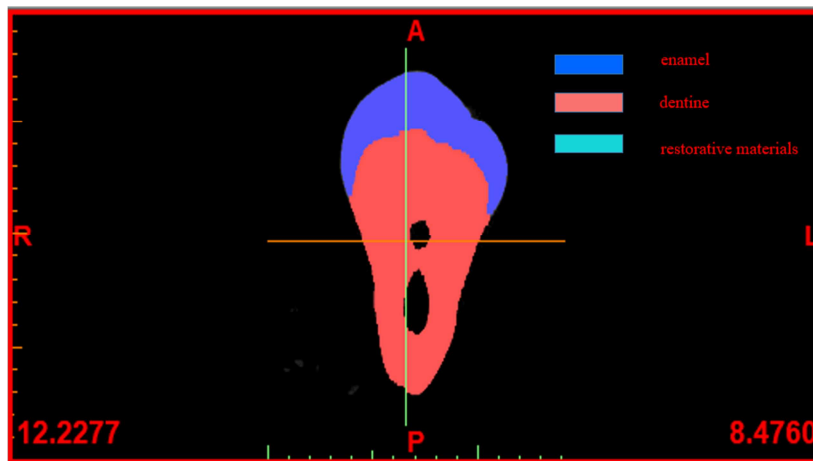


Figure 2.26 (a): Vertical upper tooth slice

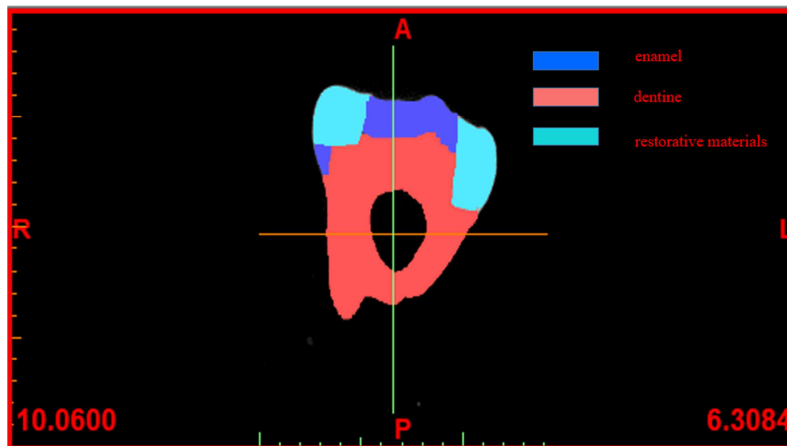


Figure 2.26 (b): Vertical upper-medium tooth slice

2. METHOD

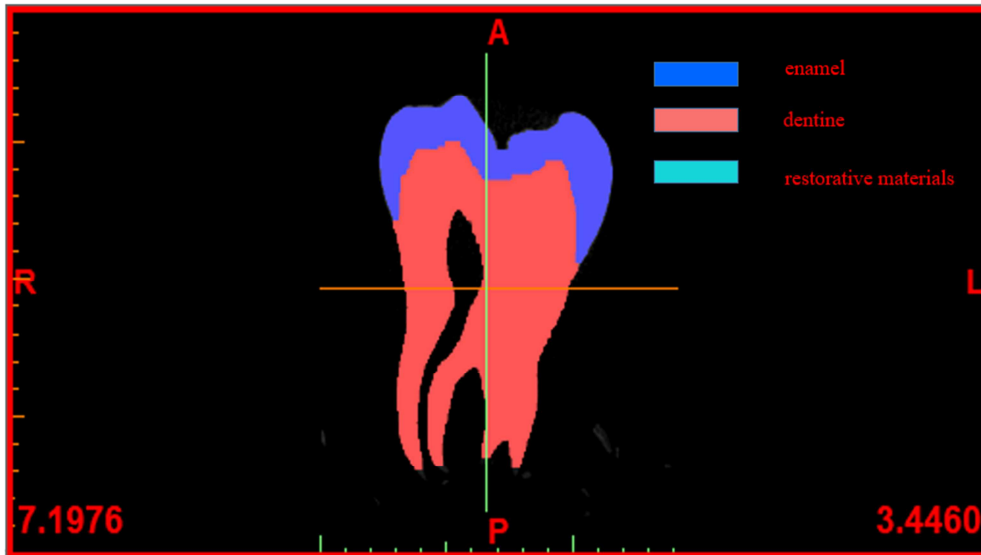


Figure 2.26 (c): Vertical lower-medium tooth slice

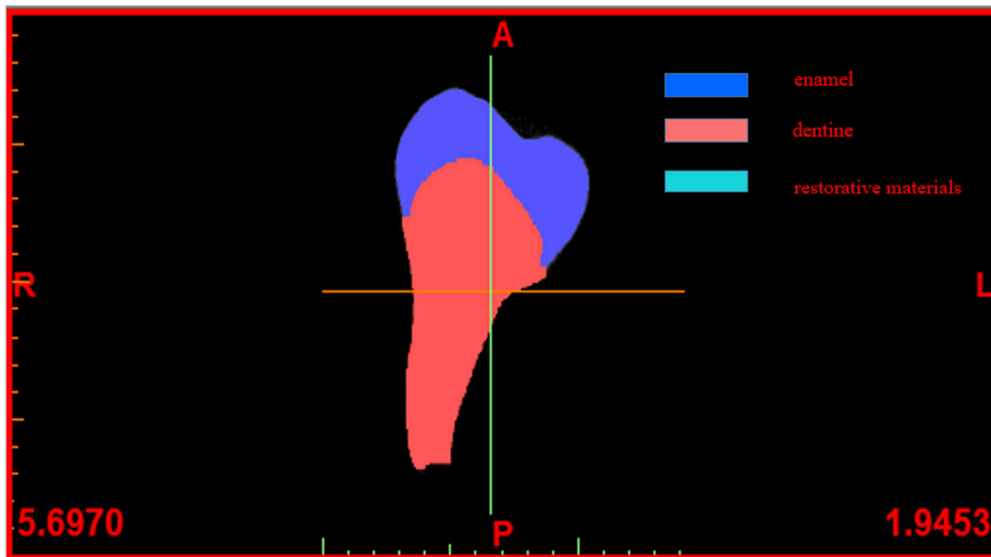


Figure 2.26 (d): Vertical lower tooth slice

Since all the scanned slices were imported in Mimics, the part generation tool fitted the masks in a accurate way by generating surfaces with the micro-CT real declared resolution.

Figure 2.27 (a), Figure 2.27 (b) and Figure 2.27 (c) illustrate part generated from these slices while Figure 2.28 (a), Figure 2.28 (b) and Figure 2.28 (c) show the final parts after smoothing and Boolean operations were performed, Boolean operation were carried out in the same way as described in the second procedure.

2.1. Workflow Definition

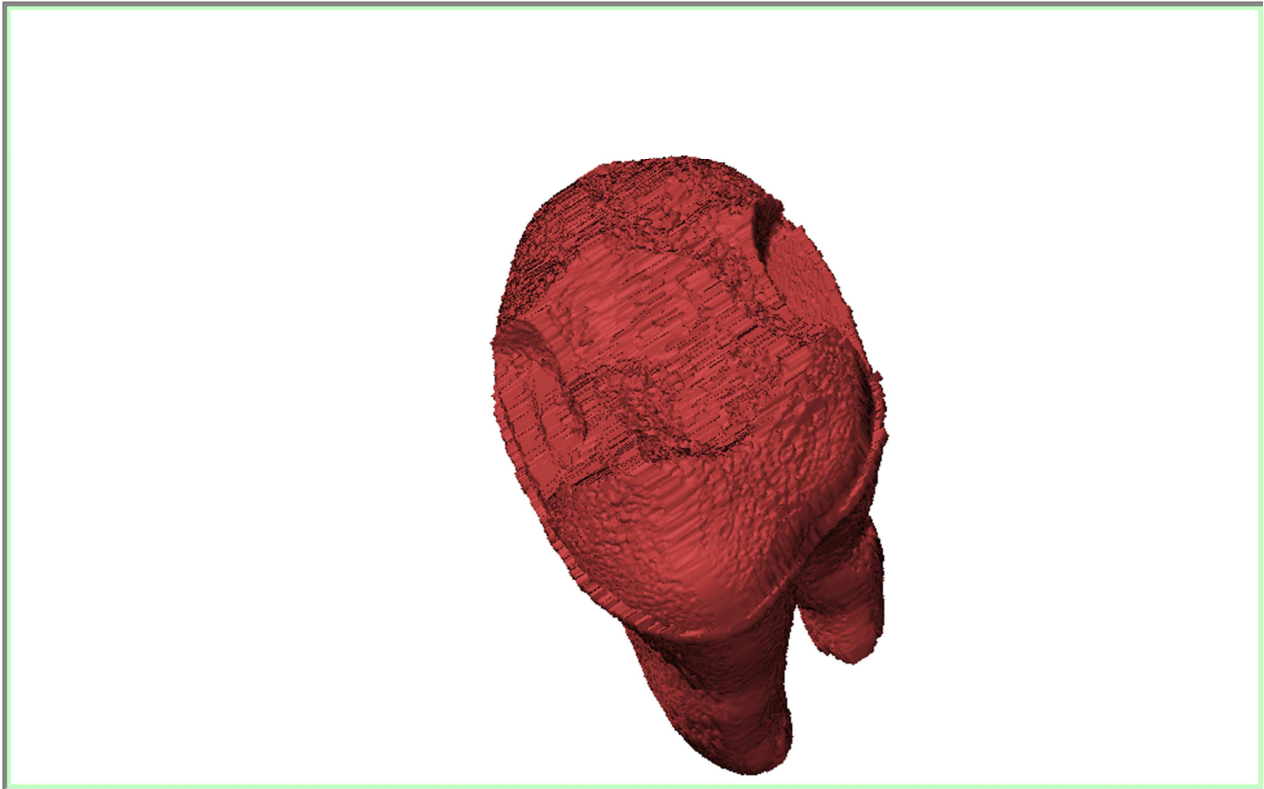


Figure 2.27 (a): Dentine generated part before the adjustments were performed

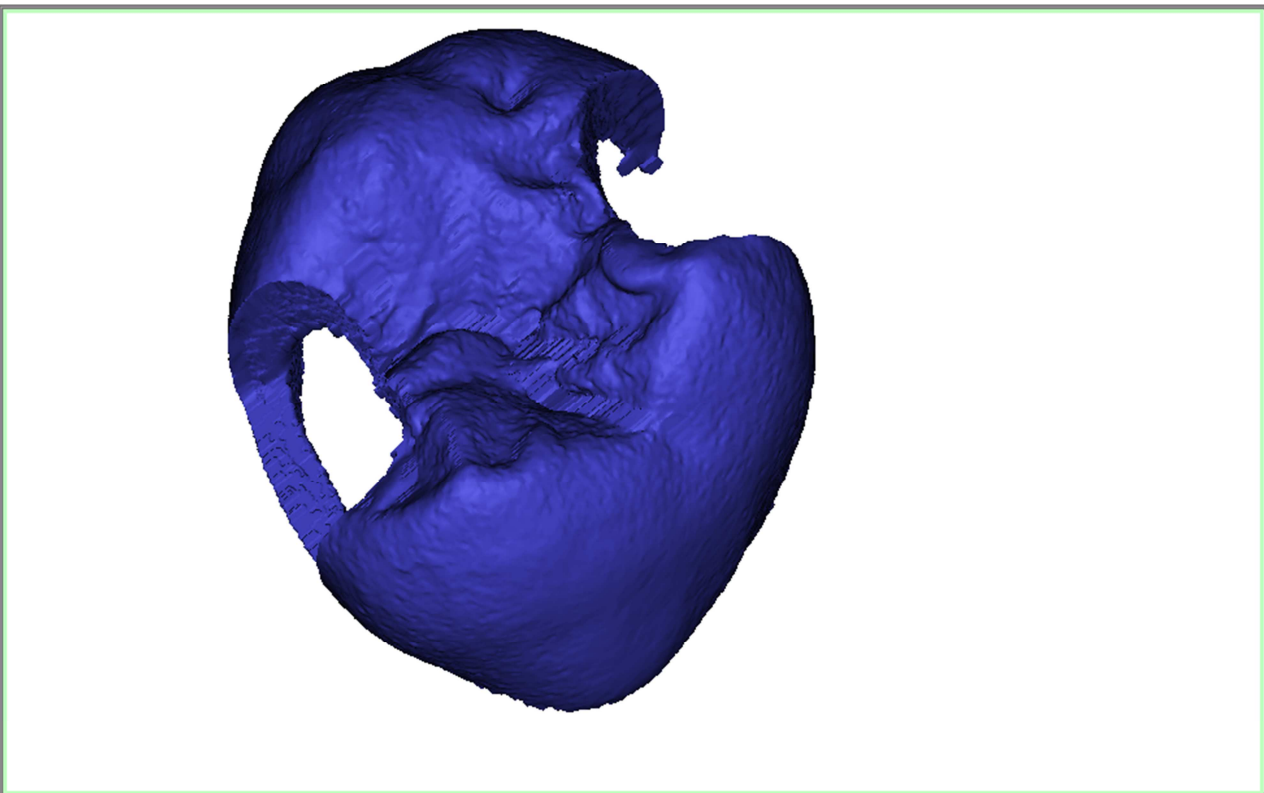


Figure 2.27 (b): Enamel generated part before the adjustments were performed

2. METHOD

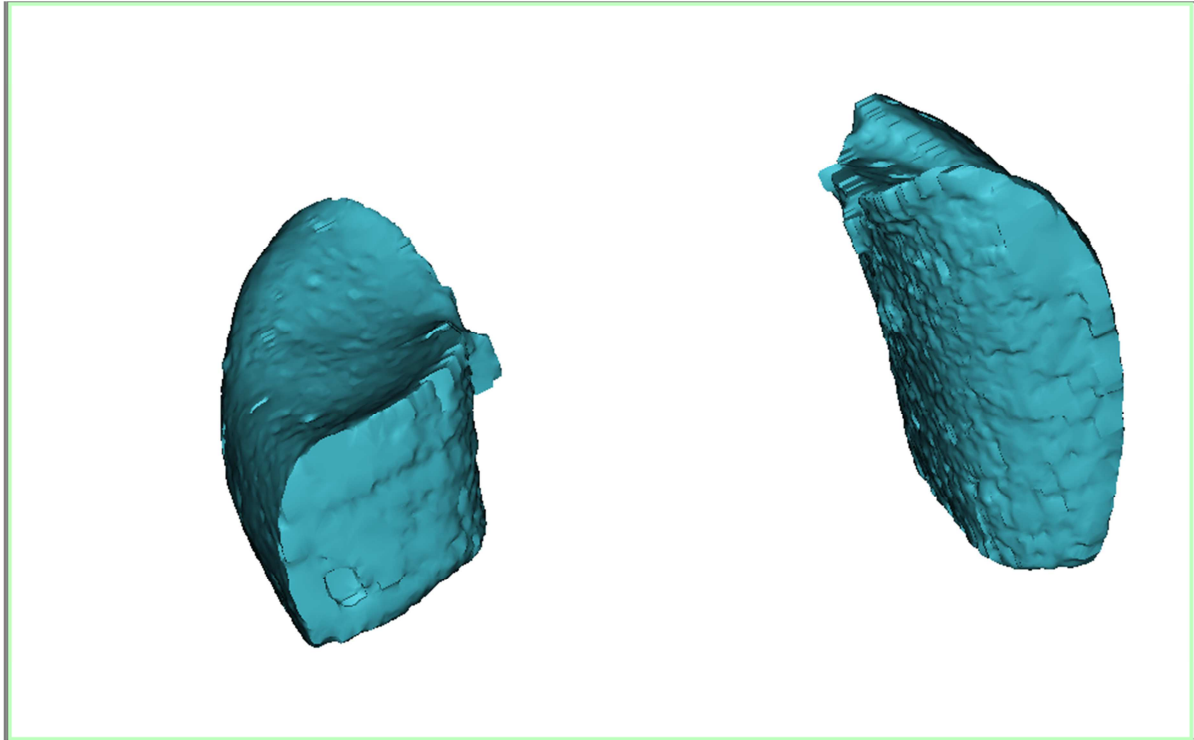


Figure 2.27 (c): Fillers generated parts before the adjustments were performed

These figures could be compared with Figure 2.14 (a), Figure 2.14 (b) and Figure 2.14 (c) , the parts morphologies were totally different from the second attempt especially in the enamel determining a good biological accuracy, which was totally compromised in the previous procedure.

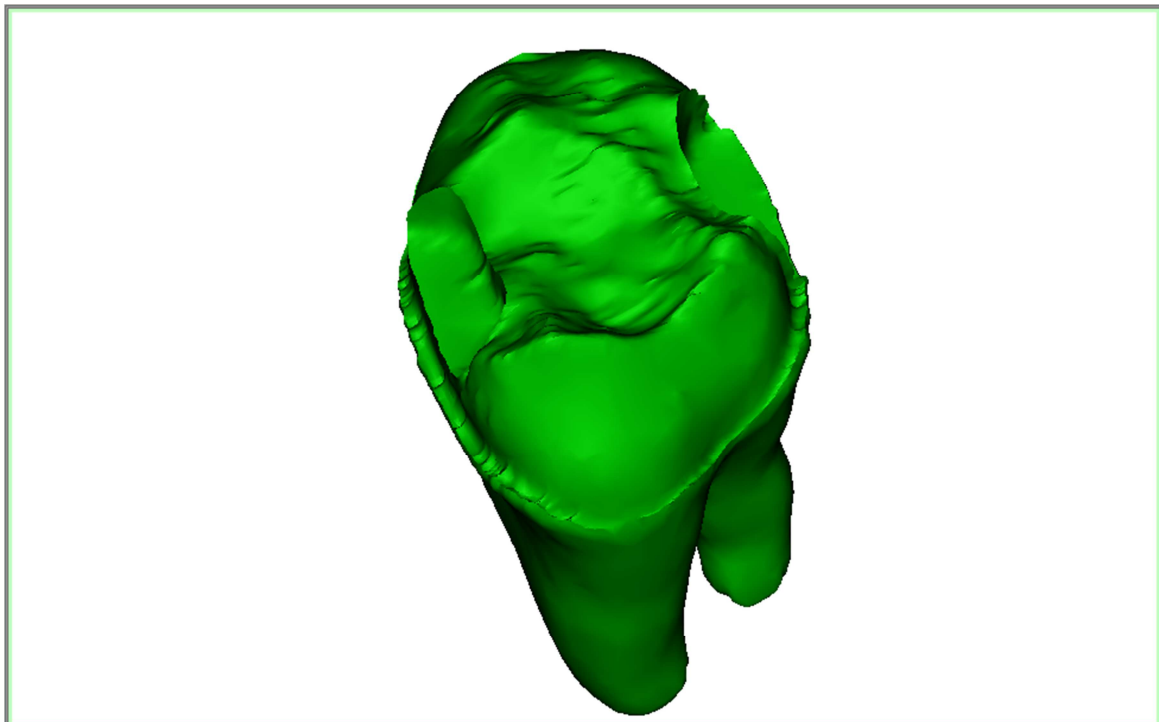


Figure 2.28 (a): Final dentine part generated after the adjustments

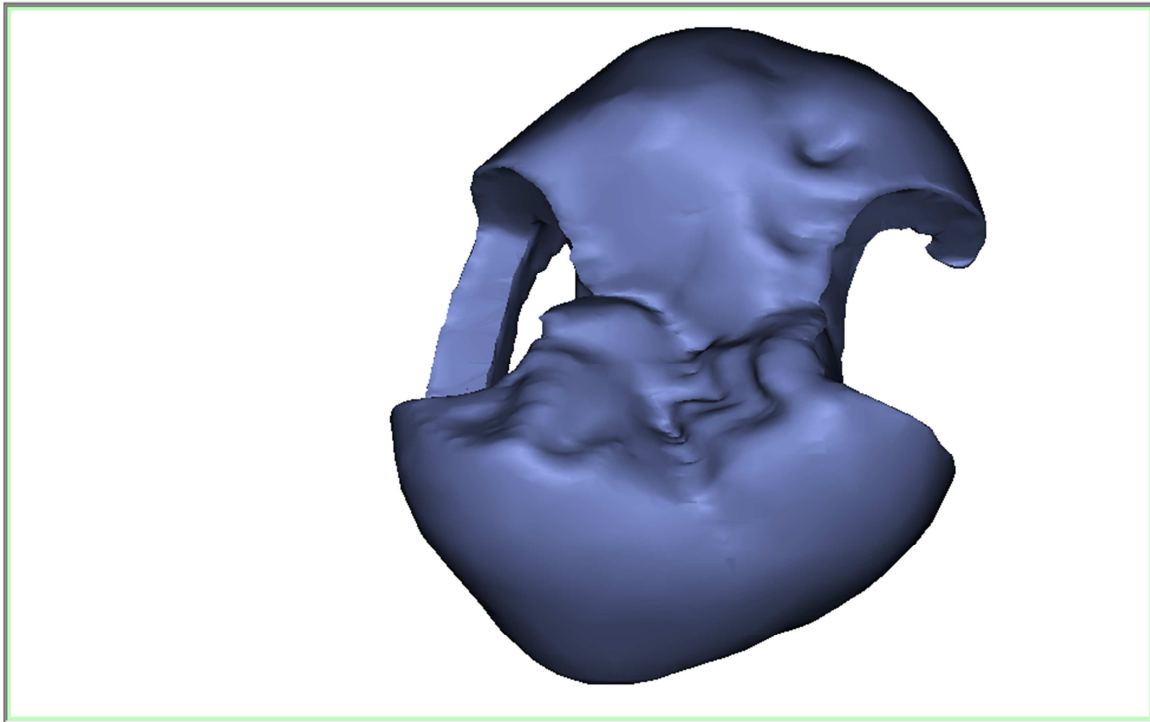


Figure 2.28 (b): Final enamel part generated after the adjustments

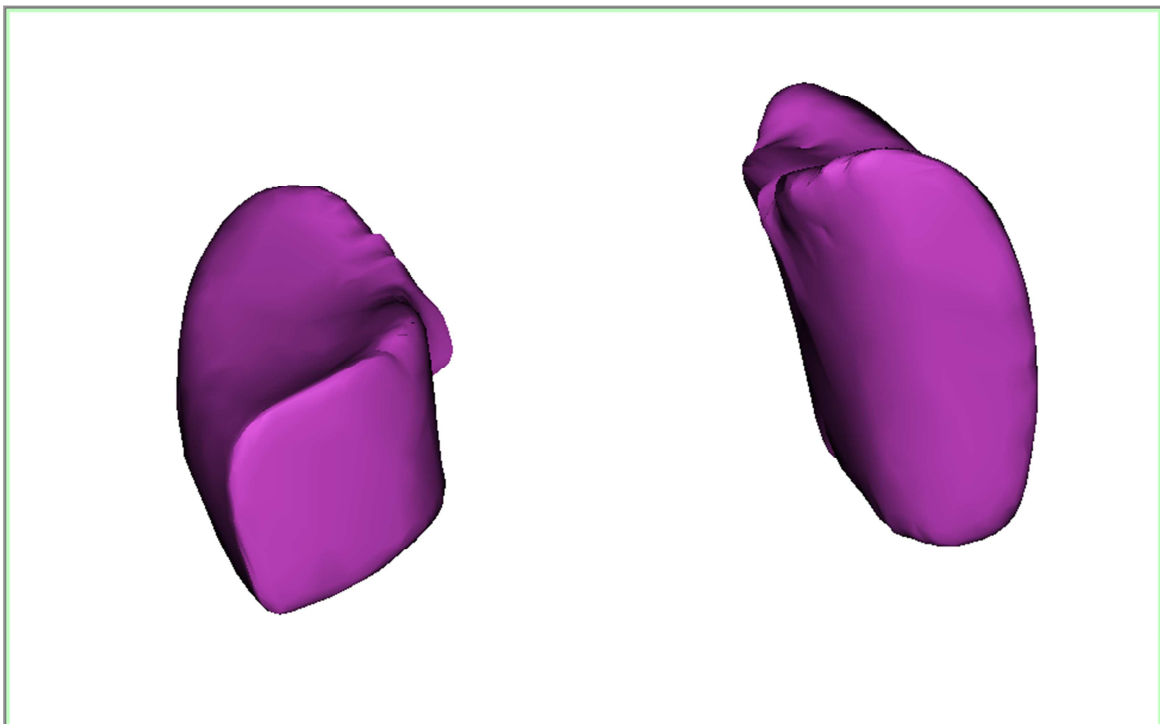


Figure 2.28 (c): Final fillers parts generated after the adjustments

Final results were definitively improved with respect to the second procedure proving that the number of imported slices was crucial for a good resolution. However, most of stages applied to obtain these results were defined in the second workflow, whose importance was undeniable.

2. METHOD

The final parts were successively converted into STL, Figure 2.29 (a) and Figure 2.29 (b) show the final files imported in Meshlab before the refinement process was performed.

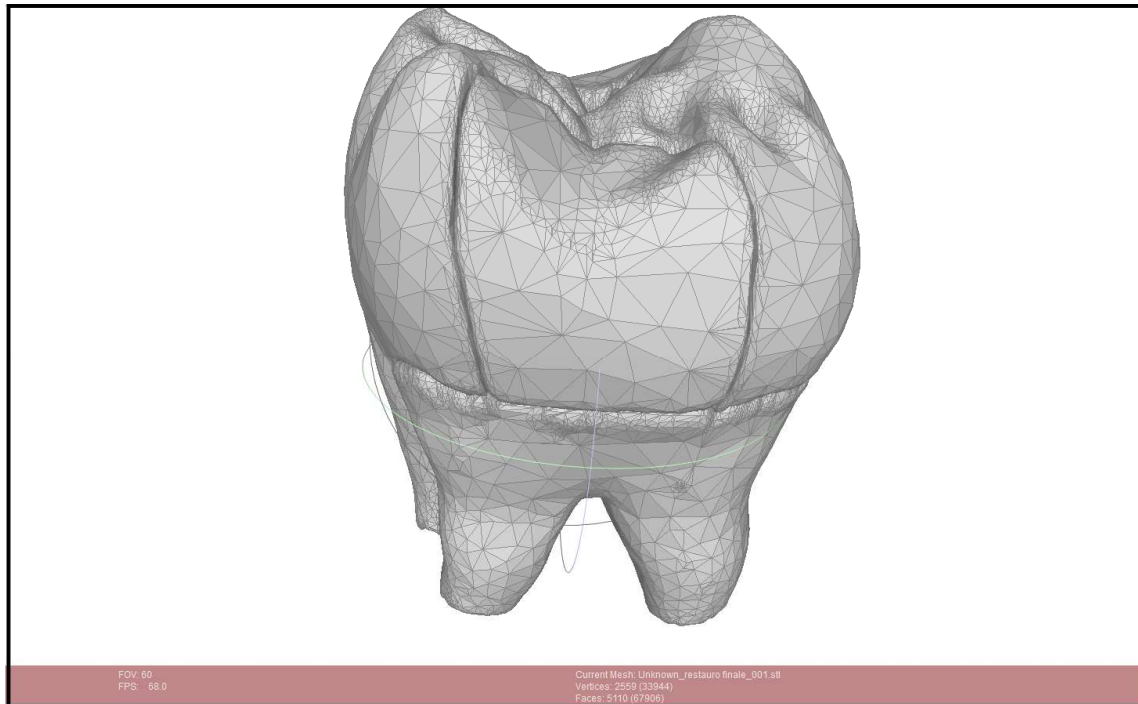


Figure 2.29 (a): Bigger filler view of STL tooth files imported in Meshlab

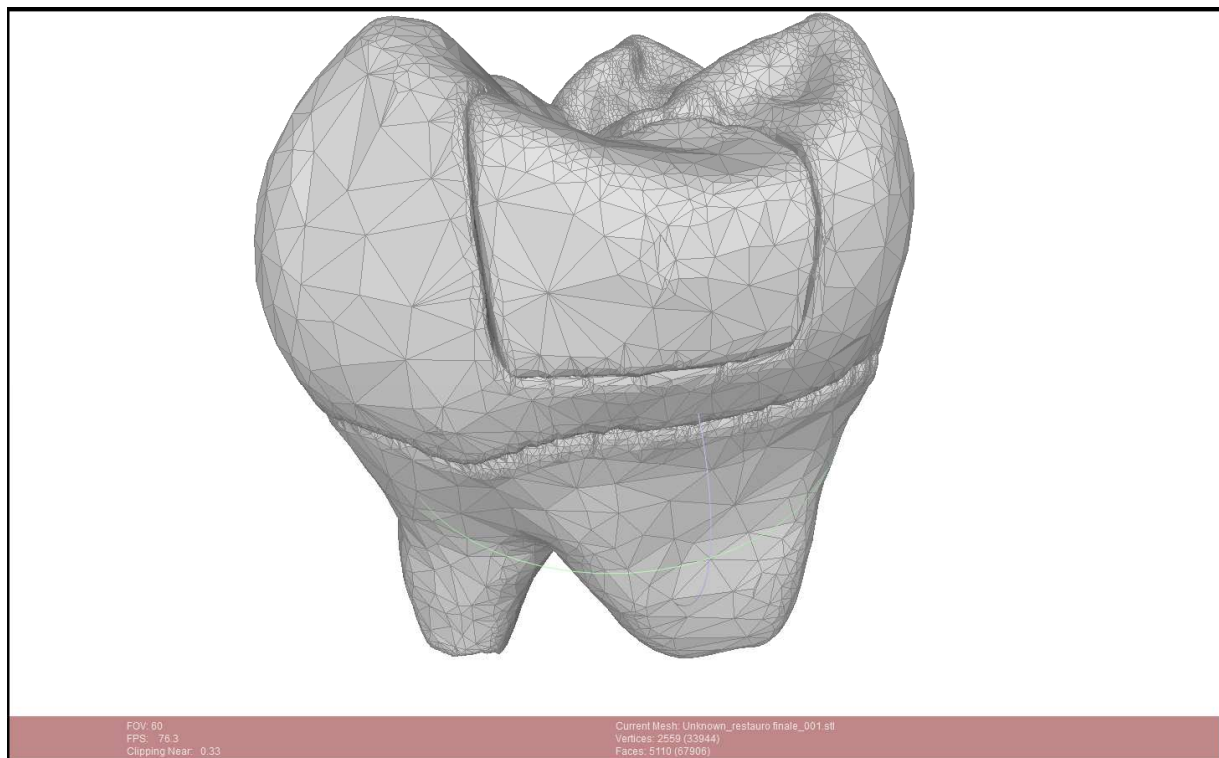


Figure 2.29 (b): Smaller filler view of STL tooth files imported in Meshlab

2.1. Workflow Definition

The elements number of these imported STL files were really small with respect to those of the second procedure, the reason was the elimination of small defects whose meshing process drastically increased the element numbers; for example, the dentine elements automatically generated on the latter procedure were 31908 ,which are few elements compared with the 685548 faces generated in the second procedure. Therefore, the STL files average element size was bigger than it used to be; the adopted mesh refinements were very similar to the previous attempt but rebuilding algorithms were not used at all.

Number elements decimation were performed and degenerated elements were eliminated, then holes were filled and normals were reoriented making the mesh suitable for volume elements generation. Imported dentine, enamel and fillers are showed in Figure 2.30 (a), Figure 2.30 (b) and Figure 2.30 (c) whereas refined parts are illustrated in Figure 2.31 (a), Figure 2.31 (b) and Figure 2.31 (c). However, Figure 2.31 (a), Figure 2.31 (b) and Figure 2.31 (c) element qualities were not optimal and remeshing operations were performed to improve their features. Consequently, a method to improve the quality of the refined mesh was needed, the approach adopted to rebuild the mesh not excessively modifying the tooth geometry will be discussed in this section.

The rebuild mesh quality will be compared with those of the refined models through the Ls-Dyna PrePost mesh quality tools in order to quantify the obtained improvements.

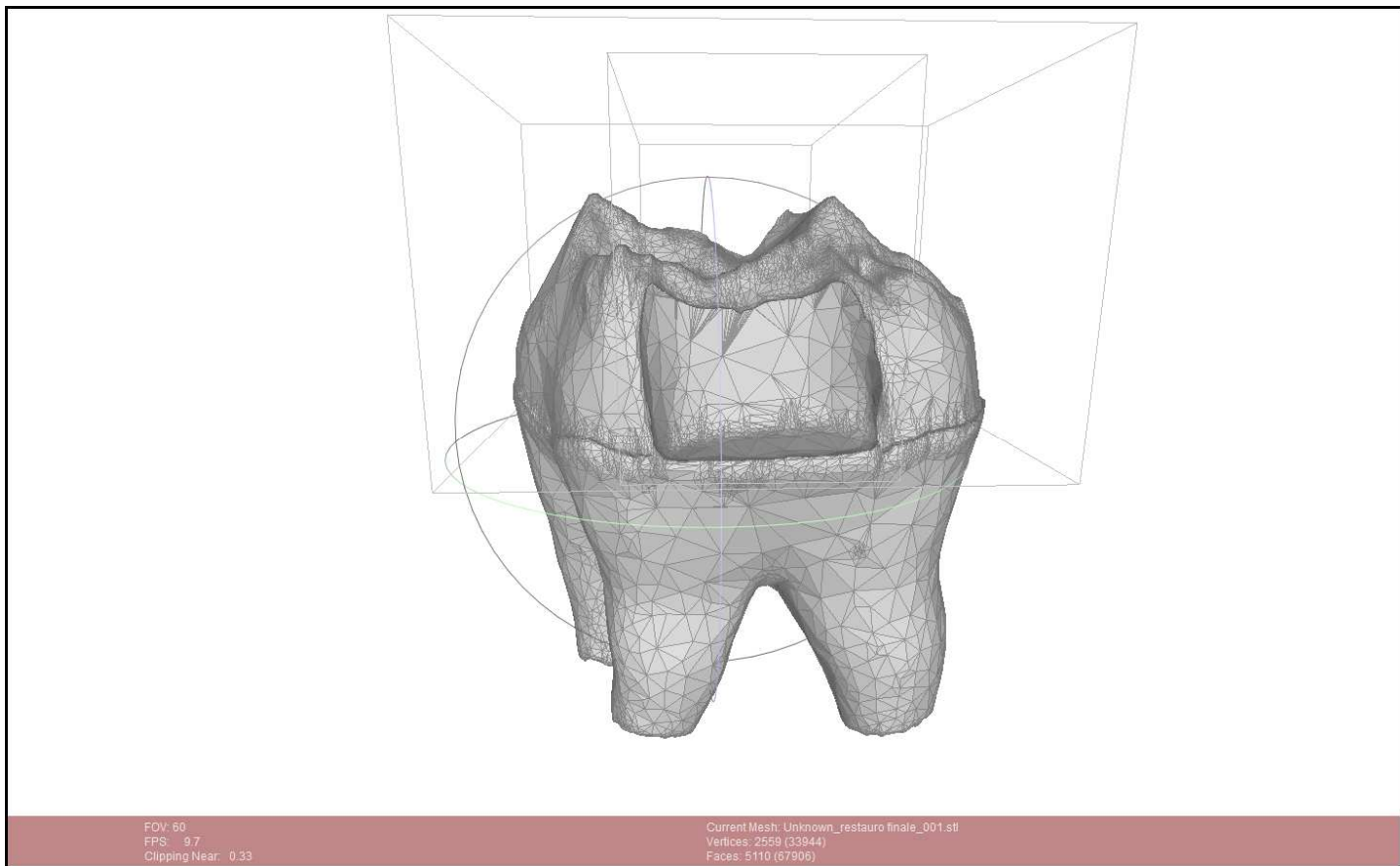


Figure 2.30 (a): Dentine STL mesh before the refining process

2. METHOD

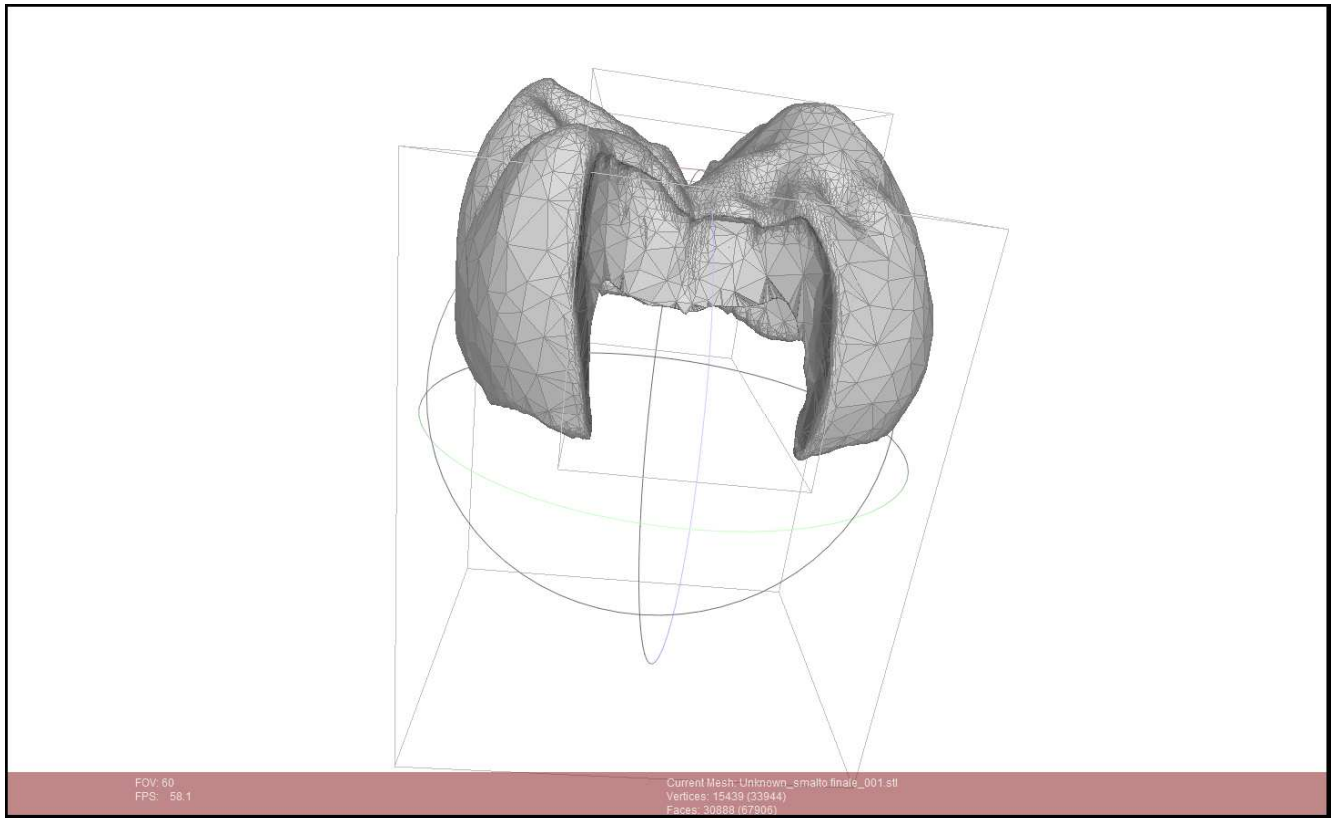


Figure 2.30 (b): Enamel STL mesh before the refining process

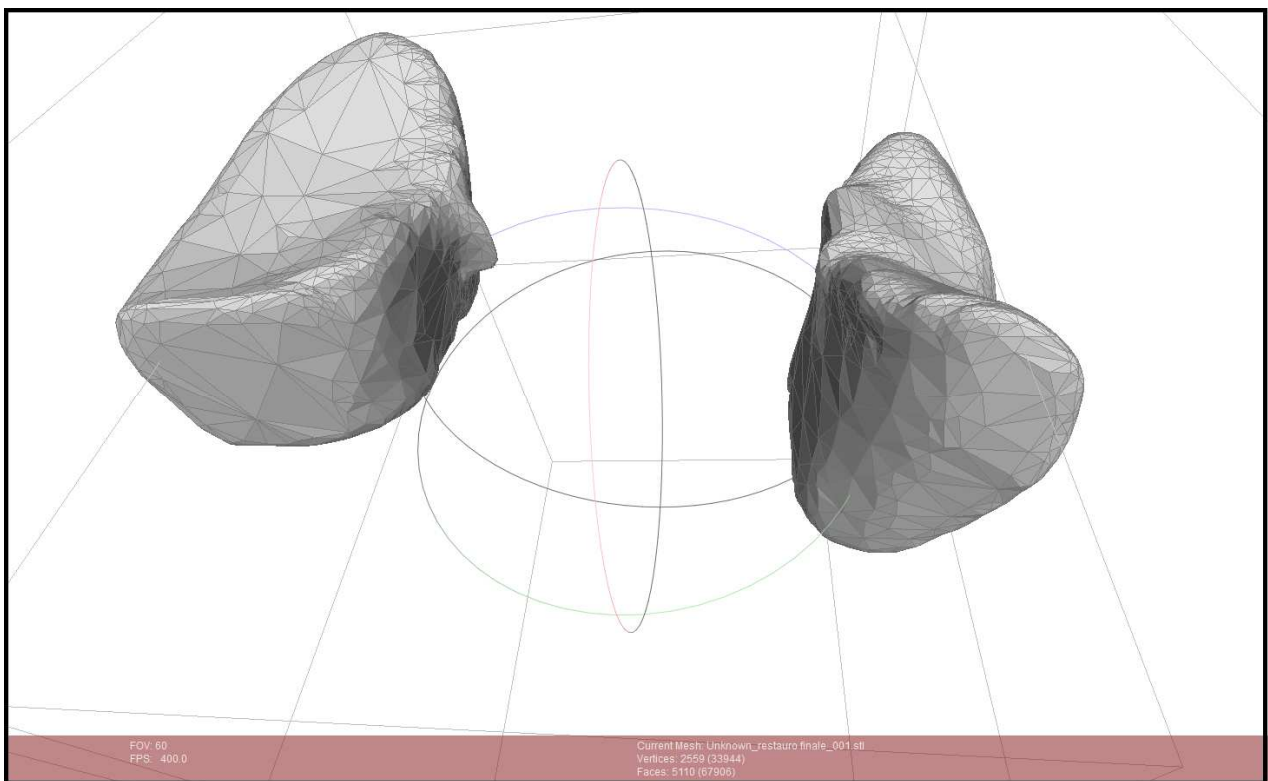


Figure 2.30 (c): Fillers STL mesh before the refining process

2.1. Workflow Definition

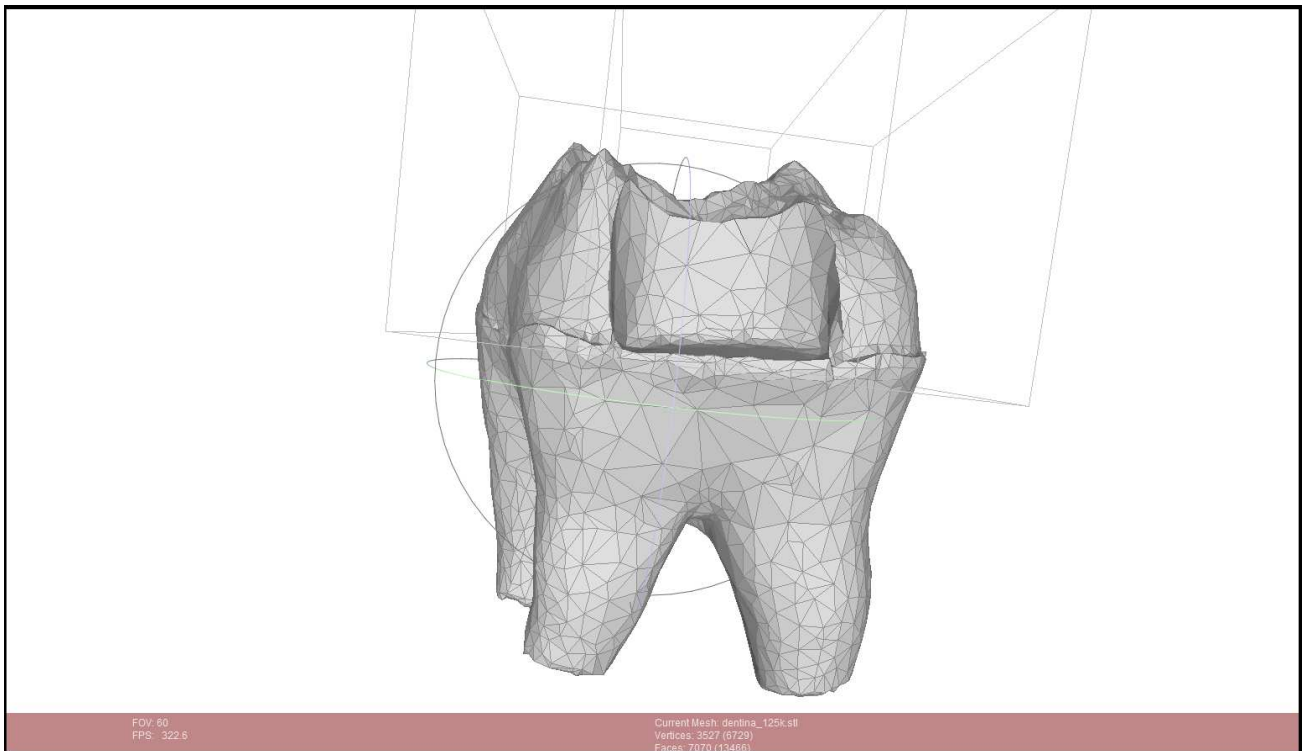


Figure 2.31 (a): Dentine STL mesh after the refining process

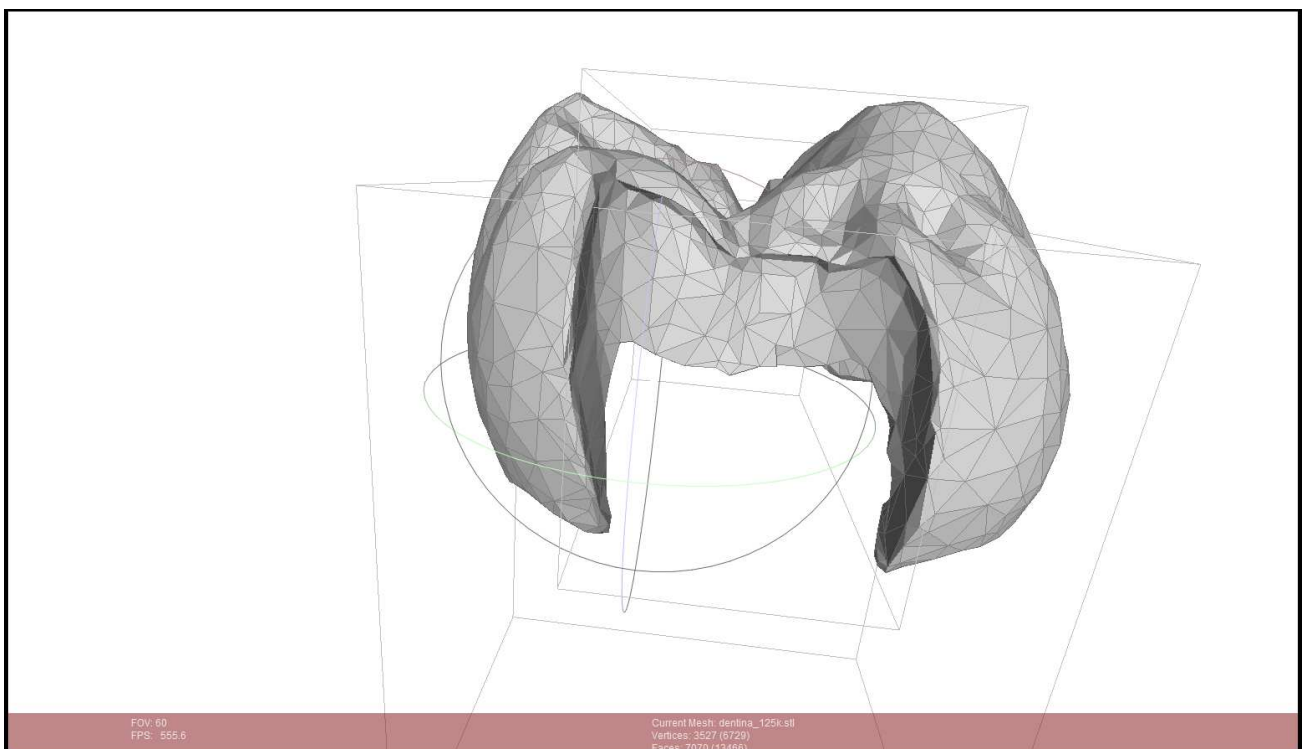


Figure 2.31 (b): Enamel STL mesh after the refining process

2. METHOD

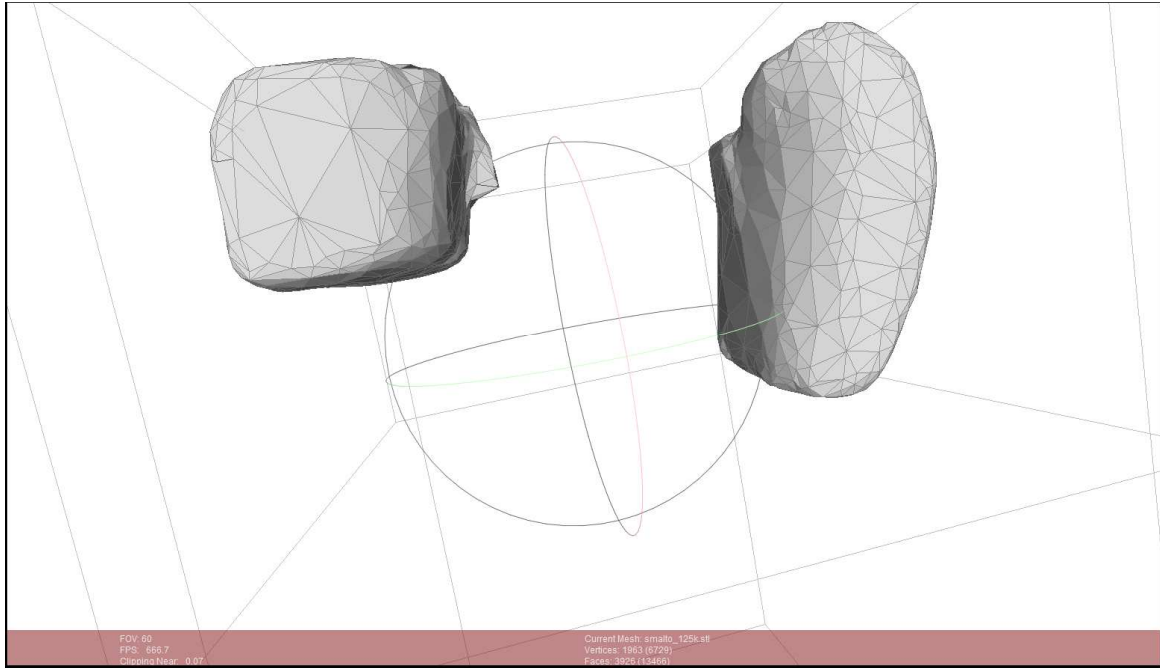


Figure 2.31 (c): Fillers STL mesh after the refining process

The two-dimensional models in Figure 2.31 (a), Figure 2.31 (b) and Figure 2.31 (c) were successively converted into a tetrahedral mesh through Ls-Dyna PrePost volumetric mesh builder. The 3-D mesh is showed in Figure 2.32 (a) and Figure 2.32 (b), the biological accuracy was drastically improved with respect to the second procedure as well as the surfaces qualities. Despite the improvements, the surface was coarsely meshed ,therefore, FEM simulations results shouldn't be considered trustworthy.

Ls-Dyna provides analysis tools to understand whether the mesh quality is good or not, in this section solid elements aspect ratio, characteristic length and time-step will be analysed to quantify the mesh quality.

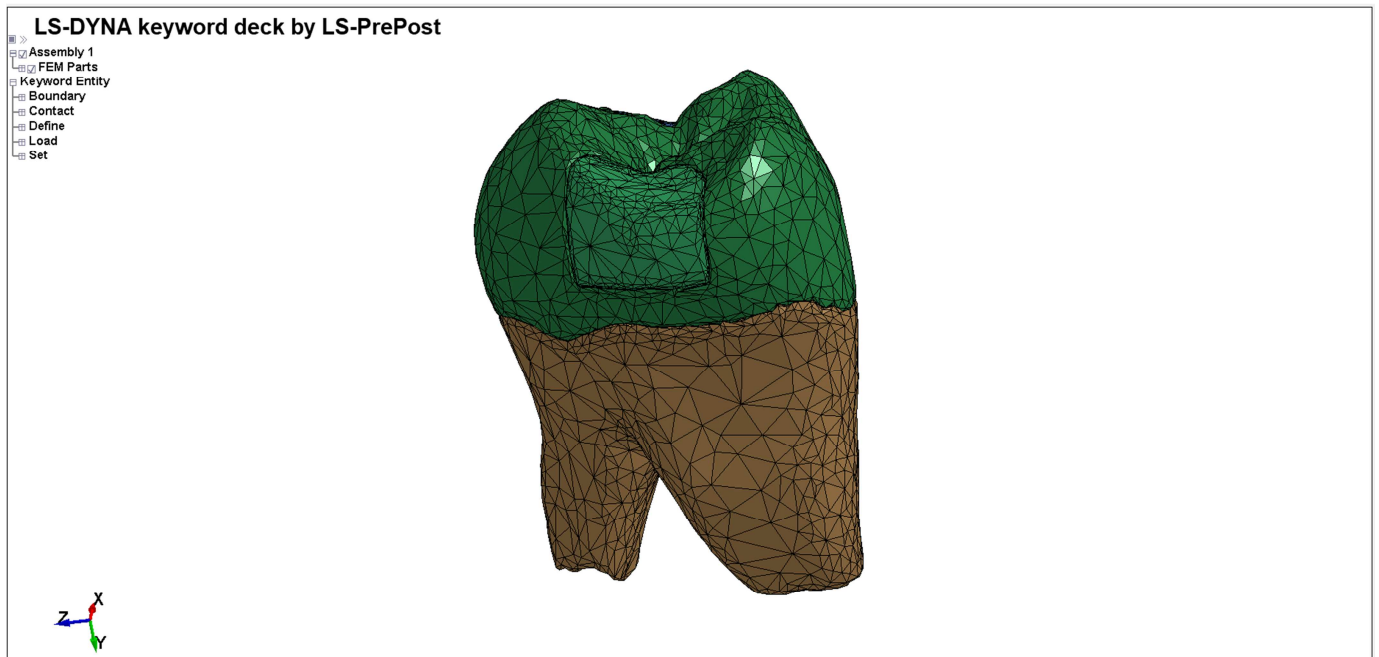


Figure 2.32 (a) : First volumetric model ,small filler view

2.1. Workflow Definition

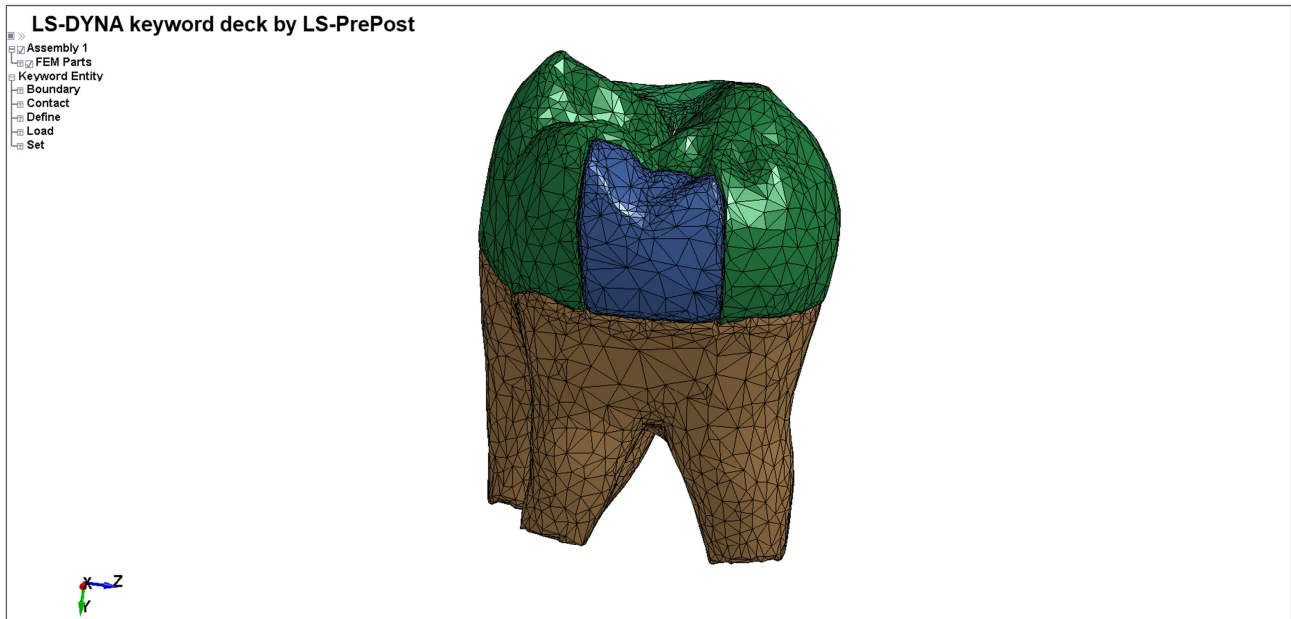


Figure 2.32 (b): First volumetric model ,big filler view

Solid elements characteristic length and aspect ratio assess the element dimension and distortion whereas time-step gives an idea about the simulation running time^[38], the element with the smaller time step set the time required to obtain the simulation results.

Therefore, time-step need to be carefully controlled in order to run complex simulation in a reasonable time. Wide ranges of solid element characteristic lengths, high aspect ratio values and small time-step are indications of coarse mesh.

Solid element aspect ratio, characteristic length and time step are showed in Figure 2.33 (a), Figure 2.33 (b) and Figure 2.33 (c), respectively.

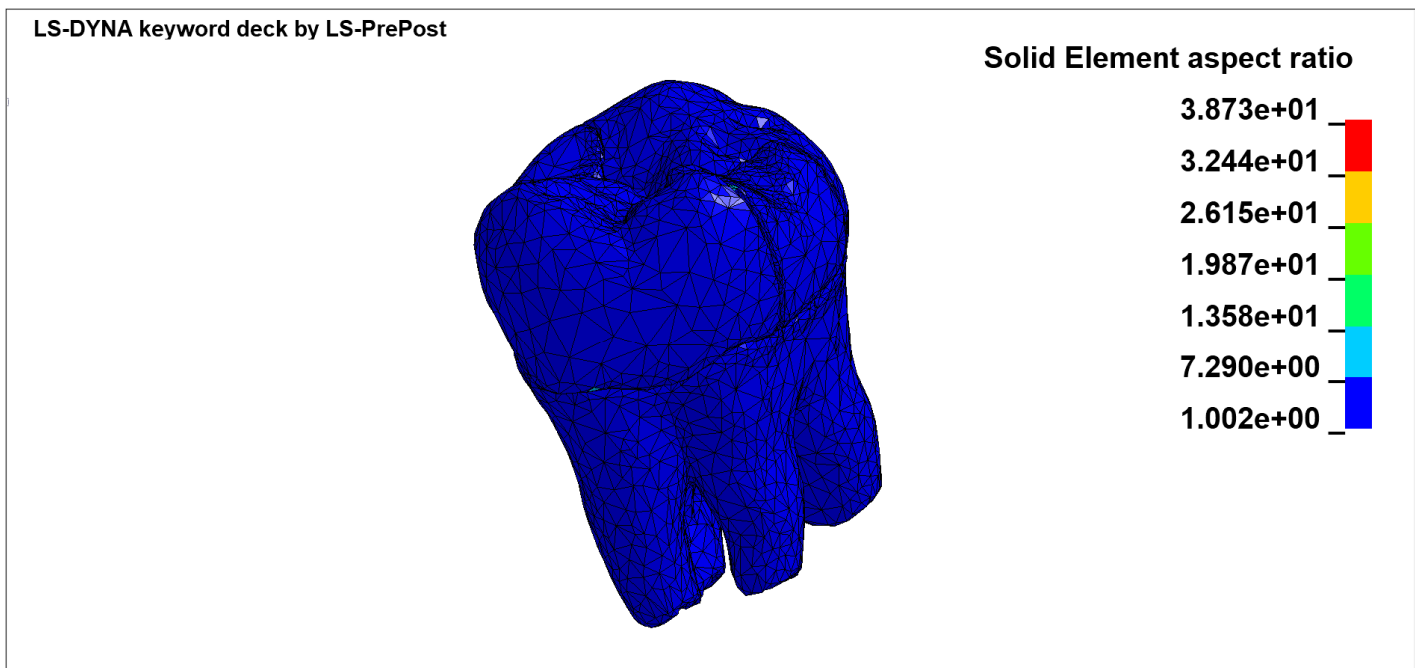


Figure 2.33 (a): Solid element aspect ratio of the refined tooth mesh

2. METHOD

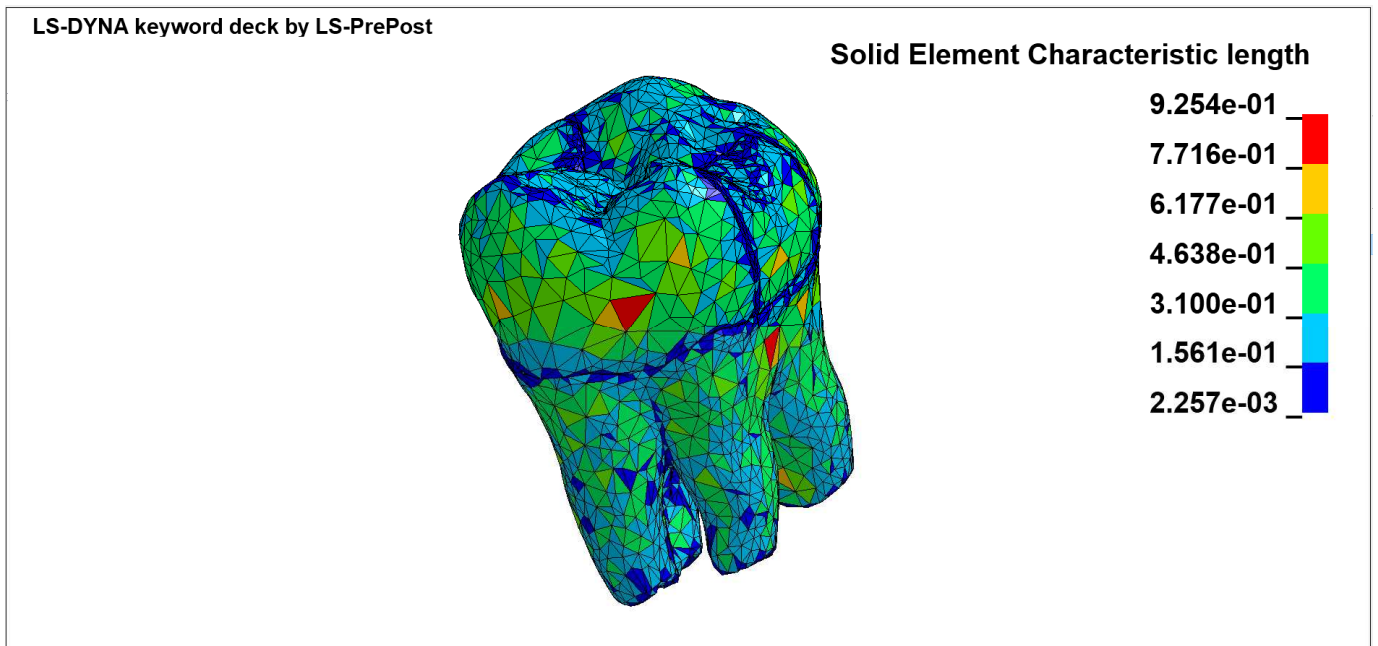


Figure 2.33 (b): Solid element characteristic length of the refined tooth mesh

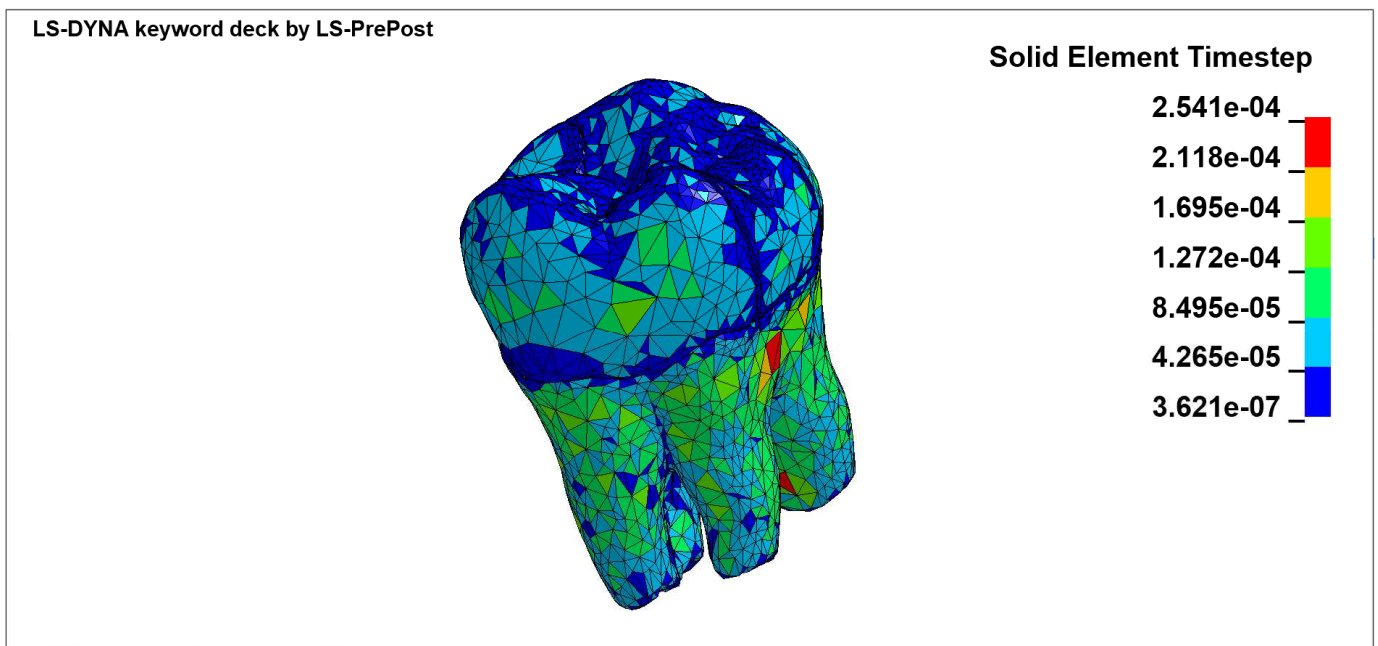


Figure 2.33 (c): Solid element time-step of the refined tooth mesh

As showed in Figure 2.33 (a), the elements aspect ratio was ranged from 1 to 38 showing the presence of deeply distorted elements, characteristic lengths were spanned over two order of magnitudes revealing an huge different size between elements. Moreover, the minimum time step was around $3 * 10^{-7} ms$ leading to unsustainable simulations running times.

Therefore, a mesh rebuilding process was required to perform reliable and efficient simulations.

2.1. Workflow Definition

As previously told, Ls-dyna PrePost is provided with an tetrahedron mesh builder, which allows to build volumetric mesh from two-dimensional mesh but it also enables to rearrange shell mesh. Three different solid models were generated from the rearranged two-dimensional mesh by employing all the solid mesh building algorithms. Since all the obtained results showed comparable improvements in matter of aspect ratio, characteristic length and time-step other parameters needed to be evaluated to choose one tetrahedron mesh builder method, the adopted criteria was to opt for the mesh made up of the fewer number of elements that led to speed up calculations. Figure 2.34 (a) and Figure 2.34 (b) show the new shell mesh created by Ls-Dyna remeshing tools.

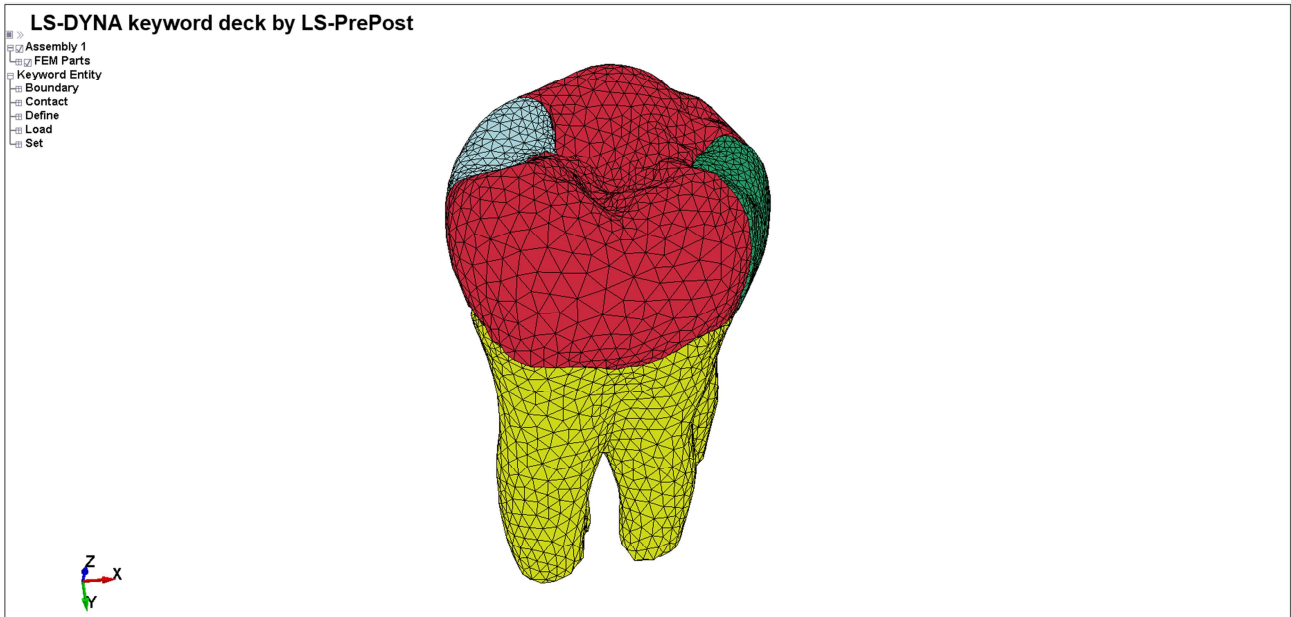


Figure 2.34 (a): View of tooth shell mesh obtained after the rebuilding process

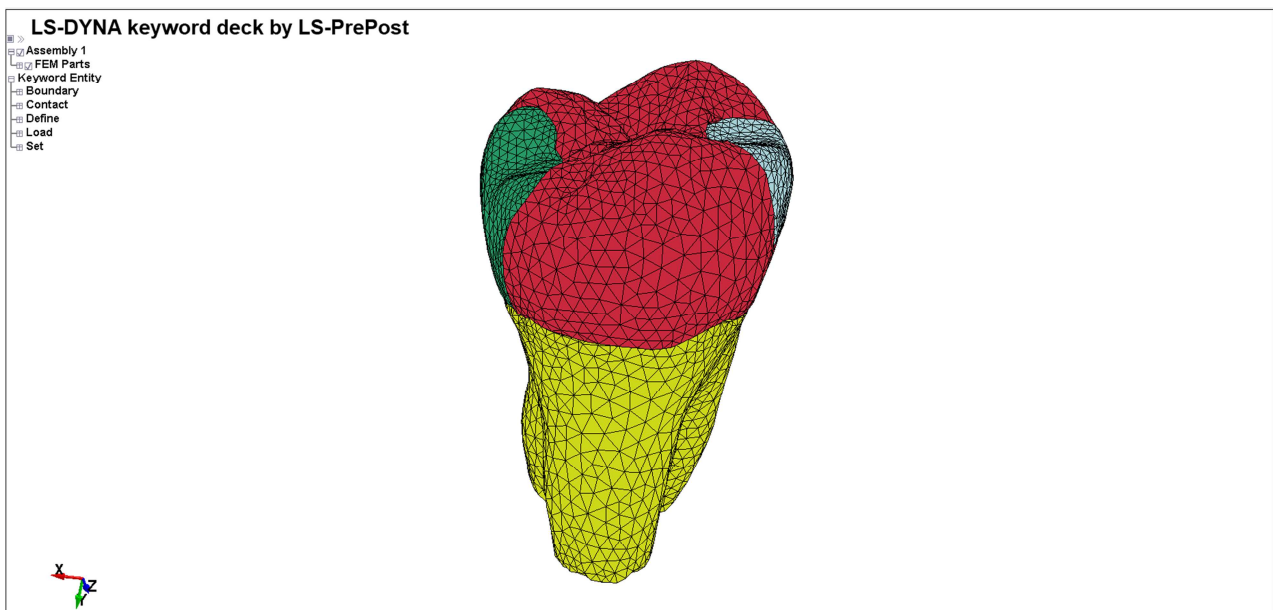


Figure 2.34 (b): Complementary view of tooth shell mesh obtained after the rebuilding process

2. METHOD

The shell mesh shown in Figure 2.34 (a) and Figure 2.34 (b) was directly produced by remeshing the model in Figure 2.32 (a), Figure 2.32 (b). The Table 2.4 makes a comparison between the refined model elements number and those of the rebuilt mesh.

Table 2.4 : Number of elements in different volumetric models.

Tetrahedron mesh builder	Number of solid elements
First volumetric model	125061
First mesh builder	85891
Second mesh builder	66738
Third mesh builder	83729

All the volumetric mesh builders led to generate models composed by fewer elements than the First volumetric models showed in Figure 2.32; the second volumetric 3-D mesh was adopted according to the above-explained criteria.

Figure 2.35 (a), Figure 2.35 (b) and Figure 2.35 (c) show the 3-D element mesh obtained with the second 3-D mesh builder.

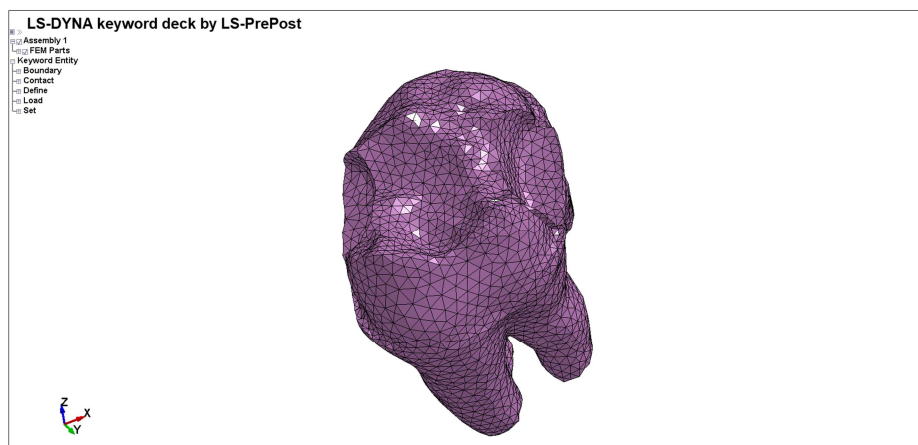


Figure 2.35 (a): Final dentine solid tri-dimensional mesh

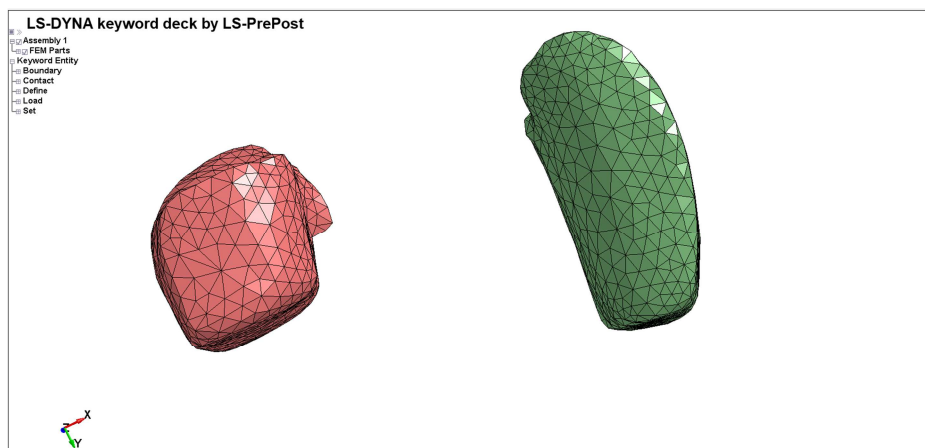


Figure 2.35 (b): Final fillers solid tri-dimensional mesh,

2.1. Workflow Definition

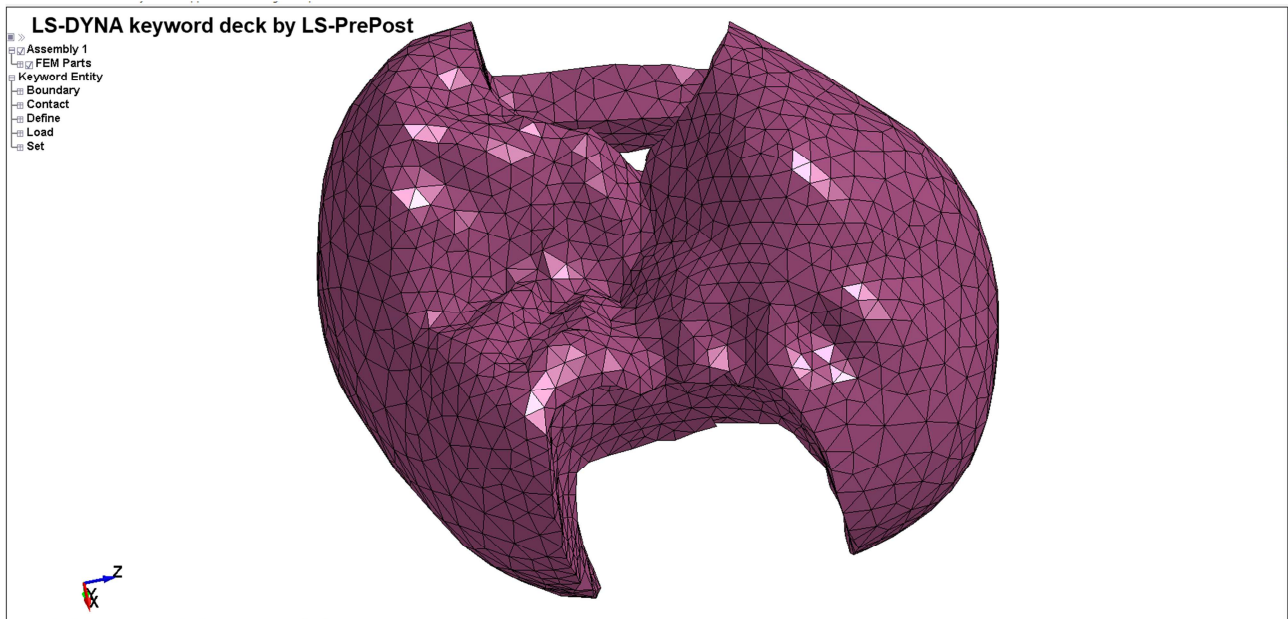


Figure 2.35 (c): Final enamel solid tri-dimensional mesh

Solid element aspect ratio, characteristic length and time step were analysed to quantify mesh improvements, the improvements are showed in Figure 2.36 (a), Figure 2.36 (b) and Figure 2.36 (c).

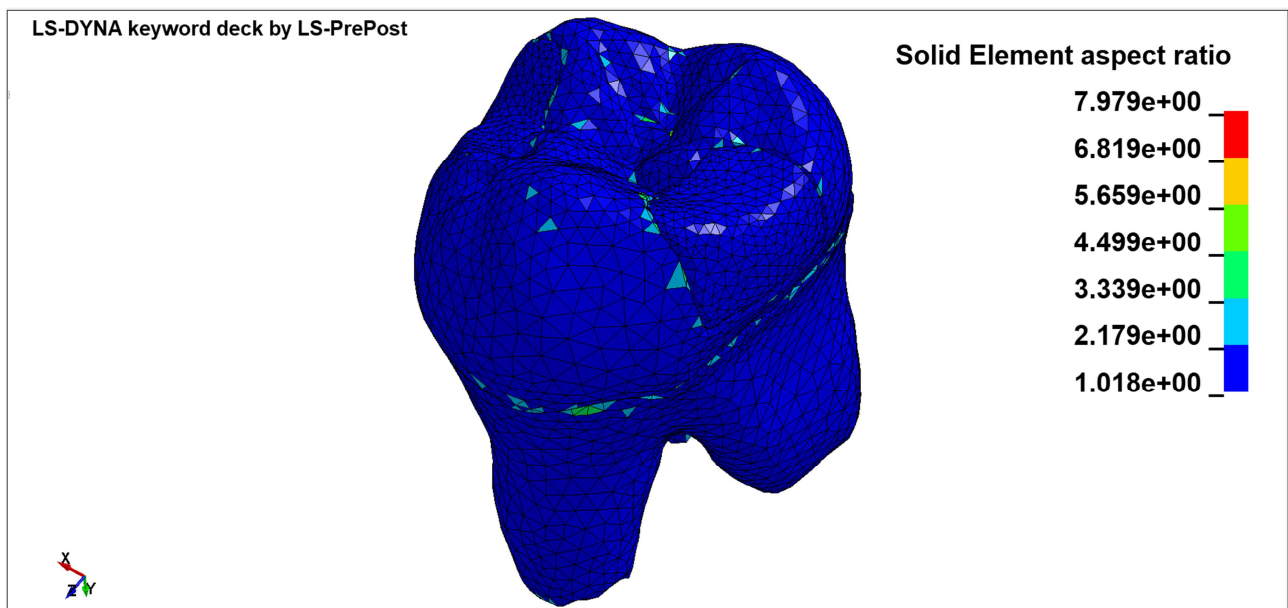


Figure 2.36 (a): Solid element aspect ratio of the final tri-dimensional mesh

The solid element aspect ratio drastically improved by reaching a peak of 8 that was around one quarter of the original maximum showed in Figure 2.33 (a); the solid element characteristic length illustrated in figure 2.36 (b) spanned over one order of magnitudes whereas the refined model characteristic length ranged over two order of magnitudes leading to an enormous difference in matter of volumes.

Finally, the solid element minimum time step illustrates in Figure 2.36 (c) was one order of magnitude bigger than the minimum showed in Figure 2.33 (c).

2. METHOD

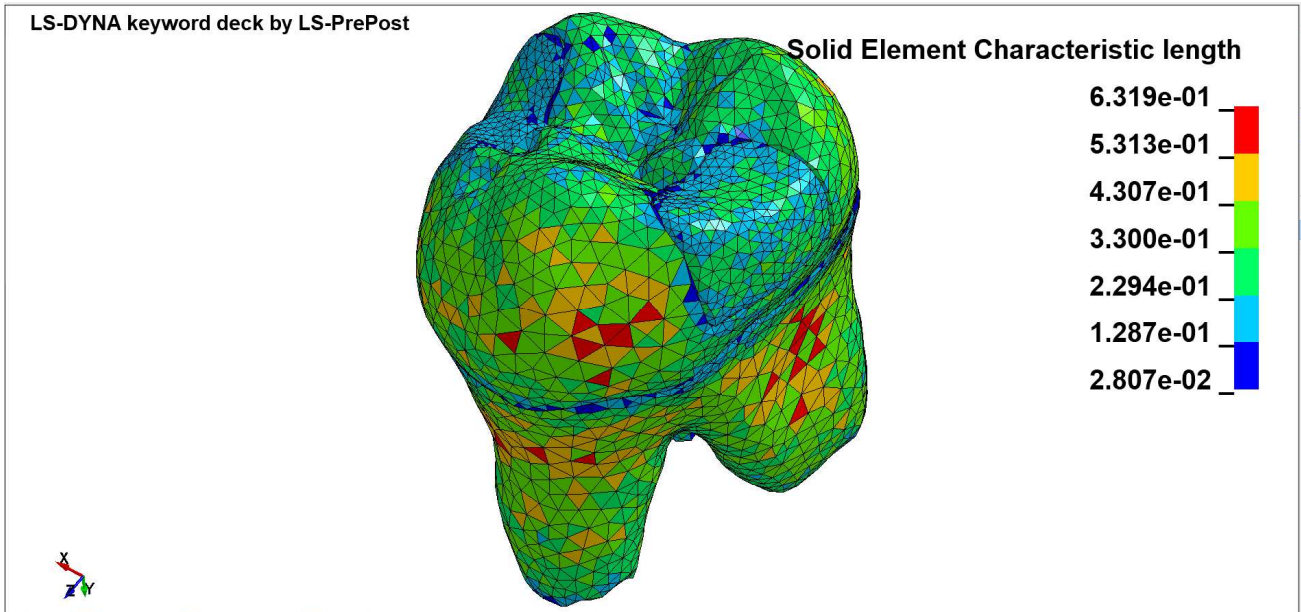


Figure 2.36 (b): Solid element characteristic length of the final tri-dimensional mesh

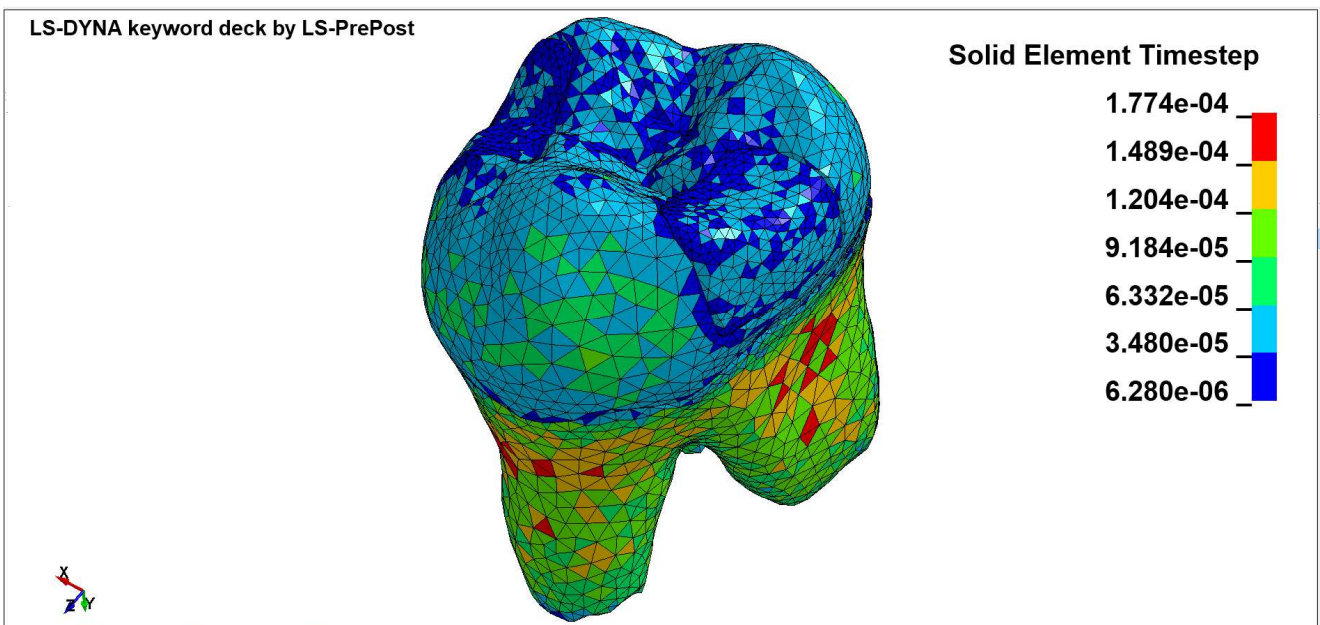


Figure 2.36 (c): Solid element time-step of the final tri-dimensional mesh

Therefore, the described tri-dimensional volumetric mesh outdid the First volumetric model by generating a mesh with elements of similar dimensions and a maximum aspect ratio that was below the Ls-Dyna suggested value of 10.

Furthermore, the simulation running time was drastically shortened by the time-step improvements as well as by the elements number halving with respect to the number of the First volumetric model.

2.2. FEM simulation

This section will deal with FEM method modelling, which was performed in order to assess the debonding stress on the interfaces between tooth and restorative materials. Therefore, the loading and boundaries conditions as well as the contacts applied to create the different 3-D FEM models will be explained in this chapter.

From now on, in order not to make confusions between the restorative materials the restoration on the left side of figure 2.35 (b) will be called small filler whereas the restoration on the right side of the same Figure will be labelled as big filler.

The final aim was to perform a chewing simulation single load cycle in order to evaluate the interface stress distributions.

As mentioned in the introduction, FEM simulation are strongly influenced by loadings and boundaries conditions. Mechanical loads can be applied in three fundamental ways:

1. By applying a force on a selected part of the model;
2. By applying a displacement or velocity law on a selected part of the model;
3. By modelling another object, which will come into contact with the interested part of the model. A smooth velocity law will be applied on this object, this scenario requires more modelling efforts but it could provide more realistic results.

Explicit simulations have more accurate results when a displacement is applied to generate a load whereas implicit simulation are more fit for direct load application ^[39];

Since the tooth simulations were carried out with an explicit method, a displacement load was applied, as matter of fact, explicit method was more suitable for the contact algorithms adopted.

Another fundamental aspect that needed to be addressed in order to obtain a reliable results was the load curve definition whose application could lead to results instability by creating oscillations in the system response. The described load is showed in Figure 2.37. This could happen because the tooth was subjected to a load variations within an infinitesimal time by causing fluctuations on the results ^[40], which could not be considered trustworthy.

A possible solution could be to define load with smooth curves, as shown in Figure 2.38, that avoided rapid variations leading to stable results. The result reliability could be easily evaluated by plotting the forces on a section to verify whether fluctuations were present or not.

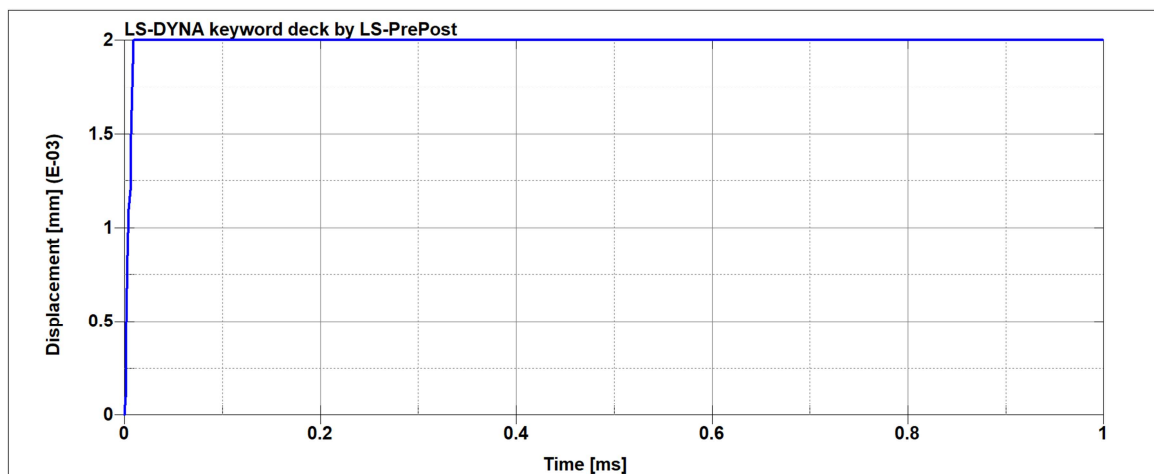


Figure 2.37 : Displacement load applied whose rapidity leads to fluctuations in the system response.

2. METHOD

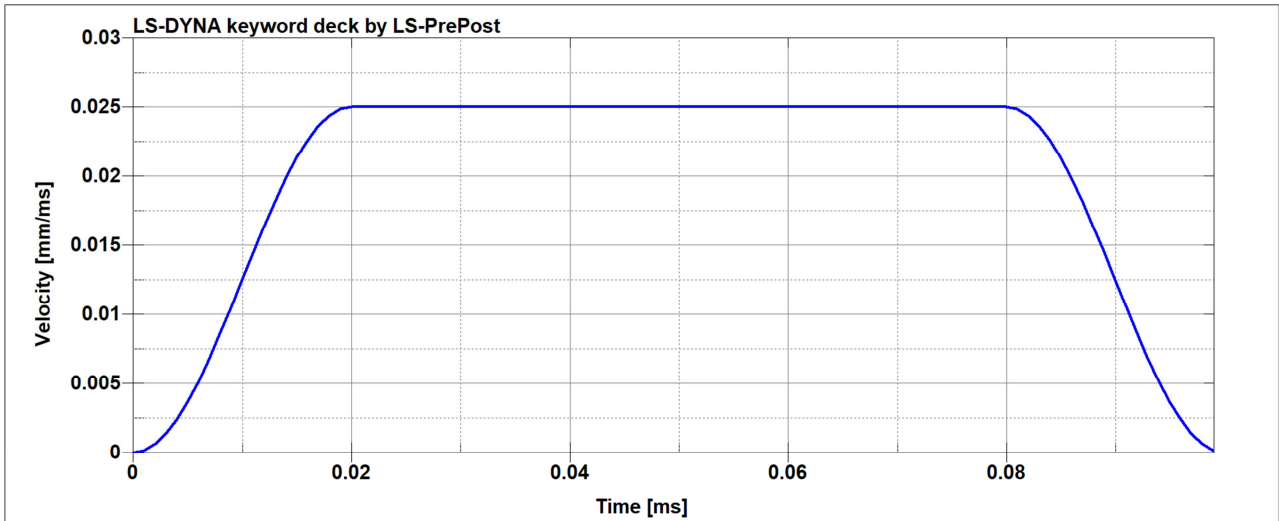


Figure 2.38: Velocity smooth curve applied as nodal set load

Figure 2.37 shows the displacement law initially applied on the node set showed in Figure 2.39. The velocity, showed in Figure 2.38, was the derivation of the displacement in Figure 2.37, the smooth curve drastically decreased the load application rate with respect to the displacement load. Finally, the node set in Figure 2.39 was loaded with the smooth curve, this operation led to automatically determine the overall stress and the strain distributions, the results accuracy will be discussed in the next sections.

Figure 2.40 illustrates the chewing load modelling ,the chewing sphere was made up of steatite with a 3 mm radius whose specific features were provided by Dental School.

The sphere creation allowed to simulate the loading without creating a node set but with a contact algorithm, which was more realistic because not all the nodes previously defined were effectively loaded during the experimental test.

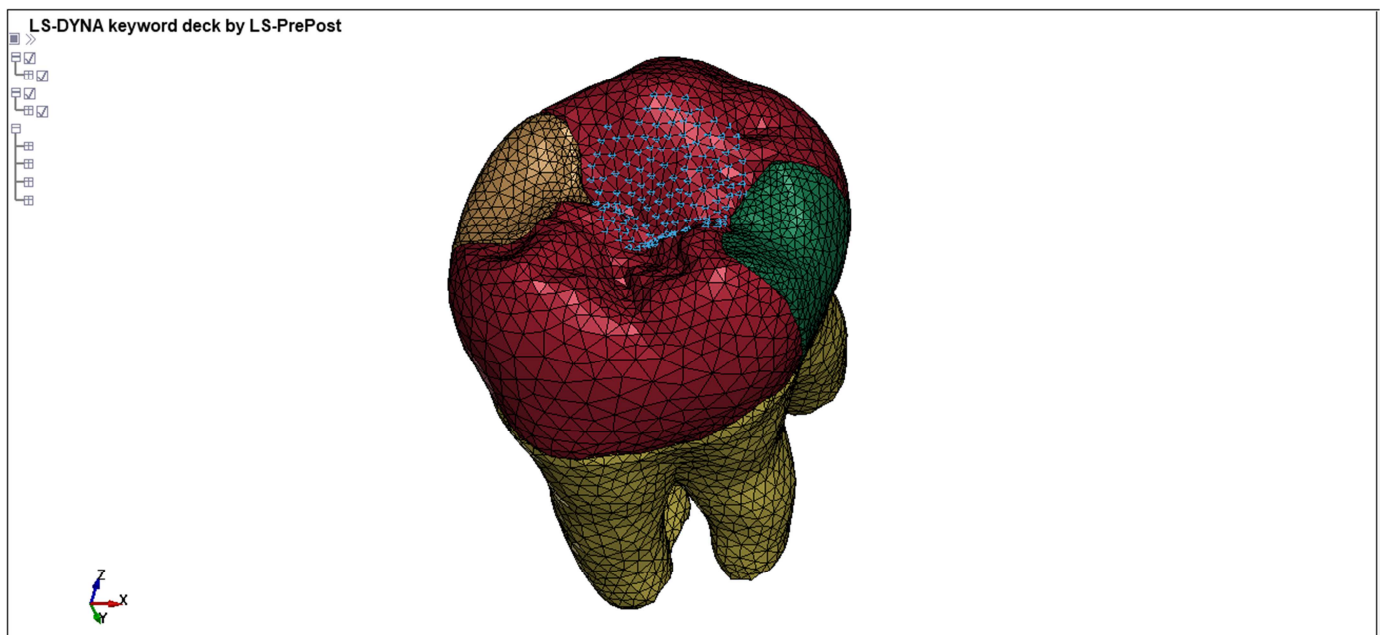


Figure 2.39: Tooth nodal set defined to apply the velocity load, the node set is a circle with 3 mm radius.

2.2. FEM simulation

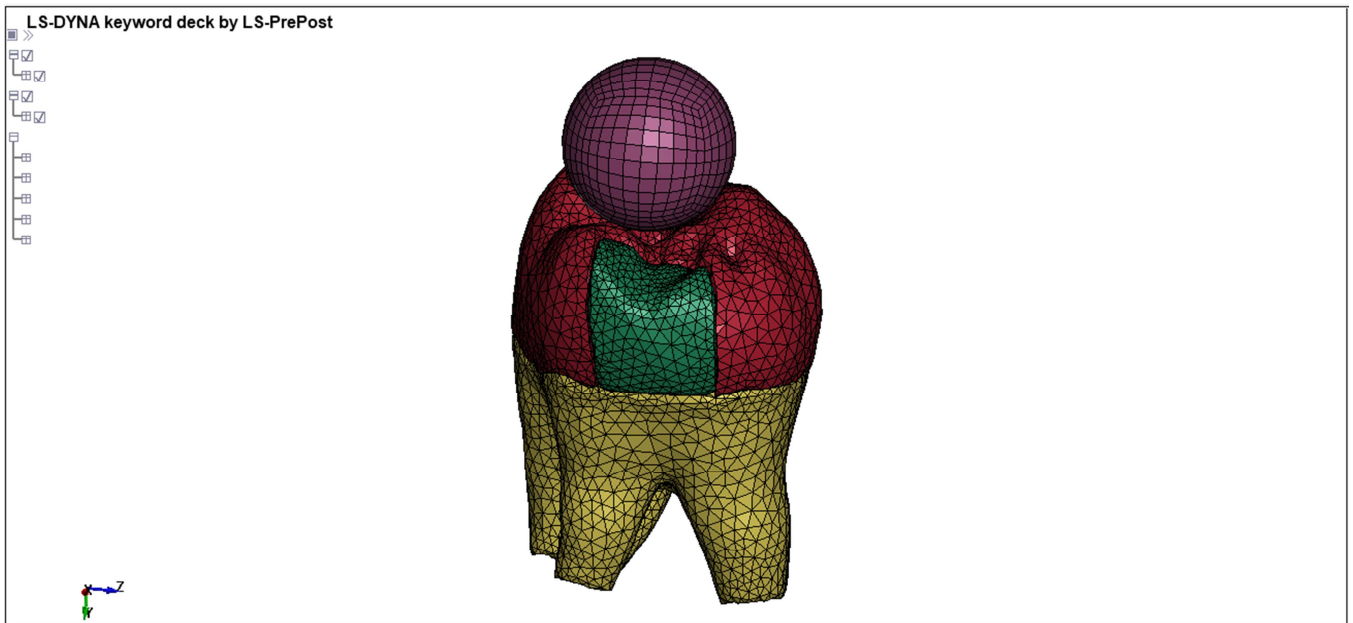


Figure 2.40: Chewing sphere modelled to define more realistic load condition.

The boundary modelling was carried out in two different ways:

1. By locking all the bottom dentine roots degrees of freedom, as shown in Figure 2.41;
2. By modelling the chewing disk support, as illustrated in Figure 2.42;

The latter condition was more realistic, the model was cut one millimetre below the dentine-enamel junction and glued with the disk through a contact algorithm, which is further discussed in this section. However, the results reliability should be confirmed by experimental tests to prove whether the models were realistic or not.

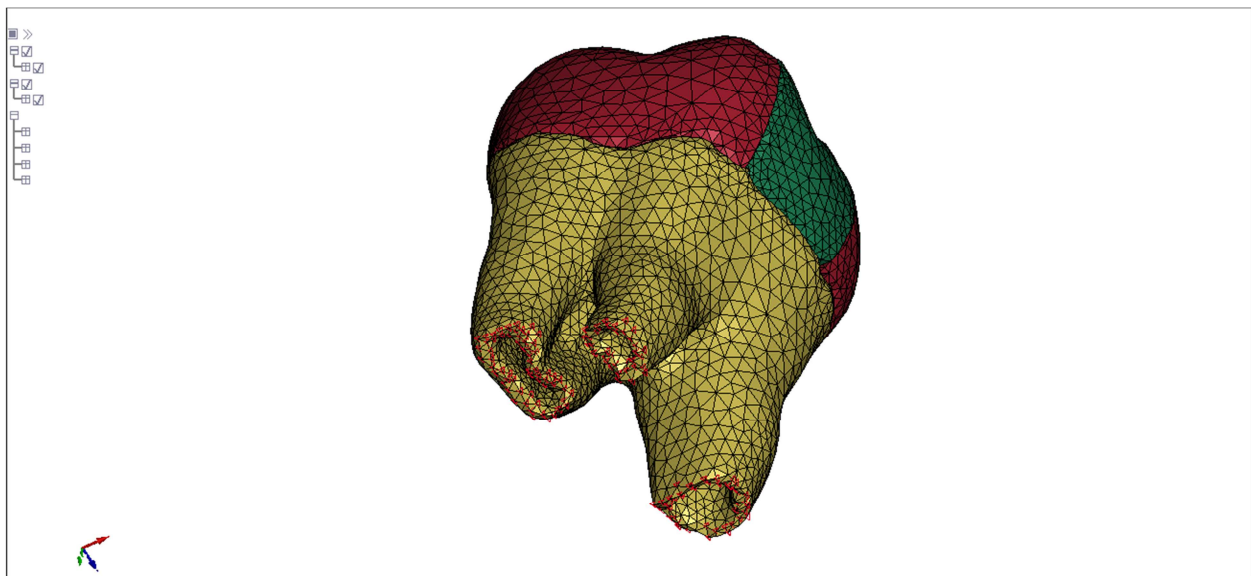


Figure 2.41: First boundary condition, dentine is locked on its lower region with three different node sets.

2. METHOD

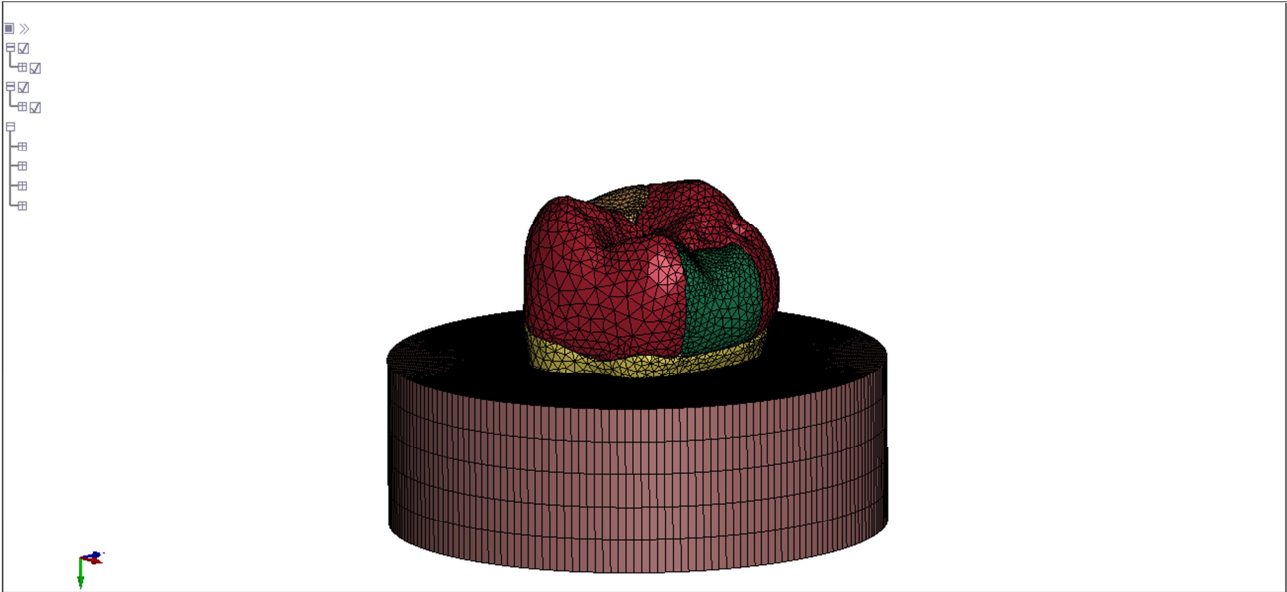


Figure 2.42: Second boundary condition, the clipped tooth is glued with the resin disk.

Boundary and loading conditions influences on final results will be assessed by comparing three different models:

1. Tooth model with load and boundaries conditions applied on different node sets, which is shown in Figure 2.43;
2. Tooth model loaded with the chewing sphere, the model is locked with nodal boundaries conditions, as shown in Figure 2.44;
3. Tooth model loaded with the chewing sphere, the model is locked with the above-described resin disk, as illustrated in Figure 2.45.

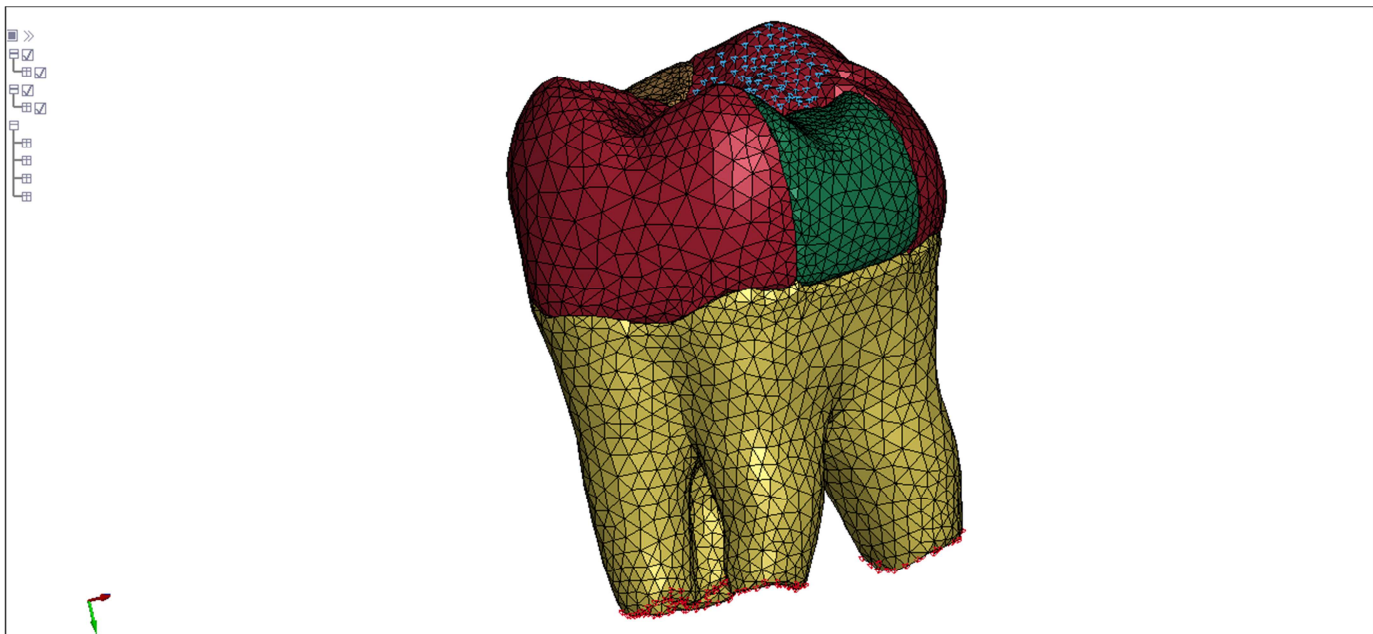


Figure 2.43: First model

2.2. FEM simulation

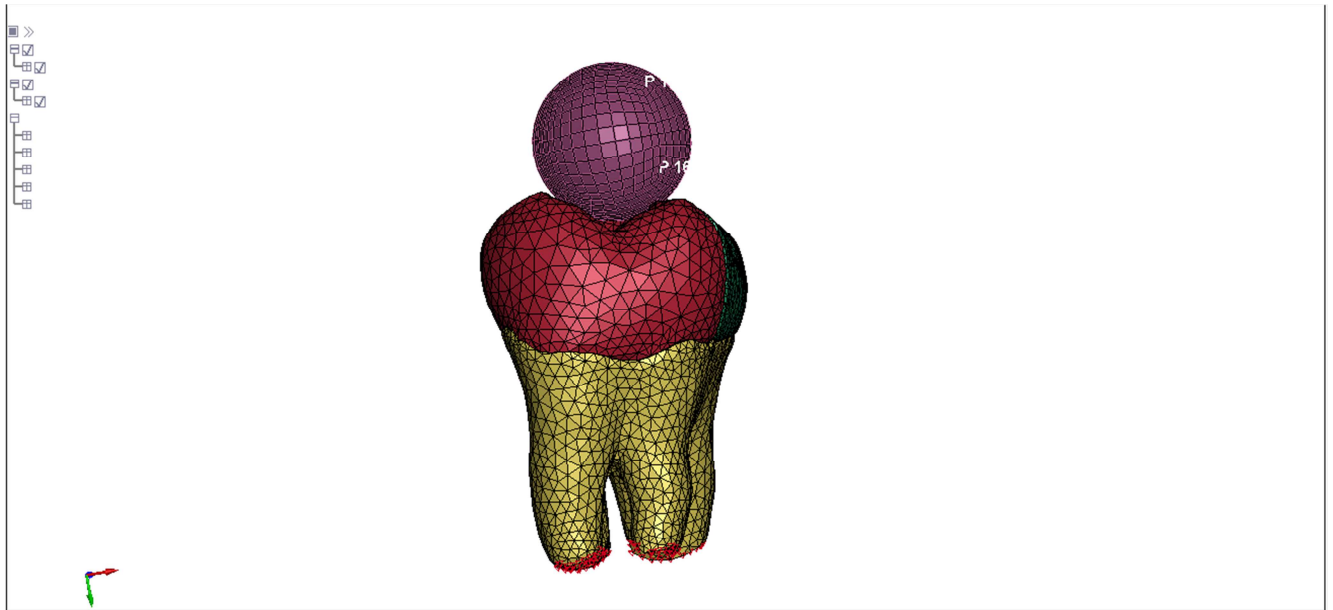


Figure 2.44: Second model

The comparison between model illustrated in Figure 2.44 and model showed in Figure 2.43 allowed assessing the loading influence on the results, since the only difference between those models was the loading condition.

The model in Figure 2.45 was identical to Figure 2.44 model but boundaries conditions was modelled through resin disk. Finally, the third model results could be compared with those of the second model to understand to what extent boundaries conditions influence the overall model.

The third model results represented the final achievements having boundary and loading conditions as close as possible to the physical chewing test.

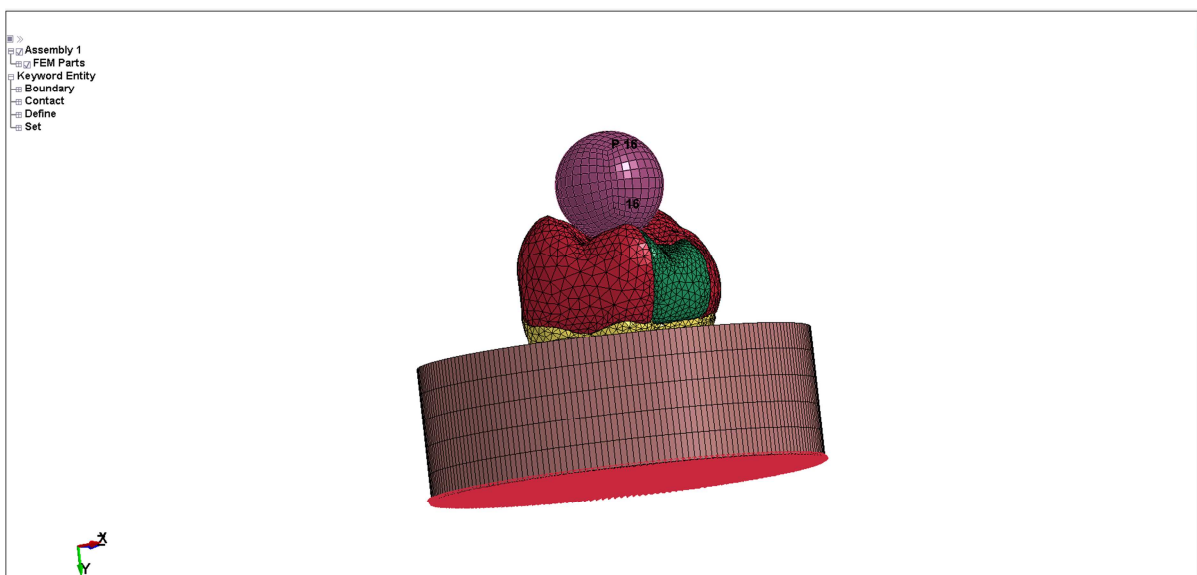


Figure 2.45: Third model

2. METHOD

The resin disk in Figure 2.45 was locked on the bottom with a boundary set, which was represented by the red nodes, whereas the tooth was glued onto the resin disk with a tied contact algorithm.

Contact modelling played an important role in the way the problem was addressed; as matter of fact, when direct restoration was performed on the tooth sample the restorative materials gluing was ensured through an adhesive layer whose thickness was usually around 50 μm .

The layer action was modelled with a contact algorithm, Ls-Dyna provides a wide range of contacts models but a tied contact was applied in order to simulate the adhesive behaviour.

Tied contact was employed to model the tooth-fillers interfaces for three principal reasons:

1. When tied contacts were applied there was no need to define friction coefficient because parts were glued;
2. Tied contact was ideal for the addressed problem allowing to simulate an adhesion between two different parts by replacing the adhesive layer;
3. Tied contacts were available with offset options, which allowed to tie master segment and slave nodes with an offset distance ^[41]. Since the tooth was slightly modified in the mesh refining process, the interface presented gaps and penetrations that needed to be handled with a contact algorithm. The robustness of offset option ensured a good management of these deeply irregular interfaces. This algorithm was also applied to define the resin disk-dentine contact in Figure 2.42.

The contact definition was carried out by creating segment sets, Figure 2.46 and Figure 2.47 show the big filler and small filler defined sets.

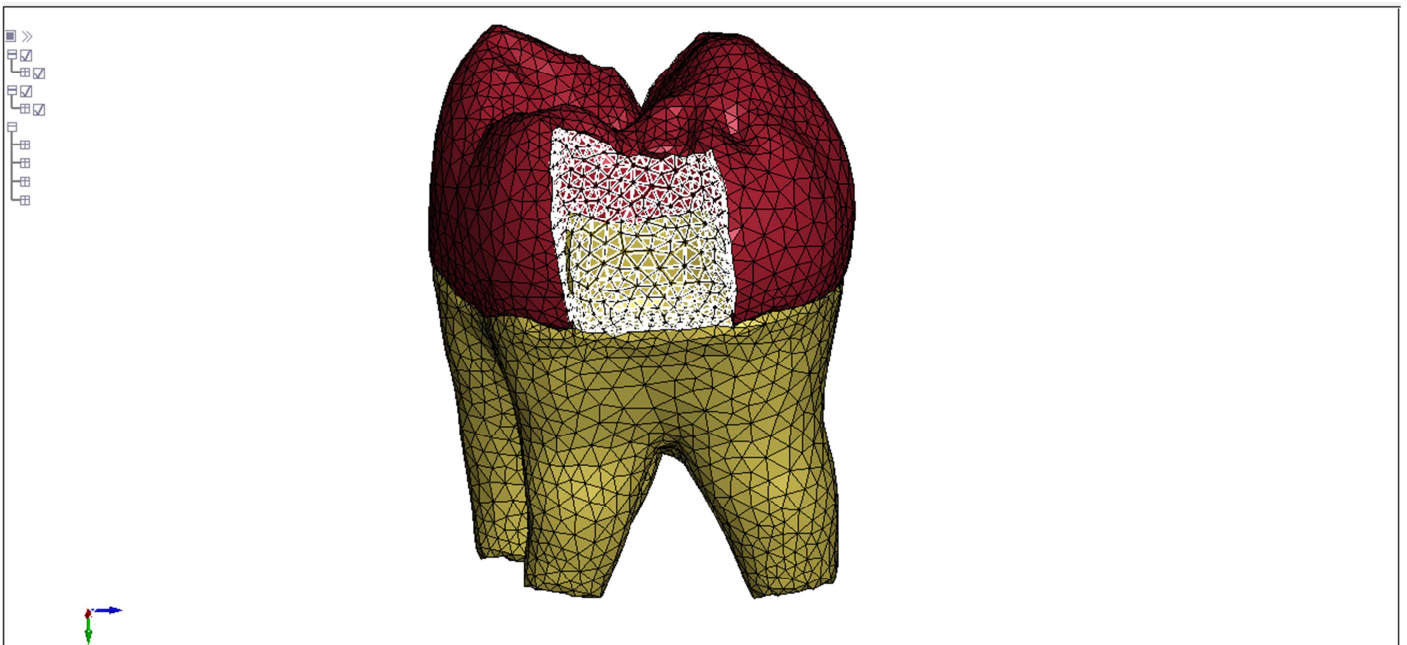


Figure 2.46: Big filler segment set defined in the tied contact

2.2. FEM simulation

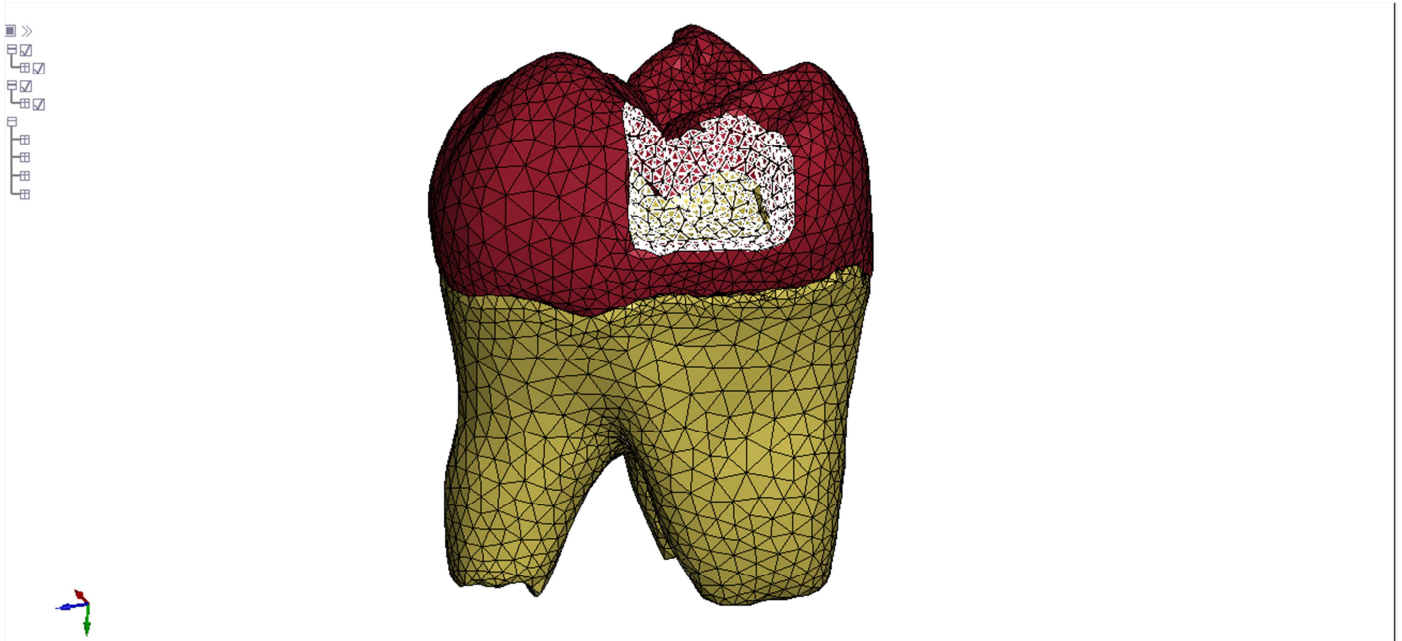


Figure 2.47: Small filler segment set defined in the tied contact

Dentine and enamel contacts were defined by merging the nodes within a tolerance of 0.08 mm, the nodes on the dentine-enamel interface were manually selected and merged, these operations allowed simulating the biological interface behaviour where dentine and enamel are perfectly merged. As matter of fact, the dentine and enamel cells extracellular secretions create a perfect and continuous contact on the interface^[42], which could be accurately simulated by merging nodes. Therefore, the pairs of nodes whose distance was below the tolerance were united to create single nodes, the merge operation is showed in Figure 2.48.

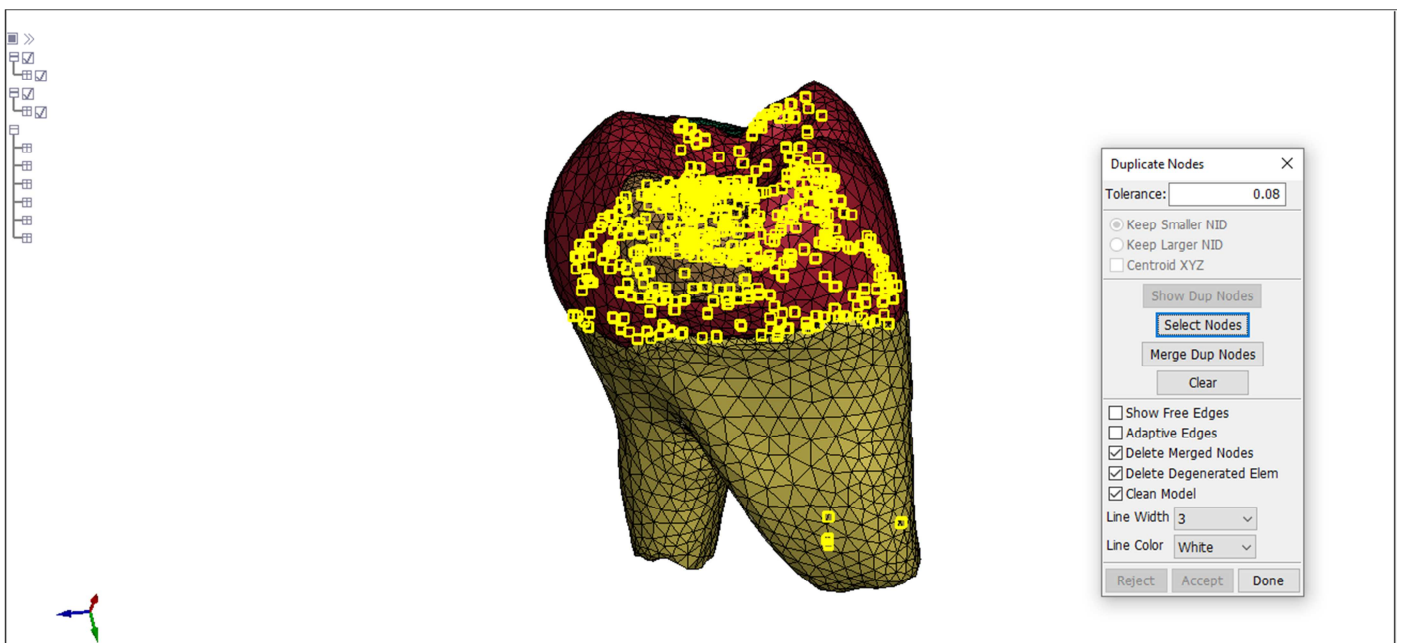


Figure 2.48: Node merging operation performed to create the dentine-enamel interface.

2. METHOD

Finally, the chewing sphere-tooth contact was defined with an automatic surface to surface contact that allowed simulating a contact where the regions that came into contact were unknown^[30], friction coefficient were found in literature.

Dentine, enamel and fillers were modelled with an elastic behaviour, which was realistic only for small load applications. Moreover, more accurate materials models required other parameters that were not present in scientific literature, as matter of fact, parameters values accurate knowledge were fundamental in order to obtain a reliable result and more complicated models needed parameters that were totally unknown for those materials.

Resin disk and chewing sphere were modelled as rigid materials, meaning that they did not undergo a deformation process, therefore, their stress were neglected, in fact, the function of these tools was only to test the tooth behaviour and no interest lied with them.

Table 2.5: Parameter settings for the materials involved in the chewing simulation

	Young Modulus [GPa]	Density [$\frac{Kg}{mm^3}$]	Poisson Ratio
Dentine	18	$2.2 * 10^{-6}$	0.23
Enamel	80	$2.9 * 10^{-6}$	0.3
Fillers	10.3	$1.9 * 10^{-6}$	0.3
Resin Disk	3.5	$1.54 * 10^{-6}$	0.33
Chewing sphere	80	$2.7 * 10^{-6}$	0.23

Chewing sphere were present only in the second and third model whereas resin disk was modelled only in the latter model.

Ls-Dyna provides the possibility to extract different data, therefore, there is no a default output option and different outputs should be chosen for different needs.

The most important and diffused outputs are d3plot files, these files contain information about the stress and the displacements of the structure. All the results are visualized by default in a global system, consequently, the stress information on the interface are difficult to be interpreted.

A possible solution could be the analysis of the principal tensions with a vector plot, in principal tension analysis all the elements had their own local systems and the results interpretation could became difficult, for this reason the principal tensions were not considered at all.

Interface stress could be extracted through the intfor database allowing to display the segment set contact output, this database provides information about the contact pressure and shear stress obtained on the interfaces local systems^[43].

Therefore, shear stress peaks could be analysed after one loading cycle, major interests lied with shear stress assessment because they accounted for debonding phenomena. Figure 2.49 shows the interface of the intfor database.

2.2. FEM simulation

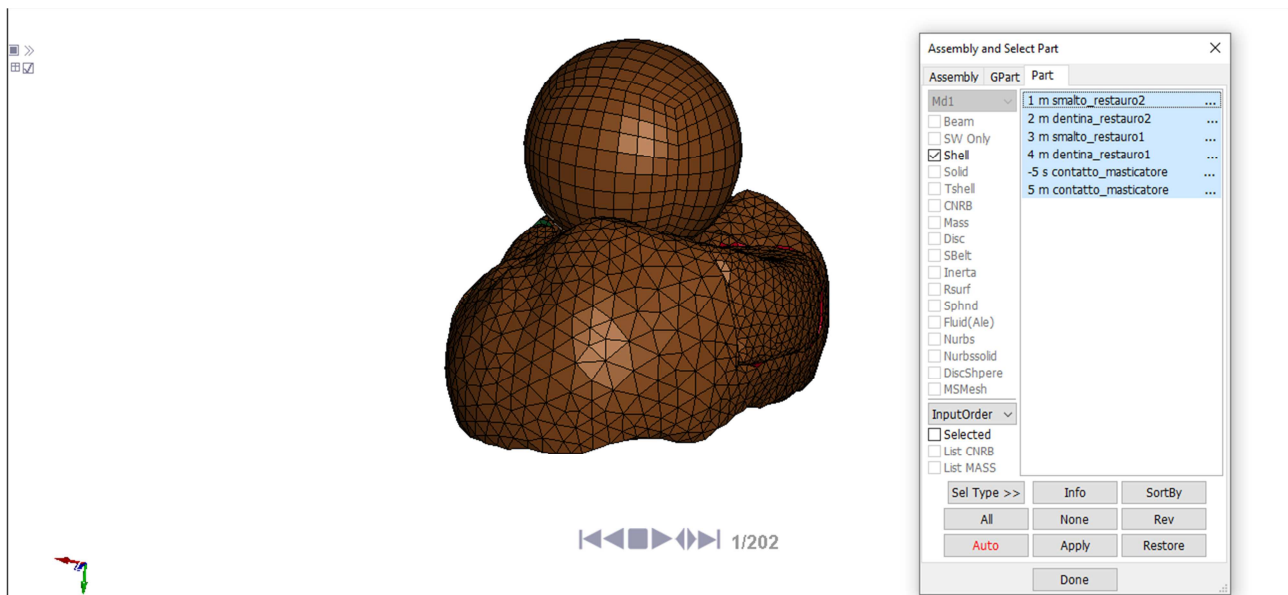


Figure 2.49: Interface force database

3. MODELS VALIDATIONS

In this chapter interface force database validation was performed on a simple model, the purpose was to establish whether the interface results were reliable or not to assess the debonding phenomena. Interface shear stress and pressure validations were carried out by comparing the database results with the analytical equations of fundamental strength of materials.

The simple model was designed to verify the database results, therefore, analytical solutions should be calculated in order to confirm the obtained results. The model was made of two cubes with the same dimensions, connected on a common surface with a tied contact algorithm. This type of contact was the same applied on the fillers-tooth interfaces. The simple model is showed in Figure 3.1.

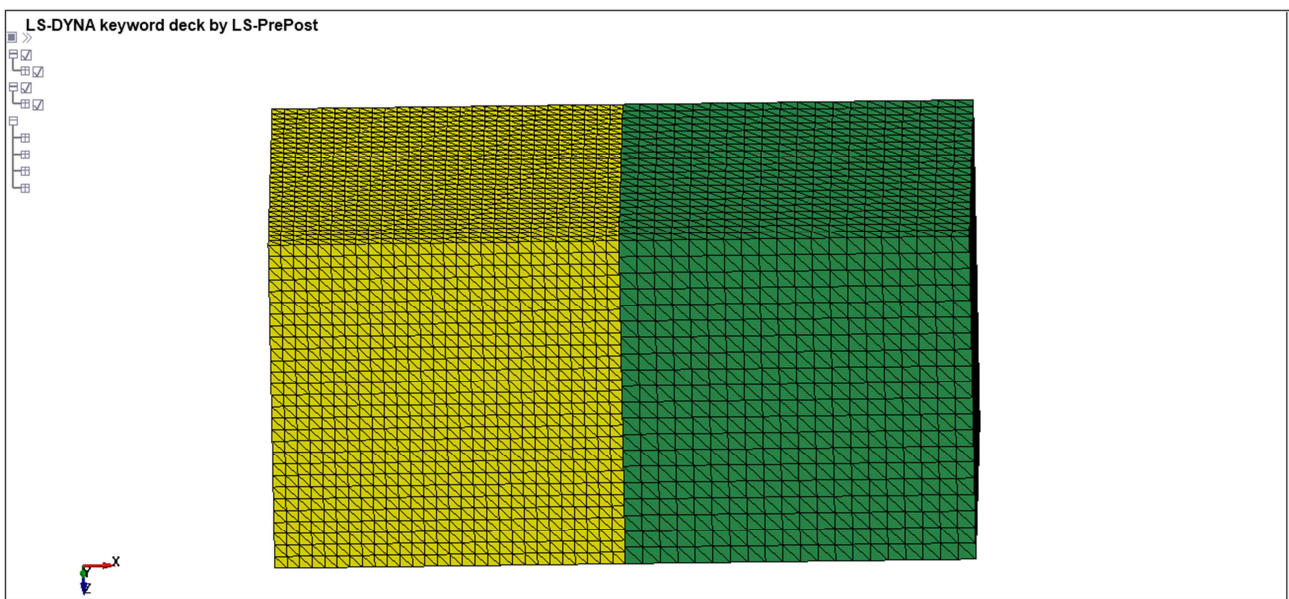


Figure 3.1: Simple model

The green cube was made of dentine whereas the yellow cube was composed by the tooth restorative material, the filler elements size was designed smaller than those of the dentine cube in order to assess the contact algorithm reliability when it was applied to parts with different element sizes.

One dimension of the cube was made parallel to the x-axes in order to make easier the results analysis. Different load and boundaries conditions were tested to perform the validation.

The load cases examined were:

- Model loaded with a tensile stress along x-axes applied on a filler surface. The dentine cube was locked on the outer surface perpendicular to the x-axes;
- Model loaded with a compression stress along x-axes applied on a filler surface. The dentine cube was locked on the outer surface perpendicular to the x-axes;
- Model loaded with a bending force along z-axes on the filler surface. The dentine cube was interlocked on the outer face perpendicular to the x axes while the filler was locked in all the degrees of freedom but the z axes;
- Model loaded with a torque along x-axes created by applying a couple with two forces directed along the z-axes on the filler cube. The dentine cube was locked on the outer surface perpendicular to the x-axes.

3. MODELS VALIDATIONS

The traction, compression and torque load were applied on a model with cube side of 5 mm whereas the bending was performed on a model with cube side of 0.5 mm. This chapter will provide also a short introduction on the theory that was required in order to confirm the simulations results.

The loading and boundaries conditions of a simple model under traction are showed in Figure 3.2.

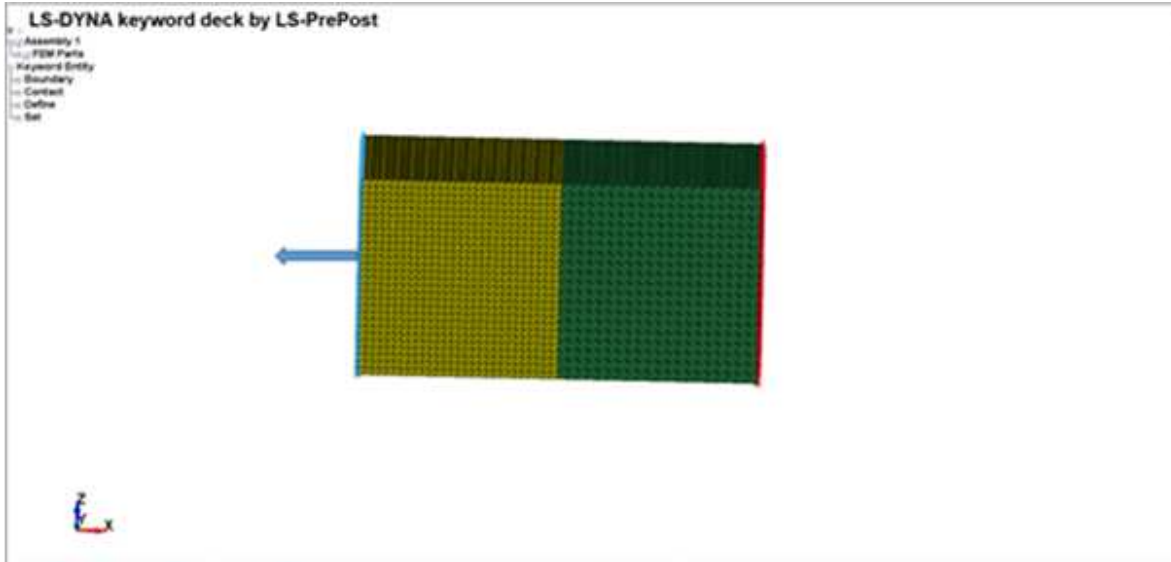


Figure 3.2: Model traction loading and boundaries conditions

The red node set is the model interlocking joint whereas the blue node set shows the loaded surface, as illustrated in Figure 3.2.

The applied tensile load is shown in Figure 2.38; according to the theory when a specimen is under traction, the axial stress distribution should be uniform and its value can be worked out dividing the exerted force by the area of the load section^[44].

The applied force can be calculated by defining a cross-section on the outer filler surface where the velocity shown in Figure 2.38 is applied as load, the defined cross-section is showed in Figure 3.3 while the above-mentioned force is illustrated in Figure 3.4.

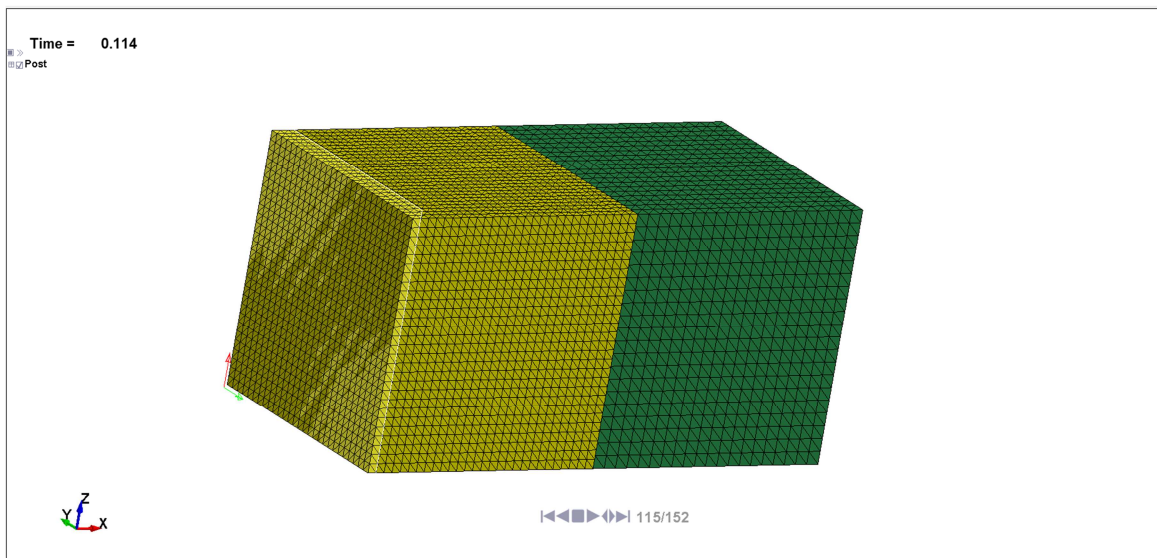


Figure 3.3: Filler cross-section

3. MODELS VALIDATIONS

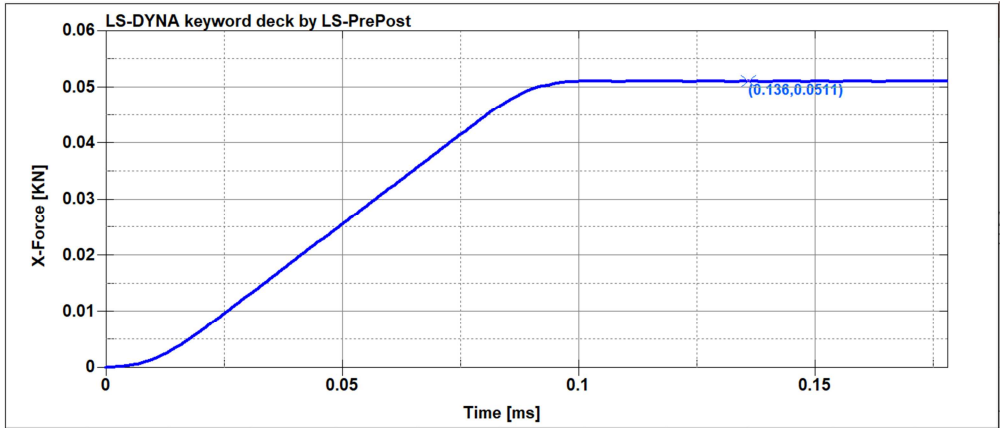


Figure 3.4: X-Force applied on the outer surface of a model under traction

The load was applied as a smooth curve with a transient of 0.1 ms, the solution levelled off after this transient by reaching a value of 0.0510 kN.

As before mentioned, the cube was created with 5 mm side, therefore, according to the above-explained theory the x-stress value was $2.04 \times 10^{-3} \text{ GPa}$.

The analytic value could be compared with dentine and filler cross-sections and with the interface distributions. Figure 3.5 and Figure 3.6 show the dentine and filler cross-sections.

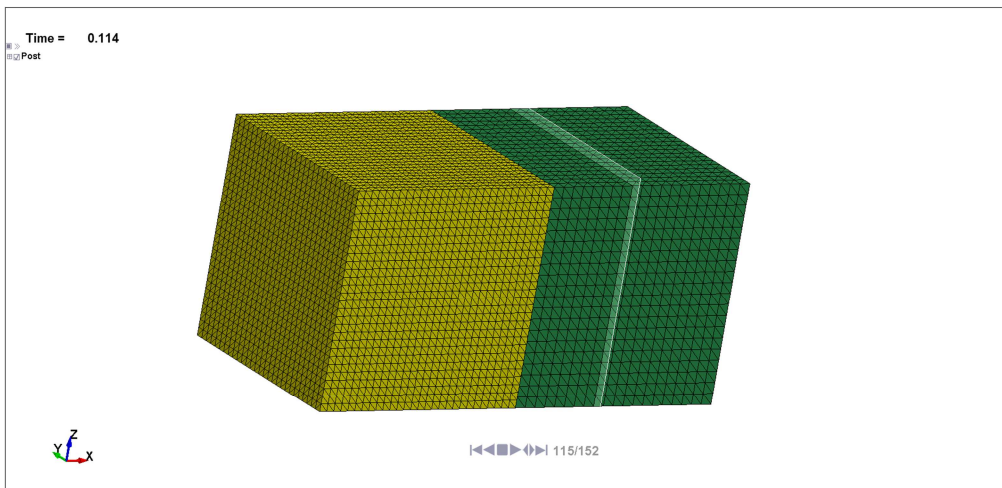


Figure 3.5: Dentine cross-section

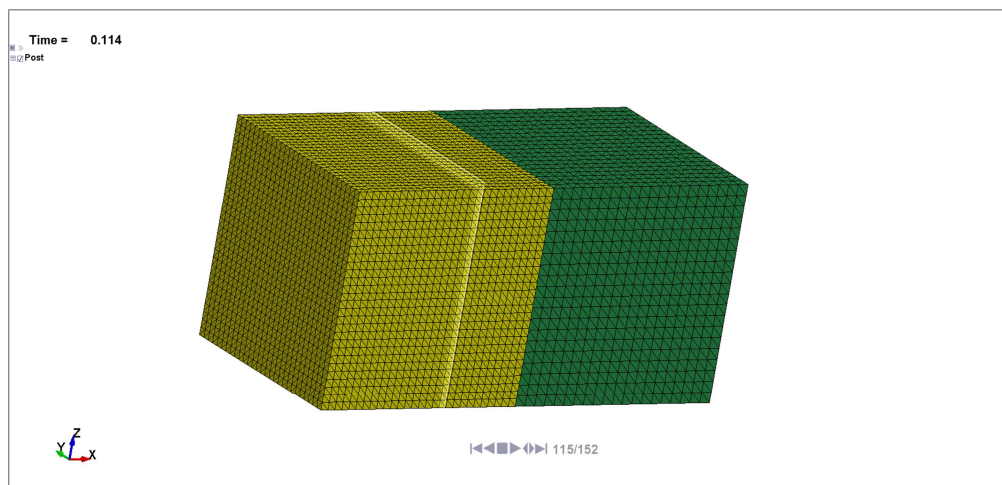


Figure 3.6: Filler cross-section

3. MODELS VALIDATIONS

As matter of fact, the cross-sections were worked out from the d3plot, which was the classical output extracted from Ls-Dyna. The interface results were compared with the cross-sections outputs, its reliability were widely proven by its large utilization in literature.

The results consistency will be discussed for all the analysed models. The final purpose of this chapter was to prove the theoretical distribution coherency both with the cross-sections results and with the interface outputs. Figure 3.7 and Figure 3.8 show the interface pressure distribution and the average x-axes force on the interface, respectively.

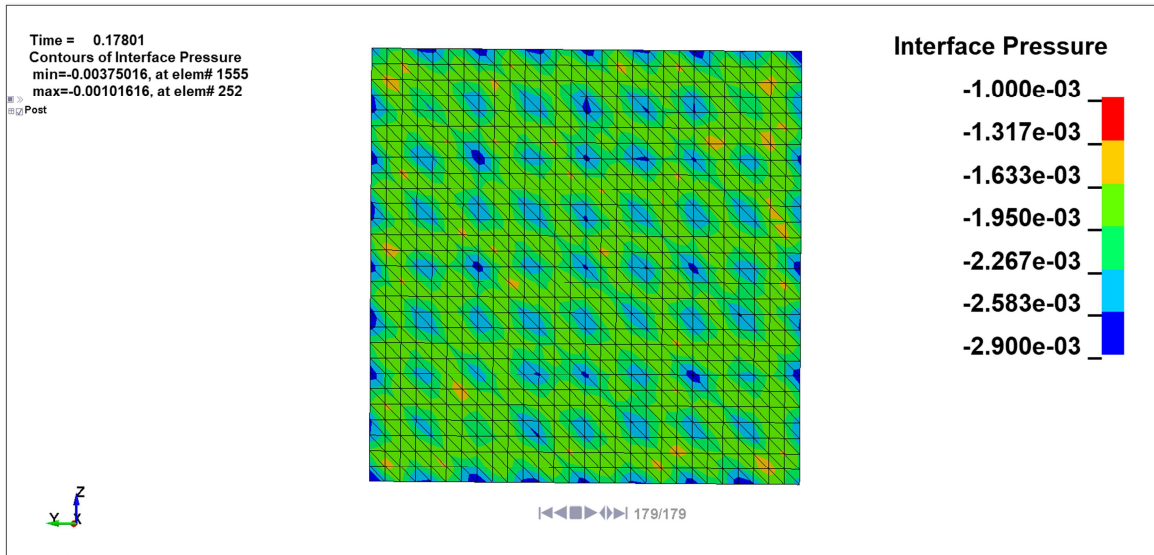


Figure 3.7: Interface pressure distribution of the model under traction

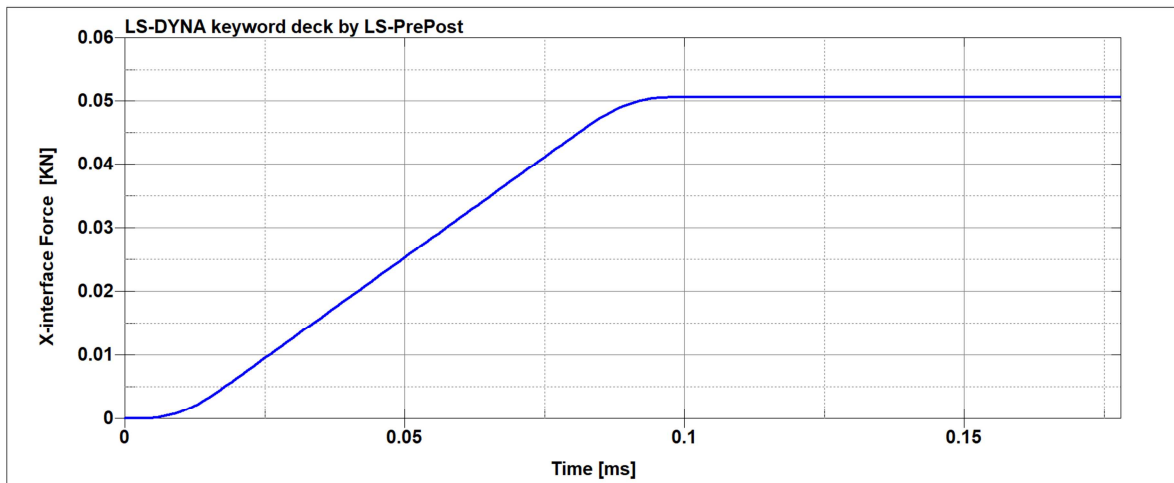


Figure 3.8: Average x-force on the interface section of the model under traction

Figure 3.8 shows an interface resultant force that is almost identical to the force applied on the filler outer surface. Moreover, Figure 3.7 prevalent colour was green whose interval stood at around $2.0 \times 10^{-3} GPa$, which was coherent with the analytical value previously calculated.

Finally, the dentine and filler cross-sections were compared with the theoretical value as well as with the interface distributions. Figure 3.9 and Figure 3.10 illustrate x-stress results for the dentine and filler cross-sections, respectively.

3. MODELS VALIDATIONS

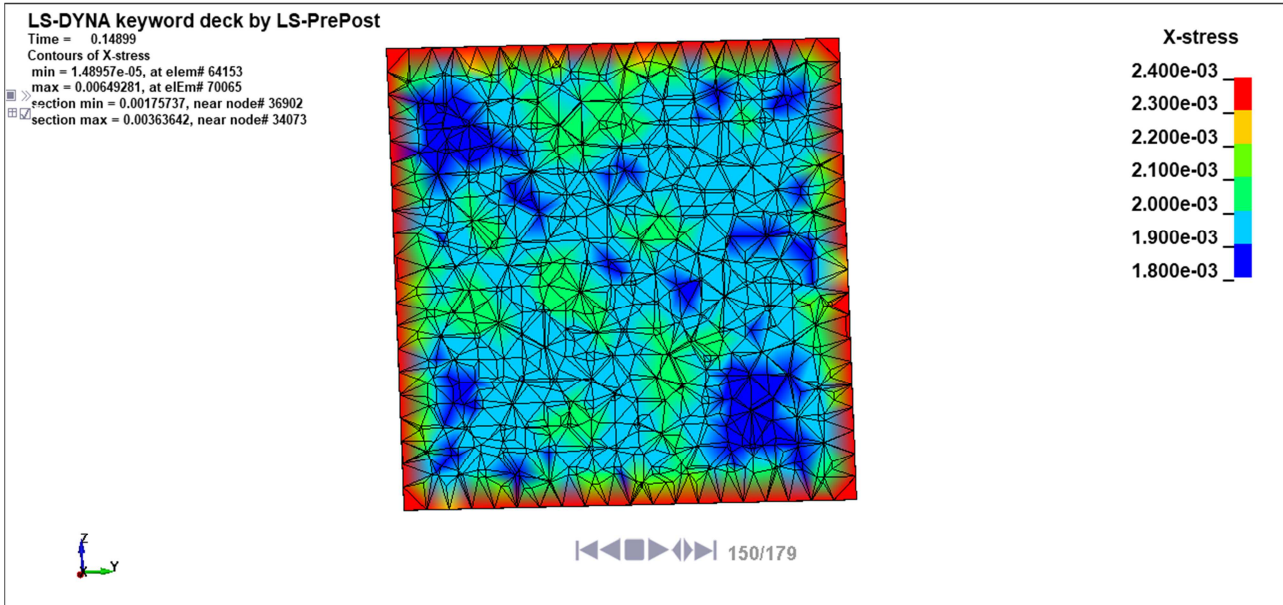


Figure 3.9: X-stress distribution on the dentine cross-section

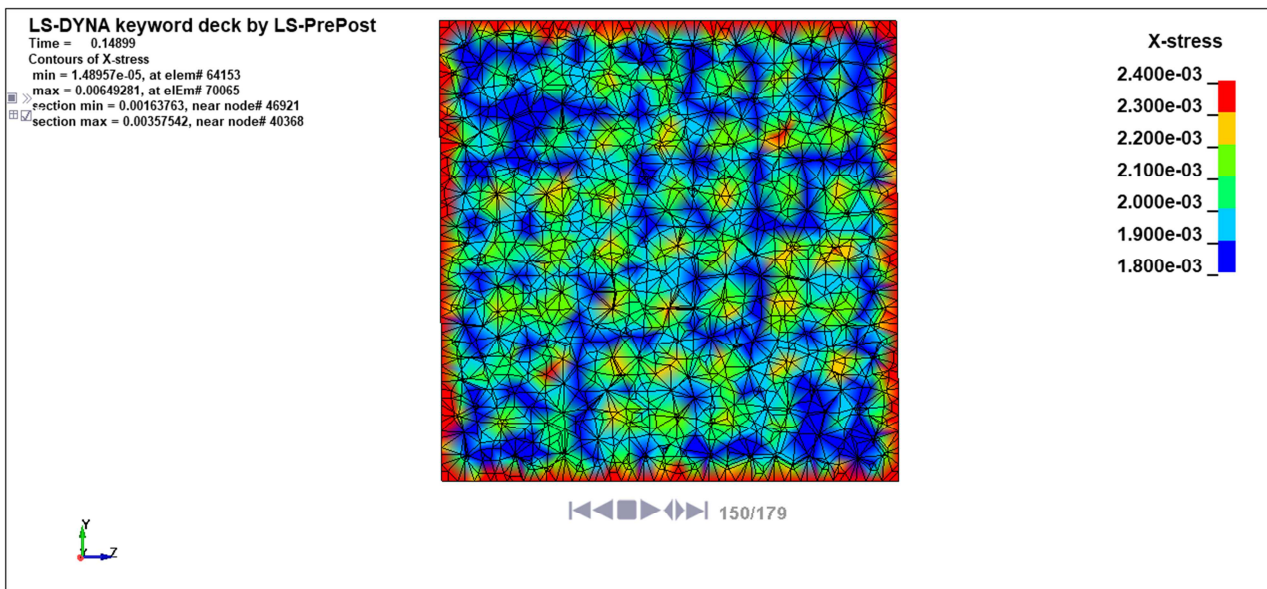


Figure 3.10: X-stress distribution on the filler cross-section

Figure 3.9 and Figure 3.10 show x-stress distributions whose average value stood at around $2.0 \times 10^{-3} GPa$, therefore, the cross-sections stress results were coherent with the theoretical value and with interface pressure output.

All the results presented edge effects on their borders that led to an approximation, the values on the external regions of both the interface and the cross-sections should not be considered reliable because of their presence.

The average x-force values were analysed in both the cross-sections to confirm the above-described results. The x-force cross-sections average values were around 0.0504 kN and 0.05 kN for the dentine and filler, respectively.

Finally, the model clearly showed a consistency between theoretical value and the results previously described, therefore, the pressure interface output reliability was confirmed.

3. MODELS VALIDATIONS

The second model was substantially identical to the first one as loading and boundaries conditions, the only difference lied with the different load sign. Therefore, all the results were equal to those of the traction but the signs were inverted and all the conclusions draw for the traction were also perfectly valid for the compression.

The third model consisted of applying the bending load on the outer filler surface, the boundaries and loading conditions are showed in Figure 3.11.

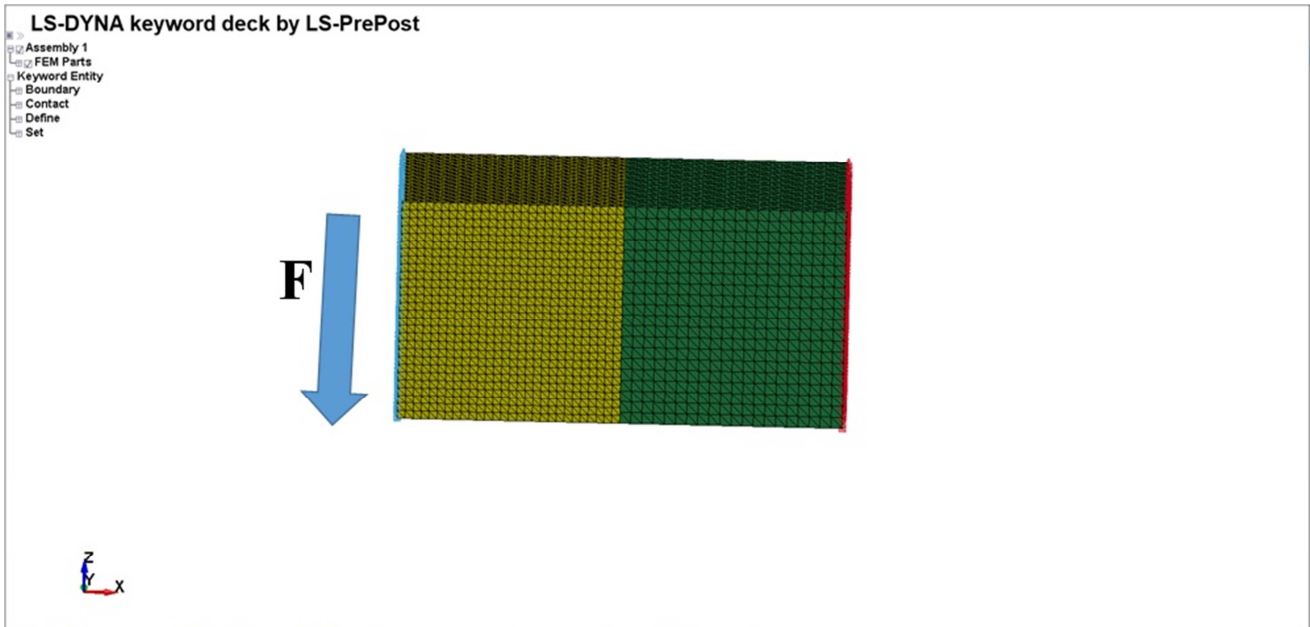


Figure 3.11: Loading and boundaries conditions on the model with a bending load applied.

When a bending load is applied on a beam Jourawsky theory states that the shear stress on the section parallel to the load application has a parabolic shape with a peak located on the central chord. Furthermore, the shear stress is constant in all the chords perpendicular to the load application^[45]. Equation 3.1 describes a formula provided by Jourawsky to work out the maximum shear stress value on the central chord in case of rectangular section^[46].

$$\tau_{max} = \frac{3 * F}{2 * A} \tag{3.1}$$

Where F is the bending force and A is the area of the section where the force is applied. The exerted force could be measured on the same way as the first method by defining a cross-section on the section where the load was defined, as shown in Figure 3.3.

Therefore, an analytical maximum can be worked out, this value can be compared with the interface and cross-sections distributions peaks.

Furthermore, their behaviours should follow the Jourawsky theory; this formula will be applied to validate the shear stress interface distribution.

As matter of fact, the traction and compression load allowed confirming the reliability of the pressure interface output whereas torsion and bending load were applied to validate the shear stress reliability. The exerted bending force is showed in Figure 3.12

3. MODELS VALIDATIONS

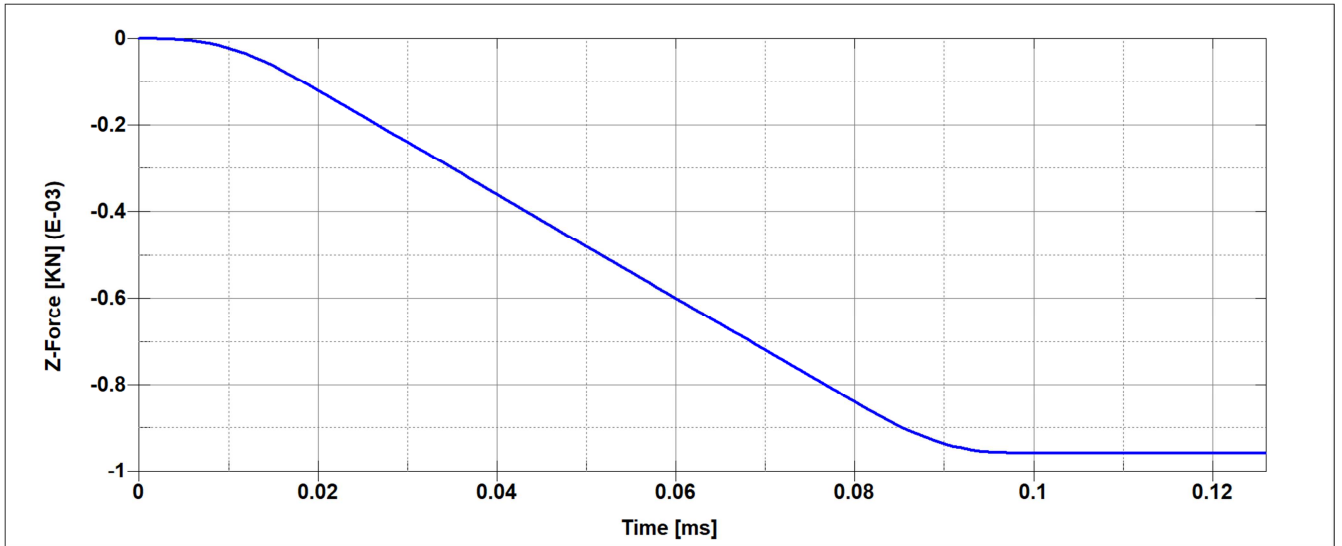


Figure 3.12: Force applied on the outer filler surface

The force levelled off after 0.1 ms by reaching a value around $1 * 10^{-3} kN$, the Area A was $0.25 mm^2$. Therefore, according to equation 3.1 the shear stress peak value stood at around $6 * 10^{-3} kN$.

The theoretical distribution was compared with the interface shear stress results, the interface output is showed in Figure 3.13.

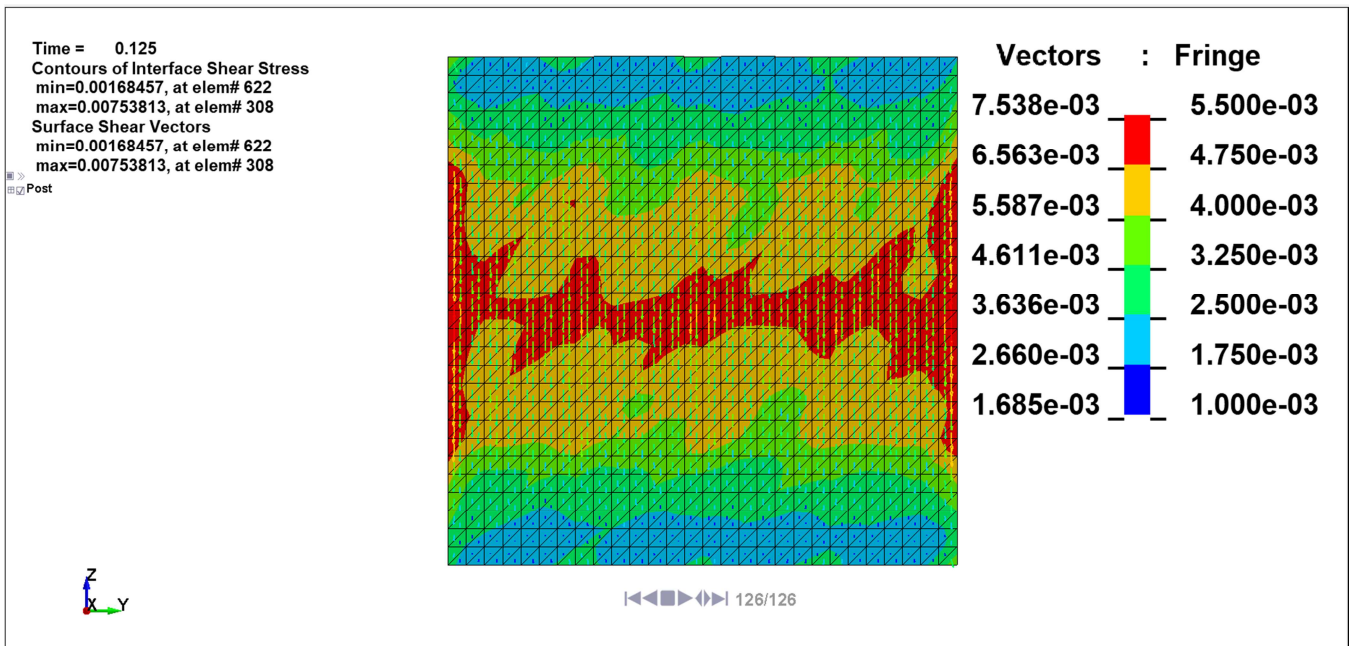


Figure 3.13: Interface shear stress distribution

The interface shear stress distribution approximately followed the Jourawsky theory. Shear stress distribution showed a parabolic behaviour. Furthermore, the maximum was reached on the central cord with a peak stood at around $5.5 * 10^{-3} kN$, which was similar to the analytic maximum value. The interface output vectors were uniquely directed towards the z-axis showing an uniform shear stress direction. The interface output was extracted by the tied contact algorithm and the noise presence was quite evident in the distribution.

3. MODELS VALIDATIONS

The shear stress was also analysed in the dentine and filler cross-sections, which are showed in Figure 3.5 and Figure 3.6, respectively .The results are showed in Figure 3.14 and Figure 3.15.

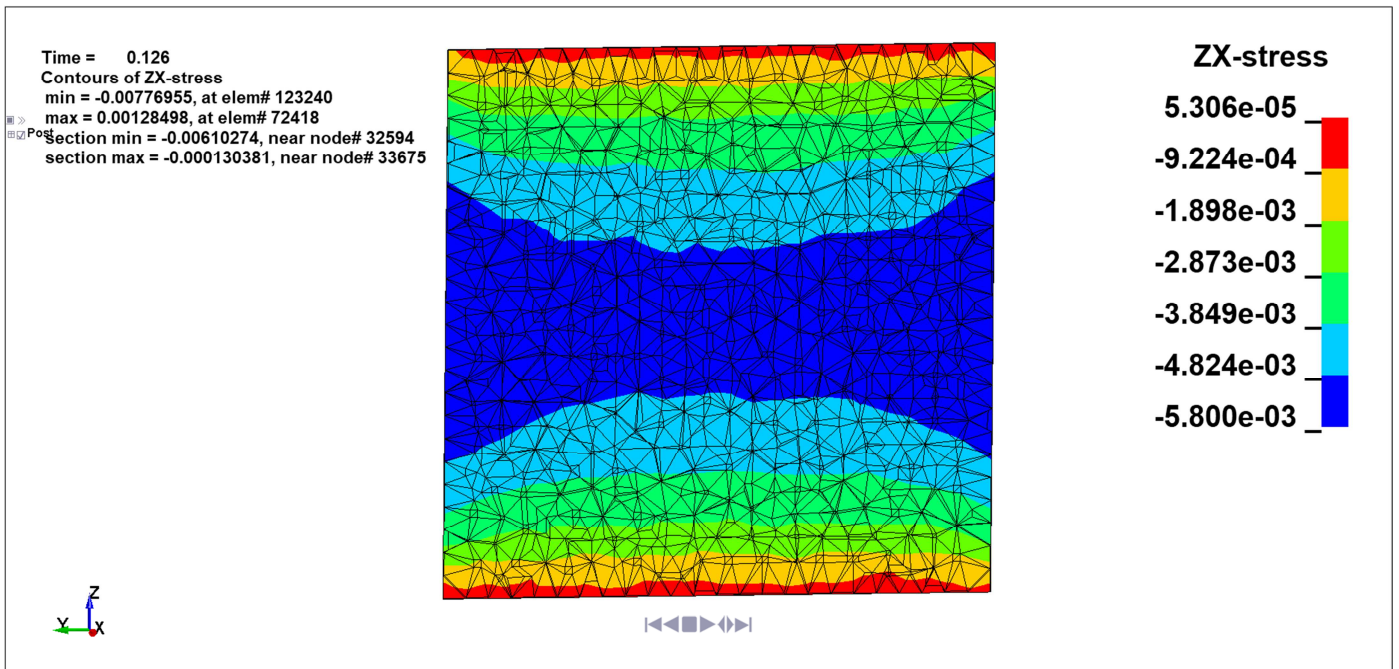


Figure 3.14: Dentine shear stress zx component on the model with a bending force applied

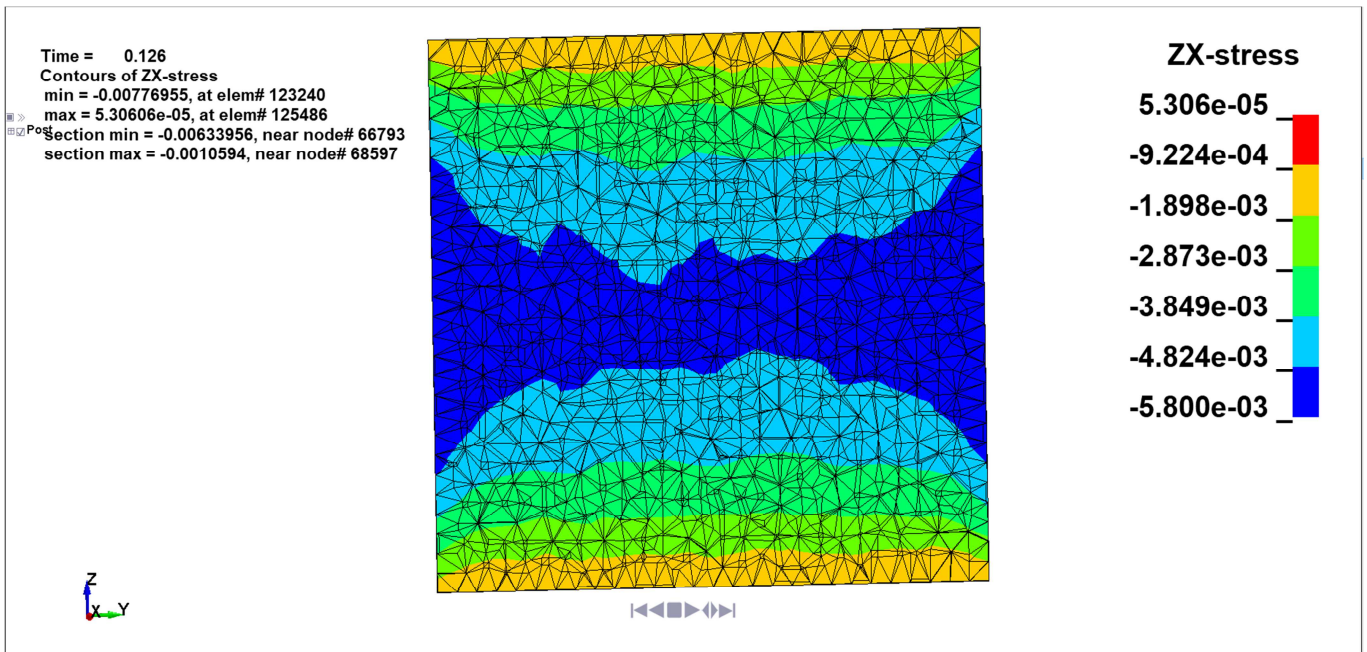


Figure 3.15: Filler shear stress zx component on the model with a bending force applied

Figure 3.14 and Figure 3.15 show the cross-sections shear stress distributions, the results clearly followed the Jourawsky theory. The stress was constant in the chords perpendicular to the load following a parabolic shape. The peaks values were located on the central chord and they were really close to the analytic value provided by the Jourawsky theory.

Therefore, these outputs were totally coherent with the interface shear stress, the main difference was the higher amount of noise that was present in the interface database.

3. MODELS VALIDATIONS

Finally, it was possible to state that the interface shear stress results validation was successfully carried out.

In order to confirm these important results also a torque loading was evaluated and compared with the analytical solution. Figure 3.16 illustrates the loading and boundaries conditions of the model with a torque applied.

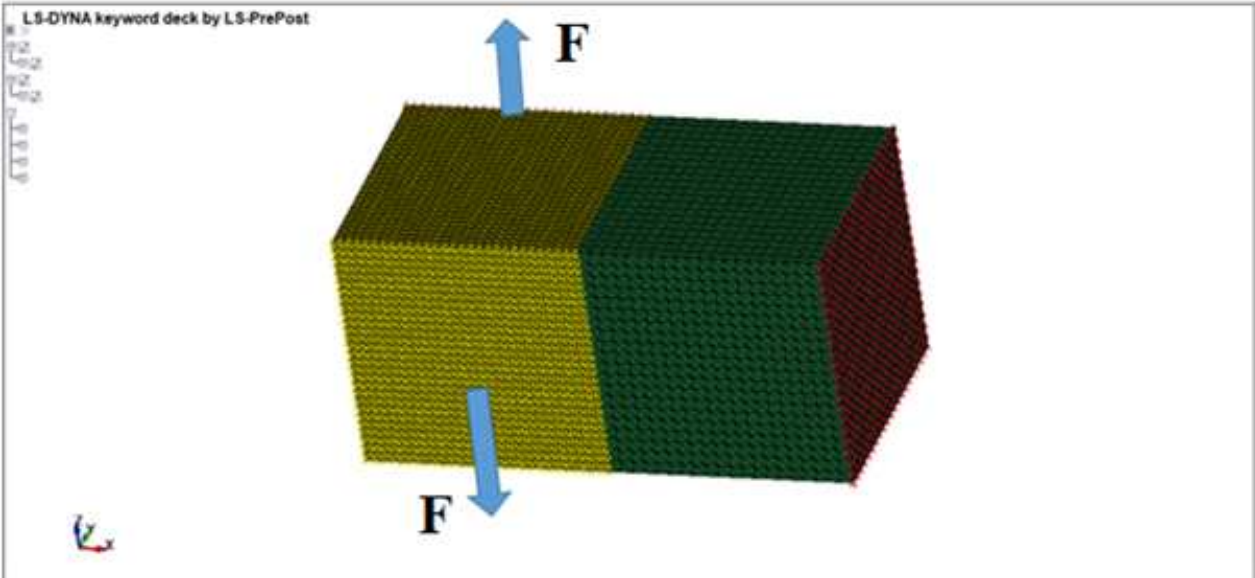


Figure 3.16: Loading and Boundaries conditions on the model with a torque load applied

When a torque load is applied on a beam with a rectangular section it is possible to exactly calculate the section shear stress. The analytic shear stress distribution is illustrated in Figure 3.17.

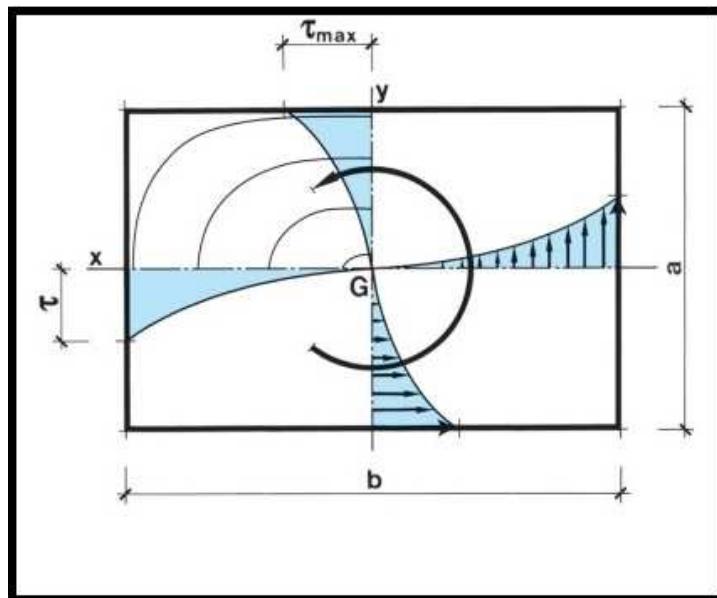


Figure 3.17: Shear stress analytic distribution for a model under torsion ^[47].

As showed in Figure 3.17 the distribution followed a parabolic shapes on the external sides with null values on the four edges. Maximum values were located on the middle of all the sides.

3. MODELS VALIDATIONS

The theoretical distribution presents also null values on the section central region, those values raise by moving towards the border directions^[48]. Equation 3.2 allowed calculating the maximum shear stress value for a rectangular specimen under torsion^[46].

$$\tau_{max} = \frac{\alpha * Mt}{a * b^2} \tag{3.2}$$

Where Mt is the torque that is calculated by multiplying the force value exerted on the filler surface for the distance between the applied forces, α is coefficient that depends on the section aspect ratio, a and b are the length of the rectangular sides. The exerted force was evaluated in a cross-section, which is shown in Figure 3.18.

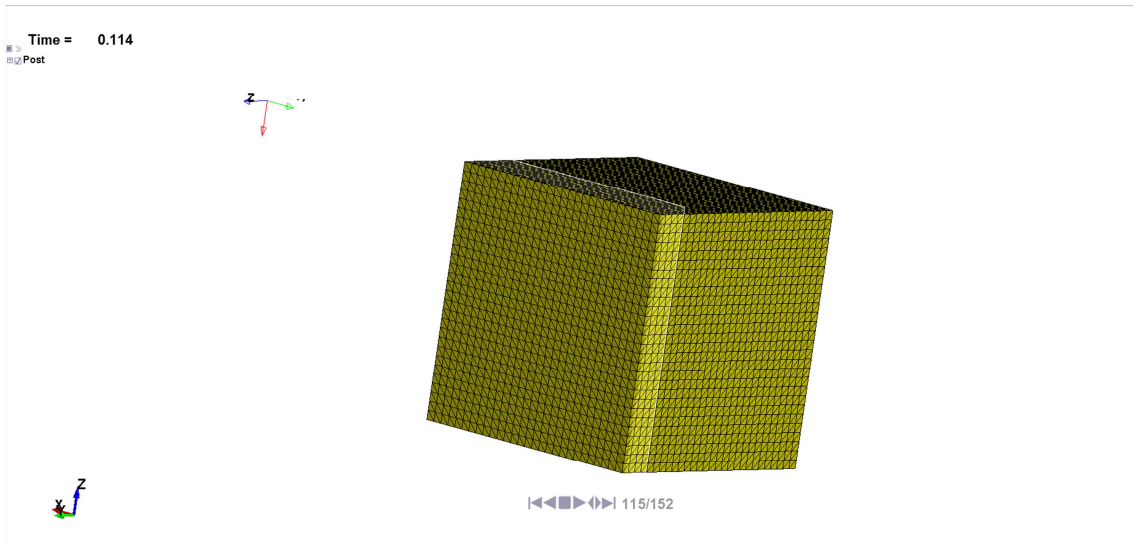


Figure 3.18: Filler cross-section defined for the force evaluation.

Figure 3.19 shows the force that was applied on the lateral filler surface.

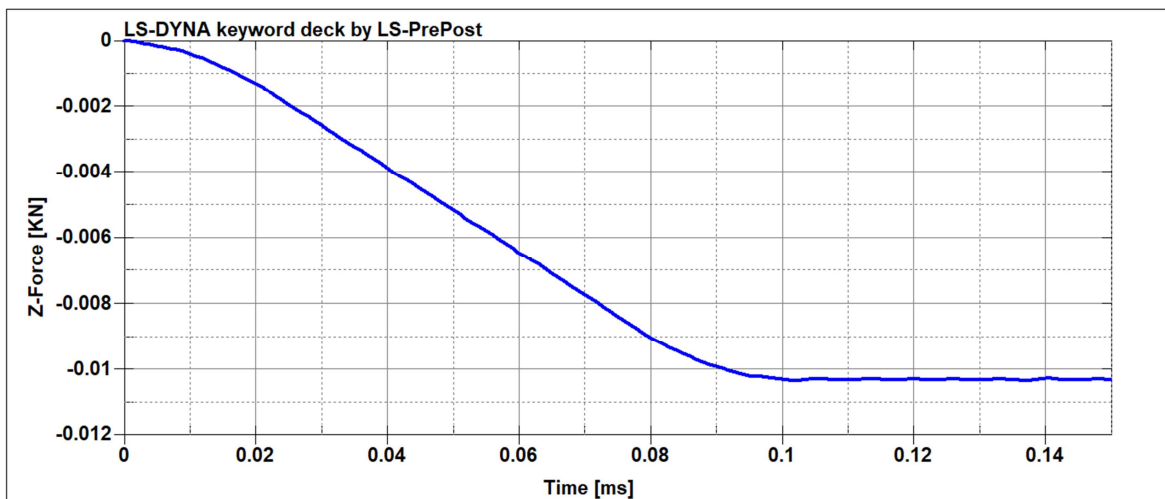


Figure 3.19: Z-force calculated on the cross-section where the load is applied for a model under torsion.

The section was a square with the side of 5 mm and α value was 4.80. Therefore, according to the equation 3.2 the maximum shear stress calculated value was $1.92 * 10^{-3} GPa$.

3. MODELS VALIDATIONS

This value was compared with the interface shear stress distribution extracted from the interface force database, the interface output is illustrated in Figure 3.20.

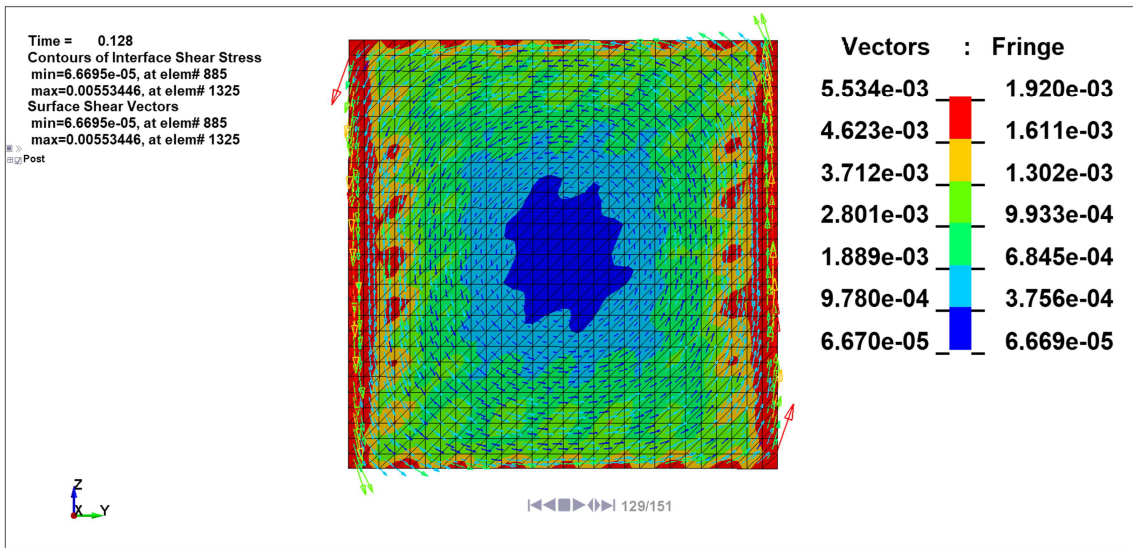


Figure 3.20: Interface shear stress distribution extracted from the tied contact for a model with a torque applied.

The result was quite similar to the analytic distribution previously described. The peaks were present in the central regions of the external sides whereas smaller values were located on the central part of the section. The interface shear stress distribution showed a certain amount of noise, as in the before discussed model. The noise led to some inaccuracies on the sides that were perpendicular to the direction where the load was applied.

Moreover, it was interesting notice that the interface vectors distribution was coherent with the theoretical vector directions showed in Figure 3.17.

The shear stress vectors were always parallel to the side directions. Therefore, the shear stress was directed along the z axes on the vertical sides and along y axes on the horizontal sides.

The shear stress was also analysed on the dentine and filler cross-sections by taking into account the xy and xz stress components. These components were visualized in order to evaluate the complex stress distributions. Dentine and filler cross-sections are showed in Figure 3.5 and Figure 3.6, respectively. Figure 3.21 and Figure 3.22 illustrate both the shear stress components of the dentine cross-section.

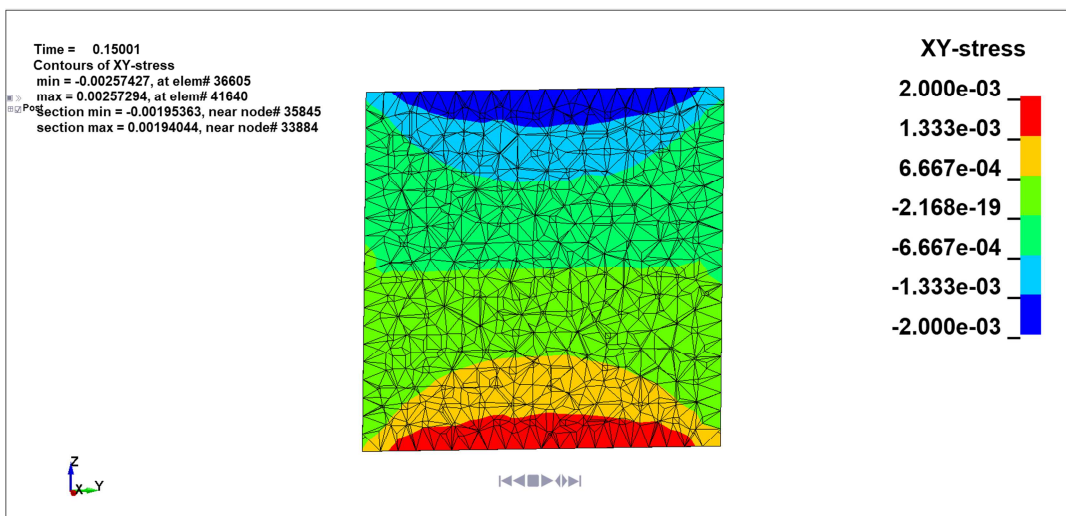


Figure 3.21: Dentine xy shear stress distribution of a model under torsion

3. MODELS VALIDATIONS

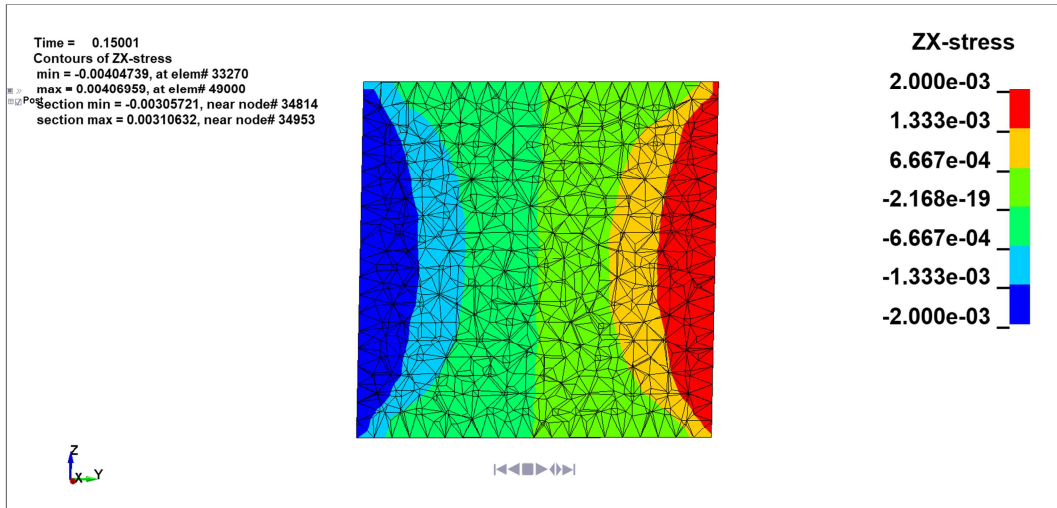


Figure 3.22: Dentine xz shear stress distribution of a model under torsion

The filler cross-section xy and xz shear stress distributions are showed in Figure 3.23 and Figure 3.24.

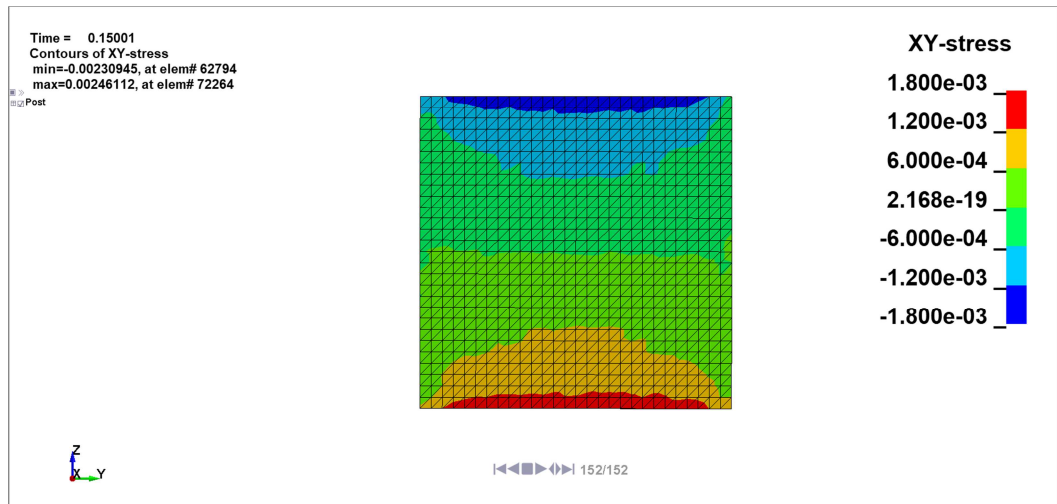


Figure 3.23: Filler xy shear stress distribution of a model under torsion

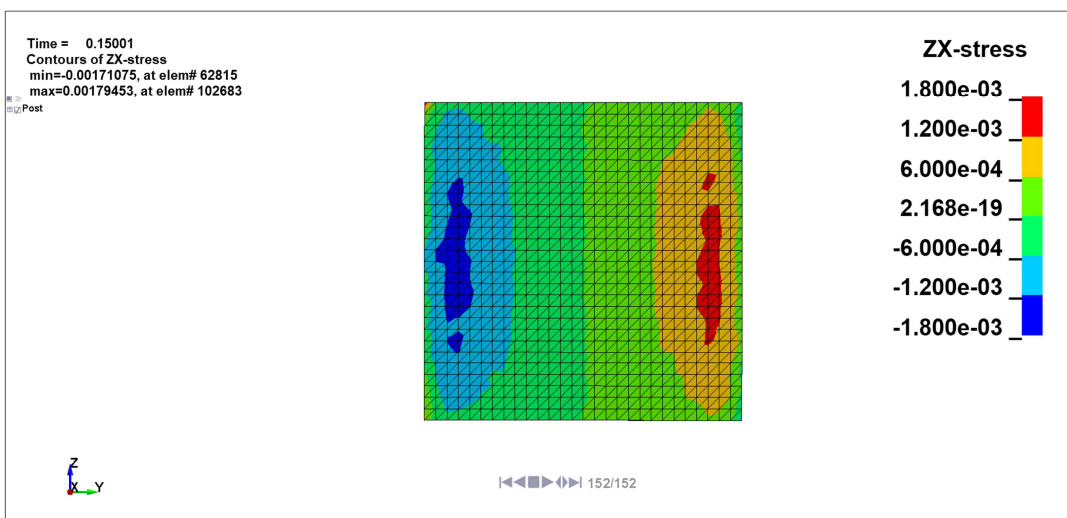


Figure 3.24: Filler xz shear stress distribution of a model under torsion

3. MODELS VALIDATIONS

The dentine and filler shear stress distributions turned out to be coherent with the theoretical torsion behaviour. Furthermore, the cross-sections peaks values were almost identical to the theoretical peak value.

The interface pressure and shear stress values and behaviour were generally coherent with the analytical equations. However, the interfaces distributions appeared to have an amount of noise higher than the cross-sections results.

In conclusion, the interface shear stress and pressure trustworthiness was proved as result of the validation procedure.

4. RESULTS AND DISCUSSIONS

4.1. First model

The results of the first model are discussed in this section, the model load and boundaries conditions were previously illustrated in the method and they were showed in Figure 2.43.

The load was applied as velocity on a node set, the equivalent force was worked out on tooth a cross-section showed in Figure 4.1. The desired load to simulate was 50 N and the solution was analysed at a time with the vertical applied force equal to the above-specified value, as shown in Figure 4.2 , the vertical chewing load was placed on the y-axes and, consequently, the y-force was analysed.

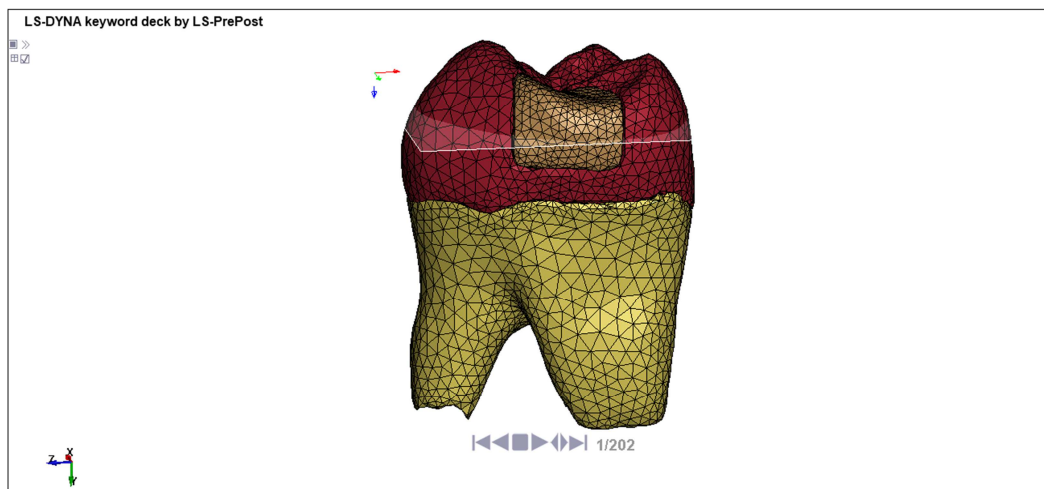


Figure 4.1: Tooth analysed cross-section

Figure 4.2 illustrates the vertical resultant load on the before-mentioned cross-section.

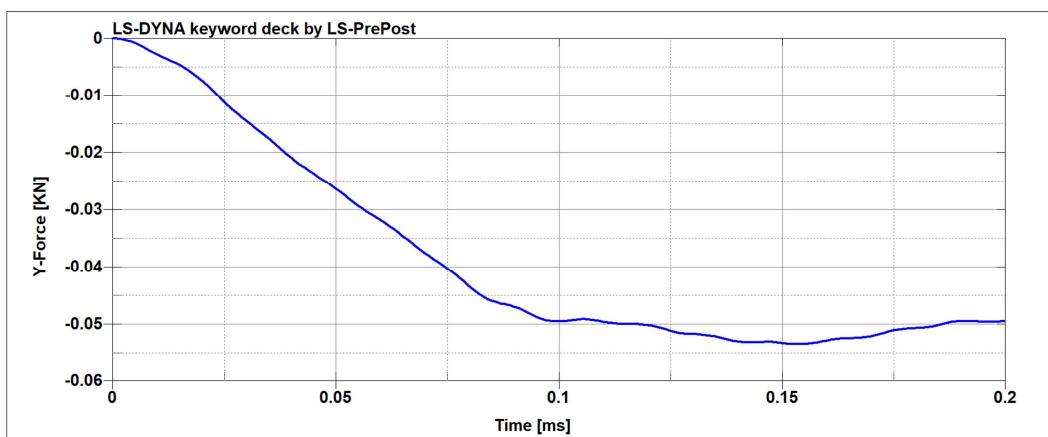


Figure 4.2: Vertical force in the cross-section, only few ripples are present because of the smooth load application.

4.1. First model

Figure 4.2 shows the equivalent vertical force on the section levelling off after 0.1 ms, which was the transient time of the smooth load curve illustrated in Figure 2.38. After this transient only small fluctuations were present and the solutions could be considered stable, the results were visualized at time equal to 0.115 ms when the equivalent load was exactly 50N.

Since major interests lied with the assessment of the fillers debonding condition, the global displacements were analysed to understand whether both the fillers tend to detach from the tooth or not, the x-axes displacements are showed in Figure 4.3 and Figure 4.4.

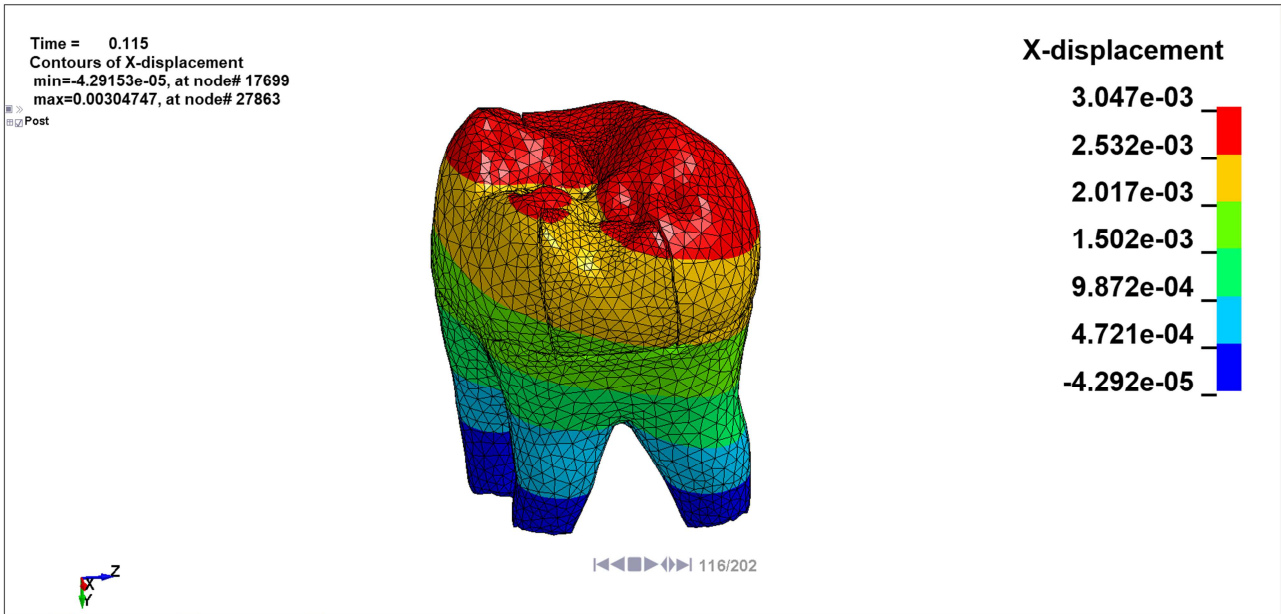


Figure 4.3: Big filler view of the horizontal displacement



Figure 4.4: Small filler view of the horizontal displacement

Figure 4.5 and Figure 4.6 show y-axes displacement whereas Figure 4.7 and Figure 4.8 illustrate the z-axes displacement

4. RESULTS AND DISCUSSIONS

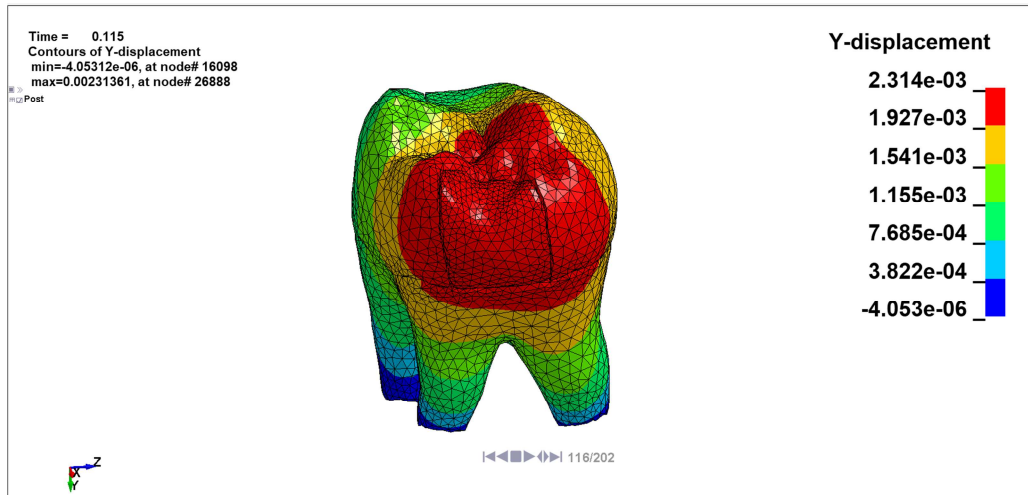


Figure 4.5: Big filler view of the vertical displacement

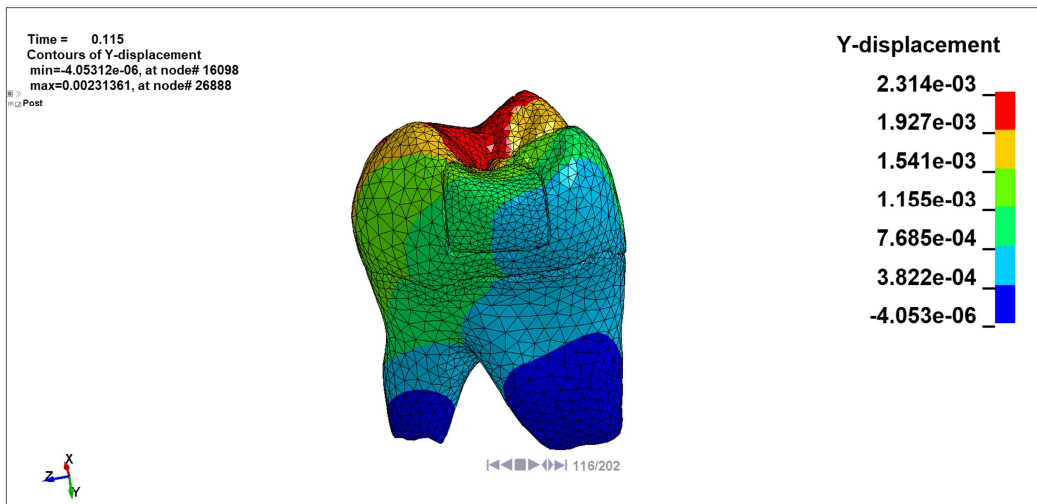


Figure 4.6: Small filler view of the vertical displacement

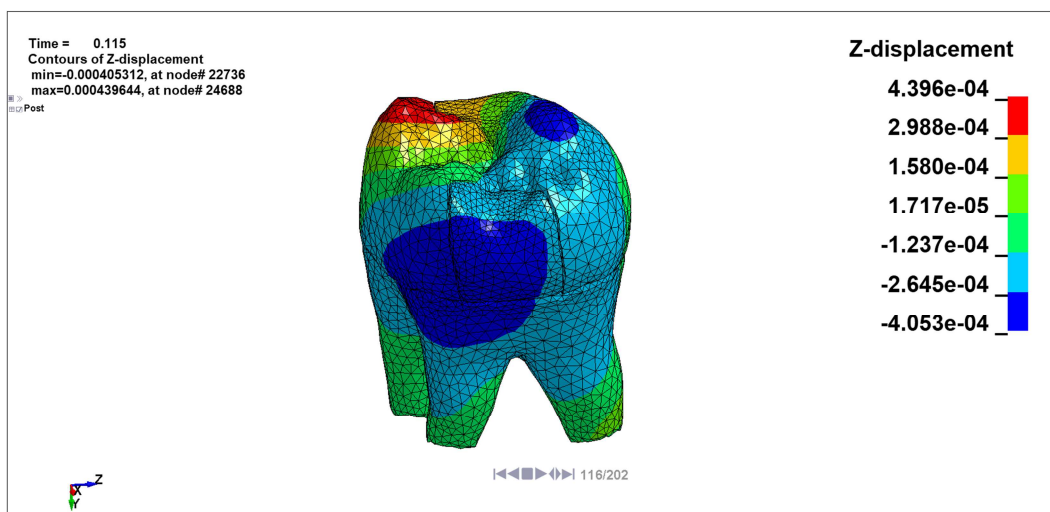


Figure 4.7: Big filler view of the z-axis displacement

4.1. First model

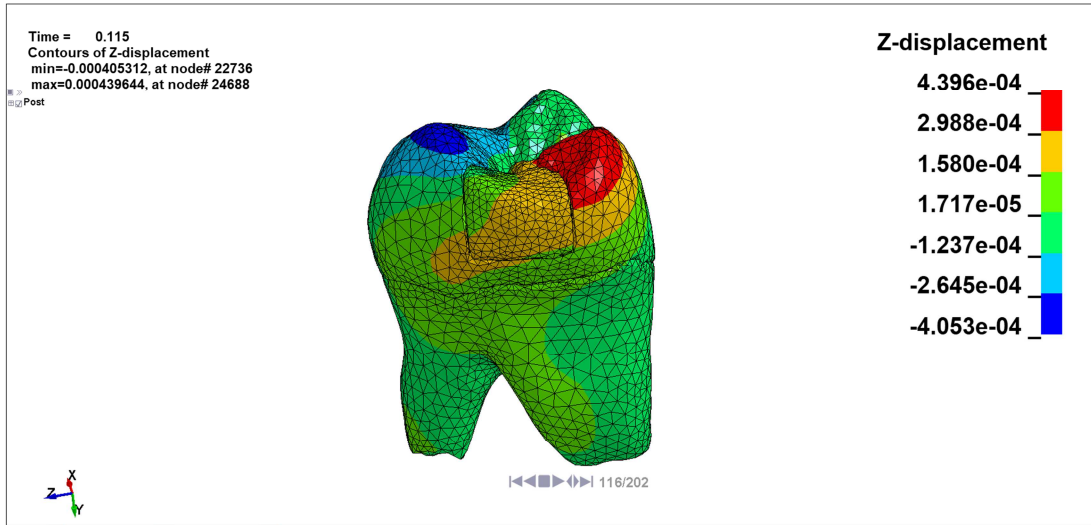


Figure 4.8: Small filler view of the z-axis displacement

The average tooth characteristic elements length was around 0.3 mm ,which was one thousand times bigger than the maximum x-axes displacements whose value was around 3 μm ; y-axes and x-axes displacements are comparable in terms of order of magnitude while z-axes displacement can be neglected because of their small values, as shown in Figure 4.7 and Figure 4.8 . Global displacements provided information to state that the small filler underwent a higher horizontal displacement then the bigger one, furthermore, the big filler vertical displacement was bigger than those of the small filler.

The tooth was subjected to a small load ,therefore, a displacement scale factor was required to assess the fillers movements.

A displacement scale factor of 1000 was determined to be sufficient to make out the fillers displacements. Figure 4.9 and Figure 4.10 show two different screenshots of a graphical animation, the first one is the unmagnified tooth displacement whereas the second is the amplified displacement.

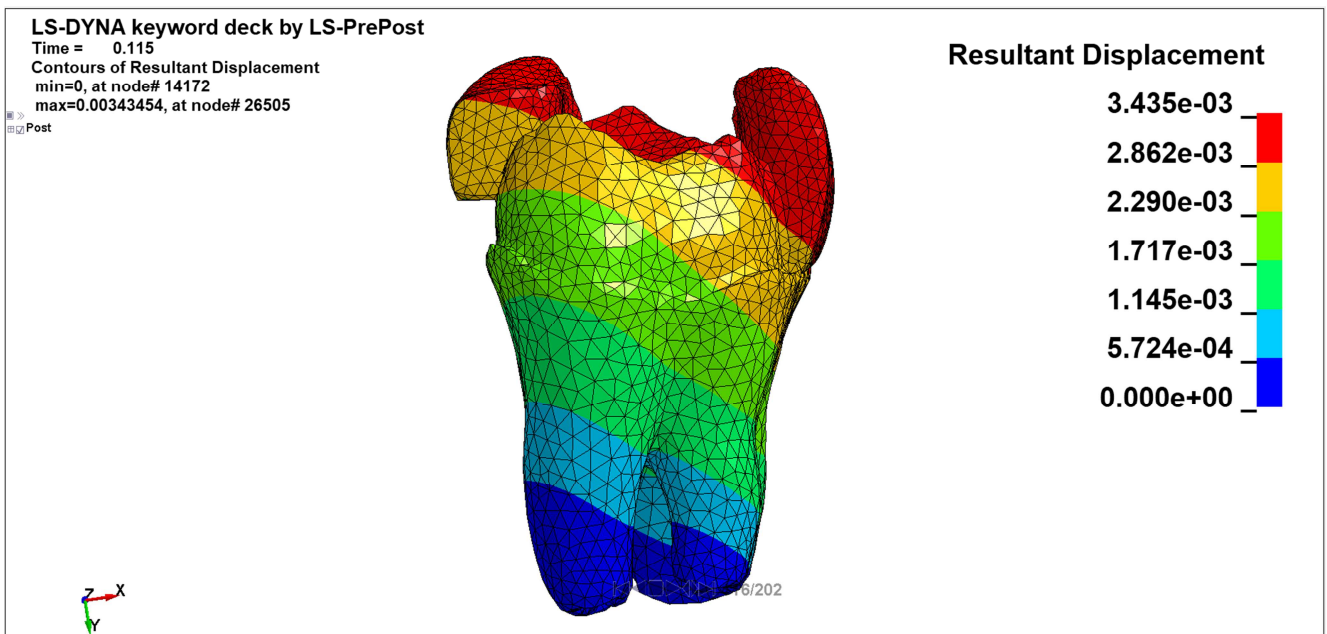


Figure 4.9: Dentine and fillers resultant displacements

4. RESULTS AND DISCUSSIONS

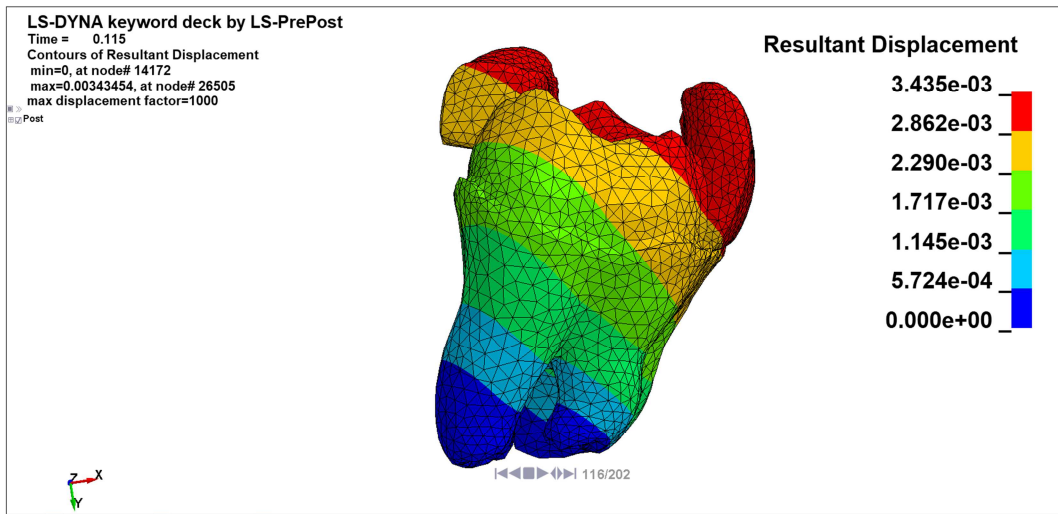


Figure 4.10: Dentine and fillers magnified resultant displacements, only these parts are plotted to highlight fillers detaching phenomena

As shown in Figure 4.9 and Figure 4.10, the big filler displacement is directed outward the tooth in a detaching direction whereas the small filler moves towards enamel and dentine making impossible a detaching process. When stress distributions were plotted their values should be compared with the displacements information meaning that stress peaks could provide useful details on the detaching process only if also the displacements were considered.

Stress results were difficult to interpret because of the complicated tooth structure, Ls-Dyna provide by default stress on global coordinate system whose values make difficult the comprehension of the interface stress condition. X-stress, Y-stress and Z-stress were analysed on the dentine and enamel parts, particular attention should be paid on the fillers borders of those distributions.

These results could not provide any information on the shear stress distribution being in a global system, however the global stress distributions will be compared with the interfaces outputs to draw general conclusions on the results as well as to look for eventual similarities; Figure 4.11 and Figure 4.12 show x-stress distributions of both the interfaces.

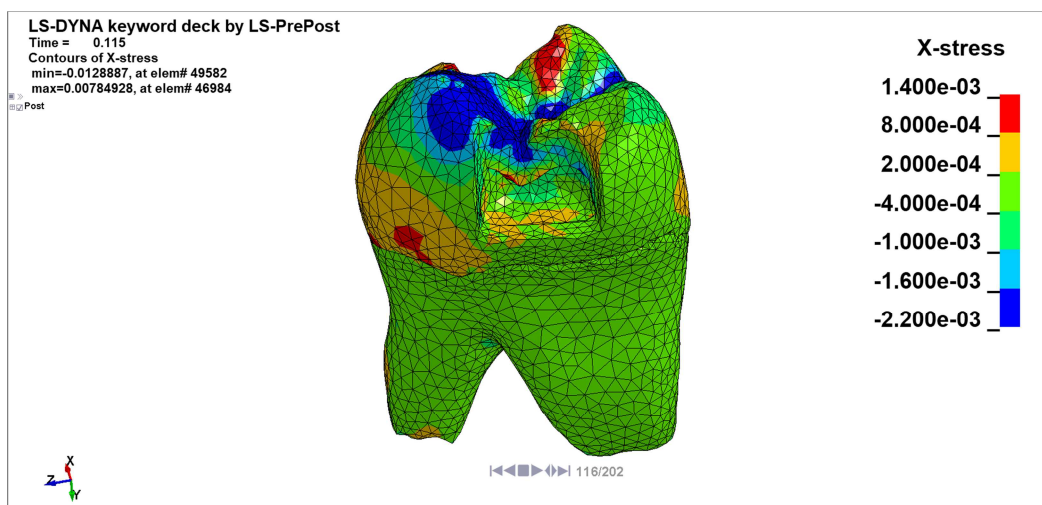


Figure 4.11: Small filler view of the x-stress distribution

4.1. First model

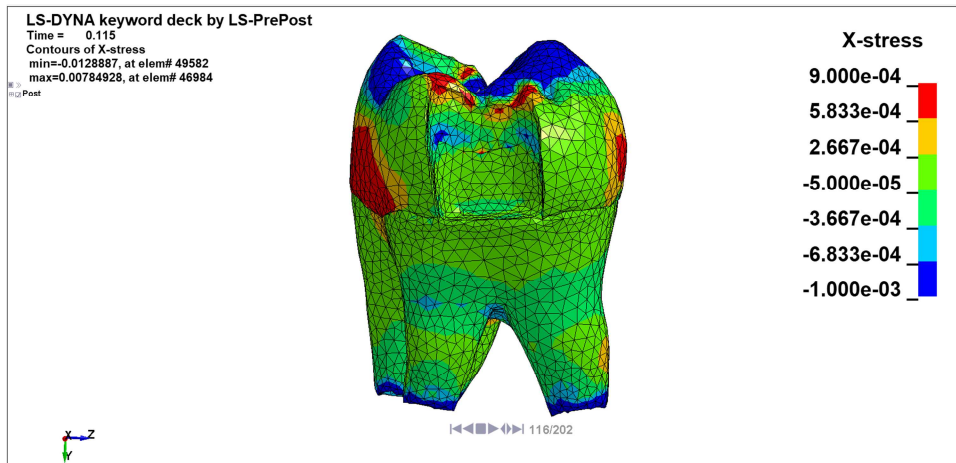


Figure 4.12: Big filler view of the x-stress distribution

Figure 4.13 and Figure 4.14 illustrate the vertical stress of the small and the big filler borders, respectively.

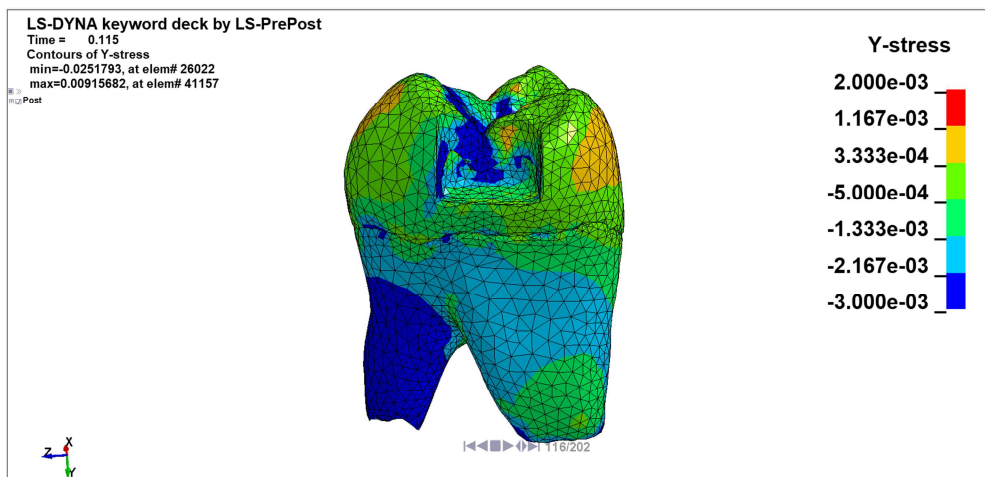


Figure 4.13: Small filler view of the y-stress distribution

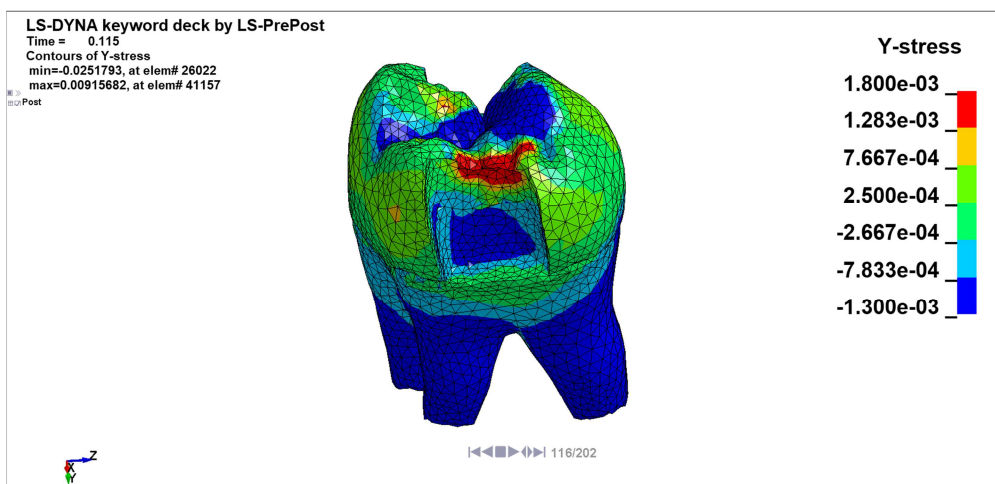


Figure 4.14: Big filler view of the y-stress distribution

4. RESULTS AND DISCUSSIONS

The z-stress distributions are showed in Figure 4.15 and Figure 4.16.

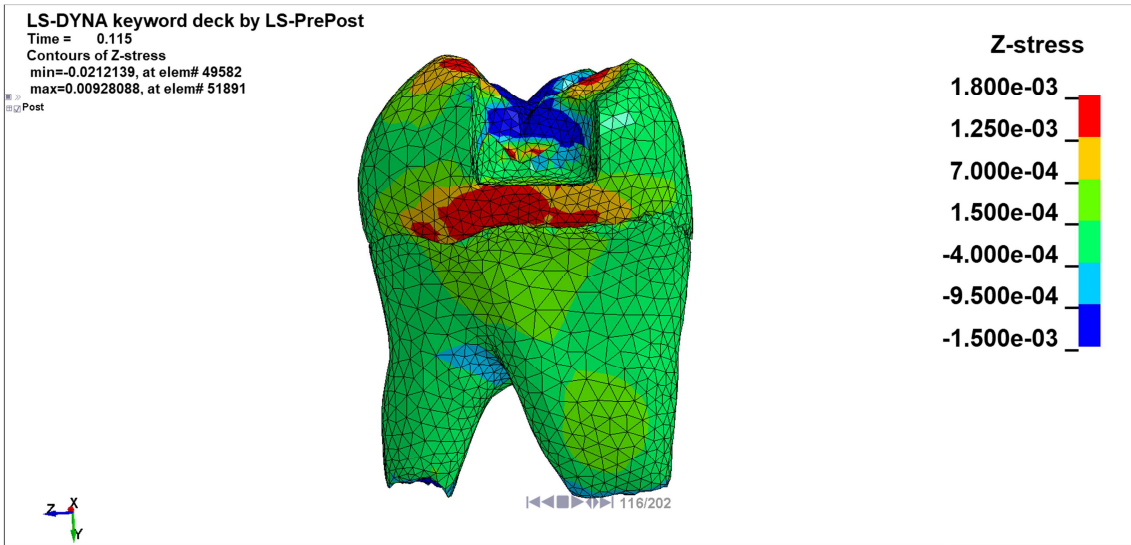


Figure 4.15: Small filler view of the z-stress distribution

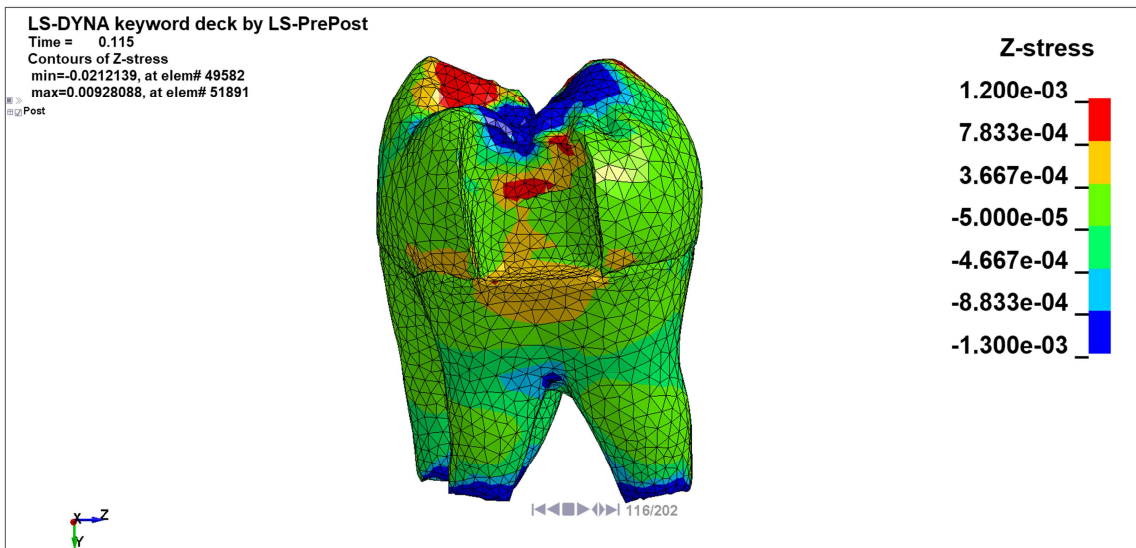


Figure 4.16: Big filler view of the z-stress distribution

Interface force file provides all the important information that can be extracted from contact, as shown in the validation chapter, pressure and shear stress can be considered reliable, therefore, they will be examined to assess the interfaces stress distributions.

Shear stress was plotted both with colour map and vectors while only vectors were displayed for pressure in order to have a clear visualization of the results.

Furthermore, shear stress were plotted with a rear view whereas pressure were visualized with a frontal view for the above-described reason. Big filler interface shear stress and pressure are showed in Figure 4.17 and Figure 4.18 while small filler interfaces distributions are illustrated in Figure 4.19 and Figure 4.20, respectively.

4.1. First model

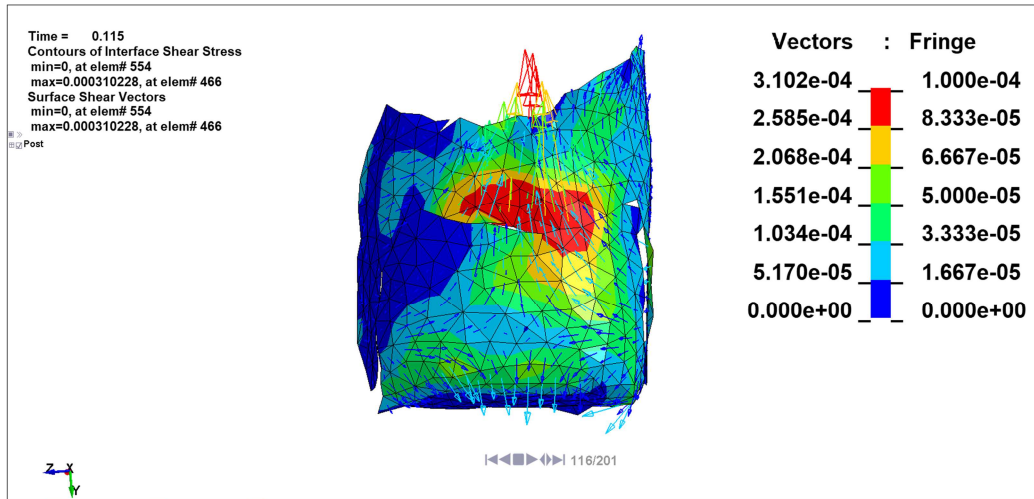


Figure 4.17: Big filler interface shear stress distribution

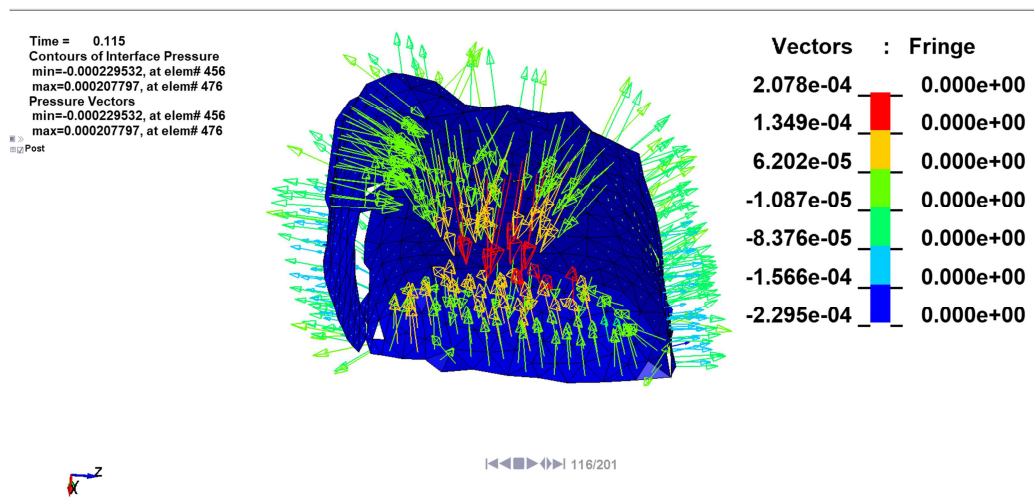


Figure 4.18: Big filler interface pressure distribution

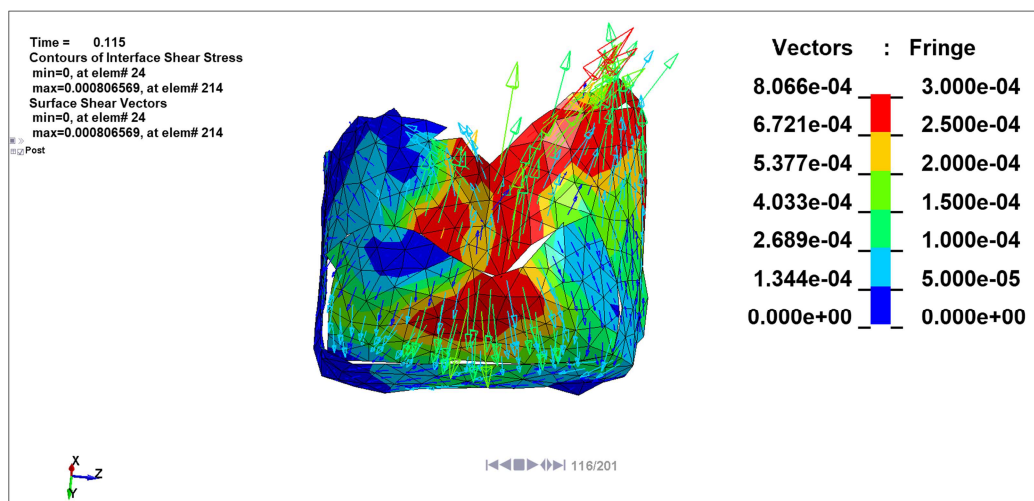


Figure 4.19: Small filler interface shear stress distribution

4. RESULTS AND DISCUSSIONS

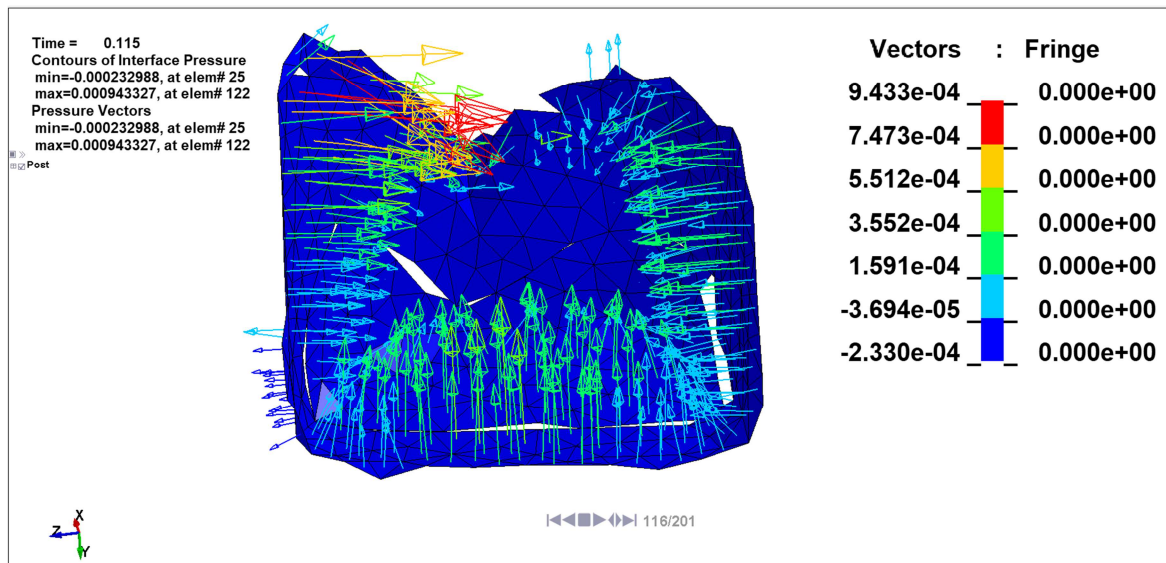


Figure 4.20: Small filler interface pressure distribution

If global stress were compared with interface shear stress it was clear that values and the distributions were different, it was also interesting notice that a certain similarities occurred between y-axes stress and shear stress.

This was reasonable, in fact, the shear stress was mainly directed along y-axes, therefore, the parts where the compression was relevant had also an high shear stress; however, the shear stress order of magnitude stood at around one-tenth of MPa, which was ten time lower than the global stress average values.

Shear stress and interface pressure were analysed in a system that was parallel or normal to the interfaces segment sets whereas d3plot stress were displayed in a global coordinate system leading to the conclusion that these results were substantially incomparable.

Y-stress values were the biggest among the global distributions being in the load direction with values standing at around 1 MPa, the prevalence of blue means that the tooth was general under compression with few red spots where peaks of traction were present. The other global distributions generally showed peaks located on the central upper part of the enamel fillers borders as well as high values on the rear base regions of the fillers.

As shown in figure 4.17 and figure 4.19, the shear stress peaks on the big and small fillers interfaces were present on the dentine central rear regions whereas for both the enamel fillers segments those stress reached the peak on the central upper part.

As discussed in the validation section, pressure provided reliable information on the interfaces stress distributions; however shear stress was responsible for debonding phenomena and big interest lied with their evaluation.

Pressure and shear stress maximum were mainly located in the same regions, therefore, it was possible to identify general regions where the stress was generally highest; pressure maximum values were slightly higher than shear stress peaks.

In conclusion, all the analysed results showed the fillers rear base and the upper central part being subjected to the highest interface tensions.

4.2. Second model

The second model is shown in Figure 2.44, it was loaded with a chewing sphere while the boundaries conditions were the same as the previous model. The load was generated through a smooth velocity applied to the chewing sphere, as shown in Figure 4.21.

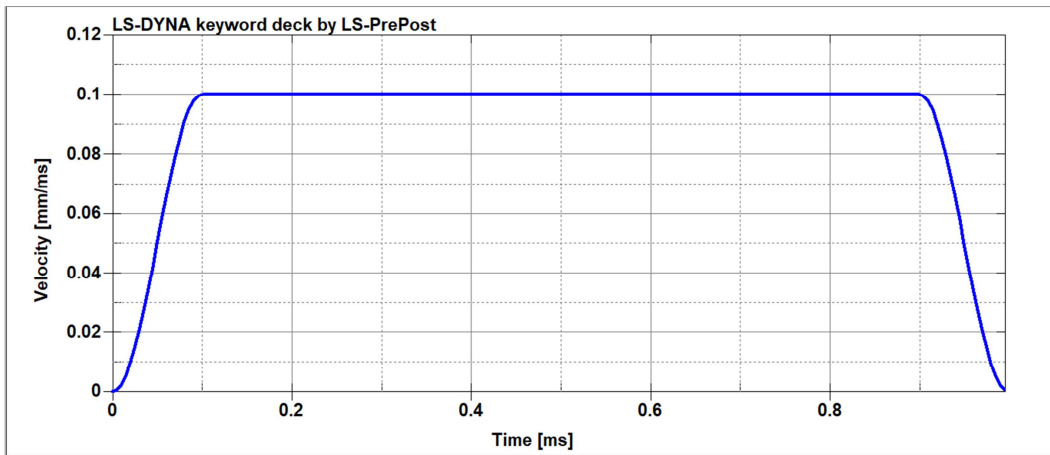


Figure 4.21: Smooth velocity curve applied to the chewing sphere

The sphere moved in vertical direction parallel to y-axis by generating a rising load, therefore, the equivalent 50N load was obtained only for a single time value , the result is illustrated in Figure 4.22.

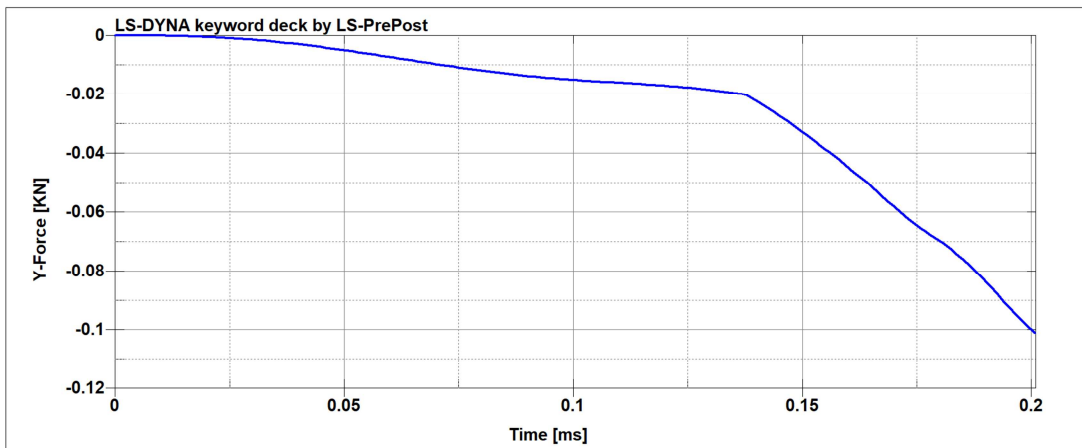


Figure 4.22: Y-Force generated in the tooth cross-section as result of the chewing load application

Figure 4.22 shows the vertical force in a cross section, which was the same showed in Figure 4.1. An equivalent load to 50N was reached at time equal to 0.164 ms , consequently, the results will be analysed at this time. In order to simulate a realistic compression the chewing sphere should be positioned with three enamel contact points, the correct positioning was verified by plotting the Von Mises stress at the analysed time, the results is shown in Figure 4.23.

4. RESULTS AND DISCUSSIONS

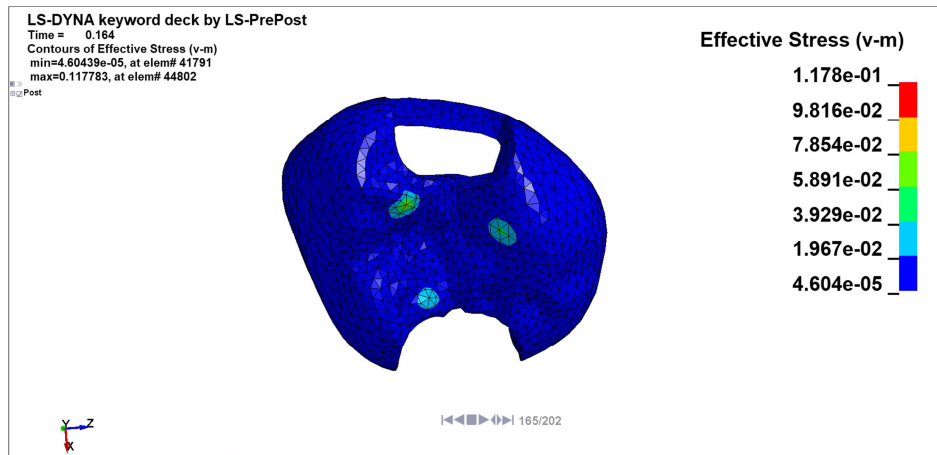


Figure 4.23: Contact points between enamel and chewing sphere at the considered time

The presence of three contact points was effectively verified at the analysed time, the chewing sphere material model was rigid, therefore, it will not be showed in the results. Since the chewing machine created peaks of stress, the contact points underwent a major displacements.

Figure 4.24 and Figure 4.25 illustrate the global x-axes displacement whereas Figure 4.26 and Figure 4.27 show the y-axes displacement.

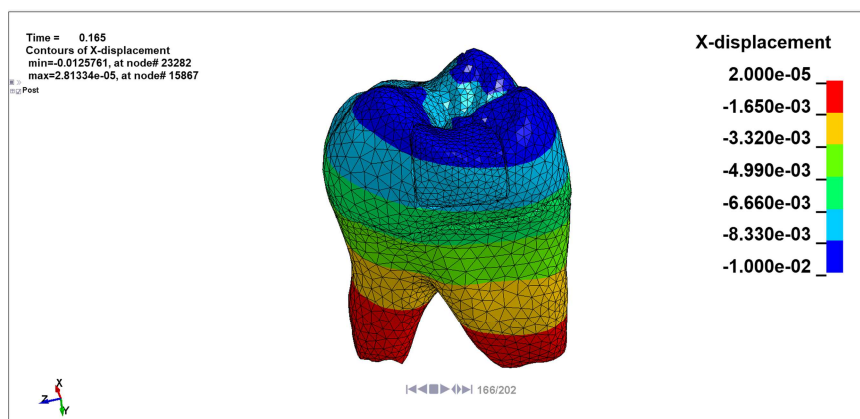


Figure 4.24: X-axes global displacement, small filler view

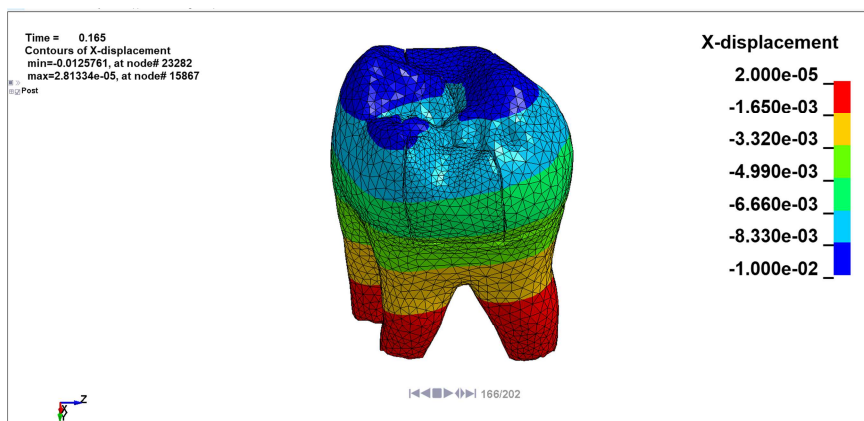


Figure 4.25: X-axes global displacement, big filler view

4.2. Second model

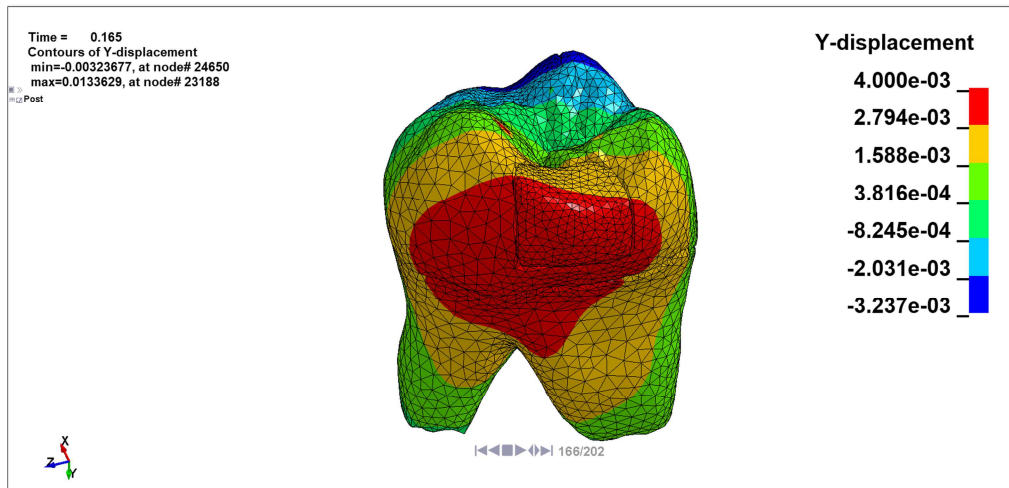


Figure 4.26: Y-axes global displacement ,small filler view

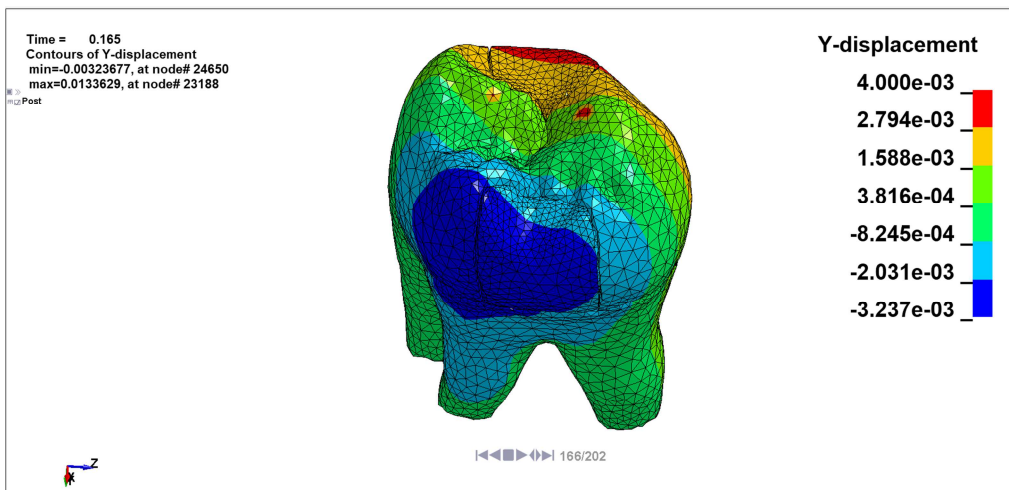


Figure 4.27: Y-axes global displacement ,big filler view

Figure 4.28 and Figure 4.29 show z-axes global displacement.

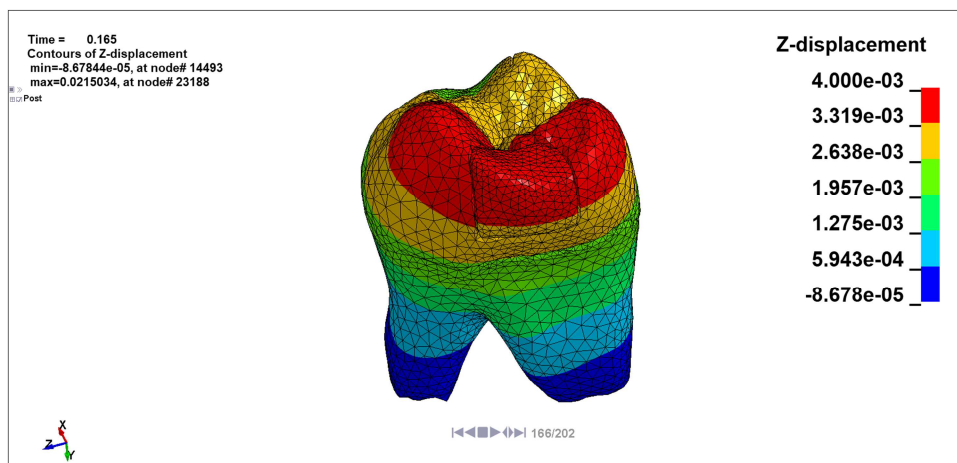


Figure 4.28: Z-axes global displacement ,small filler view

4. RESULTS AND DISCUSSIONS

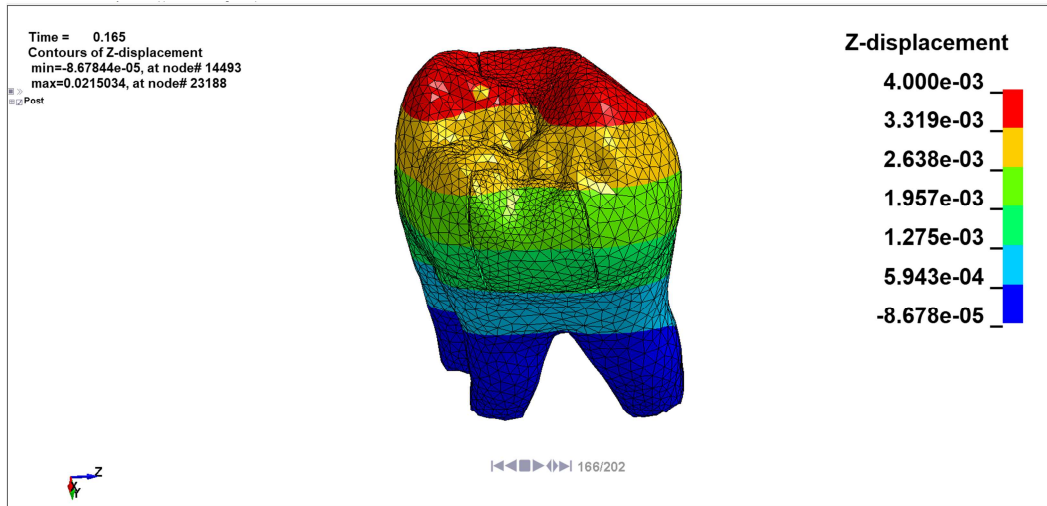


Figure 4.29: Z-axis global displacement ,big filler view

The global displacements showed a deeply different distribution from the first model, also in this case it was impossible to make out the displacement directions. The maximum global displacement was along z-axes and it stood at around 20 μm , which was fifteen time lower than the average solid element characteristic length. Figure 4.26 and Figure 4.28 show that the small filler underwent an higher displacement than the bigger; no further considerations were possible on the detaching phenomena with these results. Therefore, the displacement scale factor was set to 1000 to magnify the fillers displacement, Figure 4.30 and Figure 4.31 show two different screenshots of a graphical animation, the first one is the unmagnified tooth displacement whereas the second is the amplified displacement.

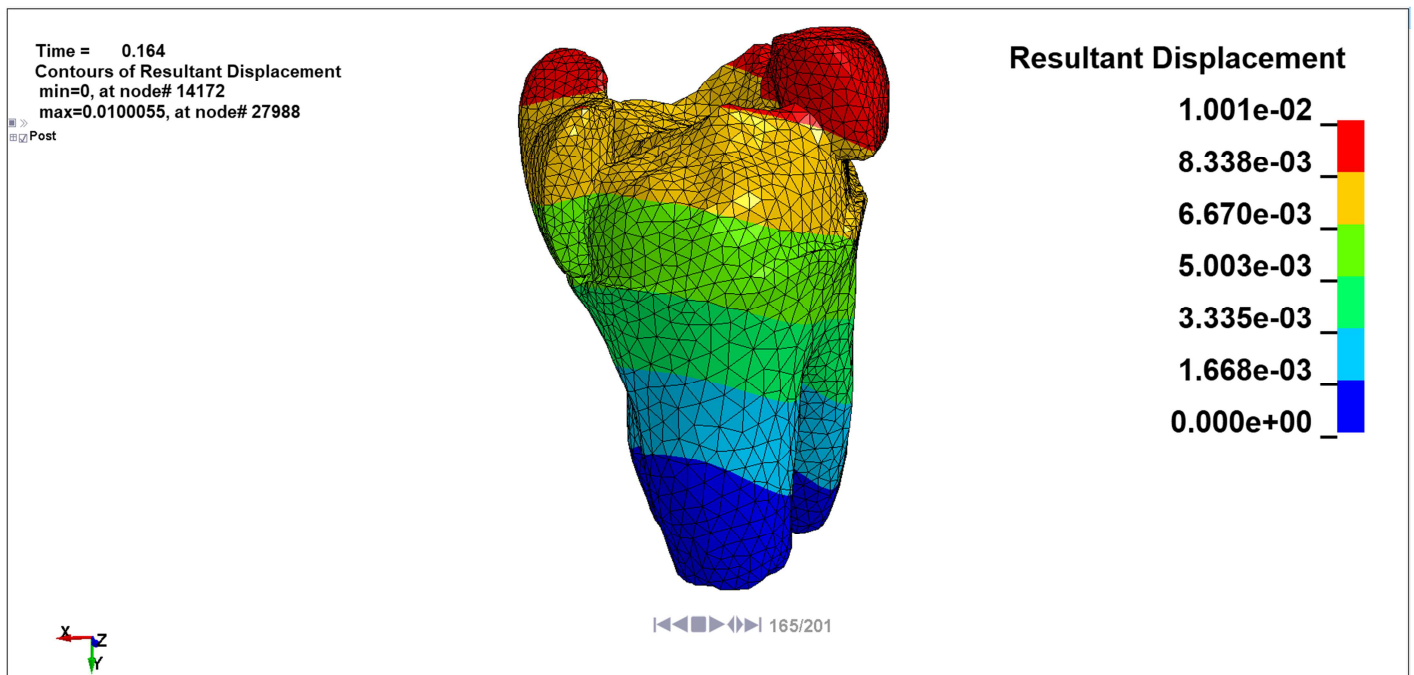


Figure 4.30: Resultant displacement before the magnification was applied.

4.2. Second model

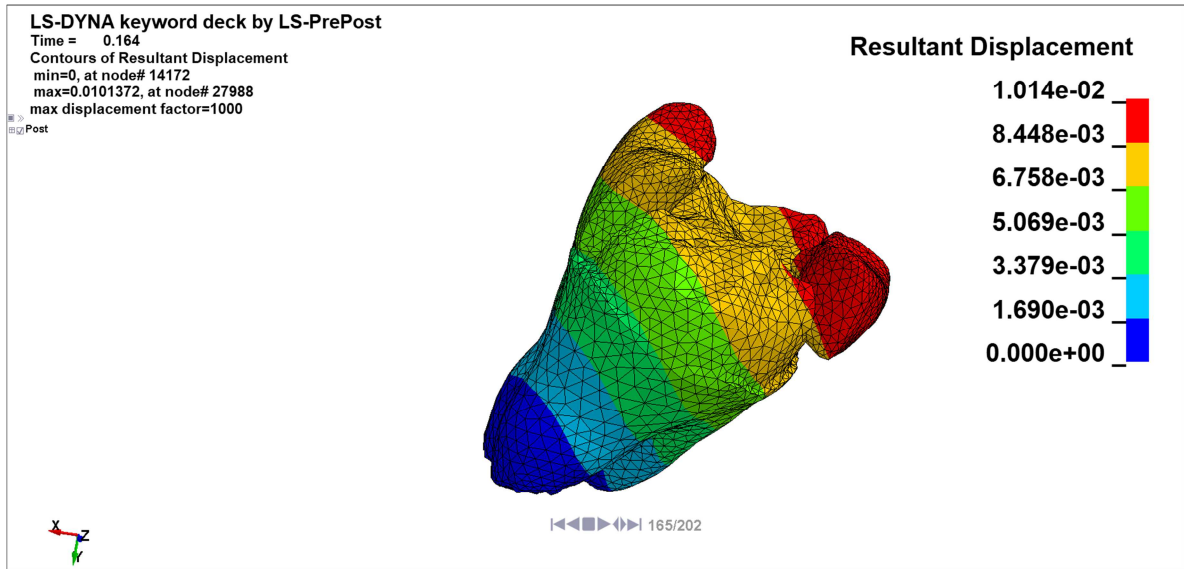


Figure 4.31: Resultant displacement after the magnification was applied.

It is clear comparing the Figure 4.30 and Figure 4.31 that the small filler is likely to be debonded whereas the big filler moves inward, therefore, for the latter filler detaching phenomena can not occur at all. This situation was opposite to the first model where the big filler moved outward in a debonding direction, certainly the second model was much more reliable than the first one.

As matter of fact, when in the first model some nodes were forced to move in a direction all the stress-strain distributions were determined leading to an approximation whose results could be really different from the reality.

The chewing sphere load application was much more realistic, since a node set load was not applied in a certain direction but the stress-strain distributions were determined through a contact algorithm, the nodes involved were different from the first model as well as the exerted loads, which were calculated during the simulation.

Global x-stress, y-stress and z-stress distributions were analysed in the same way as in the first model, these distributions could not provide reliable information on the interfaces stress conditions but they could describe the general tooth behaviour under the chewing sphere load. Enamel and dentine x-stress distributions are showed in Figure 4.32 and Figure 4.33.

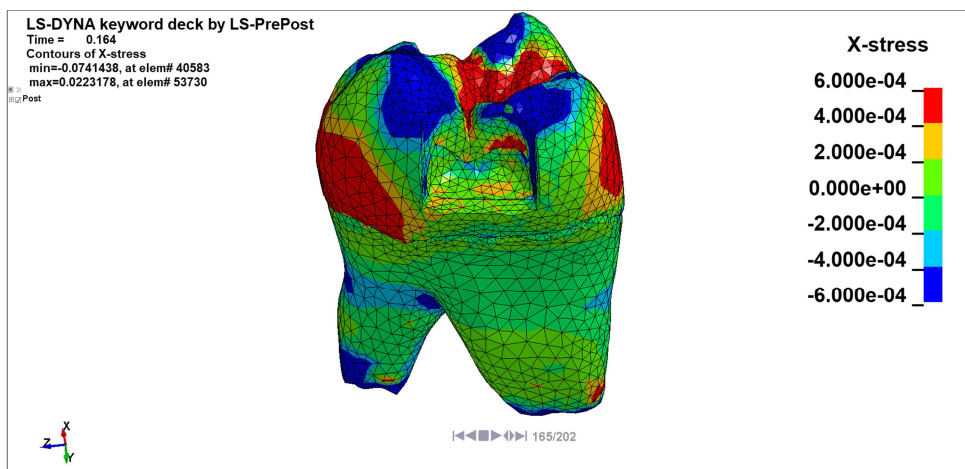


Figure 4.32: Dentine and enamel x-stress distribution, small filler view

4. RESULTS AND DISCUSSIONS

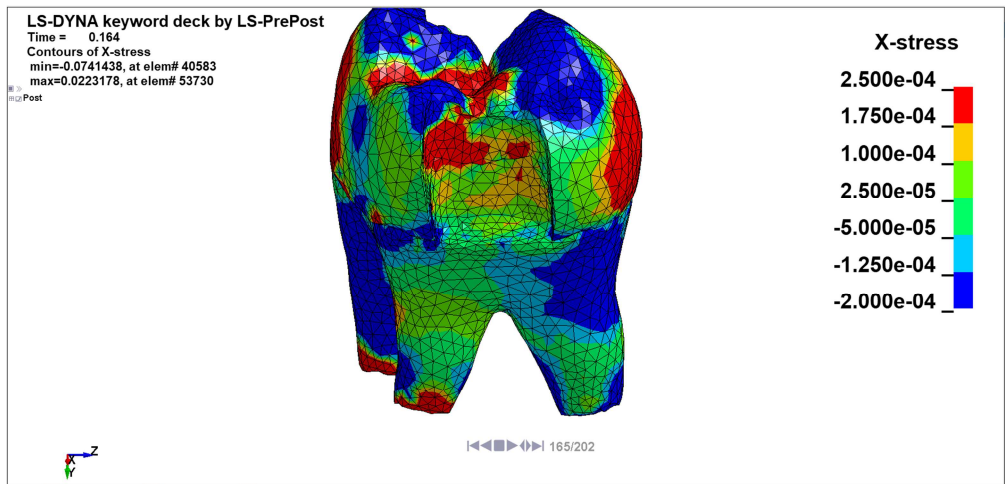


Figure 4.33: Dentine and enamel x-stress distribution, big filler view

Figure 4.34 and Figure 4.35 illustrate the global compression stress on dentine and enamel whereas Figure 4.36 and Figure 4.37 show z-stress for the same parts.

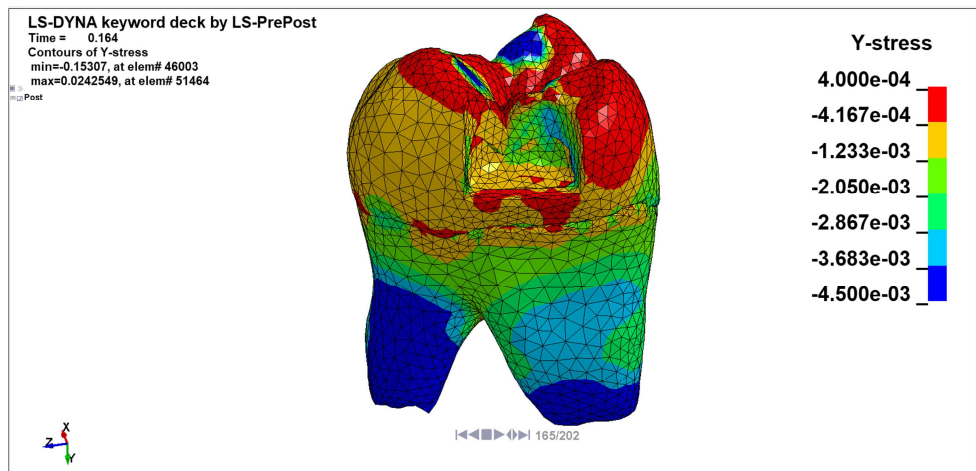


Figure 4.34: Dentine and enamel y-stress distribution, small filler view

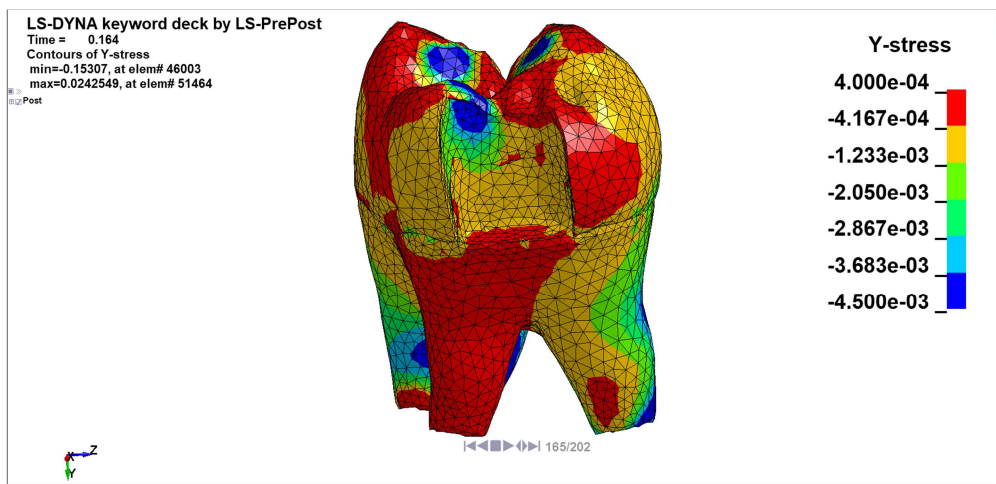


Figure 4.35: Dentine and enamel y-stress distribution, big filler view

4.2. Second model

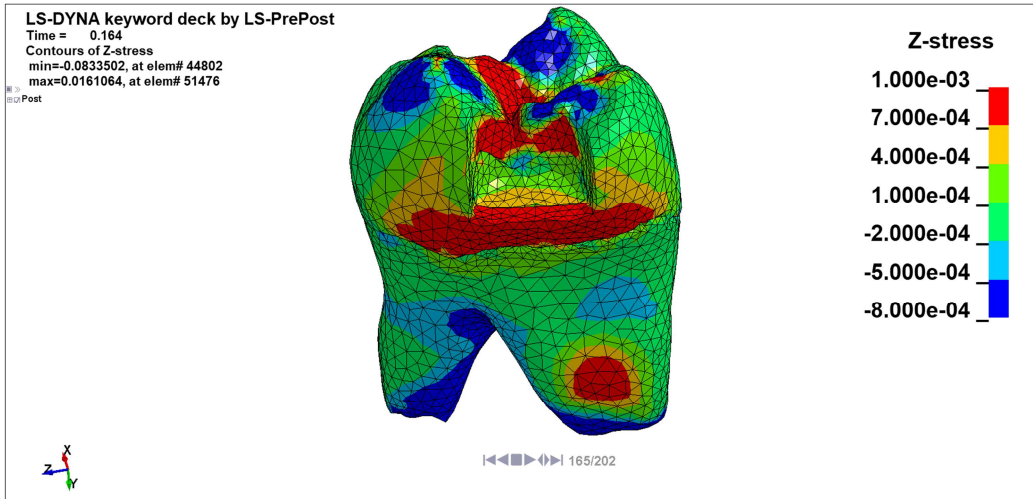


Figure 4.36: Dentine and enamel z-stress distribution, small filler view

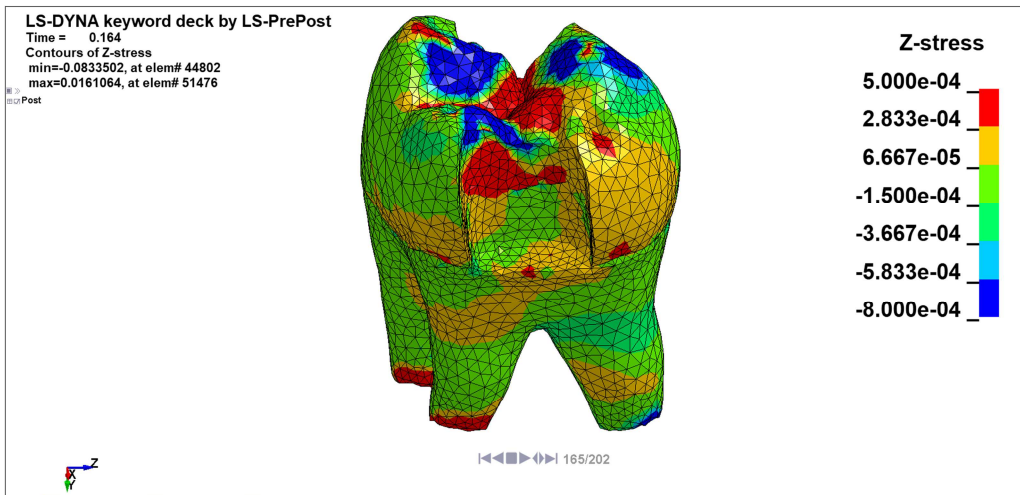


Figure 4.37: Dentine and enamel y-stress distribution, big filler view

Generally, global stress values were lower than in the first model showing that the load simulated in the previous model overestimated the stress distributions. The blue areas visible in all the global stress distributions were generated by the three chewing sphere enamel contact points, therefore, the propagations of those peaks generated the overall distributions. In general, the enamel fillers interfaces showed higher tensions than those of the dentine fillers because of its higher proximity with the sphere contact points. The peaks were located on the side that was closer to those contact points, the y-stress reached the highest values with peaks standing at around 4.5 MPa.

In general, it was possible to state that the rear base general stress of the dentine fillers interfaces in the second model was lower than those of the first model.

Interfaces shear stress were plotted both with colour map and vectors while only vectors were displayed for pressure in order to have a clear visualization of the results.

Furthermore, shear stress were plotted with a rear view whereas pressure were visualized with a frontal view for the above-described reason.

Big filler interface shear stress and pressure are showed in Figure 4.38 and Figure 4.39 while small filler interfaces distributions are illustrated in Figure 4.40 and Figure 4.41, respectively.

4. RESULTS AND DISCUSSIONS

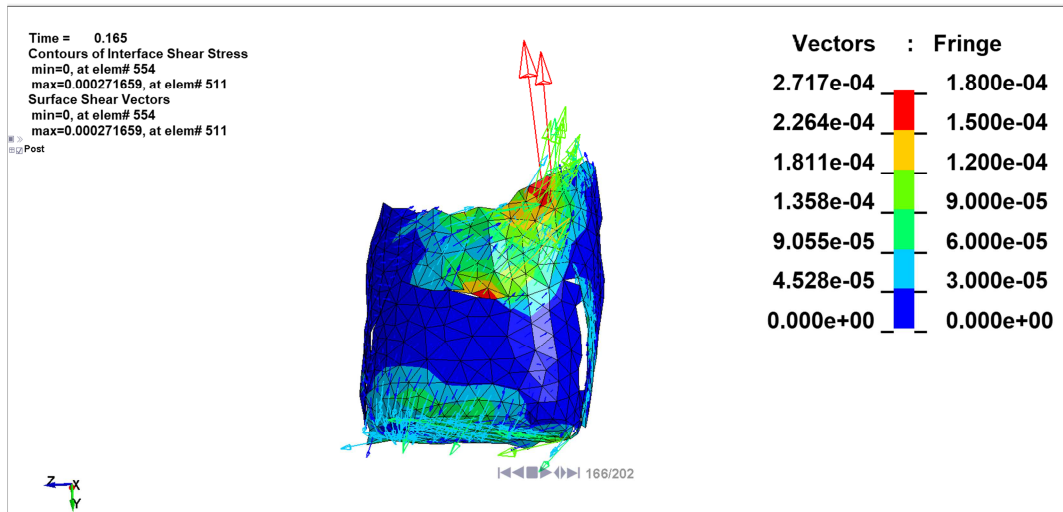


Figure 4.38 : Big filler interface shear stress

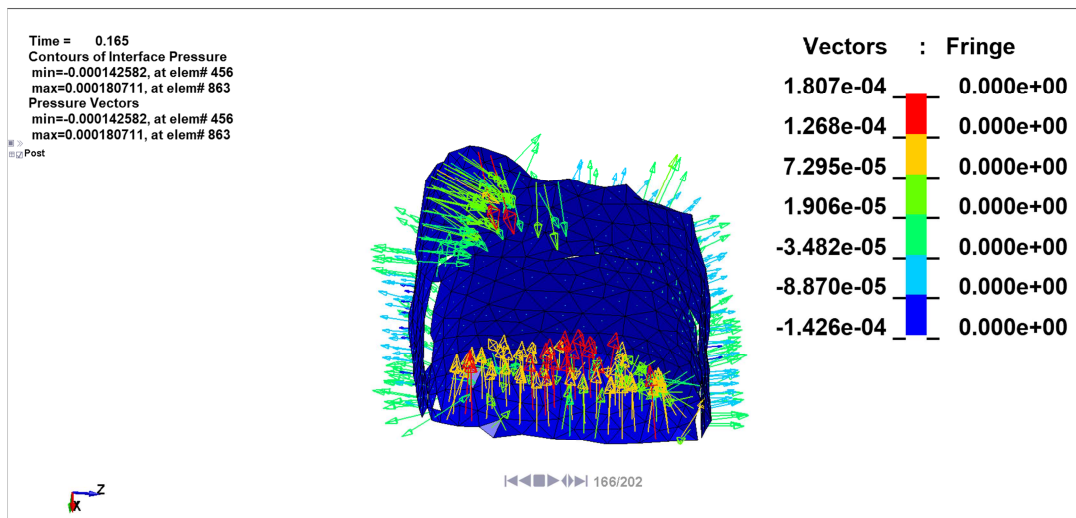


Figure 4.39 : Big filler interface pressure

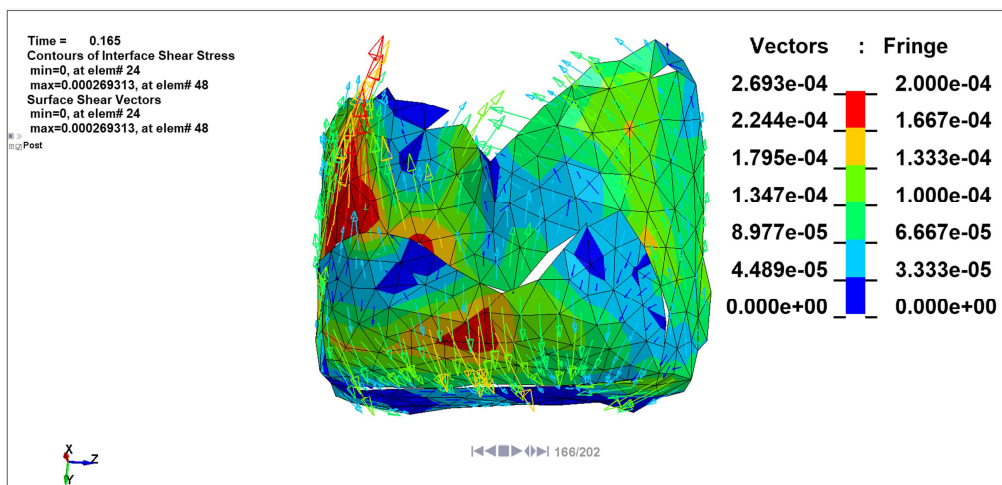


Figure 4.40: Small filler interface shear stress

4.2. Second model

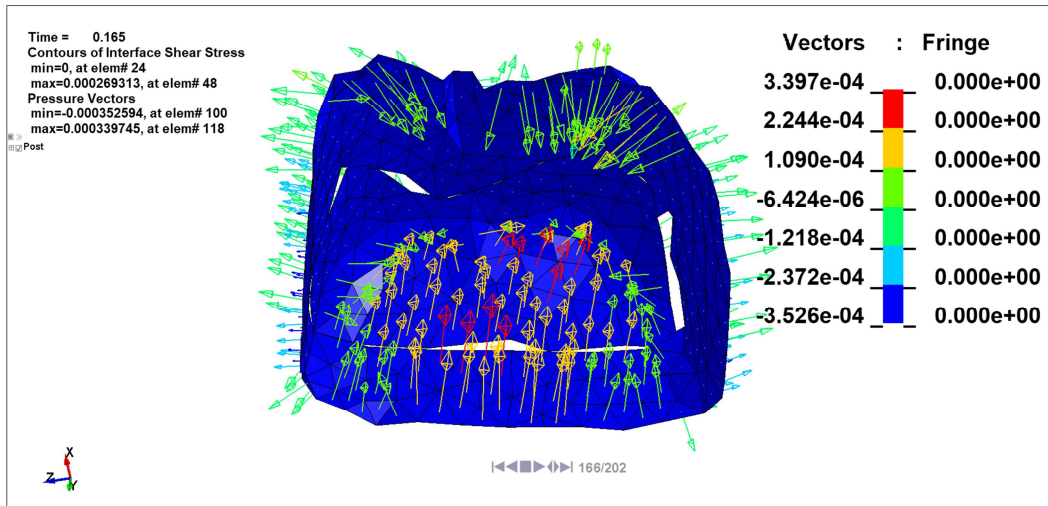


Figure 4.41: Small filler interface pressure

As previously stated in this section, only the small filler could potentially detach in this model.

The small filler interface stress values were generally higher than those of the big filler, figure 4.40 shows a peak in the enamel filler interface in the proximity of one chewing sphere enamel contact region. This was confirmed by Figure 4.23 that illustrated the chewing sphere compression maximum values, one of the peaks was really close to the upper-left part of the small filler interface. The other small filler shear stress peak was located on the rear base interface and it was directed parallel to the x-axes; it was also interesting to notice that x-axes global stress distribution showed an high value in the same region.

The big filler stress peak was located on the upper-right region as showed in Figure 4.38, as matter of fact, the shear stress big filler peak was really close to a chewing sphere enamel contact point, which was the big filler blue peak in Figure 4.35.

The pressure interface peaks location was substantially the same of the maximum shear stress value for both the interfaces, therefore, some regions presented an overall stress that was higher than others. The global stress distribution showed peaks that were in general close to the enamel chewing sphere contact points, this was coherent with the interface results. However, as widely discussed in the previous method, these results were substantially incomparable.

In conclusion, the maximum shear stress values were located on the rear base and on the upper-left region of the small filler interface.

4.3. Third model

The third model is showed in Figure 2.45; the load was applied through a chewing sphere in the same way as it was in the second model and with the same velocity smooth curve, which was shown in Figure 4.21. Therefore, the sphere moved along y-axes exactly in the same way discussed in the second method leading to a rising load generation. The results analysis was performed for an equivalent load of 50N, a tooth cross-section, which was shown in Figure 4.1, was analysed to determine the time value for the results assessment. Figure 4.42 shows the vertical force obtained on the above-mentioned cross-section.

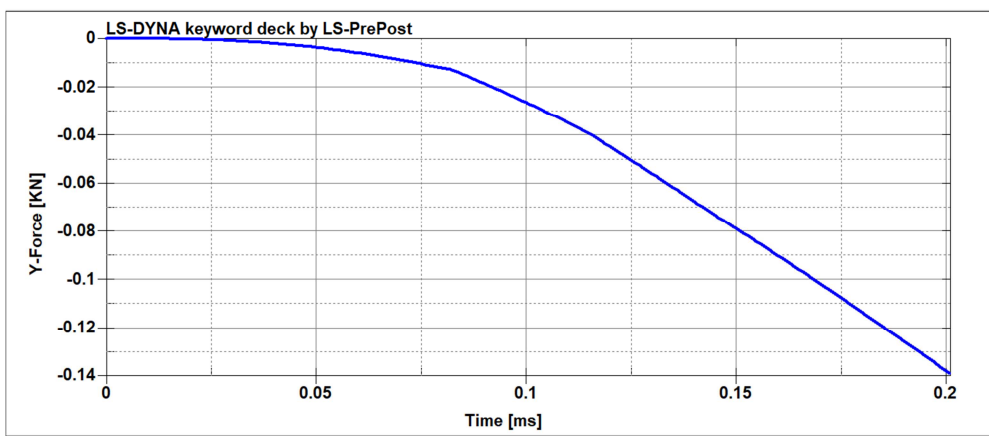


Figure 4.42 : Vertical force calculated on the tooth cross-section

The equivalent load of 50 N was reached at a time of 0.125 ms, which was different from the second method time value, the reason lied with the different boundaries conditions.

As matter of fact, the boundaries conditions influenced the contact points between the chewing sphere and the enamel determining a different load application from the second model, it was clear by comparing Figure 4.42 with Figure 4.22. Figure 4.43 shows the contact points between the enamel and the chewing sphere, those points were different from the second method contact points illustrated in Figure 4.23.

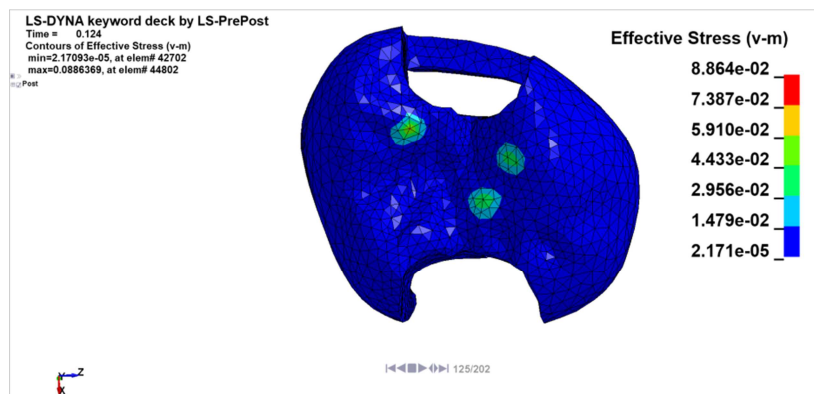


Figure 4.43: Contact points between chewing sphere and enamel in the third model

4.3. Third model

Therefore, the resin disk modelling introduced a modification on the load application that will influence the results, in this section the entities of these changes will be discussed.

The chewing sphere modelling was performed with a rigid material as discussed in the second model. As consequence of that, it will not be displayed, the chewing sphere purpose was only to apply the load in a realistic way and no interest lied with the study of its stress.

As discussed in the second model, the chewing sphere enamel contact points generated stress peaks on the enamel; therefore, fringes adjustments were required.

Figure 4.44 and Figure 4.45 show the x-axes global displacement whereas Figure 4.46 and Figure 4.47 illustrate the y-axes global displacement.

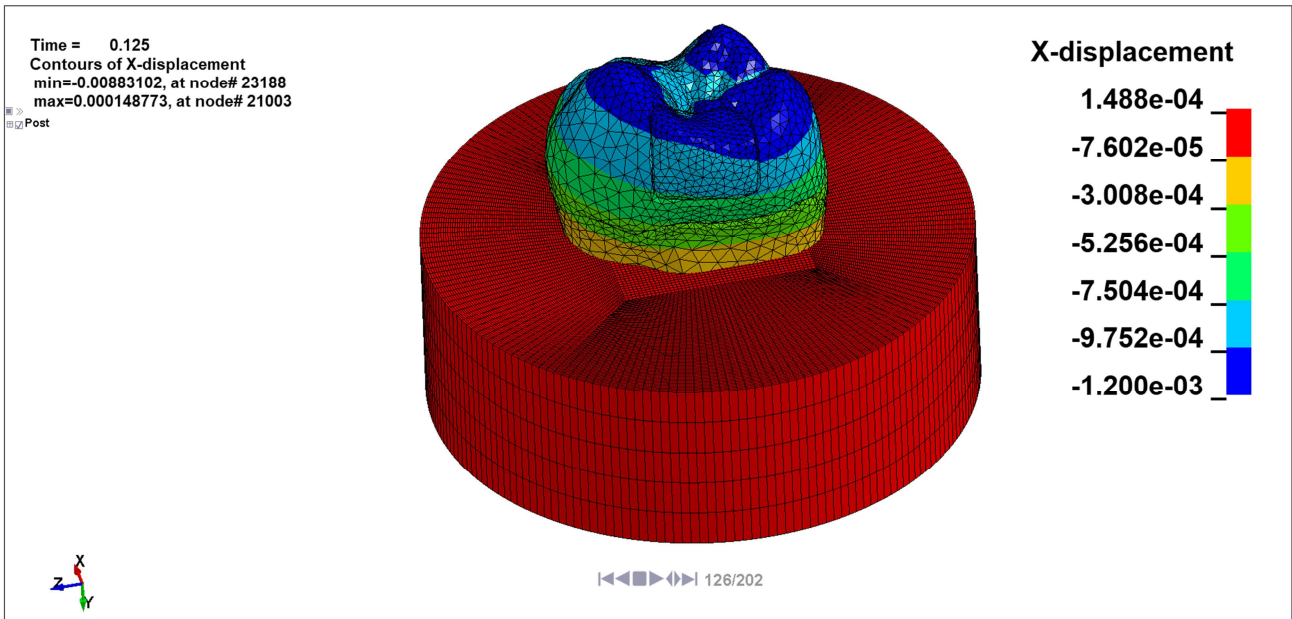


Figure 4.44: X-axes global displacement, small filler view

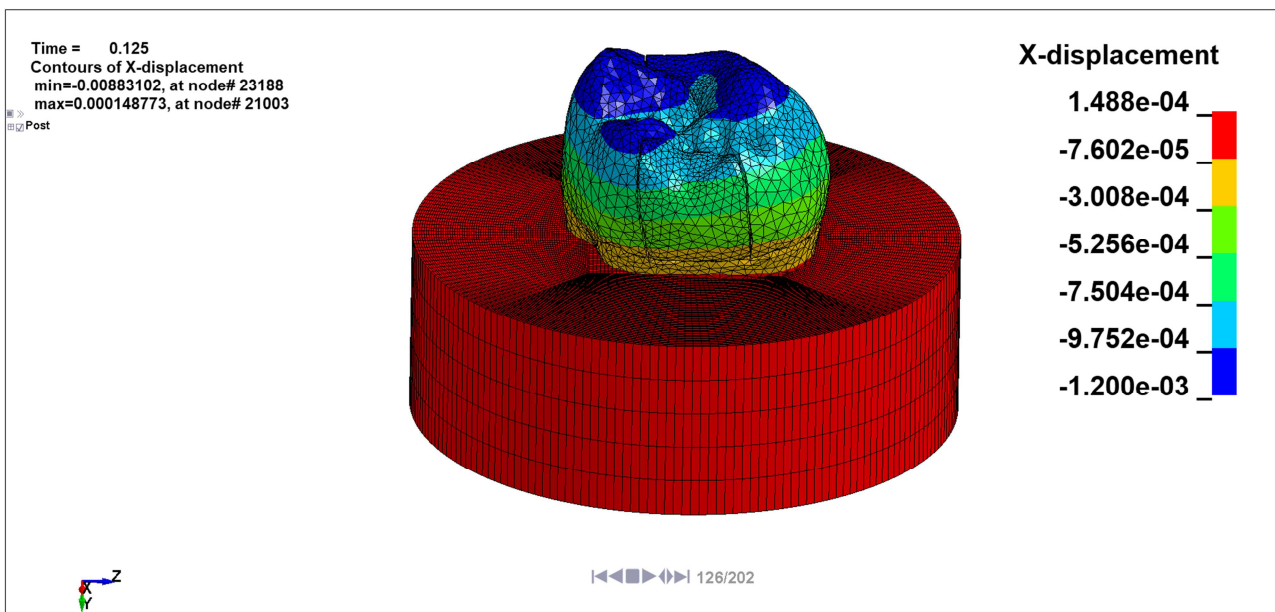


Figure 4.45: X-axes global displacement, big filler view

4. RESULTS AND DISCUSSIONS

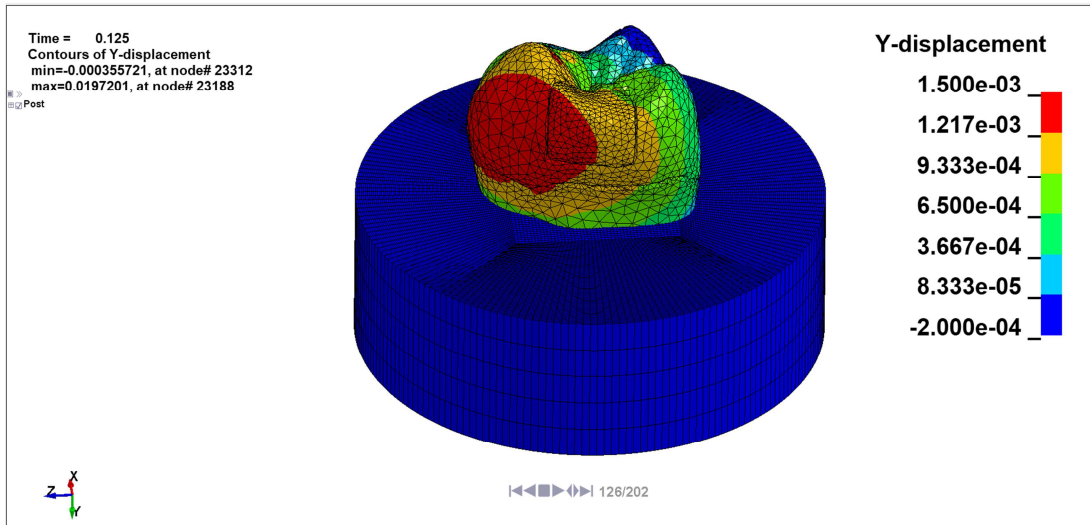


Figure 4.46: Y-axis global displacement, small filler view

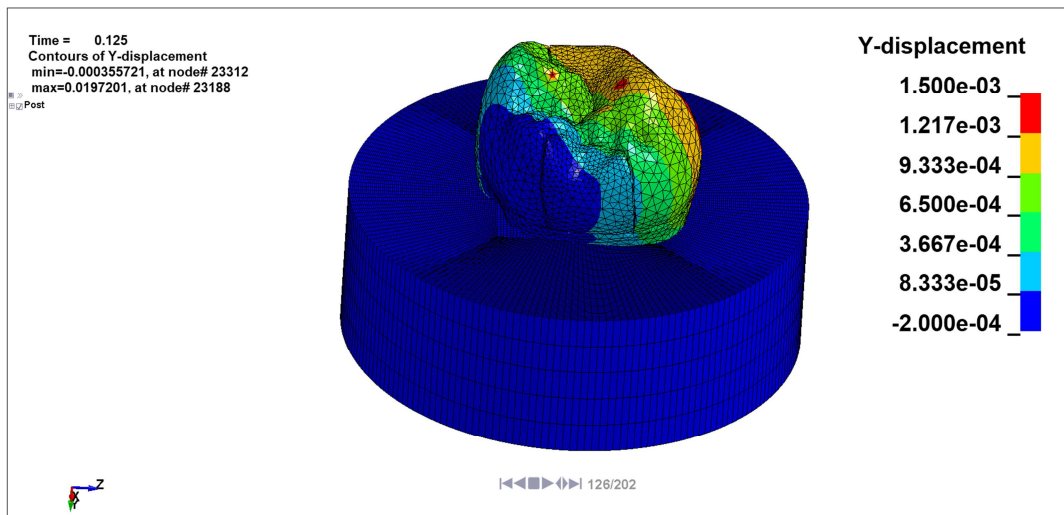


Figure 4.47: Y-axis global displacement, big filler view

Figure 4.48 and Figure 4.49 show the tooth global displacement along z-axis .

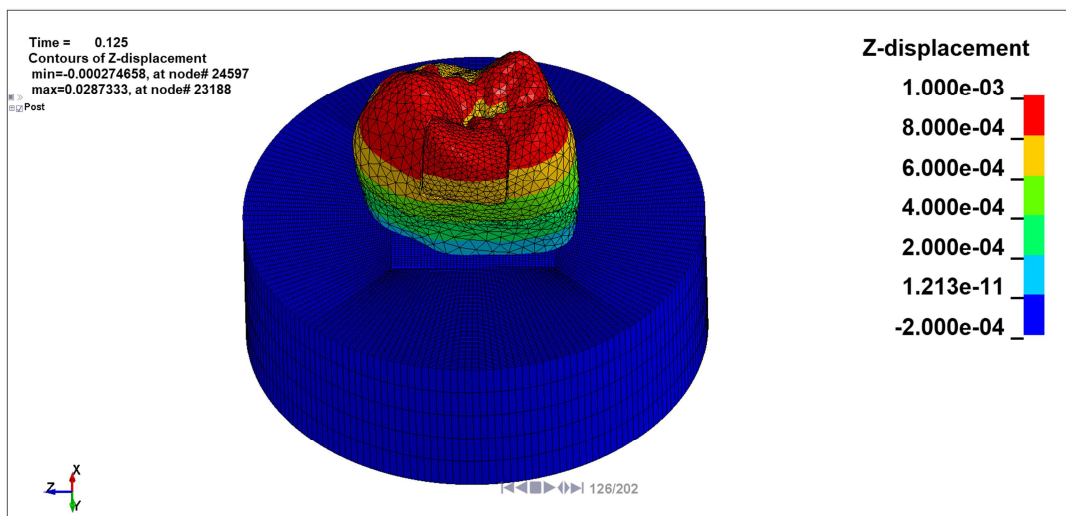


Figure 4.48: Z-axis global displacement, small filler view

4.3. Third model

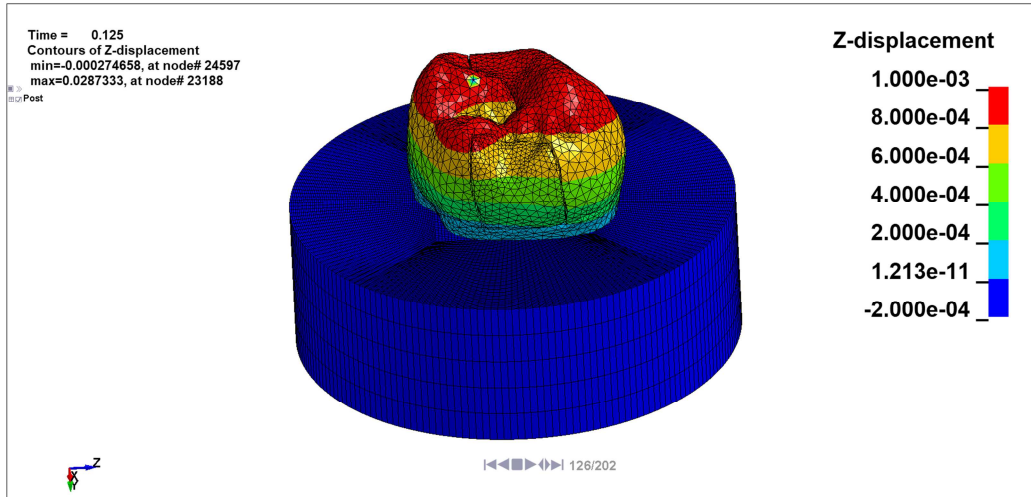


Figure 4.49: Z-axes global displacement, big filler view

The maximum y-axes global displacement for the enamel stood at around 19 μm while the rest of the tooth displacement peak was around 1.4 μm .

Figure 4.46 and Figure 4.47 could be compared with Figure 4.26 and 4.27 showing a slightly different peaks locations, as matter of fact, the maximum vertical displacements values were comparable standing at around 19 μm in the third model and 13 μm in the second ,respectively.

Although, the different enamel peaks locations determined a different colour maps, in both the cases the small filler underwent a major displacement.

In conclusion, the different boundaries conditions deeply influenced tooth global displacement distributions. As discussed in both the first and the second model, a displacement magnification was required to assess which fillers could eventually detach.

A displacement scale factor of 1000 was determined to be sufficient to make out the fillers displacements. Figure 4.50 and Figure 4.51 show two different screenshots of a graphical animation, the first one is the unmagnified tooth displacement whereas the second is the amplified displacement.

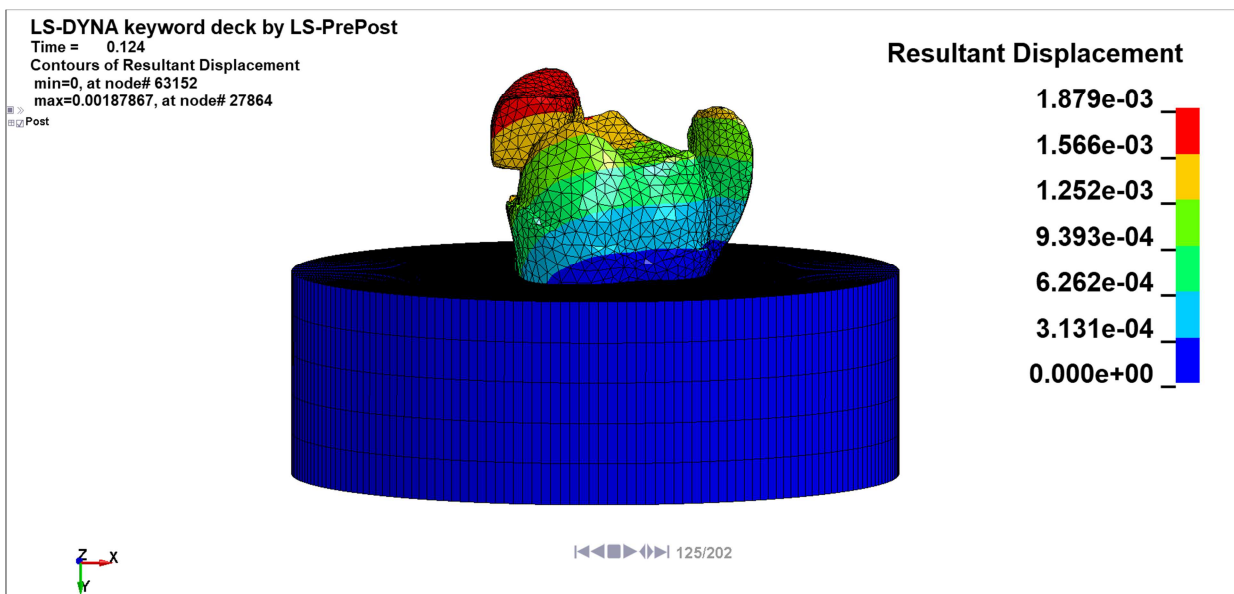


Figure 4.50: Dentine and fillers resultant displacement before the magnification was performed

4. RESULTS AND DISCUSSIONS

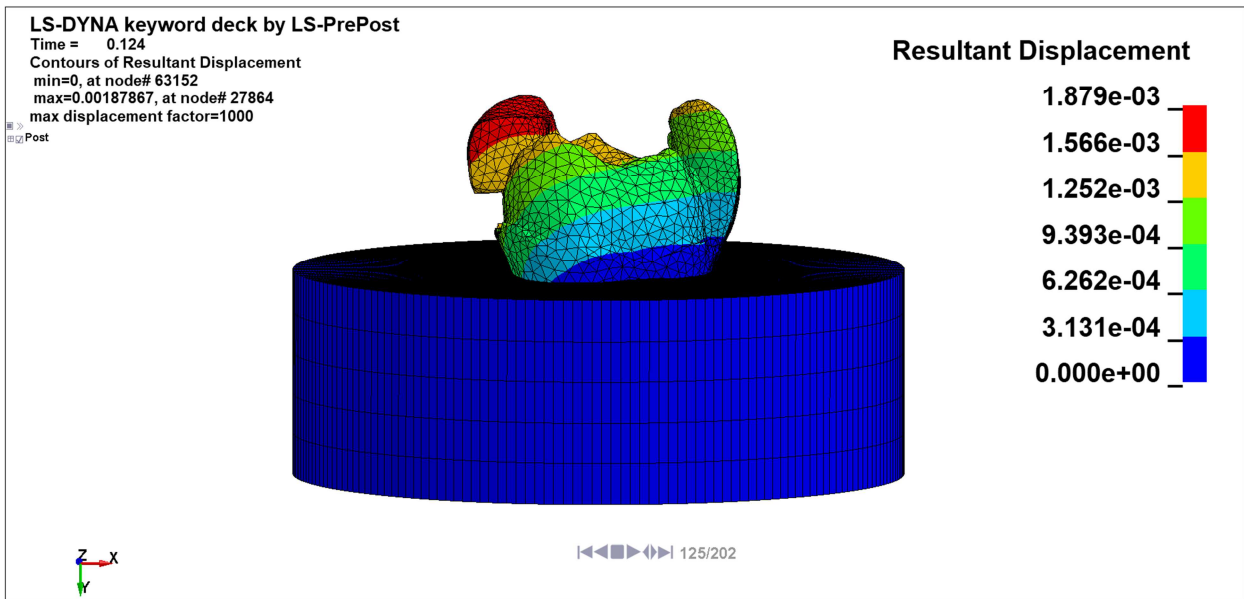


Figure 4.51: Dentine and fillers resultant displacement after the magnification was performed

As shown in Figure 4.51, the small filler moves outside in a debonding direction whereas the big filler shows an inward displacement on the dentine direction, therefore, it is possible to draw the conclusion that debonding phenomena can only occur on the small filler.

This was reasonable considering that the applied load was the same as the second model, despite the deeply different boundaries conditions, the load was proved to determine the global displacements behaviours.

Dentine and enamel global stress along the Cartesian axes was showed to assess the boundaries influence on the global results; Figure 4.52 and Figure 4.53 show x-stress on both the fillers interfaces.

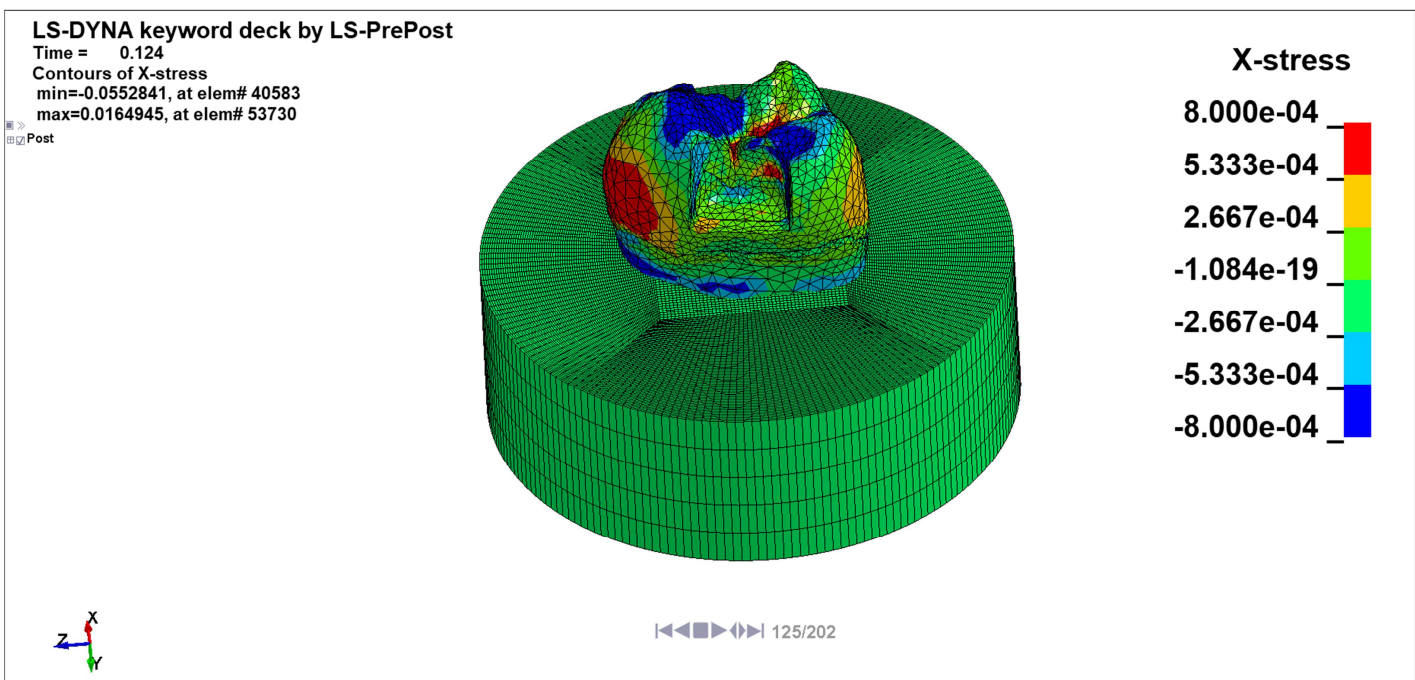


Figure 4.52: Dentine and enamel x-stress , small filler view

4.3. Third model

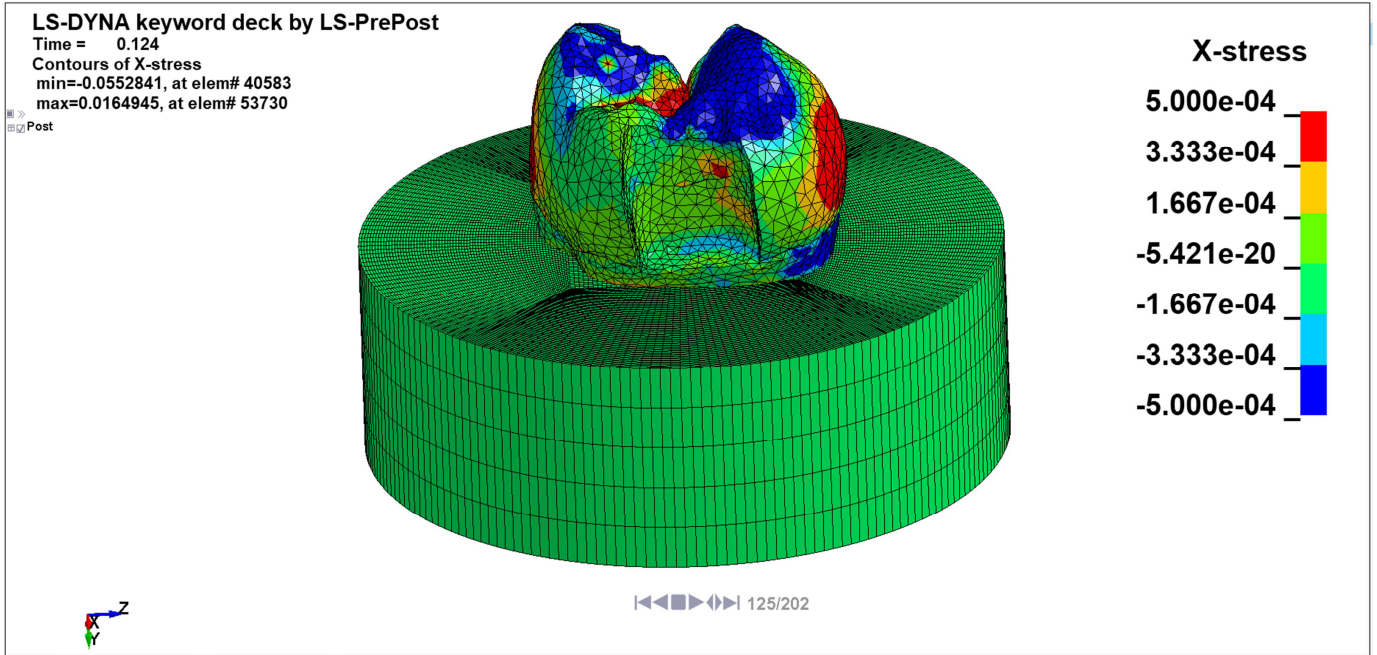


Figure 4.53: Dentine and enamel x-stress , big filler view

The x-axes stress is showed in these figures, stress peaks were present on the rear base and on the upper part of both the fillers interfaces. In general the highest stress were present in the upper regions that were closer to the chewing sphere enamel contact points. Moreover, since two chewing enamel contact point out of three were closer to the small filler, its stress values were generally higher than those of the big filler.

Figure 4.54 and Figure 4.55 show the vertical stress on both the fillers, the small filler presented higher values than the bigger one as previously described for the x-axes stress. This was caused by the chewing sphere action on the enamel, as previously discussed.

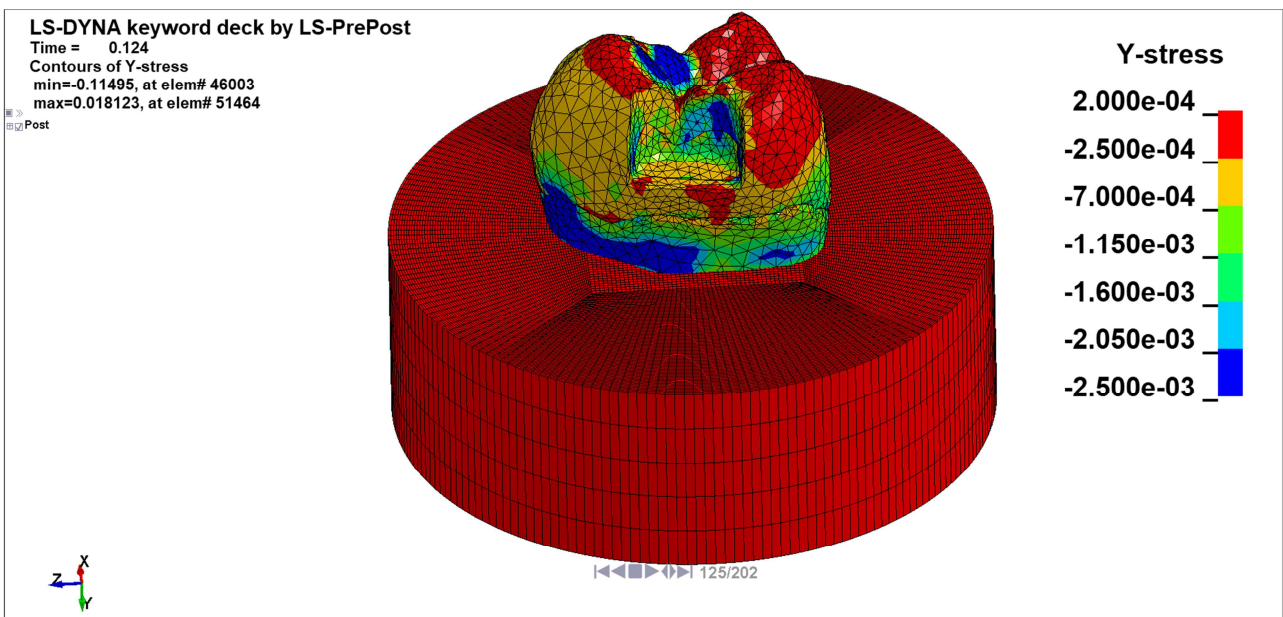


Figure 4.54: Dentine and enamel y-stress , small filler view

4. RESULTS AND DISCUSSIONS

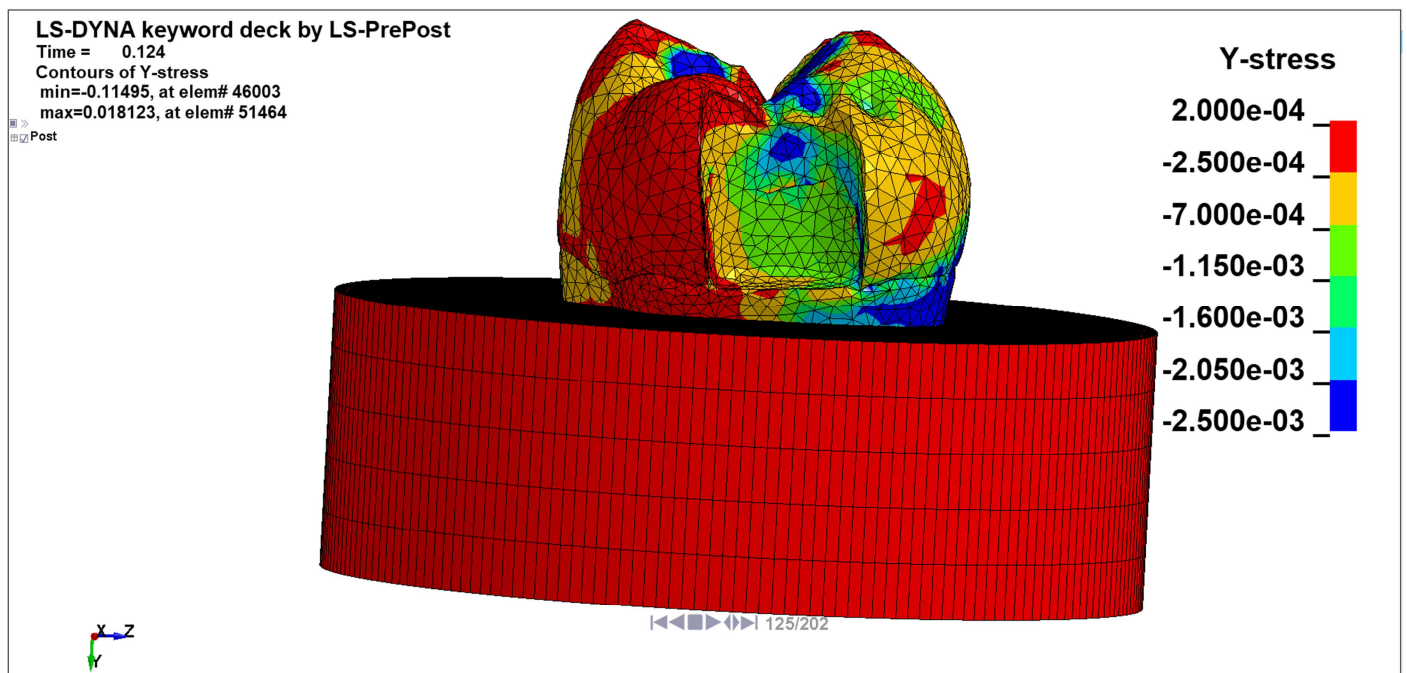


Figure 4.55: Dentine and enamel y-stress , big filler view

The z-axes stress distributions in both the fillers views are illustrated in Figure 4.56 and Figure 4.57

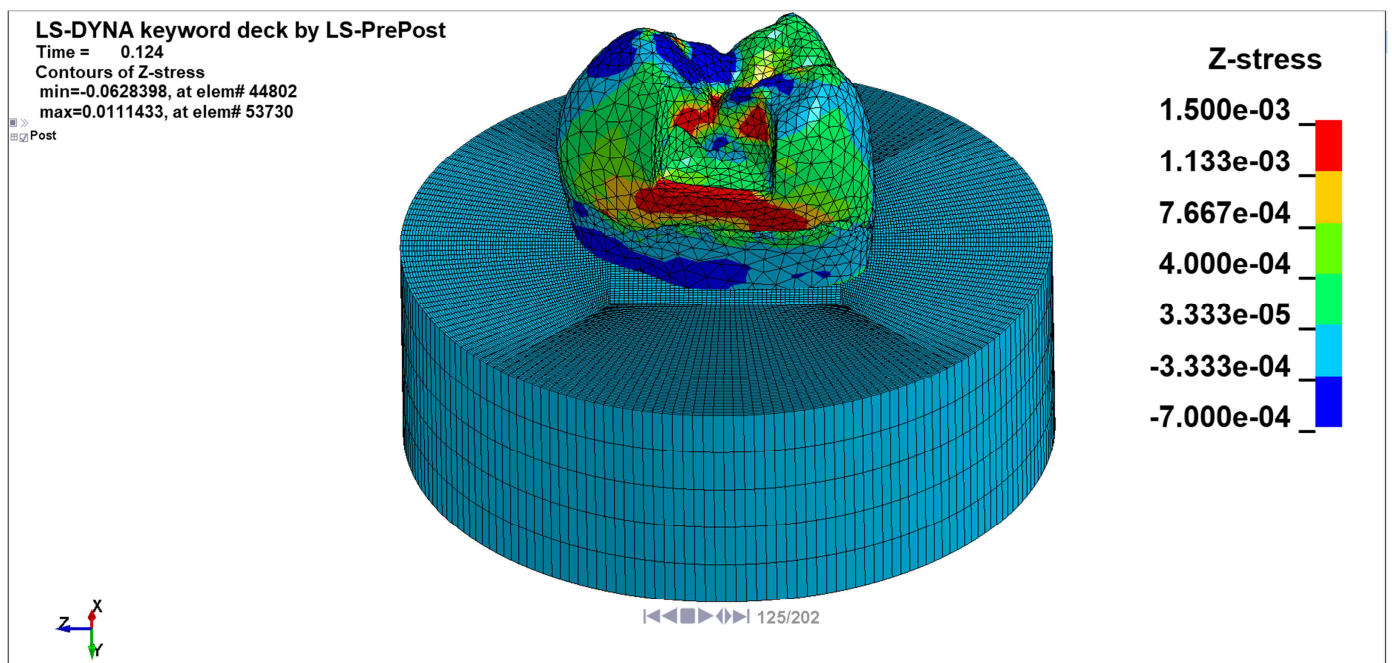


Figure 4.56: Dentine and enamel z-stress , small filler view

4.3. Third model

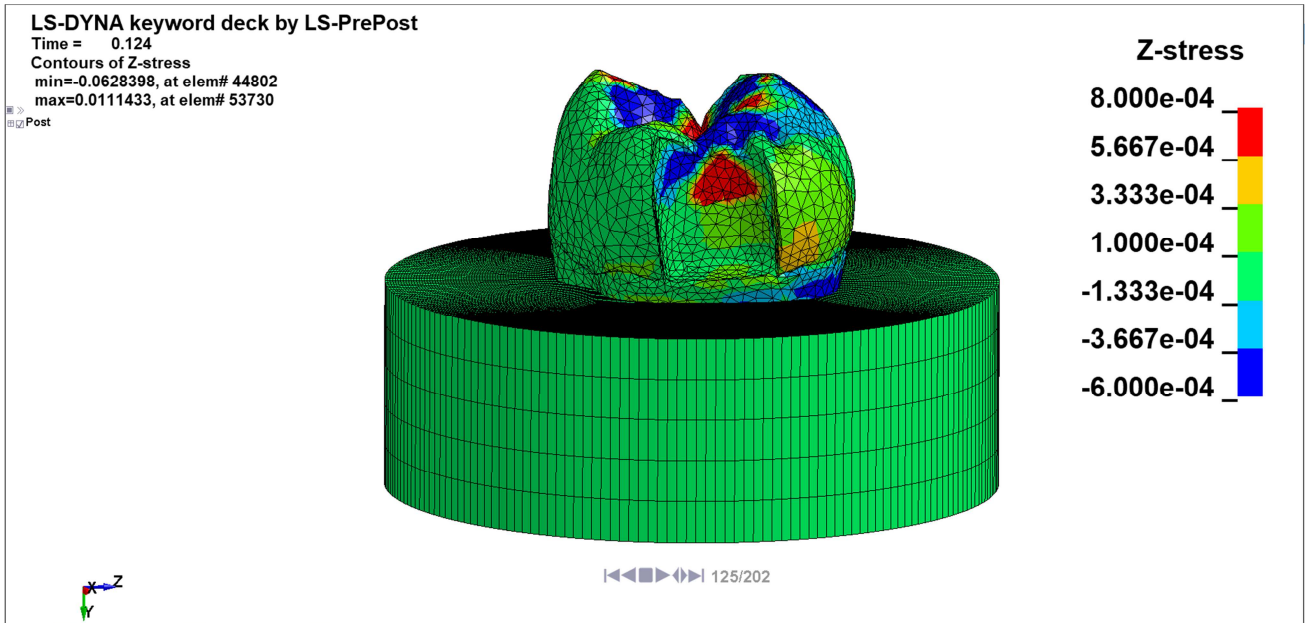


Figure 4.57: Dentine and enamel z-stress , big filler view

The z-stress distribution was quite similar to the y-stress showed in Figure 4.54 and Figure 4.55. As matter of fact, the peaks were almost located in the same regions of the vertical stress and the small filler presented values higher than those of the big filler.

The z-stress numeric values were quite similar to x-stress values but they were not comparable with the compression stress, which was parallel to the load direction.

In summary, the information provided by global stress analysis showed that the peaks were generally located on the enamel fillers interfaces.

Interfaces shear stress and pressure were finally evaluated for both the fillers, as previously discussed in the first model the interface results were substantially incomparable with the global stress distributions. Shear stress was plotted both with colour map and vectors while only vectors were displayed for pressure in order to have a clear visualization of the results.

Furthermore, shear stress were plotted with a rear view wheras pressure were visualized with a frontal view for the above-described reason.

Big filler interface shear stress and pressure are showed in Figure 4.58 and Figure 4.59 while small filler interface distributions are illustrated in Figure 4.60 and Figure 4.61, respectively.

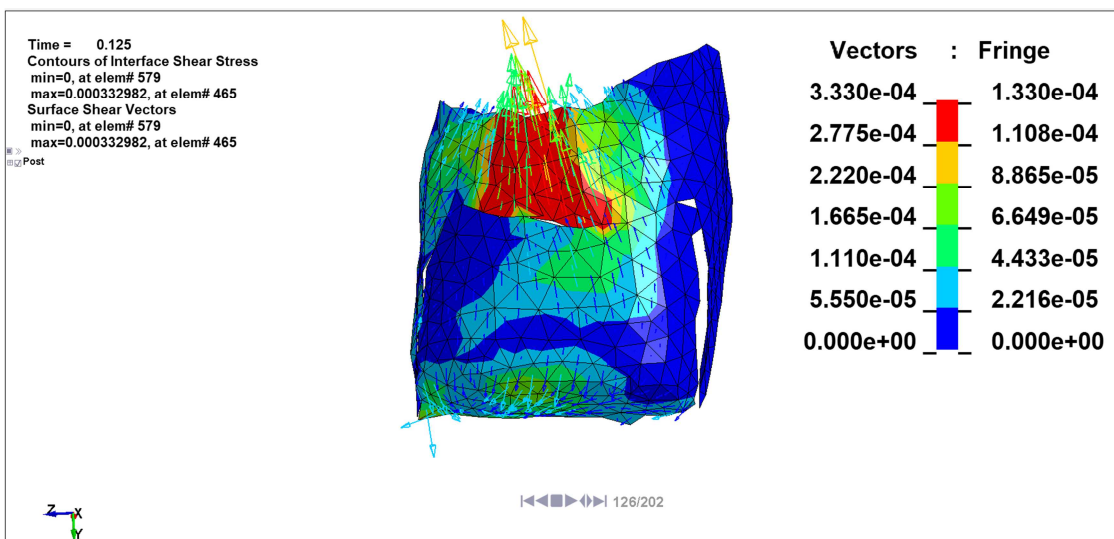


Figure 4.58: Big filler interface shear stress

4. RESULTS AND DISCUSSIONS

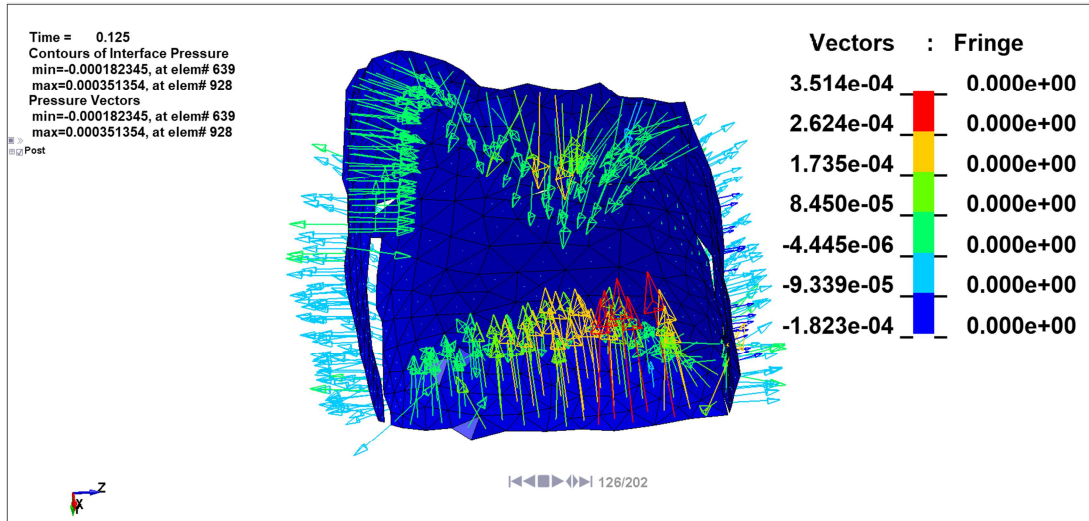


Figure 4.59: Big filler interface pressure

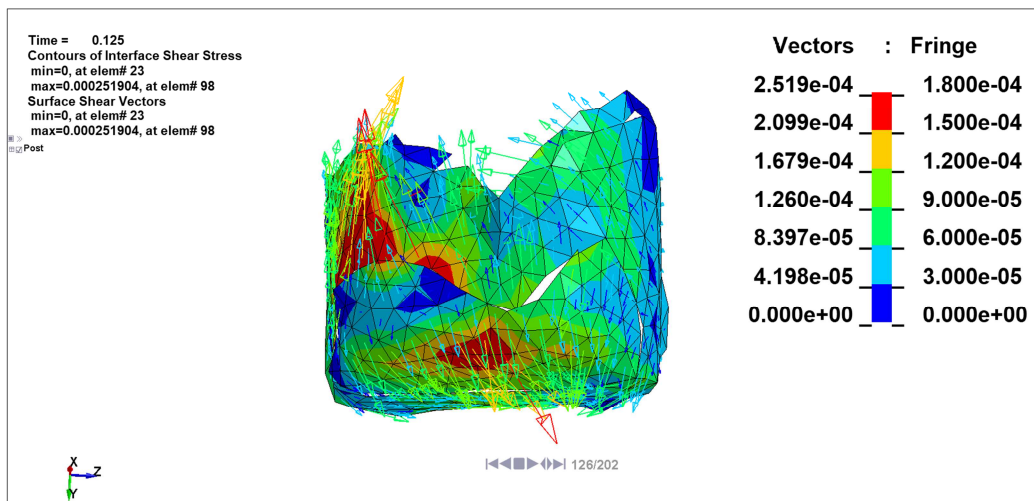


Figure 4.60: Small filler interface shear stress

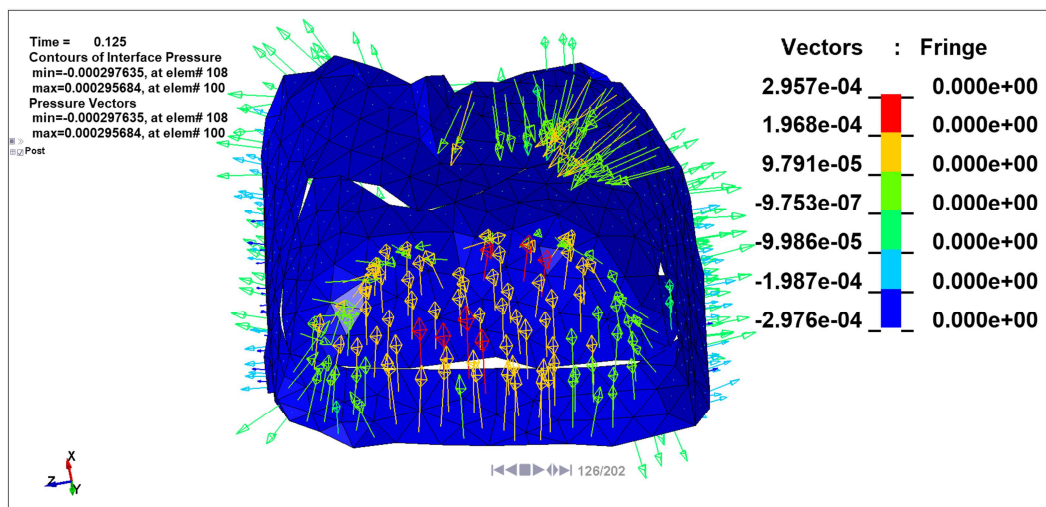


Figure 4.61: Small filler interface pressure

4.3. Third model

As previously explained in this section, debonding phenomena could occur on the small filler and particular attention should be paid on the small interface stress.

As matter of fact, the pressure and shear stress distributions were similar for both the interfaces. Moreover, the enamel fillers interfaces pressure and stress peaks for all the distributions were positioned close to the enamel chewing sphere contact points.

This was coherent with global stress distribution whose peaks were almost located in the same interface regions, it was also interesting notice that the small filler rear base presented a stress peak on its central region in all the global directions.

Despite the three analysed models had different loads and boundaries conditions, the rear base of the small filler presented shear stress peaks in all the models, this was generally verified also for the big filler.

Therefore, it was logical to think that when a vertical load was applied on the tooth, the rear base interfaces regions underwent an high shear stress; the other peaks locations for both the interfaces depended on the applied load.

The second and third model provided an important results, when a load was applied with the chewing sphere the upper interface pressure and shear stress peaks locations were generally as close as possible to the enamel chewing machine contact points.

As consequence of that, it was possible to state that the main difference between the second and the third models was the sphere contact points that led to different stress distributions.

Despite these differences, the results showed were coherent in matter of order of magnitude and peaks regions, which were different for the reasons explained before.

Consequently, boundaries conditions accurate modelling was fundamental to obtain a reliable results. The first method load modelling led to unacceptable results, the main reason lied with the impossibility to model a chewing simulation with the load node set showed in Figure 2.43.

As matter of fact, not all the loaded nodes in the above-mentioned node set were effectively involved in the chewing process. Moreover, the nodes that were effectively involved in the chewing process exerted nodal forces whose values were different point by point, this was in contrast with the first load modelling.

5. CONCLUSIONS

The aim of this work was to define a practical and feasible workflow that allowed to create 3-D FEM model from micro-CT teeth scansions. The purpose of the model creation was to simulate a single chewing load to assess the global and interfaces stress distributions.

The presented results addressed the set goals, the defined workflow allow to simulate a chewing single load cycle in a reasonable time.

The results led to determine the interface shear-stress distributions in all the investigated loading and boundaries conditions, furthermore, global displacements and stress were worked out.

The second and third model presented coherent results, debonding phenomena was likely to occur in the small filler for those models.

Furthermore, the above-mentioned models interface shear stress and pressure showed similar peaks whose locations was as close to the enamel-chewing sphere contact points as possible.

By contrast, the first model showed unrealistic results because of the nodal set load definition.

Some limitations were encountered during the simulations set-up processes, the principal limitations were the loading and boundaries definitions, the materials and the contact modelling. Despite all these aspects were addressed in a careful way , the impact of these choices needed to be quantified by comparing the simulations outputs with the experimental tests results.

The outlooks of this work will be shortly introduced in this section. First, fatigue analysis could be performed in order to assess the restorations detaching phenomena from the tooth during a chewing simulation. Teeth FEM models could be employed to predict the dental filler materials fatigue life before to restore the cavities teeth.

Furthermore, different restorative materials could be investigated on the same FEM model in order to compare their behaviours.

FEM models could be applied to assess direct and indirect restorations impact both on the stress global and interfaces distributions. The optimal restoration could be tuned for a specific surgery.

Another future application could be evaluating the dental instruments mechanical behaviours in teeth surgeries by performing a fatigue analysis. Finally, this work could represent an initial step to investigate all the before-mentioned scenarios.

REFERENCES

- [1] D. H. I. Foundation, «Dental Health Ireland Foundation,» [Online]. Available: <https://www.dentalhealth.ie/dentalhealth/teeth/structureofteeth.html>.
- [2] «Biology dictionary,» 2019. [Online]. Available: <https://biologydictionary.net/teeth/>.
- [3] Nancy, «Ten Cate's Oral Hystology,» Elsevier, p. 194.
- [4] F. Thongcai, «Effect of Periodontal Ligament on Stress Distribution and Displacement of Tooth and Bone Structure Using Finite Element Simulation,» *Engineering Journal*, 2014.
- [5] H. E. T. a. J. Cafasso, «healthline,» 25 5 2018. [Online]. Available: <https://www.healthline.com/health/dental-and-oral-health>.
- [6] W. H. Organization. [Online]. Available: <https://www.who.int/news-room/fact-sheets/detail/oral-health>.
- [7] «Member Benefits,» 2019 4 6. [Online]. Available: <https://memberbenefits.com/dental-costs-with-and-without-insurance/>.
- [8] «WebMD,» 2017 4 5. [Online]. Available: <https://www.webmd.com/oral-health/guide/dental-health-cavities#1..>
- [9] S. Watson, «verywellhealth,» 2019 5 17. [Online]. Available: <https://www.verywellhealth.com/restoration-definition-of-restoration-1059434>.
- [10] wikipedia, «Inlays and onlays,» 2019 10 14. [Online]. Available: https://en.wikipedia.org/wiki/Inlays_and_onlays.
- [11] J. L.Child, «dentaltown,» 1 07 2011. [Online]. Available: <https://www.dentaltown.com/magazine/article/3362/what-is-the-ideal-direct-posterior-restoration>.
- [12] P. A. e. Al., «Mechanical behavior of bulk direct composite versus block composite and lithium disilicate indirect Class II restorations by CAD-FEM modeling,» *Dental Materials*, 2017.
- [13] C. J. S. e. Al., «Scielo,» 28 08 2017. [Online]. Available: http://www.scielo.br/scielo.php?script=sci_arttext&pid=S1806-83242017000500207.
- [14] S. W. MD, «howstuffworks,» [Online]. Available: <https://health.howstuffworks.com/wellness/oral-care/problems/cavity-classifications.html>.
- [15] D. Mark.L.Pitel, «Dentistry today,» 01 02 2017. [Online]. Available: <https://www.dentistrytoday.com/restorative-134/10266-an-improved-glass-ionomer-restorative-system-stress-bearing-class-i-and-ii-indications>.
- [16] V. P. Foster, «dentalcare,» [Online]. Available: <https://www.dentalcare.com/en-us/professional->

education/ce-courses/ce500/surfaces-of-the-teeth.

- [17] A. Gugliotta, *Finit Elements*, Otto, 2002.
- [18] R. d. Francesco, *Fem element method introduction applied to structural and geothecnic analysis*, Flaccovio Dario, 2012.
- [19] N.-H. Kim, *Introduction to Non Linear Fem Analysis*, Springer, 2014.
- [20] M. K. PhD, «Quora,» 2018 3 28. [Online]. Available: <https://www.quora.com/Why-is-the-global-stiffness-matrix-banded-in-FEM>.
- [21] Dr.J.Dean, «Introduction to the Finite Element Method,» [Online]. Available: https://www.ccg.msm.cam.ac.uk/images/FEMOR_Lecture_1.pdf.
- [22] «Cheggstudy,» 2019. [Online]. Available: <https://www.chegg.com/homework-help/questions-and-answers/two-properties-shape-functions-use-shape-functions-1d-2-nodes-shown-following-figure-expla-q10194147>.
- [23] Alian.F.Bower, «Introduction to Finite Element Analysis in Solid Mechanics,» 2012. [Online]. Available: http://solidmechanics.org/text/Chapter7_2/Chapter7_2.htm.
- [24] R. Papalia, «nova-engineers,» 10 10 2018. [Online]. Available: <https://www.nova-engineers.com/rops-simulation>.
- [25] Abaqus, «Linear analyses versus nonlinear analyses,» [Online]. Available: <https://abaqus-docs.mit.edu/2017/English/SIMACAEGSARefMap/simagsa-c-nlnlnvsnonlin.htm>.
- [26] J.-C. Lavocat, «Active photonic devices based on liquid crystal elastomers,» May 2014. [Online]. Available: https://www.researchgate.net/publication/305728176_Active_photonic_devices_based_on_liquid_crystal_elastomers.
- [27] Abaqus, «Sources of non linearities,» [Online]. Available: <https://classes.engineering.wustl.edu/2009/spring/mase5513/abaqus/docs/v6.6/books/gsa/default.htm?startat=ch08s01.html>.
- [28] LS-Dyna, «Contact Stiffness Calculation,» 09 2001. [Online]. Available: <https://www.dynasupport.com/tutorial/contact-modeling-in-ls-dyna/contact-stiffness-calculation>.
- [29] M. M.L.J., «Contact in LS-Dyna,» [Online]. Available: http://164.100.133.129:81/econtent/Uploads/10_Session19and20_LS-DYNA3.pdf.
- [30] LS-Dyna, «Contact modelling in LS-Dyna,» [Online]. Available: <https://www.dynasupport.com/tutorial/ls-dyna-users-guide/contact-modeling-in-ls-dyna>.
- [31] S. C. G. Dogru, «A REVIEW OF FINITE ELEMENT APPLICATIONS IN ORAL AND MAXILLOFACIAL BIOMECHANICS,» *Journal of Mechanics in Medicine and Biology*, 2018.
- [32] Wei-Chih Wang University of Washington, «Photoelasticity,» [Online]. Available: <http://depts.washington.edu/mictech/optics/me557/photoelasticity.pdf>.

REFERENCES

- [33] National Instruments, «Measuring Strain with Strain Gages,» 14 03 2019. [Online]. Available: <https://www.ni.com/it-it/innovations/white-papers/07/measuring-strain-with-strain-gages.html>.
- [34] N. M. DDS, «Finite element contact analysis as a critical technique in dental biomechanics: A review,» *Journal of Prosthodontic Research*, 2014.
- [35] MathWorks, «Image Segmentation,» [Online]. Available: <https://www.mathworks.com/discovery/image-segmentation.html>.
- [36] «wikipedia,» 2018 3 5. [Online]. Available: [https://it.wikipedia.org/wiki/STL_\(file_format\)](https://it.wikipedia.org/wiki/STL_(file_format)).
- [37] CNR, 7 04 2016. [Online]. Available: http://vcg.isti.cnr.it/corsi/G3D_InfoUma/Slides_2016/08_3DScanning_in_MeshLab.pdf.
- [38] Livermore Software Technology Corporation , Ls-Dyna Keyword User's Manual Volume I, 2019.
- [39] A. Harish, «SIMSCALE,» 17 10 2019. [Online]. Available: <https://www.simscale.com/blog/2019/01/implicit-vs-explicit-fem/>.
- [40] W. Rust. [Online]. Available: <https://www.dynalook.com/conferences/european-conf-2001/44.pdf>.
- [41] LS-Dyna, «Tied,Tied-offset and Tiebreak contacts,» [Online]. Available: <https://www.dynasupport.com/howtos/contact/tied-tied-offset-and-tiebreak-contacts>.
- [42] V.Ibeni, «The dentin–enamel junction and the fracture of human teeth,» *Nature materials*, 2005.
- [43] Ls-Dyna, «Contact Output,» [Online]. Available: <https://www.dynasupport.com/tutorial/contact-modeling-in-ls-dyna/contact-output>.
- [44] University of Southern Mississippi, «Uniaxial Loading: Design for Strength, Stiffness, and Stress,» [Online]. Available: https://sites.esm.psu.edu/courses/emch13d/design/design-fund/design-notes/design_axial/axial_8.pdf.
- [45] M. Breveglieri, «Shear strengthening of RC beams using the Embedded Through-Section Technique,» 9 3 2015. [Online]. Available: prints.unife.it/1013/1/Tesi%20Breviglieri.pdf.
- [46] J. M.Gere, *Mechanic of Materials*, Cengage Learning, 2008.
- [47] University of Ferrara, «Simple torque analysis,» [Online]. Available: nife.it/interfacolta/design/insegnamenti/materiali-per-prodotto-industriale/Torsione.pdf.
- [48] A. P. Zaborsky, «Torsion,» [Online]. Available: http://limba.wil.pk.edu.pl/~az/cwicz/class_1.pdf.

RINGRAZIAMENTI

Porgo i miei più sentiti ringraziamenti vanno al Prof. Lorenzo Peroni ed Alessandro Scattina, il loro aiuto è stato prezioso nell' impostazione di un lavoro rigoroso, la loro guida ha consentito di orientarmi all' interno del panorama della modellazione ad elementi finiti.

I miei ringraziamenti vanno anche alla mia famiglia che mi ha sostenuto durante questi anni di sacrifici, a mia madre Susanna, mio padre Giuseppe e mia sorella Vittoria.

Ringrazio infine i miei compagni di viaggio Lucio, Annalisa e Leyla, la loro presenza mi ha alleviato momenti difficili e mi ha dato la forza di andare avanti.